

Generation and Fragmentation of Protein Radical Ions
in
a Fourier-transform Ion Cyclotron Resonance Mass Spectrometer

CHAN, Wai Yi

A Thesis submitted in Partial Fulfillment
of the Requirements of the Degree of
Doctor of Philosophy
in
Chemistry

The Chinese University of Hong Kong
August 2010

UMI Number: 3483859

All rights reserved

INFORMATION TO ALL USERS

The quality of this reproduction is dependent upon the quality of the copy submitted.

In the unlikely event that the author did not send a complete manuscript and there are missing pages, these will be noted. Also, if material had to be removed, a note will indicate the deletion.



UMI 3483859

Copyright 2011 by ProQuest LLC.

All rights reserved. This edition of the work is protected against unauthorized copying under Title 17, United States Code.



ProQuest LLC
789 East Eisenhower Parkway
P.O. Box 1346
Ann Arbor, MI 48106-1346

Thesis/Assessment Committee

Professor To Ngai (Chair)

Professor Tak Wah Dominic Chan (Thesis Supervisor)

Professor Bo Zheng (Committee Member)

Professor Frantisek Turecek (External Examiner)

Professor Zong Wei Cai (Second External Examiner)

ABSTRACT

In order to ascertain the impacts of the structural features of polypeptide and oligosaccharide ions on the dissociation of these biomolecules under typical collision induced dissociation (CID) and electron capture dissociation (ECD) conditions, the dissociation patterns of even-electron precursor ions generated by protonation ($[M+nH]^{n+}$)/metalation ($[Metal+M]^{n+}$), odd-electron hydrogen-deficient precursor ions ($M^{+\bullet}$) generated by SORI-CID of $[Cu(Tpy)M]^{2+}$ and odd-electron hydrogen-surplus precursor ions ($[M+2H]^{+\bullet}$) generated by ECD of $[M+2H]^{2+}$ were examined. It was found that backbone cleavages, with the generation of b/y and c/z ions, were dominant in the dissociation of $[M+H]^+$ and $[M+2H]^{+\bullet}$ respectively. Whilst in the dissociation of $M^{+\bullet}$, side chain loss reactions were the major fragments generated. For post translational modification (PTM)-containing peptides, the labile PTM groups were found to cleave preferentially in the dissociation of $M^{+\bullet}$ and $[M+H]^+$, but were found to be retained in the intact peptides and peptide fragments in the dissociation of $[M+2H]^{+\bullet}$. It is hypothesized that the different dissociation pathways is attributed to the different nature of radicals. Further to these, it was found that in the dissociation of oligosaccharides, similar cleavage patterns (glycosidic and cross-ring cleavages) were obtained regardless of the nature of the precursor ions (i.e. whether odd- or even-electron) and the ion activation conditions.

During the course of the systematic study, it was also discovered that doubly-protonated diarginated peptides containing multiple glutamic acid residues (E) ($n>4$) could suppress the backbone fragmentation of $[M+2H]^{+\bullet}$. Together with the results obtained from conformational searches, it was hypothesized that the interactions between carboxylic oxygens of E side chains and backbone amide hydrogens could stabilize the radical intermediate and thereby inhibiting the usual $N-C_\alpha$ cleavages and H^\bullet loss from $[M+2H]^{+\bullet}$.

摘要

本文著重研究多肽/蛋白質和低聚糖離子結構特徵對於其碰撞誘導裂解 (CID) 及電子捕獲裂解 (ECD) 中裂解反應的影響，分別對質子 ($[M+H]^+$) / 金屬 ($[Metal+M]^{n+}$) 離子化的偶電子前驅離子、銅三吡啶多肽聚合物 ($[Cu(Tpy)M]^{2+}$) 於持續非共振輻照碰撞誘導裂解 (SORI-CID) 中所產生的貧氫奇電子前驅離子 (M^{\bullet}) 以及電子捕獲裂解 (ECD) 所產生的富氫奇電子前驅離子 ($[M+2H]^{\bullet}$) 的裂解模式進行研究。

研究表明對於質子 ($[M+H]^+$) / 金屬 ($[Metal+M]^{n+}$) 離子化的偶電子前驅離子和富氫奇電子前驅離子 ($[M+2H]^{\bullet}$) 在裂解的過程中，主要是主鏈斷裂，產生 *b/y* 和 *c/z* 類型的碎片離子。對於貧氫奇電子前驅離子 (M^{\bullet})，則主要是支鏈裂解。對含有翻譯後修飾的肽，在質子 ($[M+H]^+$) / 金屬 ($[Metal+M]^{n+}$) 離子化的偶電子前驅離子和貧氫奇電子前驅離子 (M^{\bullet}) 裂解中，其不穩定官能團將優先斷裂；而在富氫奇電子前驅離子 ($[M+2H]^{\bullet}$) 的裂解中，則會保留。由此推斷雜原子自由基和氫原子自由基可能會促進特定的裂解反應通道。另外在進一步對於低聚糖分子的研究中發現，無論是何種類型的前驅離子以及離子活化方法，都會發生相類似的糖苷和環斷裂的裂解方式。

在以上系統的研究中，還發現谷氨酸 (E) (>4) 能夠抑止含雙精氨酸的富氫奇電子肽離子 ($[M+2H]^{\bullet}$) 主鏈碎片離子的產生。通過這項試驗現象和構像搜索發現谷氨酸支鏈羧基氧與主鏈酰胺氫原子相互作用能夠穩定中間體自由基，由此抑止常規的 N-C α 鍵斷裂和富氫肽離子氫原子解離。

ACKNOWLEDGMENTS

I would like to express my heartfelt gratitude to the following persons for making this four-year study a fruitful and rewarding experience:

- ∞ My supervisor, Prof. Dominic T. W. Chan, for his invaluable guidance, advice, patience and encouragements. He has kindly enriched my knowledge and widen my horizon by offering me the opportunity to go overseas for a research project in University of Warwick, United Kingdom;
- ∞ Prof. Peter B. O'Connor and his group members, for their enlightenments during my five-month visit in the University of Warwick. My additional thanks to them for their warm welcome and treating me as part of their group;
- ∞ Mr. Chi Chiu Chan and Mr. Ka Fai Woo, for their assistance in rendering instrumental services and resolving computer-related problems;
- ∞ My group members and colleagues, including Dr. Eva Yi Man Fung, Ms. Pui Kwan Chan, Dr. Ka Wai Chan, Ms. Po Yan Ng, Ms. Linlin Zhang, Mr. Chung Hong Cheung, Dr. Lifeng Yang, Mr. King Ho So, Mr. Xiangfeng Chen, Ms. Fan Chen, Ms. Pui Shuen Wong, Mr. Kwok Chun Li and Ms. Hoi Sze Yeung, for their valuable help and companionship during my study;
- ∞ Ms. Miu Yin Pong, for proof reading the manuscript for this thesis;
- ∞ My family, Mr. Yiu Nam Tang and my friends, for their unfailing support and continuous encouragements. I particularly wish to thank my parents and my sister, Ms. Hoi Yi Chan, for their staunch support and care-taking; and
- ∞ The Research Grants Council of the Hong Kong Special Administrative Region, China (RGC 400207), the Overseas Academic Activities Grants and the University Postgraduate Studentship from Graduate School, for their financial support.

TABLE OF CONTENTS

| | Page |
|-----------------------------------------------------------------------------------|------|
| Title Page | i |
| Abstract (English) | ii |
| Abstract (Chinese) | iii |
| Acknowledgements | iv |
| Table of Contents | v |
| List of Tables | ix |
| List of Figures | x |
| List of Schemes | xiii |
| Abbreviations | xiv |
| Dedication | xvi |
| | |
| Chapter 1 Introduction | |
| 1.1 Mass spectrometry of biomolecules | 1 |
| 1.2 Tandem mass spectrometry | 4 |
| 1.2.1 Nomenclature of peptide and oligosaccharide fragments | 5 |
| 1.2.2 Dissociation of protonated peptide ions | 6 |
| 1.2.2.1 CID of protonated peptide ions | 6 |
| 1.2.3 Dissociation of protonated/metalated peptide ions via radical intermediates | 8 |
| 1.2.3.1 ECD of protonated peptide ions | 9 |
| 1.2.3.2 CID of non-covalent complex of peptides | 11 |
| 1.3 Dissociation of peptide radical ions | 12 |
| 1.4 Overview of the project | 14 |
| | |
| Chapter 2 Instrumentation and Experimental Conditions | |
| 2.1 Fourier-transform ion cyclotron resonance mass spectrometry | 16 |
| 2.1.1 Instrumental principle | 16 |
| 2.1.2 Instrument | 20 |
| 2.1.2.1 Vacuum system | 20 |
| 2.1.2.2 Nanospray source | 23 |
| 2.1.2.3 Electrostatic ion focusing system | 25 |
| 2.1.2.4 Analyzer cell and electron emission source | 26 |
| 2.1.2.5 Data acquisition system | 30 |
| 2.2 Experimental Conditions | 30 |

| | | |
|-----------------------------------------------------------------------------------------------------------------|----------------------------------------------------------------------------------------------------------------------------------------------------------------------------------------------------------------------------|----|
| 2.2.1 | Sample preparation | 30 |
| 2.2.2 | Acquisition pulse program | 31 |
| 2.2.2.1 | MS with or without multiple-ion filling | 31 |
| 2.2.2.2 | MS ² with or without double resonance ion ejection | 33 |
| 2.2.2.3 | MS ³ | 40 |
| 2.2.3 | Calculation | 40 |
| 2.2.3.1 | <i>Ab initio</i> and Density functional theory (DFT) calculation | 40 |
| 2.2.3.2 | Molecular mechanics calculation | 41 |
| | | |
| Chapter 3 Direct Comparison of Fragmentation Patterns between Different Types of Peptide Radical Cations | | |
| 3.1 | Introduction | 42 |
| 3.2 | Experimental section | 43 |
| 3.3 | Results and Discussion | 45 |
| 3.3.1 | The G ₉ X and G ₄ XG ₄ K series | 45 |
| 3.3.1.1 | SORI-CID of [Cu(Tpy)M] ²⁺ | 45 |
| 3.3.1.2 | SORI-CID of M ⁺⁺ | 47 |
| 3.3.1.3 | Comparison between SORI-CID of [M+H] ⁺ , M ⁺⁺ and ECD of [M+2H] ²⁺ | 57 |
| 3.3.2 | The ZG ₅ XG ₅ Z' series | 61 |
| 3.3.2.1 | SORI-CID of [Cu(Tpy)(M+H)] ³⁺ | 61 |
| 3.3.2.2 | Comparison between SORI-CID of [M+H] ²⁺⁺ and ECD of [M+3H] ³⁺ | 67 |
| 3.3.2.3 | Comparison of [Cu(Tpy)(M+H)] ³⁺ between MS ² and MS ³ | 70 |
| 3.4 | Conclusion | 70 |
| | | |
| Chapter 4 Probing Structural Effect of Radical Cations on their Generation and Fragmentation | | |
| 4.1 | Introduction | 72 |
| 4.2 | Experiment section | 74 |
| 4.3 | Results and Discussion | 75 |
| 4.3.1 | Comparison of fragmentation patterns between peptide radical cations (M ⁺⁺ and [M+2H] ⁺⁺) and protonated peptides ([M+H] ⁺) with post-translational modification(s) containing peptides | 75 |

| | | |
|---------|--------------------------------------------------------------------------------------------------------------------------------------------|-----|
| 4.3.1.1 | SORI-CID of $[\text{Cu}(\text{Tpy})\text{M}]^{2+}$ | 75 |
| 4.3.1.2 | Dissociation patterns of methionine and oxidized methionine containing model peptides | 81 |
| 4.3.1.3 | Dissociation patterns of serine and phosphorylated serine containing model peptides | 84 |
| 4.3.1.4 | Comparison of dissociation patterns between $[\text{M}+\text{H}]^+$, M^+ and $[\text{M}+2\text{H}]^{2+}$ | 86 |
| 4.3.2 | Analysis of the Fragmentation Patterns of Copper Ternary Complexes and Metal-adducted Oligosaccharide under SORI-CID and/or ECD conditions | 90 |
| 4.3.2.1 | General features of spectra | 90 |
| 4.3.2.2 | Comparison between SORI-CID and ECD of $[\text{Cu}+\text{M}]^{2+}$ | 95 |
| 4.3.2.3 | Comparison of SORI-CID of $[\text{Cu}(\text{Tpy})\text{M}]^{2+}$ with $[\text{Cu}+\text{M}]^{2+}$ | 98 |
| 4.3.3 | An Investigation of the Effect of Non-Covalent binding of (12-crown-4) on Peptide Dissociation under ECD conditions | 101 |
| 4.3.3.1 | General features of spectra | 101 |
| 4.3.3.2 | DR-ECD experiments | 106 |
| 4.3.3.3 | Comparison of ECD dissociation patterns between $[\text{L}+(\text{M}+2\text{H})]^{2+}$ and $[\text{M}+2\text{H}]^{2+}$ | 109 |
| 4.3.3.4 | ECD fragmentation efficiency of $[\text{L}+(\text{M}+2\text{H})]^{2+}$ and $[\text{M}+2\text{H}]^{2+}$ | 113 |
| 4.3.3.5 | Comparison between ECD and ECID | 114 |
| 4.4 | Conclusion | 116 |

Chapter 5 Natural Structural Motifs that Suppress Peptide Ion Fragmentation after Electron Capture

| | | |
|-------|---------------------------------------------------------------------------------------|-----|
| 5.1 | Introduction | 120 |
| 5.2 | Experimental section | 122 |
| 5.3 | Results and Discussion | 123 |
| 5.3.1 | General features of ECD spectra of doubly protonated peptides | 123 |
| 5.3.2 | Comparison between ECD of $[\text{M}+2\text{H}]^{2+}$ and $[\text{M}+3\text{H}]^{3+}$ | 127 |
| 5.3.3 | Fibrinopeptide-B and its analogue | 129 |
| 5.3.4 | Structural motif that suppresses backbone cleavages in diarginated E-rich peptides | 131 |
| 5.4 | Conclusion | 141 |

| | | |
|------------------|------------------------------------------------------------------------------------------------|-----|
| Chapter 6 | Conclusions | 143 |
| References | | 145 |
| Appendix I | Proposed dissociation mechanisms of protonated peptide under low-energy CID conditions | 153 |
| Appendix II | Pulse programs for MS and MS _n experiments | 156 |
| Appendix III | Assignments of labeled side chain in mass spectra | 162 |
| Appendix IV | The hydrogen bonding patterns of the low-energy structures obtained in conformational searches | 163 |

LIST OF TABLES

| Table | | Page |
|-------|-------------------------------------------------------------------------------------------------------------------------------------------------------------------------------------------------------------------------------------------------------------------------------------------------------------------------------------------------|------|
| 3.1 | Relative abundance of SORI-CID fragments of $[\text{Cu}(\text{Tpy})\text{G}_9\text{X}]^{2+}$ and $[\text{Cu}(\text{Tpy})\text{G}_4\text{XG}_4\text{K}]^{2+}$. (%) | 48 |
| 3.2 | Relative abundance of SORI-CID fragments of $\text{G}_4\text{XG}_4\text{K}^{++}$ (M^{++}). (%) | 52 |
| 3.3 | Small fragments loss from the precursor ion and z_n^{++} in CID and ECD with peptides GGGGXGGGGK, where X is I, L, S, E and W. | 60 |
| 3.4 | Relative abundance of SORI-CID fragments of $[\text{Cu}(\text{Tpy})-(\text{ZG}_5\text{WG}_5\text{Z}'+\text{H})]^{3+}$. (%) | 66 |
| 4.1 | Relative abundance of SORI-CID fragments of $[\text{Cu}(\text{Tpy})-\text{G}_4\text{XG}_4\text{R}]^{2+}$ and $[\text{Cu}(\text{Tpy})\text{INSMLPR}]^{2+}$ (with PTM(s)). (%) | 79 |
| 4.2 | Types of side chain loss during the dissociation of CID of $[\text{M}+\text{H}]^+$; $[\text{Cu}(\text{Tpy})\text{M}]^{2+}$ and M^{++} ; ECD of $[\text{M}+2\text{H}]^{2+}$ relative to the most intense peak in the spectrum. (%) | 89 |
| 4.3 | Relative abundance of fragments species of $[\text{Cu}(\text{Tpy})\text{M}]^{2+}$ and $[\text{Cu}+\text{M}]^{2+}$ under SORI-CID and ECD conditions. (%) | 94 |
| 4.4 | Summary of spectral information in DR-ECD experiments of $[\text{L}+(\text{M}+2\text{H})]^{2+}$, where L is 12-crown-4 and M is INSMLPR. | 107 |
| 4.5 | Relative abundance and sum of fragment ions related to $[\text{M}+2\text{H}]^{++}$ and z_n^{++} in ECD of $[\text{L}+(\text{M}+2\text{H})]^{2+}$ and $[\text{M}+2\text{H}]^{2+}$, where L is 12-crown-4. (%) | 110 |
| 4.6 | Relative abundance of odd- and even-electron M and L side chain(s) loss from $[\text{M}+2\text{H}]^{++}$ and z_n^{++} in ECD of $[\text{L}+(\text{M}+2\text{H})]^{2+}$ and $[\text{M}+2\text{H}]^{2+}$, where L is 12-crown-4. (%) | 112 |
| 5.1 | Summary of fragment peaks of $[\text{RGE GEGEGEGEGEGEGR}+2\text{H}]^{2+}$ (i) under typical ECD conditions; (ii) with an extended time delay (3 s) after the electron irradiation prior to the ion excitation and detection; and (iii) with subsequent pulsing of inert gas after the electron irradiation event and followed with a 3 s delay. | 135 |
| 5.2 | Distribution of H-bond formed at backbone amide linkages of the lowest energy structures of RGE GEGEGEGEGEGEGR (contributed more than 1%) in zwitterionic form (salt bridge formed between N- and C-terminus) obtaining from conformational search. | 137 |

LIST OF FIGURES

| Figure | | Page |
|--------|-------------------------------------------------------------------------------------------------------------------------------------------------------------------------------------------------------------------------------------------------------------------|------|
| 2.1 | Schematic diagram of a typical ICR analyzer cell. | 17 |
| 2.2 | Schematic diagram of the Bruker APEX III 4.7T FTICR-MS equipped with an electrospray ion source. | 21 |
| 2.3 | Schematic diagram of the Bruker APEX III 4.7T FTICR-MS equipped with a homemade nanospray ion source. | 24 |
| 2.4 | Schematic diagram of the ion optics inside the FTICR-MS with their typical potential gradient curve. | 27 |
| 2.5 | Schematic diagram of the heated filament electron source with the analyzer cell. | 29 |
| 2.6 | Pulse sequence program for ESI-FTICR-MS experiments. | 34 |
| 2.7 | Pulse sequence program for MIF-FTICR-MS experiments. | 35 |
| 2.8 | ECD spectra of substance P (a) without and (b) with using MIF. | 36 |
| 2.9 | Pulse sequence program for ESI-(SORI-CID)-FTICR-MS experiments. | 38 |
| 2.10 | Pulse sequence program for ESI-(ECD/DR-ECD)-FTICR-MS experiments. | 39 |
| 3.1 | Typical SORI-CID spectra of $[\text{Cu}(\text{L})\text{M}]^{2+}$, where L is Tpy and M is (a) G ₉ I, (b) G ₉ W, (c) G ₄ IG ₄ K and (d) G ₄ WG ₄ K. | 46 |
| 3.2 | Typical SORI-CID spectra of $\text{G}_4\text{XG}_4\text{K}^{2+}$, where X is (a) I, (b) E and (c) W. | 49 |
| 3.3 | Three binding modes of truncated peptide binding to the copper-terpyridine complex. | 54 |
| 3.4 | Typical mass spectra of G ₄ LG ₄ K (M) in (a) SORI-CID of $[\text{M}+\text{H}]^+$, (b) SORI-CID of M^{2+} and (c) ECD of $[\text{M}+2\text{H}]^{2+}$. | 58 |
| 3.5 | SORI-CID mass spectra of $[\text{Cu}(\text{L})(\text{M}+\text{H})]^{3+}$, where L is Tpy and M is (a) RG ₅ WG ₅ R, (b) RG ₅ WG ₅ K, (c) KG ₅ WG ₅ R and (d) KG ₅ WG ₅ K. | 63 |
| 3.6 | SORI-CID mass spectra of $[\text{Cu}(\text{Tpy})(\text{M}+\text{H})]^{3+}$, where M is (a) RG ₅ WG ₅ H, (b) HG ₅ WG ₅ R and (c) HG ₅ WG ₅ H. | 64 |

| Figure | | Page |
|--------|------------------------------------------------------------------------------------------------------------------------------------------------------------------------------------------------------------------------------------------------------------------------------------------------|------|
| 3.7 | Dissociation patterns of (a) SORI-CID of $[\text{RG}_5\text{WG}_5\text{K}+\text{H}]^{2+}$, (b) SORI-CID of $[\text{KG}_5\text{WG}_5\text{R}+\text{H}]^{2+}$, (c) ECD of $[\text{RG}_5\text{WG}_5\text{K}+3\text{H}]^{3+}$ and (d) ECD of $[\text{KG}_5\text{WG}_5\text{R}+3\text{H}]^{3+}$. | 68 |
| 4.1 | SORI-CID spectra of $[\text{Cu}(\text{L})\text{G}_4\text{XG}_4\text{R}]^{2+}$, where L is Tpy and X is (a) M, (b) M(O), (c) S and (d) pS. | 77 |
| 4.2 | SORI-CID spectra of $[\text{Cu}(\text{L})\text{M}]^{2+}$, where L is Tpy and M is (a) INSMLPR, (b) INSM(O)LPR and (c) INpSMLPR. | 78 |
| 4.3 | Mass spectra of $\text{G}_4\text{MG}_4\text{R}$ (M) in (a) SORI-CID of $[\text{M}+\text{H}]^+$; (b) SORI-CID of M^{++} ; and (c) ECD of $[\text{M}+2\text{H}]^{2+}$. | 82 |
| 4.4 | Mass spectra of $\text{G}_4\text{M}(\text{O})\text{G}_4\text{R}$ (M) in (a) SORI-CID of $[\text{M}+\text{H}]^+$; (b) SORI-CID of M^{++} ; and (c) ECD of $[\text{M}+2\text{H}]^{2+}$. | 83 |
| 4.5 | Typical mass spectra of (a) SORI-CID of $[\text{G}_4\text{SG}_4\text{R}+\text{H}]^+$, (b) ECD of $[\text{G}_4\text{SG}_4\text{R}+2\text{H}]^{2+}$, (c) SORI-CID of $[\text{G}_4\text{pSG}_4\text{R}+\text{H}]^+$ and (d) ECD of $[\text{G}_4\text{pSG}_4\text{R}+2\text{H}]^{2+}$. | 85 |
| 4.6 | Dissociation patterns of (a) SORI-CID of $[\text{Cu}(\text{L})\text{M}]^{2+}$, (b) SORI-CID of $[\text{Cu}+\text{M}]^{2+}$ and (c) ECD of $[\text{Cu}+\text{M}]^{2+}$, where L is Tpy and M is maltoheptaose. | 91 |
| 4.7 | Dissociation patterns of (a) SORI-CID of $[\text{Cu}(\text{L})\text{M}]^{2+}$, (b) SORI-CID of $[\text{Cu}+\text{M}]^{2+}$ and (c) ECD of $[\text{Cu}+\text{M}]^{2+}$, where L is Tpy and M is 3 α ,6 α -mannopentaose. | 93 |
| 4.8 | The low-energy structures of (a) $[\text{Cu}(\text{Tpy})\text{M}]^{2+}$ and (b) $[\text{Cu}+\text{M}]^{2+}$ obtained by conformational searches. The dotted lines represent the interactions between the copper center and the oligosaccharide (interactions with ligand were also included). | 100 |
| 4.9 | ECD mass spectra of (a) $[\text{L}+(\text{M}+2\text{H})]^{2+}$ and (b) $[\text{M}+2\text{H}]^{2+}$, where L is 12-crown-4 and M is ENSMLPR. | 103 |
| 4.10 | Mass spectra of $[\text{L}+(\text{M}+2\text{H})]^{2+}$ (a) ECD, (b) DR-ECD of $[\text{M}+2\text{H}]^{2+}$ and (c) DR-ECD of $[\text{M}+2\text{H}]^{++}$, where L is 12-crown-4 and M is INSMLPR. | 105 |
| 4.11 | The calculated ECD fragmentation efficiency values of $[\text{L}+(\text{M}+2\text{H})]^{2+}$ and $[\text{M}+2\text{H}]^{2+}$, where L is 12-crown-4. | 115 |

| Figure | | Page |
|--------|---------------------------------------------------------------------------------------------------------------------------------------------------------------------------------------------------------------------------------------------------------------------------------------------|------|
| 5.1 | Typical ECD spectra of $[M+2H]^{2+}$, where M is (a) RGGGGEGGGEGGGGR, (b) RGE GGEGGGEGGEGGR and (c) RGE GEGEGEGEGEGEGGR. | 124 |
| 5.2 | (a) Percentage loss of H ⁺ loss from $[M+2H]^{2+}$ of diarginated model peptides and (b) Probability for dissociation in ECD of diarginated model peptides. | 126 |
| 5.3 | Typical ECD spectra of $[M+3H]^{3+}$, where M is (a) RGGGGEGGGEGGGGR, (b) RGE GGEGGGEGGEGGEGGR and (c) RGE GEGEGEGEGEGEGEGGR. | 128 |
| 5.4 | ECD spectra of (a) $[M+2H]^{2+}$ and (b) $[M+3H]^{3+}$ where M is N-arginated Fibrinopeptide-B. | 130 |
| 5.5 | Typical ECD spectra of $[M+2H]^{2+}$ where M is (a) EGVNDNEEGFFSAR (Fribinopeptide-B) and its analogue (b) REGVNDNEEGFFSA. | 132 |
| 5.6 | ECD spectra of $[RGE GEGEGEGEGEGEGEGGR+2H]^{2+}$ (a) with an extended time delay (3 s) after the electron irradiation prior to the ion excitation and detection; and (b) with subsequent pulsing of inert gas (1.2ms) after the electron irradiation event and followed with a delay (3 s). | 134 |
| 5.7 | The lowest energy zwitterion structures of $[RGE GEGEGEGEGEGEGEGGR+2H]^{2+}$ obtained by conformational search. Hydrogen bonds between carboxylic oxygen of E side chain and backbone amide hydrogen are illustrated by dotted lines. | 139 |

LIST OF SCHEMES

| Scheme | | Page |
|--------|---------------------------------------------------------------------------------------------------------------------------------------------------------------------------------------------------------------------------|------|
| 1.1 | The cleaving sites and the notations of peptide fragments. | 5 |
| 1.2 | The cleaving positions and notations of oligosaccharide fragments. | 6 |
| 1.3 | Cornell mechanism for ECD of peptide ions. | 10 |
| 1.4 | Utah-Washington mechanism for ECD in ground and excited electronic states of peptide ions. | 11 |
| 3.1 | The proposed dissociation pathways of (a) K even-electron side chain loss from M^{++} , (b) L odd-electron side chain loss from M^{++} , (c) z ion. | 50 |
| 3.2 | Dissociation pathway of of $[Cu^{II}(Tpy)M]^+$, where M is truncated peptide, using B3LYP/6-31+G(d,p)[C,H,N,O]/ECP/LANL2DZ[Cu]//B3LYP/3-21G(d)[C,H,N,O]/ECP/LANL2DZ[Cu]. | 55 |
| 3.3 | Dissociation pathway of of $[Cu^{II}(Tpy)M]^+$ for bm2 and bm3, where M is truncated peptide, using B3LYP/6-31+G(d,p)[C,H,N,O]/ECP/LANL2DZ[Cu]//B3LYP/3-21G(d)[C,H,N,O]/ECP/LANL2DZ[Cu]. | 56 |
| 3.4 | A proposed dissociation pathway of the consecutive loss of NH_3 and side chain. | 62 |
| 4.1 | The proposed dissociation pathways of odd- and even-electron M(O) side chain (a) CH_3SO^{\bullet} , (b) CH_2SO^{\bullet} , (c) $C_2H_5SO^{\bullet}$ and (d) $C_3H_6SO^{\bullet}$ loss from heteratom peptide radical. | 87 |
| 4.2 | The proposed dissociation pathways of odd- and even-electron pS side chain (a) $H_2PO_4^{\bullet}$ and (b) PO_3^{\bullet} loss from heteratom peptide radical. | 88 |
| 4.3 | Proposed dissociation pathway of (a) Z_n^+ , (b) B_n^+ (further dissociate to generate $m/z = 145.0495$) and (c) M^{++} . | 96 |
| 4.4 | Proposed dissociation pathway of CuTpy and Cu adducted glycosidic fragments (a) C ion and (b) B ion. | 102 |
| 4.5 | Dissociation channels of $[L+(M+2H)]^{2+}$ under ECD conditions. | 108 |
| 5.1 | A possible mechanism to account for the stabilization of $[M+2H]^{++}$ by using interactions between carboxylic oxygen of E side chain and backbone amide hydrogen. | 140 |

ABBREVIATIONS

| | |
|-------------------------|---------------------------------------------|
| AI | Activated ion |
| <i>B</i> | Magnetic field strength |
| B3LYP | Becke-3-Lee Yang-Parr |
| BIRD | Blackbody infrared radiation dissociation |
| BK | bradykinin |
| CE | Crown ether |
| CI | Chemical ionization |
| CID | Collision-induced dissociation |
| Da | Daltons |
| DFT | Density functional theory |
| DR | Double resonance |
| EA | Electron affinity |
| ECD | Electron capture dissociation |
| ECD _{frag-eff} | ECD fragmentation efficiency |
| ECID | Electron capture induced dissociation |
| ECP | Effective core potential |
| EED | Electron excitation dissociation |
| EI | Electron impact ionization |
| EID | Electron ionization dissociation |
| ESI | Electrospray ionization |
| ETD | Electron transfer dissociation |
| eV | Electron volt |
| FAB | Fast atom bombardment |
| FD | Field desorption |
| FFT | Fast Fourier transform |
| FID | Free induction decay |
| FTICR | Fourier-transform ion cyclotron resonance |
| HECD | Hot electron capture dissociation |
| HPLC | High performance liquid chromatography |
| ICR | Ion cyclotron resonance |
| IRMPD | Infrared multiphoton dissociation |
| LMCS | Low Mode conformational search |
| K | Kelvin (temperature) |
| M ⁺ | Peptide/oligosaccharide radical cation |
| MALDI | Matrix-assisted laser desorption ionization |
| Mb | Megabytes |

| | |
|-----------------|----------------------------------------------------------------------|
| μs | microseconds |
| MECA | Multiple excitations for collision activation |
| MIF | Multiple-ion filling |
| MMFFs | Merck molecular force fields |
| M(O) | Methionine oxidation |
| MS | Mass spectrometry/mass spectrometer |
| MS ⁿ | Tandem mass spectrometry |
| <i>m/z</i> | Mass to charge ratio |
| pepy | 2-(4'-carboxypyrid-2'-yl)-4-carboxamide group |
| PD | Plasma desorption |
| pS | Serine phosphorylation |
| PTMs | Post-translational modifications |
| <i>rf</i> | Radio frequency |
| SID | Surface induced dissociation |
| SIMS | Secondary ion mass spectrometry |
| SORI | Sustained off-resonance irradiation |
| TMP | 2,4,6-trimethylpyridinium |
| TMPP-ac | Tris-(2,4,6-trimethoxyphenyl)-phosphonium-methylenecarboxamido group |
| TNCG | Truncated Newton-Raphson Conjugate Gradient |
| Tpy | Terpyridine |
| VLE | Very low-energy |
| XA | External accumulation |
| \emptyset | Diameter |

Dedication

to

My Parents

Chapter 1

Introduction

1.1 Mass spectrometry of biomolecules

Biomolecules such as carbohydrates, DNA and proteins assume important roles in biological functions. Carbohydrates play a crucial part in cellular processes like energy storage, structural support, signaling and extra-cellular interactions [1, 2], whereas malfunction of DNA or abnormal abundance of certain kinds of protein can cause different types of diseases [3]. In order to understand more about the biomolecules in human bodies and to discover biomarkers for diseases and drug targets, scientists have started doing proteomic researches. Since the structures of biomolecules provide useful information about their biological functions, sequencing is very often taken as the first step in proteomic studies.

Proteins and DNA are linear biomolecules. Others such as saccharide units stick to each other through a variety of linkages to form non-linear carbohydrates with branching structures. As any slight changes in these linkages or branches would greatly affect the conformations and biological activities of the carbohydrates, it is more difficult to obtain sequence information for oligosaccharide than protein.

There are several ways to perform protein and oligosaccharide sequencing, which can largely be classified as chemical and mass spectrometric approaches. Edman degradation [4-6] and enzymatic digestion (using glycosidases) are examples of chemical approach. The former was established as a routine technique to gain sequence information for peptide/protein while the latter was often used for sequence analyses related to oligosaccharide [7, 8]. Both approaches have their

limitations. They require lengthy analysis time and involve large amounts of samples and tedious sample purification procedures. Also, they cannot be used for obtaining sequence information for certain kinds of biomolecules such as peptide/protein with N-terminal blocked or post-translational modifications (PTMs). Given these limitations, the chemical approach is gradually phasing out and mass spectrometry (MS), characterized by its ultrahigh sensitivity and accuracy in mass measurement, is now widely used as an analytical technique for biomolecules sequencing.

The concept of MS was first introduced by J. J. Thomson in 1899 [9]. It was then one of the most sensitive and accurate analytical techniques to obtain the molecular mass of an atom. With the subsequent development of different types of ionization methods, the capability of MS to analyze large biomolecules has been greatly enhanced. Classic ionization techniques such as electron impact ionization (EI) [10] and chemical ionization (CI) [11] are suitable for dealing with volatile and thermally stable molecules. For analyses involving involatile and thermally labile molecules, field desorption (FD) [12], fast atom bombardment (FAB) [13], secondary ion mass spectrometry (SIMS) [14] and plasma desorption (PD) [15] have been commonly used. FAB was first developed for peptide sequencing [16] but limited to relatively low mass biomolecules (<1500 Da). In the late 1980s, matrix-assisted laser desorption ionization (MALDI) [17] and electrospray ionization (ESI) [18] were introduced. These two techniques are ideal for high mass biomolecules analyses and have become indispensable tools for MS of a great variety of substances, including high mass biomolecules and synthetic products.

ESI has advantages over other ionization techniques in several ways. First, it enables sample solution to be analyzed directly without any matrix involvement and

tedious sample workup. Second, it enables analyses of biomolecules with theoretically unlimited masses (mass limit depending only on the type of mass analyzer used). Third, it produces multiply-charged ions instead of singly-charged ions and thus allows the use of mass range in lower mass/charge (m/z) region with even high mass biomolecules.

In 1984, Fenn and co-workers demonstrated the coupling of ESI to MS [19]. In a typical ESI experiment of biomolecules, the sample is first dissolved by using a suitable solvent. Sample solution is then introduced into a hypodermic needle connected to a syringe pump at a flow rate of $\sim 1 \mu\text{L}/\text{min}$. Owing to the high potential difference (~ 4 kilovolts) between the metal capillary and the counter-electrode, a Taylor cone [20] protrudes. When the coulomb repulsion force exceeds the surface tension of the sample solution, droplets of liquid with excess charges are generated and a small jet of fine mist with charge droplets produced; and under the influence of the electric field, the charged droplets migrate towards the counter-electrode. With the use of an appropriate nebulizing gas (such as dry nitrogen) at an elevated temperature of typically $250 - 300 \text{ }^\circ\text{C}$, the solvent molecules evaporate continuously from the droplets, leading to a reduction of the droplet volume. The increasing charge density of the droplets eventually causes explosion of the droplets into even finer droplets. There was a suggestion that the rapid evaporation of the migrating droplets promotes a sequence of coulomb explosions that gives rise to droplets with a radius of curvature so small that the electric field on their surfaces becomes high enough to desorb solute ions into the ambient gas. If the analyte molecules have multiple basic residues, multiply-charged ions are generated. Since ESI produces analyte ions directly from the sample solution, it is very often a method of choice to couple MS with liquid separation methods such as high

performance liquid chromatography (HPLC).

1.2 Tandem mass spectrometry

With the advancement of instrumentation by various tandem mass spectrometry (MS^n) techniques, mass spectrometer has become a useful tool for structural analyses of large biomolecules.

MS^n is a fast and selective analytical technique for sequencing biological samples in complex mixture without requiring extensive sample purification. In this technique, the ions of interest (i.e., precursor ions) are first isolated and then activated. The activated ions subsequently undergo unimolecular dissociation and the fragment ions produced (i.e. product ions) are then recorded and analyzed. This cycle can be repeated as anyone of the resulting fragment ions can be further isolated and activated to give secondary fragments. Depending on the methods of ion activation, fragmentation can occur at different positions along the peptide backbone to produce several sequence specific fragment ions.

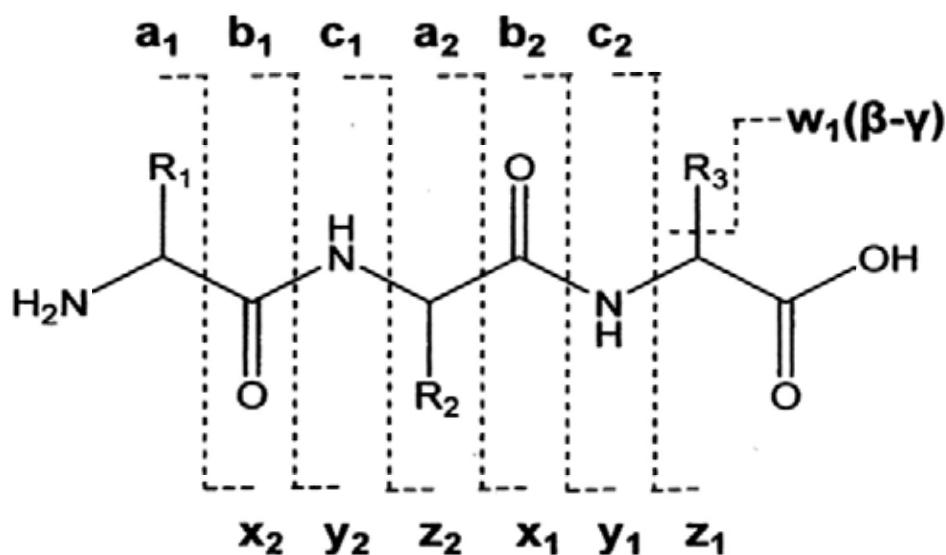
The fundamental approaches for protein sequencing by MS can be classified as bottom-up and top-down strategies. In the bottom-up approach, large proteins are subjected to enzymatic digestion and the peptides or small proteins resulted are analyzed by MS [21]. Known and unknown proteins can then be rapidly identified by comparing the fingerprint of the digested products against the hypothetical pattern generated from protein databases. This peptide mass fingerprinting, however, requires several peptide fragments to uniquely identify a protein. In the top-down approach, intact protein ions are selected and subjected to gas phase fragmentation for MS analysis, and protein identification is based on the accurate mass measurement of sequence tags generated by MS^n [22]. This strategy has an

advantage over the bottom-up approach [23] in that it avoids enzymatic digestion and prevents neglect of PTM(s), and for this reason is useful for localization and characterization of PTM(s) [24].

1.2.1 Nomenclature of peptide and oligosaccharide fragments

To facilitate understanding of the labeling of the fragment ions in MS^n spectra to be mentioned in the ensuing chapters, the nomenclature of different peptide and oligosaccharide systems is briefly described below.

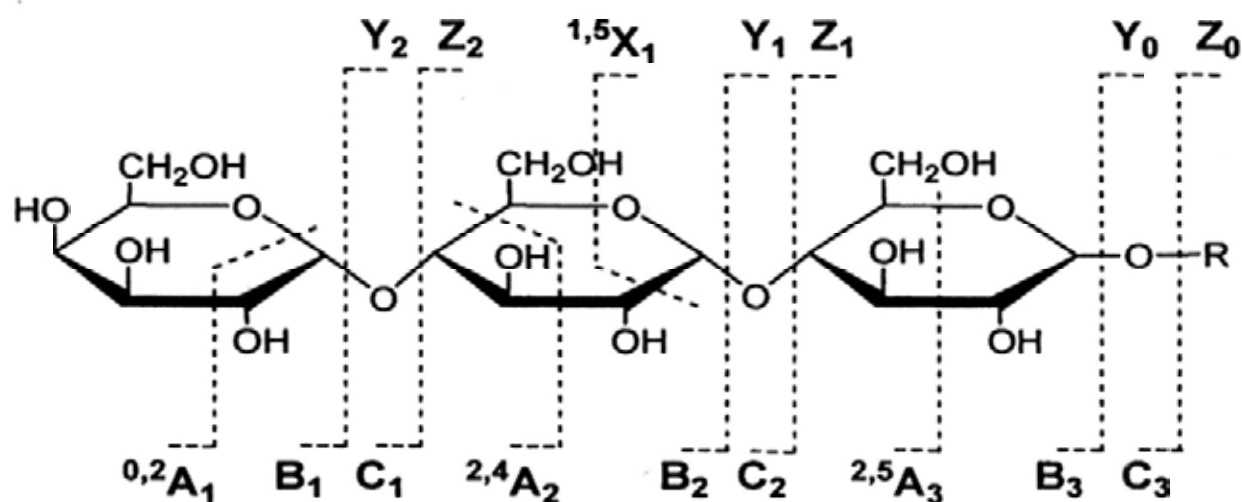
The cleaving sites and the notations of peptide fragments under the systemic nomenclature suggested by Roepstorff and co-worker [25] in 1984, which was subsequently modified by Johnson and co-workers [26], are shown in Scheme 1.1. Under this system, if the charge is retained on the N-terminal, the ion is named as *a*, *b* or *c*; but if the charge is retained on the C-terminal, the ion is *x*, *y* or *z*. Additional side chain loss from *z* ions is labeled as *w* ion. Each of the subscripts indicates the number of residues in the fragment.



Scheme 1.1

The systematic nomenclature generally used for carbohydrate fragmentation

was introduced by Domon and Costello in 1988 [27]. Under this system, fragment ions containing the non-reducing end is either A, B or C, whereas ions containing the aglycone (or the reducing end for carbohydrates) is labeled as X, Y or Z. The glycosidic bond linking to the aglycone is numbered 0. The cleaving positions and notations in this regard are shown in Scheme 1.2.



Scheme 1.2

1.2.2 Dissociation of protonated peptide ions

Conventionally used MS^n techniques include collision induced dissociation (CID) [28, 29], surface induced dissociation (SID) [30], blackbody infrared radiation dissociation (BIRD) [31] and infrared multiphoton dissociation (IRMPD) [32]. The principles of all these techniques are based on excitation of the vibration modes of ions (i.e. the weakest bond in the ions would cleave preferentially during the redistribution of vibrational excitation energy).

1.2.2.1 CID of protonated peptide ions

CID is one of the dissociation techniques widely used for protein sequencing. It was introduced by Jennings in 1968 and has become an important tool in MS^n . In

1982, Frelser and co-workers first reported CID experiments performed in Fourier-transform ion cyclotron resonance mass spectrometer (FTICR-MS).

In a typical CID MSⁿ experiment in FTICR-MS, the ions of interest, i.e. the precursor ions, are isolated by over-excitation of the unwanted ions. The ions are then subjected to a short *rf*-excitation waveform (whose frequency is identical to the cyclotron frequency of the precursor ions) under an elevated background pressure (10^{-6} - 10^{-7} Torr) of inert gas. As a result of multiple collisions, some of the translation energy of the precursor ions is converted to internal energy. The internal energy randomizes over all degrees of freedom in the ions, eventually leading to their dissociation.

Depending on the power, duration and frequency of the excitation waveform(s), CID can be subdivided into several classes, including on-resonance CID, sustained off-resonance irradiation CID (SORI-CID) [33], very low-energy CID (VLE-CID) [34] and multiple excitations for collision activation (MECA) [35]. Among these, SORI-CID is the most widely adopted method for inducing dissociation of large biomolecule ions in FTICR-MS.

CID of peptides and oligosaccharides usually cleave amide [36] and glycosidic [27] linkages respectively to form a series of *b/y* and *B/Y* ions. Besides the generation of sequence specific fragments, losses of small neutral molecules (e.g. water, ammonia and carbon dioxide) are always observed. This is more prominent in cases of protein with PTM(s). Owing to their lability, PTM groups will lose preferentially upon vibrational excitations.

For peptides/proteins, a “mobile proton model” [37-41] has been proposed to account for their dissociation patterns. It is believed that under collision activation

conditions, the added protons in the precursor ions will migrate from the protonation site along the amide backbone to induce cleavages at different inter-residual linkages [37]. It is also believed that the initial protonation site is located at the side chain of basic amino acids; while for peptides with no basic amino acid, the initial protonation site is at the N-terminal amino group [42].

Several mechanisms have been proposed for the dissociation of protonated peptide under low-energy CID conditions. They include 'amino-O' pathway [43-45], 'aziridinone' pathway [46], 'diketopiperazine' pathway [46-48], 'a₁-y_x' pathway [49, 50] and 'oxazolone' pathway [43, 51-53]. The first pathway mentioned is initiated by protonation of hydroxyl oxygen while the others are initiated by protonation of amide nitrogen. Protonation action weakens the C(O)-N bond, causing carbonyl carbon to become more electrophilic and therefore susceptible to attacks by the nearby nucleophilic groups such as N-terminal amino nitrogen and carbonyl oxygen. Details of the five dissociation pathways are in Appendix I.

1.2.3 Dissociation of protonated/metalated peptide ions via radical intermediates

There are many ways in the literature to generate peptide/protein radical ions. Among them are laser ionization [54], neutralization-reionization [55], homolytic cleavages of covalent bonds between the chemical/chromophore groups (or radical initiators) and peptides [56-58], peptide ion-electron/ion-ion interaction methods [59-62] and dissociation of the noncovalent complexes of peptides [63]. Of these, peptide ion-electron/ion-ion interaction methods are more widely used as they can simplify the analysis process by avoiding prior covalent modification, complexes formation and/or additional isolation/activation steps.

1.2.3.1 ECD of protonated peptide ions

Relatively new MSⁿ techniques involving the dissociation of ion species are electron capture dissociation (ECD) [59], electron transfer dissociation (ETD) [62] and electron ionization dissociation (EID) [61], all of which are complementary to conventional dissociation techniques.

Introduced by McLafferty and co-workers in 1998, ECD has been commonly used for structural analyses of biomolecules because of its fragmentation properties. For peptides/proteins, cleavages in ECD are relatively non-specific [64]. Owing presumably to the cyclic nature of proline, fragment ions corresponding to the cleavage at the N-terminal side of proline have not been observed [65]. Since ECD cleaves almost every N-C_α bond between amino acid residues, it generates lots of sequence specific fragments to reveal the amino acid sequence of protein.

In a typical ECD experiment of biomolecules, multiply-charged precursor ions (e.g. cations) are subjected to high energy (>10 eV) or low energy (< 0.2 eV) electron irradiation for a pre-defined period of time. Upon electron capture, one charge is neutralized, and a certain amount of recombination energy is converted from electronic energy to vibrational energy. The precursor ions then undergo fast dissociation with the following reaction:

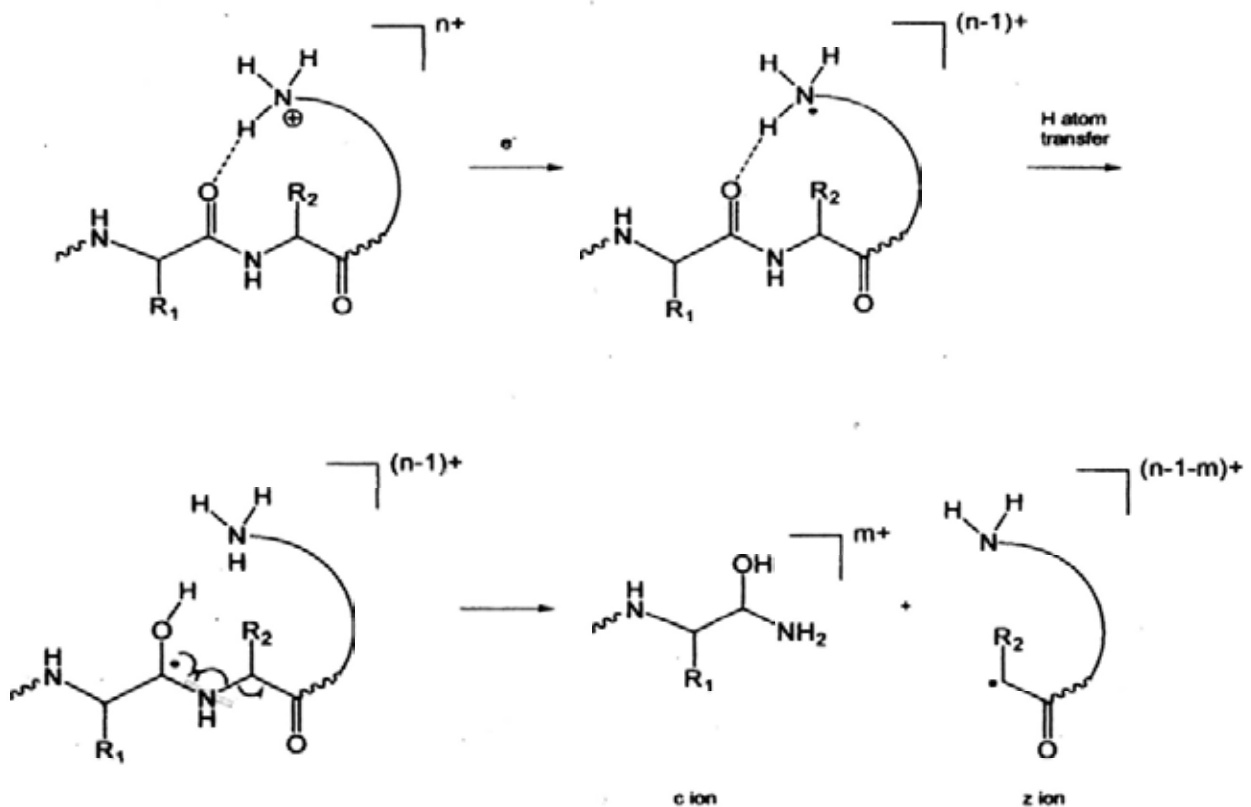


Many ECD-based experiments have been developed with the aim of further improving ECD's analytical capability. They include activated ion ECD (AI-ECD) [66], use of indirectly heated dispenser cathode as electron source [67], combination of external accumulation with ECD (XA-ECD) [68], hot electron capture dissociation (HECD) [69, 70] and sustained off-resonance irradiation electron

capture dissociation (SORI-ECD) [71].

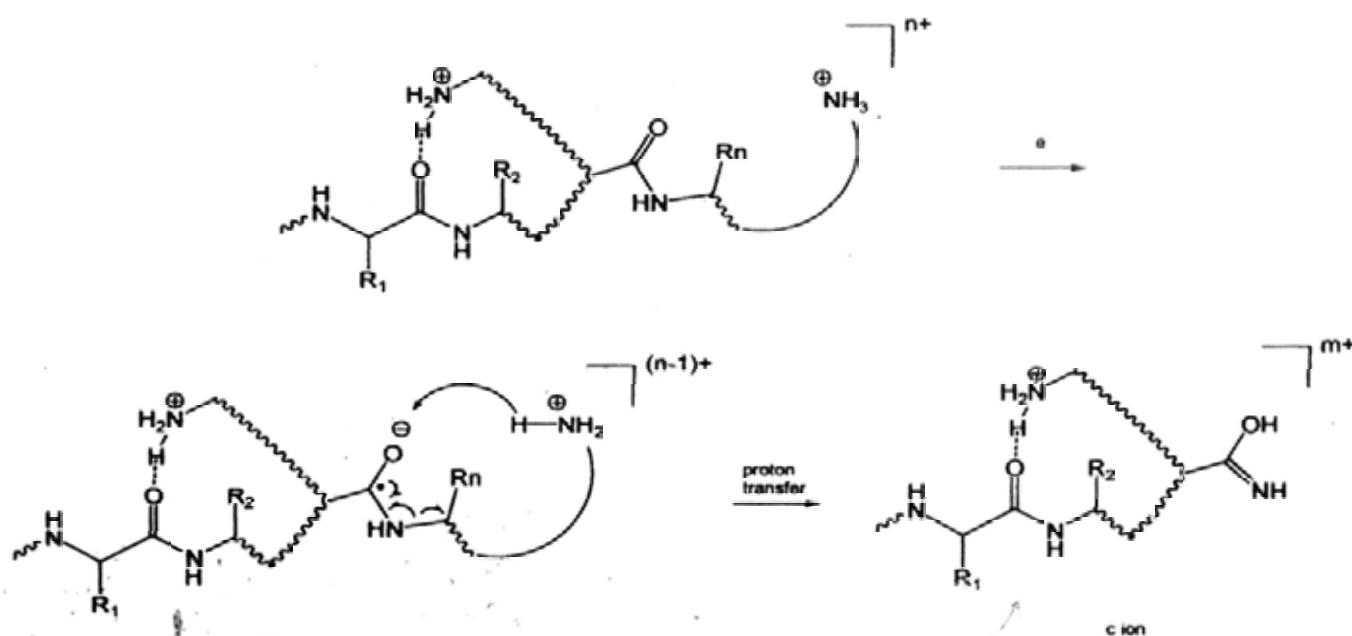
Unlike conventional dissociation techniques, dissociation of peptide ions in ECD is believed to be initiated by radical. For peptides/proteins, the resulting sequence specific ions are mainly *c/z'* ones. Currently, there are two proposed ECD mechanisms: 'hot hydrogen atom' model [64] and 'amide-superbase' model [72], the details of which are set out below.

The 'Hot hydrogen atom' model (called Cornell mechanism [73]) suggests that electron capture occurs at one of the protonation sites on peptide/protein. This results in the formation of a hypervalent radical intermediate which readily releases a hydrogen atom that is in turn captured by the carbonyl oxygen in an amide group. The aminoketyl radical intermediate resulted then rapidly dissociates via the cleavage of the adjacent N-C_α bond as illustrated in Scheme 1.3.



Scheme 1.3

The 'Amide-superbase' model (called Utah-Washington mechanism, and UW for short) pinpoints the importance of the remote charge. It proposes that high electron affinity (EA) amide π^* orbital will capture an electron exothermically since the EA of amide groups increases with the presence of remote charge. After capturing the electron by amide π^* orbital, the basicity of the amide carbonyl oxygen increases and will abstract a proton from the protonated functionalities in the vicinity. Consequently, a labile aminoketyl radical will be formed and dissociate readily by cleaving N-C α bond cleavage. This mechanism explains why electron capture induces N-C α bond cleavage in systems which lack guanidinium groups as the hydrogen atom donor. Scheme 1.4 shows how this mechanism works.

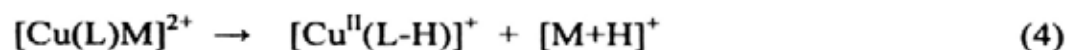
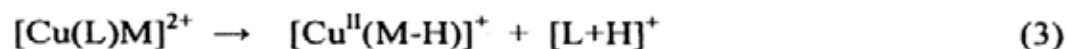
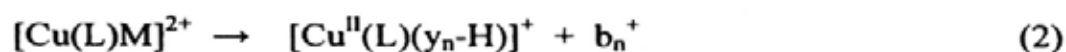
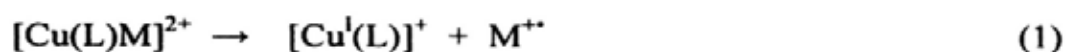


Scheme 1.4

1.2.3.2 CID of non-covalent complex of peptides

An alternative way to generate peptide radical ions involves CID of copper ternary complex, $[\text{Cu}(\text{L})\text{M}]^{2+}$ (L and M refer to ligand and peptide respectively). As first demonstrated by Siu and co-worker in 2000 [74], CID of $[\text{Cu}(\text{L})\text{M}]^{2+}$ would

undergo several dissociation channels as follows:



In this dissociation method, fragment ions corresponding to proton transfer reaction from auxiliary ligand to peptide moiety (channel 4) will not be observed, presumably due to the absence of acidic proton in the ligand [75]. The presence of basic amino acid in the peptide ion can probably hold the proton tighter and therefore reduce the chance of its dissociation through channels 2 and 3 [76, 77]. Of all the dissociation channels as mentioned above, channel 1 is the desired one as it is the only channel that produces peptide radical cation (M^{++}) and for this reason is useful in studies concerning the dissociation pattern of M^{++} .

Systematic studies on the roles of auxiliary ligands [77, 78] have revealed that the degree of steric hindrance on auxiliary ligands is an important factor influencing the formation of M^{++} from $[\text{Cu}(\text{L})\text{M}]^{2+}$. Researches have also reviewed the capability of trivalent transition metal ions to generate metal ternary complexes. These ions, which include Cr^{3+} , Mn^{3+} , Fe^{3+} and Co^{3+} , can be used to generate peptide radical ions by using salicylaldehyde (a dianionic ligand) as the auxiliary ligand [79].

1.3 Dissociation of peptide radical ions

Protein radicals are important intermediates in enzymatic reactions [80]. Apart from being important biological intermediates, peptide/protein radical ions

have recently proven to be interesting precursor ions for structural characterization of peptide/protein moiety in MS. This is because comparison of the dissociation patterns between peptide radical ions and their corresponding protonated species provides useful sequence diagnostic and complementary information which can increase significantly the sequence coverage.

Dissociation of peptide radical ions generated by ECD complements conventional dissociation techniques in several ways. First, labile PTM(s) in proteins are found to cleave preferentially when compared to backbone cleavages. The fragment ions produced by conventional techniques could only characterize the type, but not the site(s), of modifications. But in ECD, the labile groups are usually retained in the fragment ions during the dissociation of peptide radical species. It is possible to confirm the characterization as well as localization of PTM(s) [81-85] by comparing the ECD and CID spectra of peptide with PTM(s).

Second, ECD shows preferential cleavage of disulphide bonds. This special feature facilitates the sequencing of proteins which contain disulphide bonds. Complementary sequence information could be obtained from ECD of peptide radical ions plus CID of the corresponding protonated species.

Third, ECD has demonstrated that aspartic acid (D) and isoaspartic acid (isoD) can be differentiated by generation of diagnostic ion(s) unique to each form [86-89]. Deamidation of asparagine (N) and isomerization of aspartic acid to form a mixture of aspartic and isoaspartic acid are non-enzymatic PTM(s) that occur spontaneously in proteins [90]. As it is difficult to differentiate the isomers [91] with conventional dissociation techniques, ECD can be used to distinguish aspartic acid from isoaspartic acids. Since isoaspartic acid does not contain any N-C_α bonds, its fragmentation under ECD conditions is different from that of aspartic acid. Instead

of c and z' ions, a diagnostic ion pair, $c_{l-n}^+ + 58$ and $z_n^+ - 57$ (l being the length of the peptide, n being isoaspartic acid) will be observed; and the identity and position(s) of the isoaspartic acid can then be determined.

Fourth, ECD enables the differentiation of isomeric amino acid leucine (L) from isoleucine (I). Although L and I can be distinguished in FAB or high energy CID (as different side chain loss from L (43.055Da) and I (29.039Da) can be observed after backbone cleavages [92]), these techniques can only be applied to small peptides, say, peptides containing less than five amino acid residues. For the larger peptides/proteins, L and I can be differentiated by the secondary fragmentation of z' ions under HECD. It has been demonstrated by Zubarev and co-workers that identification of 80 % of L and I residues in a bovine milk protein PP3 can be achieved [93] by HECD.

Although many studies have been conducted on the mechanisms for dissociation of peptide radical ions, some of the proposed dissociation pathways and fragmentation patterns of peptide radical ions are not clear enough. To secure proper spectral interpretations for protein sequencing, it is vitally important to identify the roles of the radicals in different types of peptide radical ions, including both hydrogen-deficient ($[M+(n-2)H]^{(n-1)+}$) and hydrogen-surplus ($[M+nH]^{(n-1)+}$) species, in the dissociation process.

1.4 Overview of the Project

This project aims to study the generation and fragmentation of peptide/protein radical ions via a FTICR-MS. Two dissociation techniques, namely SOIR-CID and ECD, were used in this study. Chapter One of this thesis introduces the related mass spectrometry methods and the underlying mechanisms of

SORI-CID and ECD. Chapter Two describes in detail the principles and setting of FTICR-MS used in this study. It also outlines various experimental conditions and the typical experimental procedures for acquisition of tandem mass spectra. Chapter Three summarizes the fragmentation patterns and sequence information of peptide radical cations generated by CID of copper ternary complexes. The fragmentation patterns are then cross-compared with SORI-CID and ECD of the corresponding protonated peptides. Chapter Four discusses about the dissociation preferences of peptide radical cations, both with and without PTM functional groups generated by SORI-CID of copper ternary complexes. The fragmentation patterns of SORI-CID of copper-ligand oligosaccharide complexes are also studied. These dissociation patterns are then cross-compared with those derived from SORI-CID and ECD of protonated peptides and metal-adducted oligosaccharides. In addition, the retention of weak non-covalent interactions between 12-crown-4 and peptide after ECD was evaluated. It also summarizes the impacts of 12-crown-4 to peptides on the dissociation patterns and fragmentation efficiency of peptides under typical ECD conditions. Chapter Five gives an example of natural structural motifs suppressing peptide ion fragmentation after electron capture under typical ECD conditions. Concluding remarks for the whole project are set out in Chapter Six.

Chapter 2

Instrumentation and Experimental Conditions

2.1 Fourier-transform ion cyclotron resonance mass spectrometry

The first experiment using Fourier transform ion cyclotron resonance mass spectrometer (FTICR-MS) was carried out by Comisarow and Marshall in the early 1970's [94]. For the past two decades, the instrument has been an important analytical tool for researches, especially in biological studies. It not only allows analyses of a wide variety of samples owing to its ability to couple different types of ionization sources (e.g. EI/CI, MALDI and ESI), but is also much more accurate in mass measurement than other mass spectrometers. Its ultra-high resolving power, moreover, enables identification of the isotopic peaks of ions and hence determination of the latter's charge states. Further to this, its ability to store ions for a long period of time (in the analyzer cell) allows ion-molecule/ion-electron reaction for ion dissociation and in so doing generates lots of structural information for analysis purposes.

2.1.1 Instrumental principle

In a typical FTICR-MS, the analyzer cell is placed under a strong and static magnetic field. Two trapping plates, perpendicular to the magnetic field, are located at both ends of the analyzer cell. Figure 2.1 shows a typical ICR analyzer cell. The motions of ions within the cell are constrained by both static magnetic and electric fields which are perpendicular to each other. There are three independent motions in the analyzer cell – cyclotron motion, trapping harmonic oscillation and magnetron motion [95, 96], each of which is outlined below.

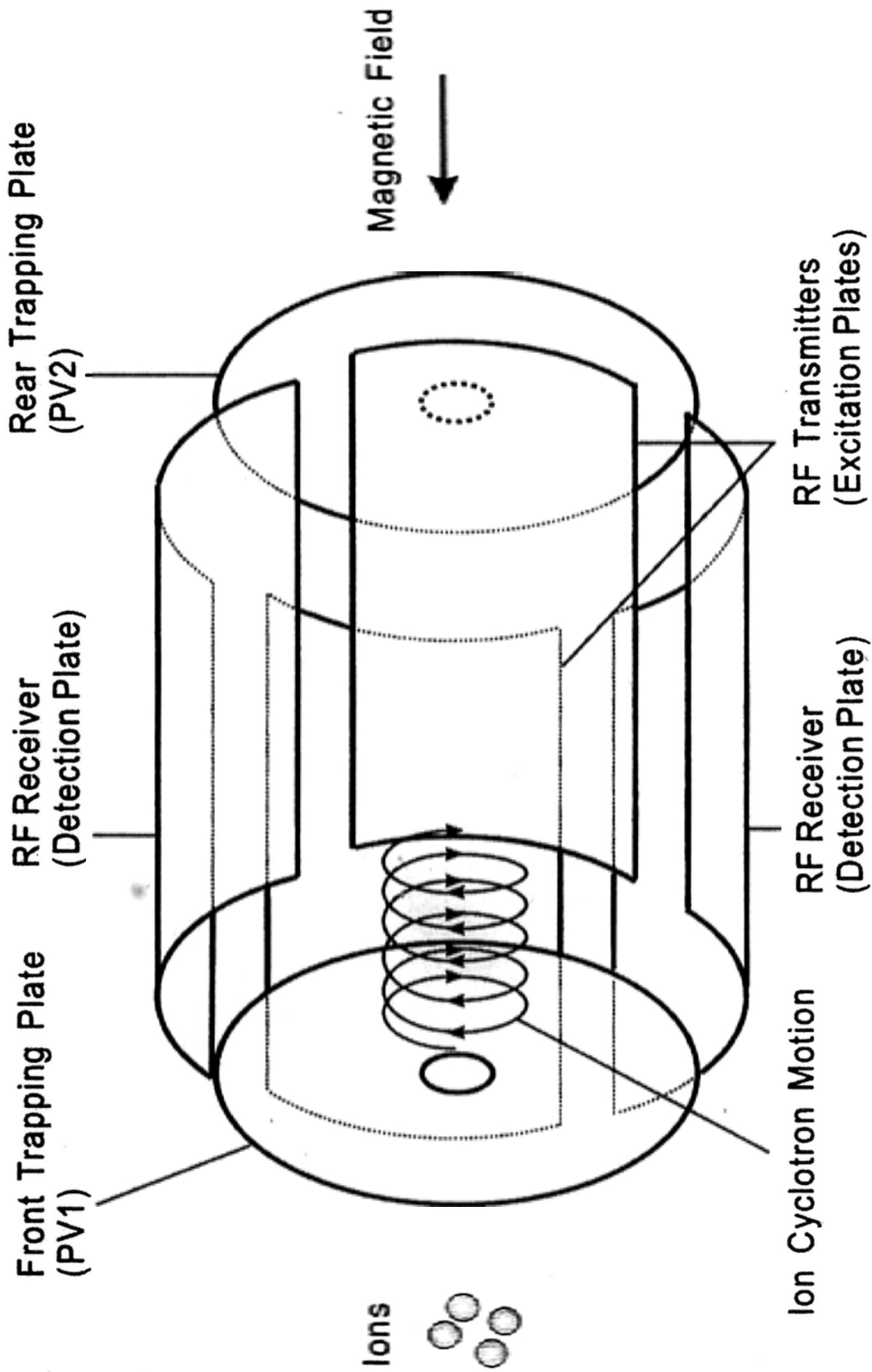


Figure 2.1 Schematic diagram of a typical ICR analyzer cell

Cyclotron motion of the trapped ions is derived from the interaction of ions with the magnetic field. Ions move in a circular orbit with a constant speed (i.e. no collisions) and experience a force, called the Lorentz force, which is perpendicular to the magnetic field (i.e. xy plane) and the direction of the ions. The analytical expression in this regard is shown in equation 2.1 as follows:

$$Bqv_{xy} = \frac{mv_{xy}^2}{r} \quad [2.1]$$

B is the magnetic field strength (Tesla); and q , m , r and v_{xy} are respectively the charge, mass, cyclotron radius and angular velocity of the ion in xy plane. Using the angular cyclotron frequency (ω_c), equation 1.1 can be transformed to equation 2.2 as below:

$$\omega_c = \frac{v_{xy}}{r} = \frac{qB}{m} \quad [2.2]$$

The ion cyclotron frequency is directly proportional to the magnetic field strength (B) and inversely proportional to the mass-to-charge ratio (m/q or m/z) of the ions. It is independent of the ion velocity and thus kinetic energy. If magnetic field B is homogeneous and stable, it can be treated as a constant. And the cyclotron frequency of the orbiting ions can then be accurately determined from the image current and very precise mass measurement is possible.

Trapping harmonic oscillation along the z -axis of the ions is caused by the electric field generated by the trapping plates at both ends of the analyzer cell. The trapping frequency (ω_T) of an ion is correlated to the mass-to-charge ratios (m/z), the trapping potential (V_T), the geometry factor (α) and the dimension (a) of the cell. The analytical expression in this connection is shown in equation 2.3:

$$\omega_T = \sqrt{\frac{2qV_T\alpha}{ma^2}} \quad [2.3]$$

Magnetron motion of the ions is caused by the interaction between the trapping potentials and the magnetic field [97-100]. Owing to the nonlinear gradient of the electric field, the trapping potentials exert a radial force of magnitude $(\frac{qV_T\alpha}{a^2}r)$ onto the orbiting ions. The analytical solution of the ion motion is modified from equation 2.1 to equation 2.4 as follows:

$$\omega^2 - \frac{qB}{m}\omega + \frac{qV_T\alpha}{ma^2} = 0 \quad [2.4]$$

By solving equation 2.4, the reduced cyclotron frequency (ω_R) and the magnetron frequency (ω_M) can be obtained in equations 2.5 and 2.6:

$$\omega_R = \omega_+ = \frac{\omega_c}{2} + \sqrt{\left(\frac{\omega_c}{2}\right)^2 - \frac{\omega_T^2}{2}} \quad [2.5]$$

$$\omega_M = \omega_- = \frac{\omega_c}{2} - \sqrt{\left(\frac{\omega_c}{2}\right)^2 - \frac{\omega_T^2}{2}} \quad [2.6]$$

ω_c in the above equations is the “unperturbed” cyclotron frequency. Since the magnetron motion of an ion moves at the same plane as the cyclotron motion, the observed cyclotron frequency (ω_o) is slightly lower than its original cyclotron frequency as shown in equation 2.7:

$$\omega_o = \omega_c - \omega_M \quad [2.7]$$

In order to detect ions in the analyzer cell, a radio frequency (*rf*) waveform is used to excite the trapped ions. This *rf* electric field serves to align the trapped ions to move in a spatially coherent manner and to accelerate them to a larger radius of motion. Each cyclotron ion species emits *rf* signal intensity (image current) to the detection plates at its characteristic frequency. Unlike other mass analyzers, FTICR-MS does not rely on spatial separation to distinguish ions of different

mass-to-charge ratios [101].

2.1.2 The Instrument

All experiments were performed by using a 4.7 Tesla FTICR-MS (APEX III, Bruker Daltonics Inc., Boston, MA), a schematic diagram of which is shown in Figure 2.2. The instrument consisted of several parts, including a vacuum assembly, a homemade nanospray ion source (modified from a standard commercially available external electrospray ion source), an electrostatic ion focusing system, an ICR analyzer cell, a 65 mm wide-bore 4.7 Tesla horizontal superconducting magnet and a standard electrically heated filament electron source. The details and functions of these integral parts are set out below.

2.1.2.1 Vacuum system

Vacuum system could be subdivided into three regions, namely the ion source region, the ion focusing region and the analyzer cell region. In order to minimize ion-molecule collision and prevent perturbation of ion motion during analysis, the pressure in the analyzer cell region was maintained at ultrahigh vacuum conditions. Owing to the existence of a small opening in the ion source region for ions entry, a differential pumping system as depicted below was adopted in order to achieve an ultrahigh vacuum condition.

The vacuum system worked on two sets of pumps. The first set of pumps included an auxiliary rotary pump (E2M28, Edwards Corporation, UK), a roughing rotary pump (E2M18, Edwards, Corporation, UK) and a 250 L/min turbomolecular pump (EXT250HI, Edwards Corporation, UK). The auxiliary rotary pump and turbomolecular pump (inter-connected to each other) were installed inside the ion

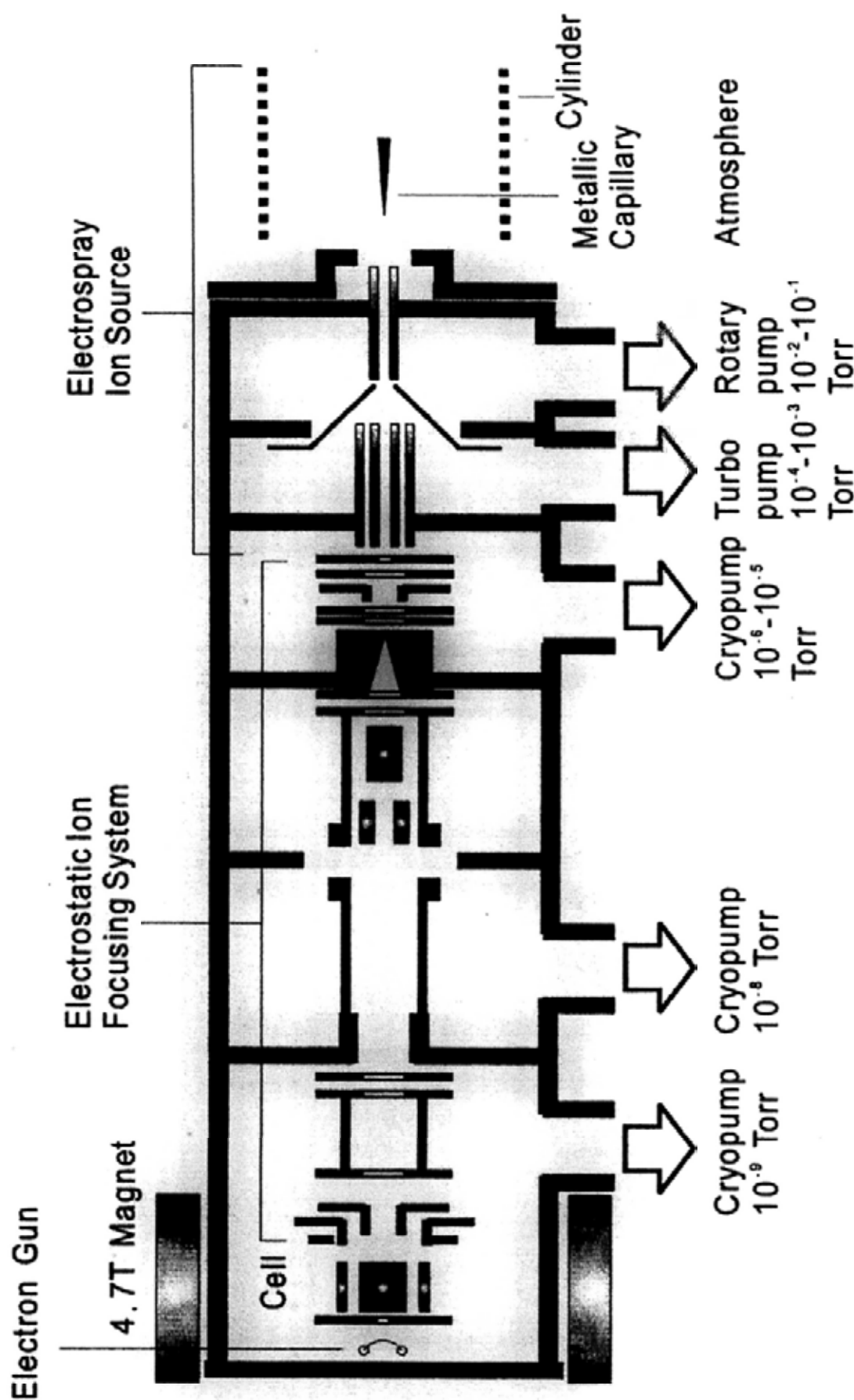


Figure 2.2 Schematic diagram of the Bruker APEX III 4.7T FTICR-MS equipped with an electropray ion source

source region, whilst the roughing rotary pump was connected to the front of the ion transfer region for source roughing.

The other set of pumps comprised a Coolstar cryopump 800 (L/min) (Edwards Corporation, UK) installed in the ion source region, a Coolstar cryopump 400 (L/min) (Edwards Corporation, UK) in the ion transfer region and a Coolstar cryopump 800 (L/min) (Edwards Corporation, UK) in the analyzer cell region. All of these cryopumps were controlled by a Cryodrive 3.0 (Ricor Limited, Israel) which could be computer-controlled through a program called Ricor PLC Communication.

Under typical pumping process, compressed liquid helium supplied by the cryodrive was circulated by the three cryopumps, and the cryodrive was then cooled by a refrigerated recirculator (CFT-150, Neslab, US). The temperature of the cold head and the pumping performance of the cryopumps were monitored by the hydrogen gas thermometer associated with each cryopump. In normal working conditions, the pressure in the dielectric capillary and the hexapole ion guide were around 10^{-2} - 10^{-1} Torr and 10^{-4} - 10^{-3} Torr respectively, the pressure in the front and the rear of the ion focusing region are 10^{-6} - 10^{-5} Torr and 10^{-8} Torr respectively, while the pressure in the analyzer cell region was about 10^{-9} Torr.

The vacuum conditions of the analyzer cell region and the ion focusing region were monitored by two cold cathode gauges (IKR 020, Balzers, Liechtenstein). Since the cold cathode gauges located above the two Coolstar cryopumps 800 could only operate when the pressure was lower than 1×10^{-4} Torr, when the pressure of the ion focusing region reached 1×10^{-4} Torr, the cold cathode gauges were turned off and a pirani gauge (TPR 010 Balzers, Liechtenstein) was used to measure the pressure inside the analyzer cell region and the ion focusing region.

To facilitate venting of the ion source chamber for exchange of ion sources and cleaning of the dielectric capillary while preserving the ultrahigh vacuum conditions of the analyzer cell region and the pumping status of the front Coolstar cryopump 800 in the ion source region, a Vatterfly valve (DN160 Vatterfly Valve Series 20, Vat Vakuumventile AG, Haag) was installed to isolate the front Coolstar cryopump 800 from the ion source region, while a mini UHV-Schieber gate valve (DN50, VAT Vakuumventile AG, Haag) was installed to separate the ion source region from the analyzer cell region.

In addition to the above two valves, a leak valve (controlled manually by adjusting its knob) and an electromagnetic pulse valve (controlled by a TTL pulse generated by the console) were installed near the analyzer cell region. The former was used for introducing volatile sample while the latter for introducing argon as collision/cooling gas, into the analyzer cell.

2.1.2.2 Nanospray source

Nanospray ion source was adapted from a commercially available electrospray ionization source (Analytical, Bradford, CT, USA). A homemade nanospray assembly [102] as shown in Figure 2.3 was established after modifications as described below.

The platinum wire inside the capillary was grounded to produce a stable spray solution. Negative potential, V_{cap} (~ 1,000 voltage), was applied to the entrance metal cap of the dielectric capillary (18.0 cm in length and was made of glass) for the positive ion mode, and positive potential for the negative ion mode. A flow of heated dry nitrogen gas (~ 275 °C) was used to facilitate solvent evaporation from the sprayed droplets.

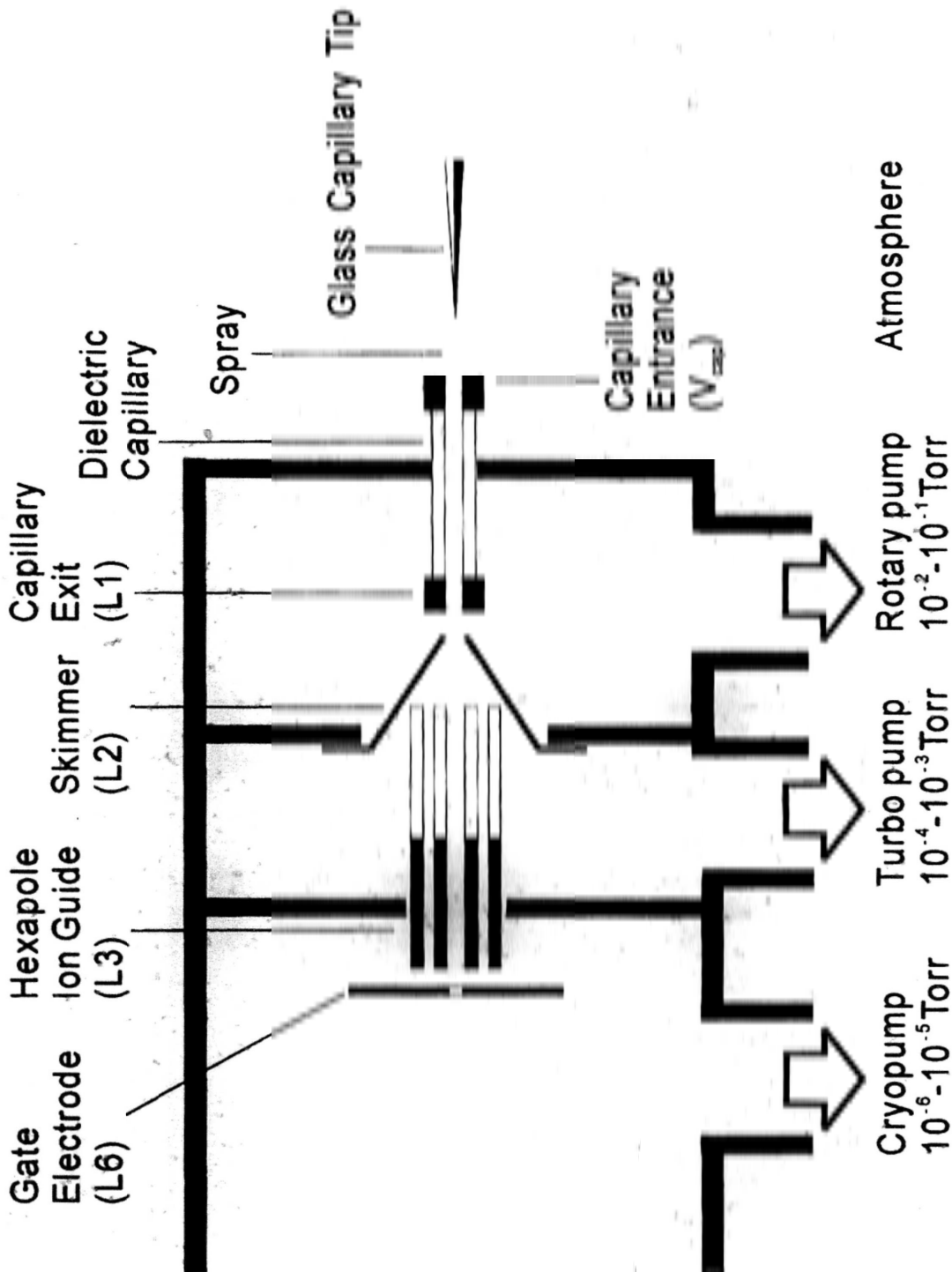


Figure 2.3 Schematic diagram of the Bruker APEX III 4.7T FTICR-MS equipped with a homemade nanospray ion source

The ion focusing optics was located in the low vacuum region of the nanospray assembly. It included a skimmer (L2), an IrisTM hexapole ion guide (L3) and a gated electrode (L6). The hexapole ion guide was used for external ion accumulation. It provided a strong focusing optics to guide ions across the relatively high pressure region.

The small orifice of the dielectric capillary and the skimmer were used to limit gas flow from the atmosphere into the vacuum region of the nanospray. By using a rotary pump, the region between the capillary and the skimmer was pumped to a low vacuum of around 10^{-1} - 10^{-2} Torr. At the same time, pressure in the region between the skimmer and the hexapole ion guide was reduced to around 10^{-3} - 10^{-4} Torr with a 250 L/min turbomolecular pump.

The potential applied to L1 was typically about 100 V (positive potential for positive ion mode and vice versa). This 100 V potential was a potential barrier for transmission of analyte ions. The flow of ions across this potential barrier was believed to be the result of gas flow due to the pressure difference between the atmospheric region and the capillary skimmer region ($\sim 10^{-1}$ - 10^{-3} Torr). To enhance the signal intensity of the analyte ions, ions were accumulated in the hexapole ion guide for a predefined time before they were extracted and directed to the analyzer cell through the ion transfer region. In positive ion mode, ions were trapped inside the hexapole ion guide while L6 was held at positive potential. Upon approaching of a negative potential pulse to L6, the analyte ions were extracted to the ion focusing region.

2.1.2.3 Electrostatic ion focusing system

The electrostatic ion focusing system was installed to guide ions from the ion

source to the analyzer cell. It was composed of a series of electrostatic lenses. Figure 2.4 shows a schematic diagram of different ion optics with their typical potential gradient curves.

There were two kinds of ion optics inside the system – the ion focusing lens (HVO, PL1, PL9, FOCL1 and FOCL2) and the ion beam steering electrodes (PL2/DPL2, PL4/DPL4, XDFL and YDFL). HVO is a high potential electrode with a typical potential of about -2.5 kV for positive ion mode and 2.5 kV for negative ion mode. It was used to accelerate ions to a higher velocity, thereby increasing the efficiency of ion transmission. DPL2 and DPL4 are low energy beam steering electrodes, while XDFL and YDFL are high energy beam electrodes used for fine steering of ion beam. The potentials of the ion beam steering electrodes were set to some preset-values in order to guide ions into the analyzer cell.

EV1 in Figure 2.4 was the entrance electrode of the analyzer cell. A slightly negative potential (for the positive ion mode) was applied on EV1 so as to pull the decelerated ions into the analyzer cell. A pair of split electrodes, EV2 and DEV2, was located behind EV1. EV2 defined the center potential at the cell entrance while DEV2 controlled the voltage gradient across the cell entrance. They provided the “kicker voltage” to deflect the ion beam along the x-y plane to increase the trapping efficiency of the analyzer cell. In order to trap ions in the analyzer cell, trapping potentials (PV1 and PV2) were applied at the trapping plates.

2.1.2.4 Analyzer Cell and electron emission source

An InfinityTM Cell [103] (Bruker-spectrospin, Fällanden, Switzerland), measuring 60 mm in diameter and 60 mm in length and containing gold-coated electrodes, is used as the analyzer cell of the FTICR-MS in this study.

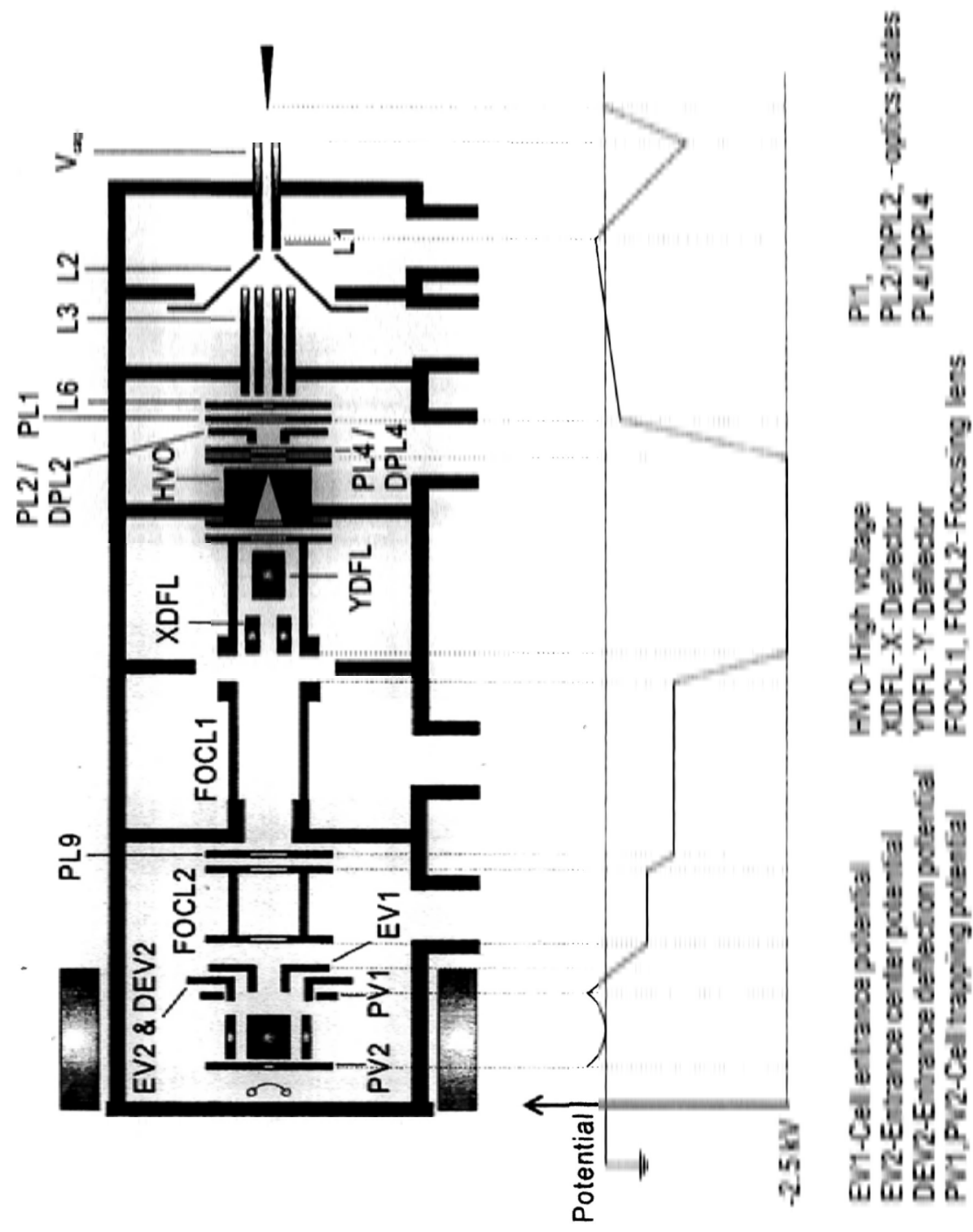


Figure 2.4 Schematic diagram of the ion optics inside the FTICR-MS with their typical potential gradient curve

In order to prompt ion-electron reaction in the InfinityTM Cell, the Cell was connected to a standard electrically heated filament source. As illustrated in the schematic diagram in Figure 2.5, two trapping electrodes (PV1 and PV2) were located at the front and rear ends of the InfinityTM Cell and a circular aperture (6 mm in diameter) was located at the center of each trapping electrodes for entry and exit of ions and/or electrons. Four curved electrodes were installed orthogonal to the trapping plates. The shorter pair of electrodes provided two excitation plates through which *rf*-excitation pulses would be transmitted. The other pair of electrodes acted as two detection plates for image current generated by the cyclotron motion of the trapped ions.

The InfinityTM Cell was used because of its advantages over the standard cell. First, the InfinityTM Cell is equipped with segmented trapping plates to avoid undesirable z-axial ejection of the trapped ions during ion excitation at frequencies of $\omega_c + 2\omega_r$. Second, the front trapping potential (PV1) of the InfinityTM Cell is kept constant throughout the whole event.

During the ion accumulation process, the potential of EV1, EV2 and DEV2 electrodes were changed to some preset-values for admission of ions into the Cell. After ion accumulation, the InfinityTM Cell was closed by restoring the potentials of these electrodes to the same value as the PV1.

The InfinityTM Cell was equipped with a filament made from a ~0.5 mm-wide rhenium ribbon and spot-welded onto two metal pins, pin1 and pin2, with a parting distance of ~6 mm. It had a resistance of 0.5 Ω under ambient conditions. At the back of the filament, a metal plate was directly connected to pin2. Under typical conditions of no filament heating current and electron irradiation, equal

Under normal conditions, the voltage changes at Pin1 and Pin2 for on/off electron irradiation

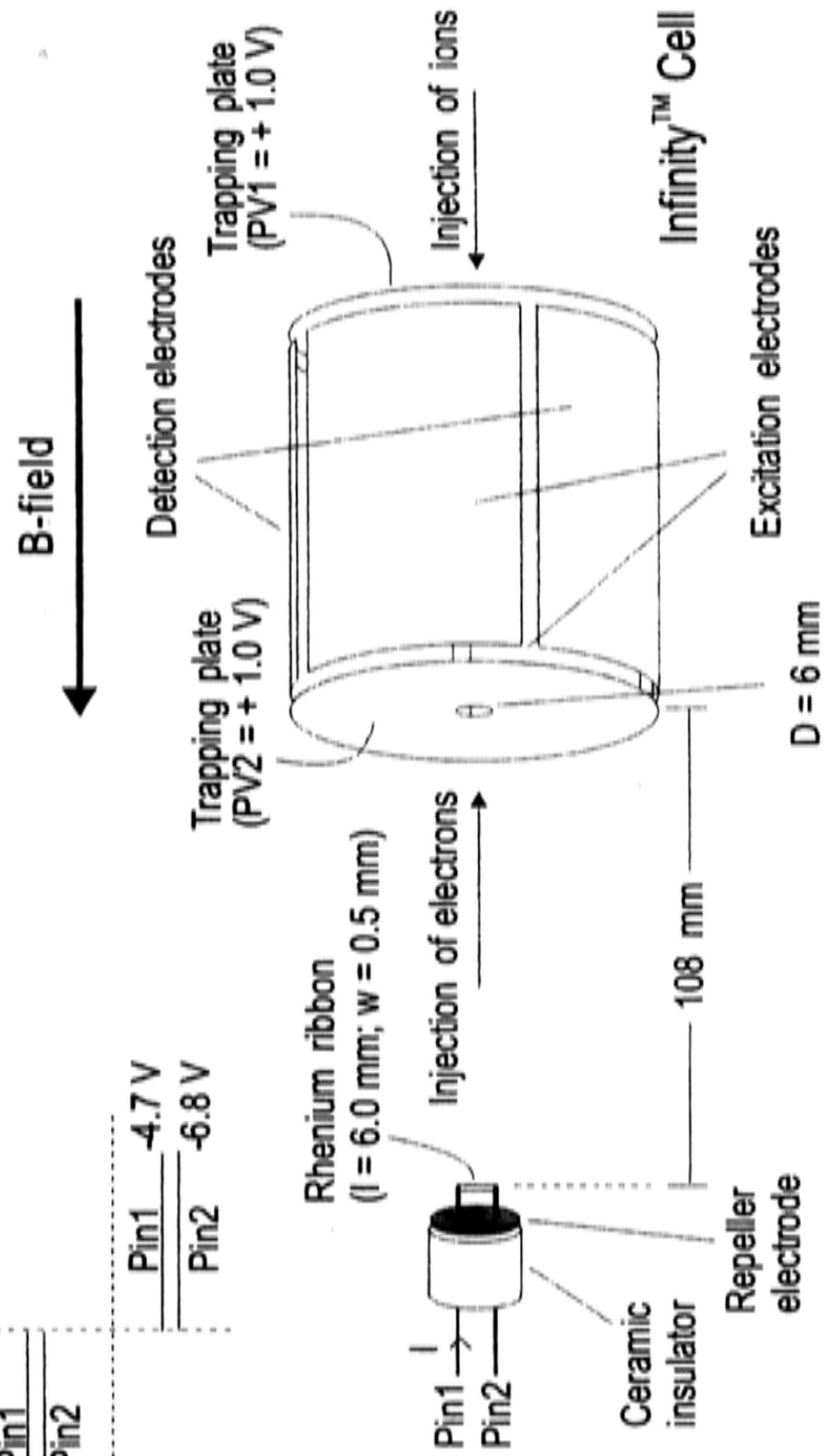
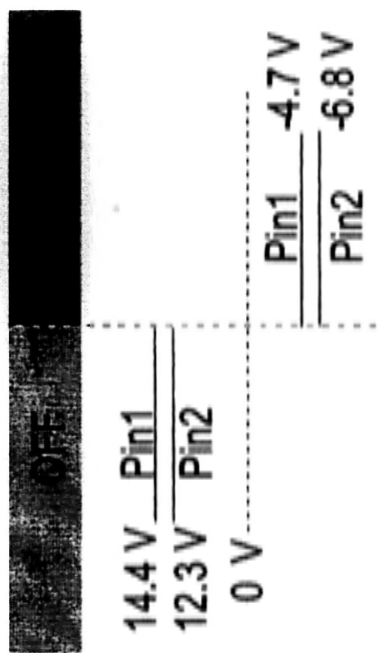


Figure 2.5 Schematic diagram of the heated filament electron source with the analyzer cell

potentials of +13.2 V were loaded onto both pin1 and pin2. When current flew through the filament, different potentials were loaded onto pin1 and pin2 such that the potential of pin1 was higher than that of pin2. During electron irradiation in ECD, the potentials of pin1 and pin2 were ramped down from a positive to a negative condition. When negative potential was applied onto pin2, electrons emitted from the filament were repelled from the metal plate into the Infinity™ Cell.

2.1.2.5 Data acquisition system

The console of the FTICR-MS used in this study was connected to a Dell window-based workstation PWS530 (Dell Computer Corporation, Texas, US) which was equipped with an Intel (R) XEO microprocessor and 32 megabytes (Mb) of base memory and operated under Microsoft Windows 2000 System. Tuning of experimental parameters, data acquisition and data manipulation were carried out using the user-interface program XMASS version 6.1.0 (Burker Daltonics, Billerica, US) running on the workstation.

The free induction decay (FID) signal received was amplified by either the FADC 12-bit digitizer (for board-band mode) or the SADC 16-bit digitizer (for narrow-band mode). The maximum size of the time-domain signal was 1 Mb. After completion of data acquisition, the FID signal was transferred to the Dell workstation. It was first zero-filled and subsequently converted to frequency-domain signal (mass spectrum) by the Fast Fourier transform (FFT) algorithm and magnitude calculation method.

2.2 Experimental Conditions

2.2.1 Sample preparation

Sample solution (~10 μL) was loaded into a homemade glass capillary tip placed a few centimeters away from the opening of the dielectric capillary in the nanospray ion source. The capillary tip was secured on a platform which could be finely adjusted along x, y and z directions. A thin gold-plated tungsten wire ($\text{\O} = 10.0 \mu\text{m}$), spot-welded onto a platinum wire ($\text{\O} = 0.3 \text{ mm}$) to facilitate manipulation, was then placed inside the capillary tip to establish electrical contact. This was followed by positioning the nanospray tip to 1 to 2 mm in front of the dielectric capillary.

2.2.2 Acquisition pulse program

Data acquisition from the performed FTICR-MS experiments was done via a pulse program, which is the execution of a sequence of pulses to different units of the FTICR-MS to control the corresponding events during data acquisition. The source codes of all the pulse programs used are in Appendix II.

2.2.2.1 MS with or without multiple-ion filling

The pulse program used for acquiring data from the ESI-FTICR-MS experiments involved four steps – ion quench, ion accumulation, ion excitation and ion detection, each of which is explained in detail below.

Ion quench, the first step for each acquisition cycle, referred to the control pulses used to ensure the removal of all ions from the InfinityTM Cell. Under this process, a pulse was sent to the voltage control board to pulse the potential of the rear trapping electrode (PV2) to negative voltage (-10 V) for the positive ion mode (and +10 V for the negative ion mode). This was followed by another quench control pulse sent to the voltage control board to change the potential of the gate electrode inside the ESI source to negative voltage for the positive ion mode (and positive

voltage for the negative ion mode). As a result, residue positive ions, if any, in the hexapole ion guide were removed. After the quench pulses, there was a short delay to restore the potential of the rear trapping electrode and gated electrode back to the preset values.

After quenching the source, ion accumulation was performed by storing the ions (generated from the nanospray source) in the hexapole ion guide for a preset delay period. Then an ion injection pulse was executed by first adjusting the gate electrode to the preset extraction potential so as to extract the ions from the hexapole ion guide to the electrostatic ion focusing region. This was followed by adjusting the deflector voltages (DPL2 and DPL4) and the entrance electrodes of the InfinityTM Cell (EV1, EV2 and DEV2) to the preset values to guide the ion beam towards the Cell. After the ions were accumulated for a predefined period of time, the deflector voltages were restored to ground voltages and the voltages of the entrance electrodes reset to the same potential as PV1.

The ion excitation pulse was executed after the injection of ions into the InfinityTM Cell. With the pulse, a *rf*-waveform (chirp for board-band mode or pulse for narrow-band mode) of scanning was transmitted from the cyclotron frequency of the lowest detection mass (highest frequency) to the highest detection mass (lowest frequency) through the excitation electrodes of the InfinityTM Cell. Following the pulse, the amplitude and duration of the *rf*-waveform were optimized to give an intense signal.

The entire pulse program concluded with the *rf*-receiver plates of the analyzer cell detecting the image current generated from the cyclotron motions of the excited ions and eventually an FID signal was generated.

For illustration purpose, a basic pulse program meant for ESI-FTICR-MS experiments is shown in Figure 2.6.

In order to increase the sensitivity for ion detection, the ion accumulation step was modified to a multiple-ion filling (MIF) approach. Instead of accumulating ions in the hexapole ion guide for a predefined period of time (1-2 seconds) before transferring them into the InfinityTM Cell (as with the ESI approach), ions were first injected into the Cell within a short-time accumulation in the hexapole ion guide. Cooling gas (argon) was then pulsed into the Cell to remove the excessive z-axial kinetic energy of the ions and to prevent substantial loss of trapped ions during the admission of another pulse of ions. Ion injection and pulsing of cooling gas as aforesaid were repeated for 10 times. An enhancement of the sensitivity for ion detection and in turn improved the quality of the mass spectrum.

Figure 2.7 shows the concept of the above mentioned pulse program. The ECD spectra of substance P generated under ESI and MIF approaches are shown in Figures 2.8 (a) and 2.8 (b) respectively.

2.2.2.2 MS² with or without double resonance ion ejection

The pulse programs of MS² involved the addition of two events, i.e. ion selection and ion activation, after the ion accumulation process.

Under the ion selection process, an ion selection pulse was executed once ions were accumulated in the InfinityTM Cell. The ions of interest were then isolated by irradiation with a correlation sweep (a modified chirp of *rf*-waveform) to over-excite all unwanted ions. This was followed by careful adjustment of the amplitude, *rf*-waveform duration and “ejection safety belt” to minimize the excitation of ions of interest and to maximum the ion ejection efficiency.

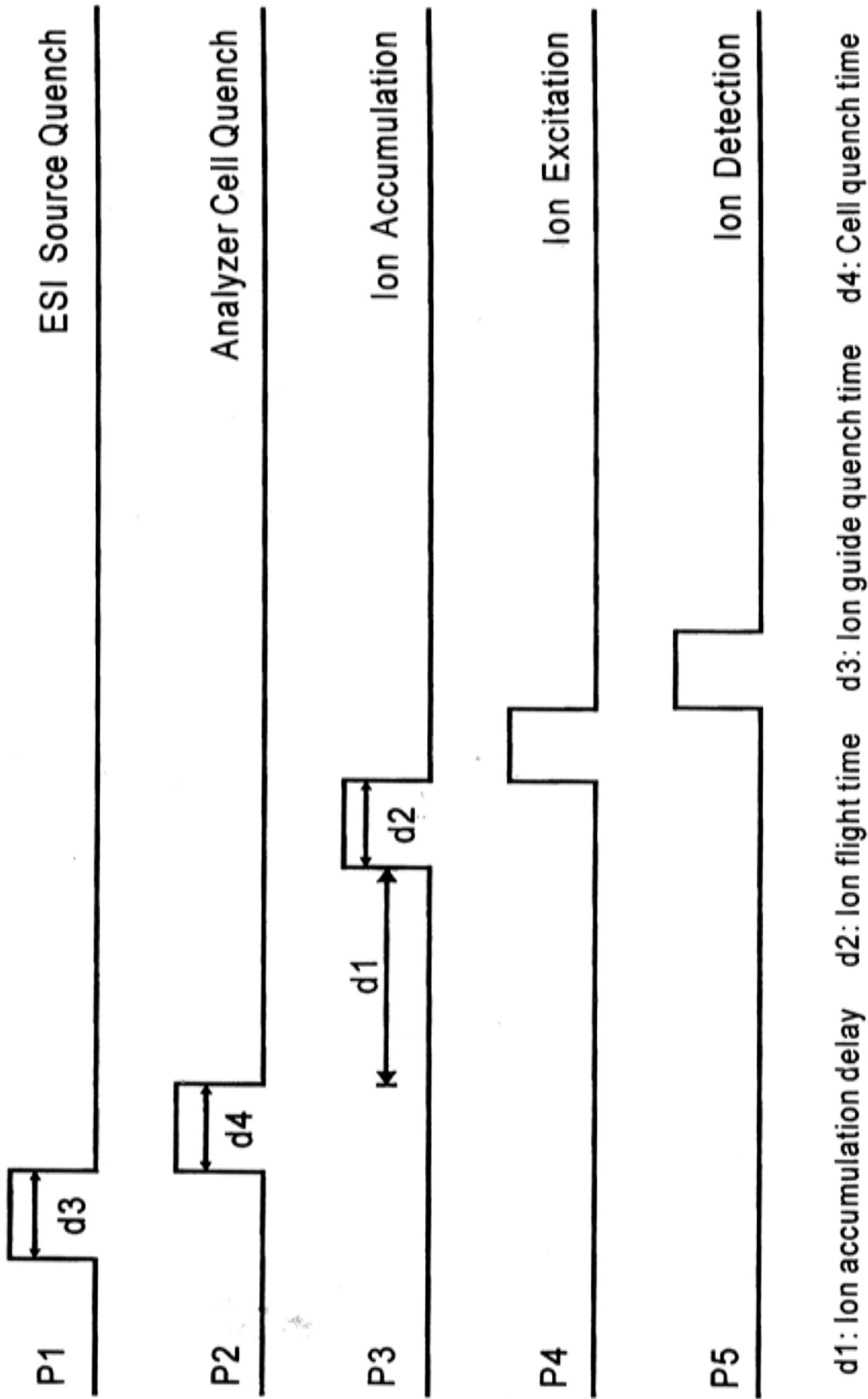


Figure 2.6 Pulse sequence program for ESI-FTICR-MS experiments

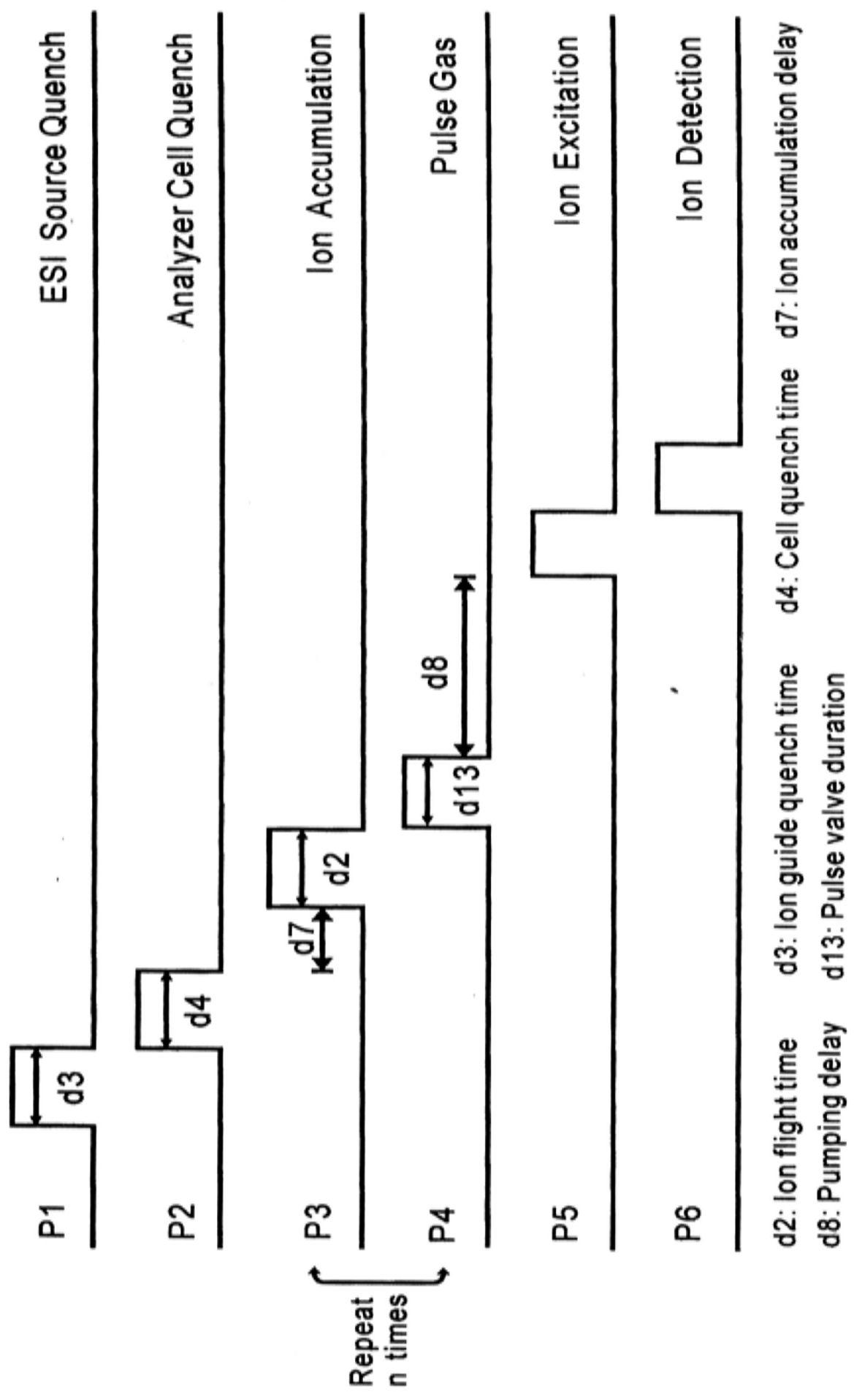


Figure 2.7 Pulse sequence program for MIF-FTICR-MS experiments

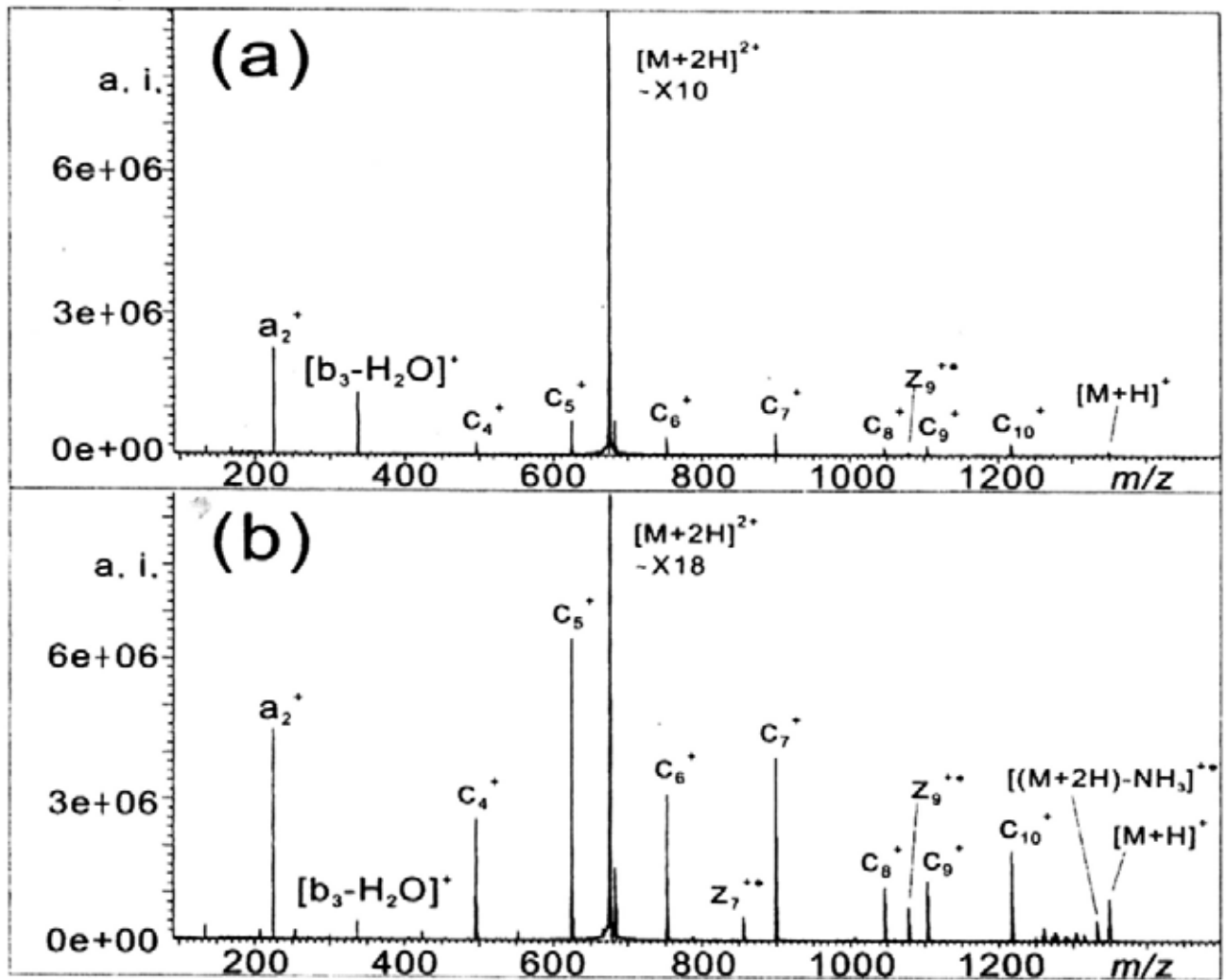


Figure 2.8 ECD spectra of substance P (a) without and (b) with using MIF

Among the numerous ion activation methods applicable to FTICR-MS, SORI-CID and ECD were adopted for use in this project.

The ion activation process in SORI-CID involved the pulsing of collision gas and ion activation with pumping delay. An inert collision gas (argon) was first pulsed into the InfinityTM Cell region immediately after the ion selection process. Then, the pressure of the high vacuum chamber was temporarily increased to $\sim 3.0 \times 10^{-7}$ mbar, whilst the magnitude of the pressure pulse was controlled by adjusting the cylinder pressure and the duration of the pulse gas event. The ion activation process ensued with the application of a 500 ms long *rf*-waveform to the excitation plates (at a frequency offset of 1,000 Hz relative to the frequency of the selected ions). The precursor ions were then excited/de-excited and eventually collided with the collision gas to generate fragment ions. Ultimately, the amplitude of the *rf*-waveform was adjusted to optimize the fragment ion intensities. After this ion activation process, there was a delay of 3.5 seconds to allow pressure within the Cell to be pumped back to the base level for the detection event. Figure 2.9 shows the pulse program used for ESI-(SORI-CID)-FTICR-MS experiments.

The ion activation process in ECD only involved an electron irradiation pulse, which was executed once the ions of interest had been selected and trapped in the InfinityTM Cell. This was followed by changing the potentials of the two pins on the electron source from positive to negative condition. The electron beam emitted thereafter was directed into the Cell to interact with the selected ions for a preset period of time. The electron flux and electron energy were then adjusted by varying the filament heating current and the average filament bias voltage to maximize the ECD fragments intensities. Figure 2.10 shows the pulse program for ESI-ECD-FTICR-MS experiments.

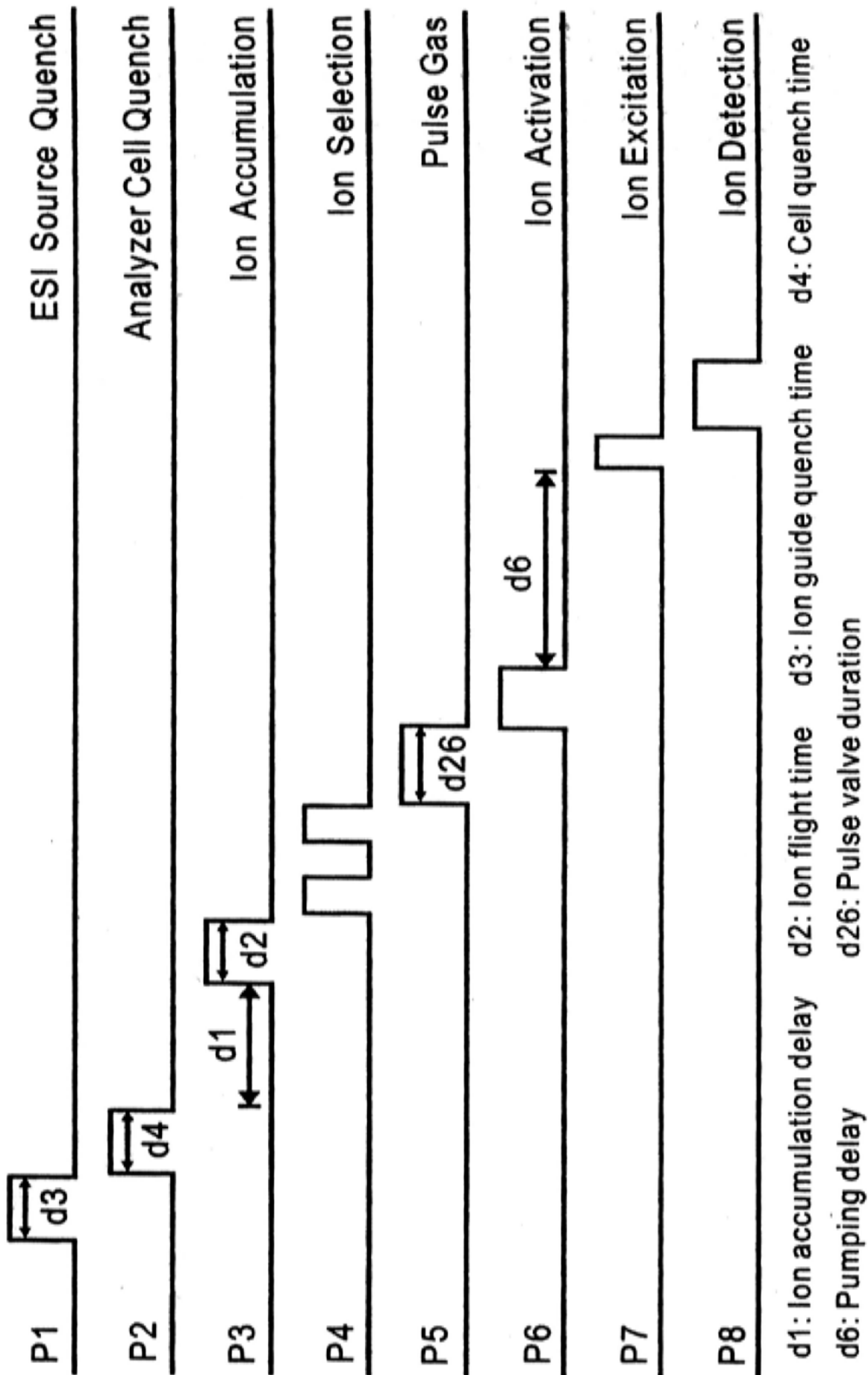


Figure 2.9 Pulse sequence program for ESI-(SORI-CID)-FTICR-MS experiments

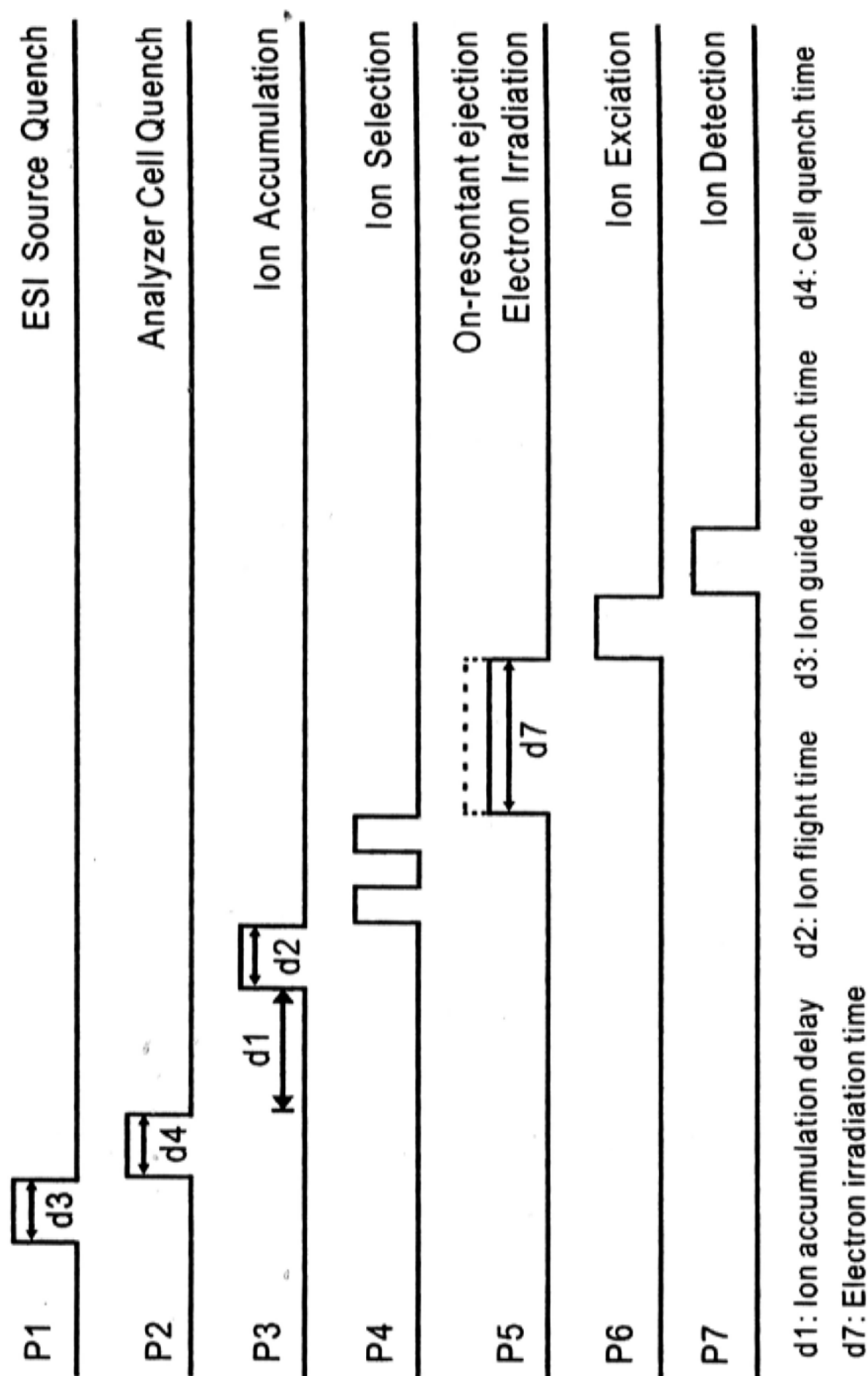


Figure 2.10 Pulse sequence program for ESI-(ECD/DR-ECD)-FTICR-MS experiments

In order to perform on-resonant ejection of a particular ion (usually the reduced precursor ion produced in ECD) during the electron irradiation process, the ECD experiment was modified to double resonance (DR) ECD experiment. This was achieved by executing an on-resonant ejection pulse and electron irradiation pulse simultaneously. As a result, all secondary ions derived from the ejected ion were generated. Please see Figure 2.10 for the pulse program used in an ESI-(DR-ECD)-FTICR-MS experiment.

2.2.2.3 MS³

To further investigate the structure of the fragment ion generated in MS², the fragment ion of interest was selected and dissociated in MS³ experiment, which was performed by adding the ion selection and ion activation processes before the ion excitation process in the pulse program for MS².

2.2.3 Calculation

2.2.3.1 *Ab initio* and Density functional theory (DFT) calculation

Calculations were performed using Gaussian 03 molecular orbital package [104]. For all copper ternary complexes [Cu^{II}(Tpy)(M-H)]⁺⁺, geometry optimizations were performed using Becke's hybrid B3LYP functional [105-107], with 3-21G(d) basis set applied to the H, C, N and O atoms in the complexes. The LANL2DZ basis set was used to place an effective core potential (ECP) on Cu [108, 109]. Spin-unrestricted calculations (UB3LYP) were employed for the open-shell system. The optimized structures were characterized by harmonic frequency analysis as local minima (all frequencies real) and first order saddle points (single imaginary frequency); and the frequencies were corrected by 0.96 for calculation of

zero-point vibrational corrections [110]. Single-point energies were calculated at B3LYP level using the 6-31 + G(d,p) basis set on H, C, N and O atoms plus LANL2DZ with ECP on Cu. Spin contamination in calculations with unrestricted wave functions was negligible to moderate. The $\langle S^2 \rangle$ operator expectation values were 0.75-0.76 for B3LYP with LANL2DZ calculations of local minima and transition state.

2.2.3.2 Molecular mechanics calculation

Merck molecular force fields (MMFFs) and conformational searches (Low Mode conformational search, LMCS) were used to predict the low-energy conformers using MacroModel program (v5, Schrodinger Inc., Portland, OR). In general, Truncated Newton-Raphson Conjugate Gradient (TNCG) was used to perform energy minimization. The low-mode conformational search was conducted using Monte Carlo [111] method with a random variation of all bonds [112]. Low-energy conformers were found in 5000 steps. Only structures with energies within 50 kJmol⁻¹ from the lowest-energy structure were stored. From the results of the initial search, the lowest-energy structure and up to 10 structurally different conformers were used as starting geometries for another 5000 steps conformational searches. Energies of all structures found in these conformational searches were aligned; and low-energy conformers within 15 kJmol⁻¹ from the lowest energy conformer were then used to compute the hydrogen-bonding pattern of the molecular ions. The relative contribution of hydrogen-bonding from each low-energy conformer was calculated using Boltzmann distribution. Finally, the overall distribution of hydrogen bonds was obtained by adding up the relative abundance of hydrogen-bonding formed at the backbone amide linkages (which were contributed by the low-energy conformers)

Chapter 3

Direct Comparison of Fragmentation Patterns between Different Types of Peptide Radical Cations

3.1 Introduction

Since dissociation of peptide radical ions can yield complementary information for structural characterization of peptides/proteins, lots of studies have been conducted to investigate the factors governing the dissociation pathways of peptide radical ions. The role of radicals in peptide radical ions is believed to be amongst such factors. According to the findings of a recent comprehensive study conducted by O'Hair and co-workers on the dissociation patterns of peptide radical cations produced from copper ternary complexes [77] and protonated peptides under the tripeptide model, GXR (X being one of the 20 common amino acids), the fragmentation reactions of hydrogen-deficient peptide radical cations are radical directed whereas the CID of their corresponding protonated peptides are proton initiated.

In order to probe into the role played by radical in the dissociation process, the fragmentation patterns of hydrogen-deficient peptide radical cations ($[M+(n-2)H]^{(n-1)+}$) generated by CID of copper ternary complex ($[Cu(L)(M+(n-2)H)]^{n+}$, where L = ligand and M = peptide) were compared with those of hydrogen-surplus peptide radical ions ($[M+nH]^{(n-1)+}$) generated by ECD. As one of the proposed dissociation mechanisms of ECD is remote by hydrogen radical (H^\bullet) released by neutralization of the captured electron, it is believed that examination of the dissociation pathways of hydrogen-deficient peptide radical cations $[M+(n-2)H]^{(n-1)+}$ (M^{++} when $n = 2$) may shed light on the fragmentation

mechanism of peptide radical cations.

Aiming to acquire more information on the dissociation mechanisms of copper ternary complexes, the dissociation pathways and fragmentation patterns of peptide radical cations generated by SORI-CID and a series of custom-synthesized peptides were analyzed. The general sequences of the peptides are G_9X (where X is either I, L or W), G_4XG_4K (where X is either I, L, W, S or E) and ZG_5WG_5Z' (where Z and Z' are R, K or H). The glycine spacers in all these peptides were used to separate functionalized amino acid residues in an effort to minimize the complication(s) arising from specific interactions between adjacent residues.

A larger system of peptides, G_4XG_4K (versus GXR), was used in this study as in order to facilitate an additional insight into the fragmentation behaviours of $[Cu(Tpy)M]^{2+}$ and M^{+} . In order to investigate the role of radical in subject dissociations, the results of SORI-CID of M^{+} were cross-compared with those of SORI-CID and ECD of their protonated species (i.e., $[M+H]^+$ and $[M+2H]^{2+}$). As regards ZG_5WG_5Z' , its hydrogen-deficient peptide radical cations ($[M+H]^{2+}$) contain an extra hydrogen (which is non-existent in G_4XG_4K). Thus the role of proton in the dissociation process could be examined and their ECD fragmentation patterns of $[M+H]^{2+}$ compared to those of $[M+3H]^{2+}$.

3.2 Experimental Section

A series of custom-synthesized model peptides G_9X (where X = I, L or W), G_4XG_4K (where X = I, L, W, S or E) and ZG_5WG_5Z' (where Z and Z' = R, K or H) were purchased from Pepton Inc. (Daejeon, South Korea) and used without further purification. Ternary copper complexes were prepared *in situ* by first mixing 49 μ L of 1.6 mM $CuSO_4 \cdot 5H_2O$ (Riedel-de Haen, Seelze, Germany) with 49 μ L of 300 μ M

peptide in 50:50 (v:v) water:methanol solution. The sample was vortexed for one minute and 2 μL of saturated 2,2':6',2''-terpyridine (Tpy) (Sigma-Aldrich, St. Louis, MO, USA) was added to the 98 μL sample. For SORI-CID and ECD experiments related to protonated peptides, the analyte solutions were prepared at peptide concentrations of 250 μM in 50:50 (v:v) water:methanol solution with 3% acetic acid (Riedel-de Haen, Seelze, Germany).

All experiments were conducted by using a 4.7 Tesla FTICR-MS (APEX I, Bruker Instrument Inc., Boston, MA, USA), a computer system and associated electronics which were upgraded to APEX III. For detailed instrumental arrangements and sample preparation procedures, please refer to Chapter 2.

In SORI-CID experiments, precursor ions were first mass-selected by preferentially exciting and ejecting other unwanted ions. Argon gas was pulsed from a pressure-regulated cylinder (~ 0.35 bar) into the analyzer region using a solenoid pulse-valve with a fixed duration of 1200 μs , and pressure within the analyzer cell was temporarily increased from $\sim 8.0 \times 10^{-9}$ Torr (basic pressure) to $\sim 3.0 \times 10^{-7}$ Torr. The isolated precursor ions were then activated by using a 500 ms *rf*-waveform with a frequency offset of 1000 Hz to the corresponding ion cyclotron frequency of the molecular ions. This was followed by careful adjustment of the *rf*-waveform's amplitude to maximize the intensities of the fragment ions from 2 to 6 $V_{\text{peak-to-peak}}$. A delay of 3.5 s was used after the ion activation process to allow metastable fragmentation of the activated ions and resumption of the base pressure before excitation and detection of the resulting ions. 10 cycles of MIF were performed for SORI-CID of copper ternary complex with a series of ZG_5WG_5Z' . 50 scans were summed to improve the signal-to-noise ratio in SORI-CID of copper ternary complex, whereas in the case of protonated peptides, 30 scans were summed. All mass spectra

were acquired in broadband mode with time-domain signals of 256k data points and were zero-filled once prior to Fourier transformation.

In ECD experiments, a standard electrically-heated filament source was used to produce pulses of electron beam. Typical experimental conditions were 3.2 A filament heating current, 4.5 V average filament bias voltage and 300 ms electron irradiation time. 30 scans were summed to improve the signal-to-noise ratio. All ECD mass spectra were acquired in broadband mode using 128k data points and zero-filled twice prior to Fourier transformation.

For all structures of copper ternary complexes $[\text{Cu}^{\text{II}}(\text{Tpy})(\text{M-H})]^{2+}$ tackled in this chapter, calculations were performed using Gaussian 03 molecular orbital package. Please refer to Chapter 2 for the detailed parameters of the calculations.

3.3 Results and Discussion

3.3.1 The G₉X and G₄XG₄K series

3.3.1.1 SORI-CID of $[\text{Cu}(\text{Tpy})\text{M}]^{2+}$

Figure 3.1 shows the typical SORI-CID mass spectra of $[\text{Cu}(\text{Tpy})\text{M}]^{2+}$, where M is (a) G₉I, (b) G₉W, (c) G₄IG₄K and (d) G₄WG₄K. Assignments of all labeled side chain in the spectra are shown in Appendix III. It can be seen from the spectra that dissociation of $[\text{Cu}(\text{Tpy})\text{M}]^{2+}$ generated mainly peptide radical cations ($\text{M}^{+\bullet}$), copper-related species such as $[\text{Cu}(\text{Tpy})]^+$, $[\text{Cu}(\text{Tpy})(\text{y}_n\text{-H})]^+$, $[\text{Cu}(\text{M-H})]^+$ and protonated ligand $[\text{Tpy}+\text{H}]^+$. The occurrence of these fragment ions matched nicely with the first three of the dissociation channels [76, 77, 113, 114] as proposed by Siu and co-workers below:



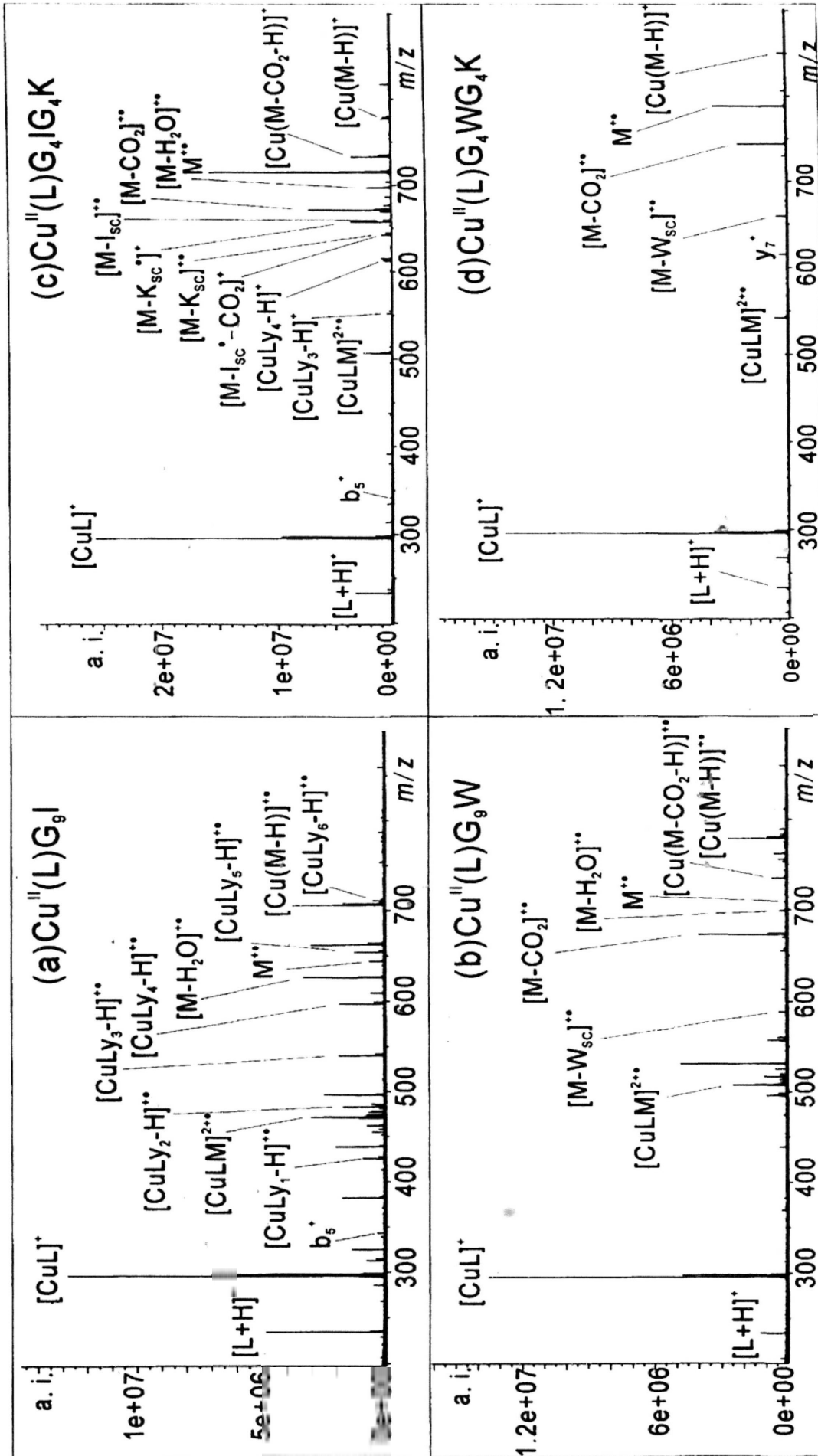
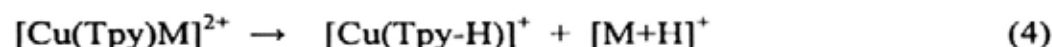
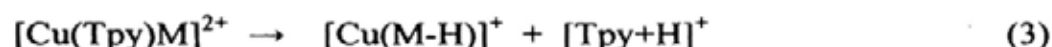
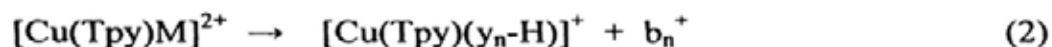


Figure-3.1 Typical SORI-CID spectra of $[\text{Cu}(\text{L})\text{M}]^{2+}$, where L is Tpy and M is (a) G_9I , (b) G_9W , (c) $\text{G}_4\text{IG}_4\text{K}$ and (d) $\text{G}_4\text{WG}_4\text{K}$.



The fourth dissociation channel was not observed in this study, presumably due to the absence of acidic proton in terpyridine (Tpy) [75].

The general information obtained from the SORI-CID spectra concerned are summarized in Table 3.1, which shows that G₄XG₄K generated mainly M⁺⁺ related fragments. It is also indicated in Figure 3.1 (c) and (d) that the presence of lysine (K) greatly depleted dissociations through channels 2 and 3. These observations are in line with the finding of Siu et al., who postulated that the presence of basic amino acid could prevent competing pathways via mobile proton and acid-base reaction [76]. G₄XG₄K was therefore used in the study on the dissociation patterns of M⁺⁺ as described below.

3.3.1.2 SORI-CID of M⁺⁺

Figure 3.2 shows the typical SORI-CID mass spectra of M⁺⁺, where M is (a) G₄IG₄K, (b) G₄EG₄K and (c) G₄WG₄K. It indicates that odd- and even-electron side chain loss reactions were much more abundant than backbone fragments as the relative intensities of backbone fragments were below 30%. This suggests dissociation of M⁺⁺ would result in X or K side chain loss when the heteroatom radical abstracted a α- or γ-hydrogen atom from X or K. The possible dissociation pathways of the odd- and even-side chain loss from M⁺⁺ are proposed in Scheme 3.1 (a) and (b).

As can be seen from Figure 3.2, backbone cleavages were minor dissociation channels compared to abundant side chain loss reactions. Since the dissociation of

Table 3.1 Relative abundance of SORI-CID fragments of $[\text{Cu}(\text{Tpy})\text{G}_9\text{X}]^{2+}$ and $[\text{Cu}(\text{Tpy})\text{G}_4\text{XG}_4\text{K}]^{2+}$. (%)

| Peptide | X | M^{2+} | M^{2+} related species | | | $[\text{Cu}^{\text{II}}(\text{Tpy})(\text{Y}_a\text{-H})]^+$ | b_n^+ | $[\text{Cu}^{\text{II}}(\text{M-H})]^+$ | $[\text{Tpy+H}]^+$ | |
|---------------------------------|---|---------------------|---------------------------------|----------------------------------------|----------------------------------------|--------------------------------------------------------------|---------|-----------------------------------------|--------------------|------|
| | | | $[\text{M-H}_2\text{O}]^{2+}$ | $[\text{M}^{2+}\text{-K}_{\text{sc}}]$ | $[\text{M}^{2+}\text{-X}_{\text{sc}}]$ | | | | | |
| G_9X | I | 3.6 | 14.7 | N/A | -- | 100.0 | 39.3 | 2.7 | 44.5 | 44.6 |
| | L | 2.1 | 13.0 | N/A | -- | 100.0 | 31.8 | -- | 18.0 | 12.0 |
| | W | 2.8 | 4.6 | N/A | 3.2 | 100.0 | -- | -- | 36.9 | 7.3 |
| | | (48.9) ^a | | | | | | | (6.9) | |
| $\text{G}_4\text{XG}_4\text{K}$ | I | 58.7 | 8.3 | 15.7 | 4.5 | 100.0 | 7.8 | 0.7 | 2.9 | 7.7 |
| | L | 38.9 | 5.6 | 10.9 | 4.4 | 100.0 | 5.0 | 1.0 | 2.0 | 12.3 |
| | S | 23.4 | 4.5 | 5.3 | - | 100.0 | -- | -- | -- | 8.0 |
| | | (26.6) | | (3.7) | | | | | (13.2) | |
| | | (16.3) | | (3.3) | (9.5) | | | | | |
| | | (6.8) | | | | | | | | |
| | E | 24.2 | 2.6 | 4.4 | 5.9 | 100.0 | -- | -- | 2.3 | 21.0 |
| | W | 22.3 | 0.8 | 1.6 | 3.2 | 100.0 | -- | -- | 2.2 | 4.3 |
| | | (14.6) | | | (2.6) | | | | | |

^aThe value in () indicates loss of CO_2 from the corresponding species.

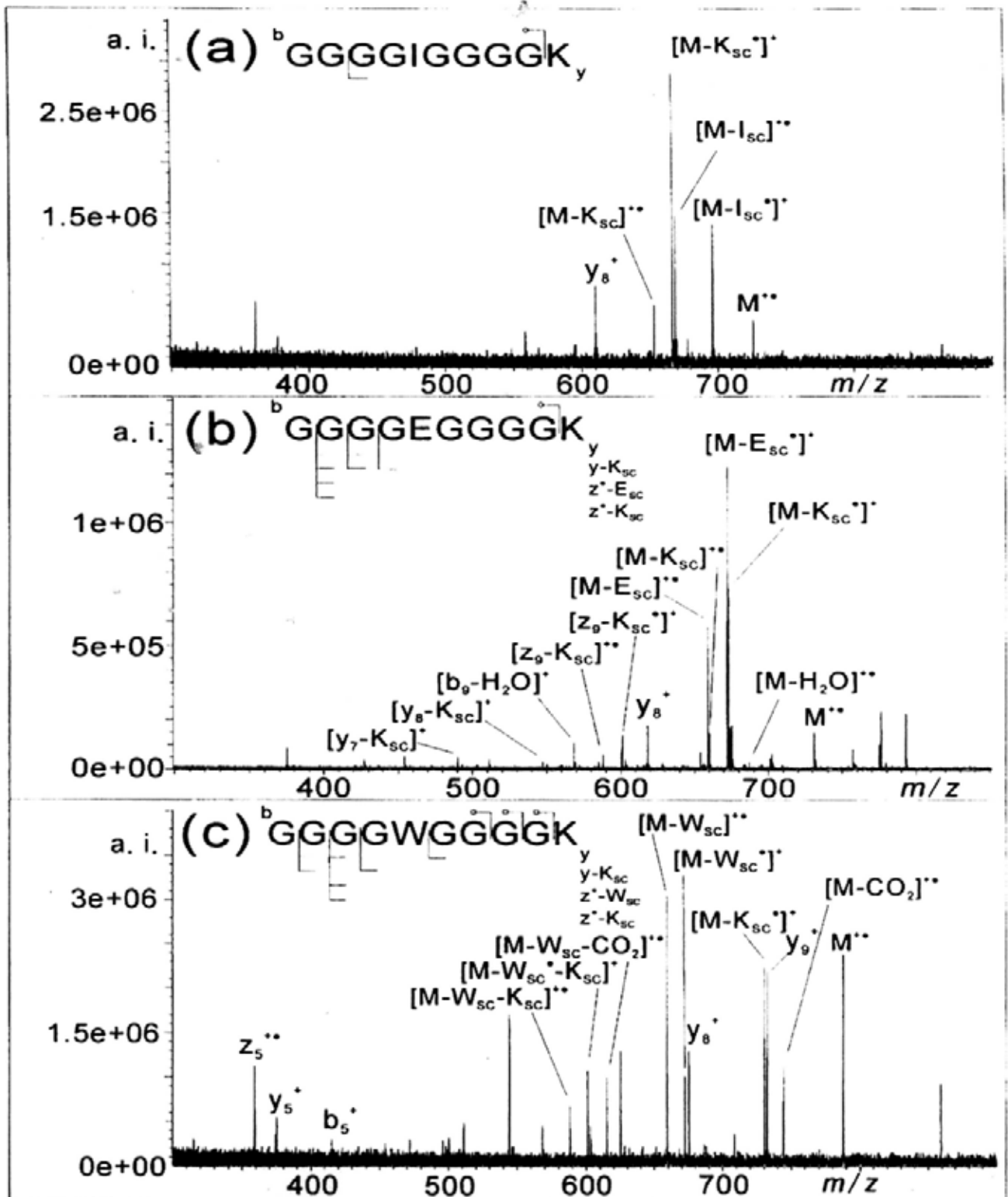
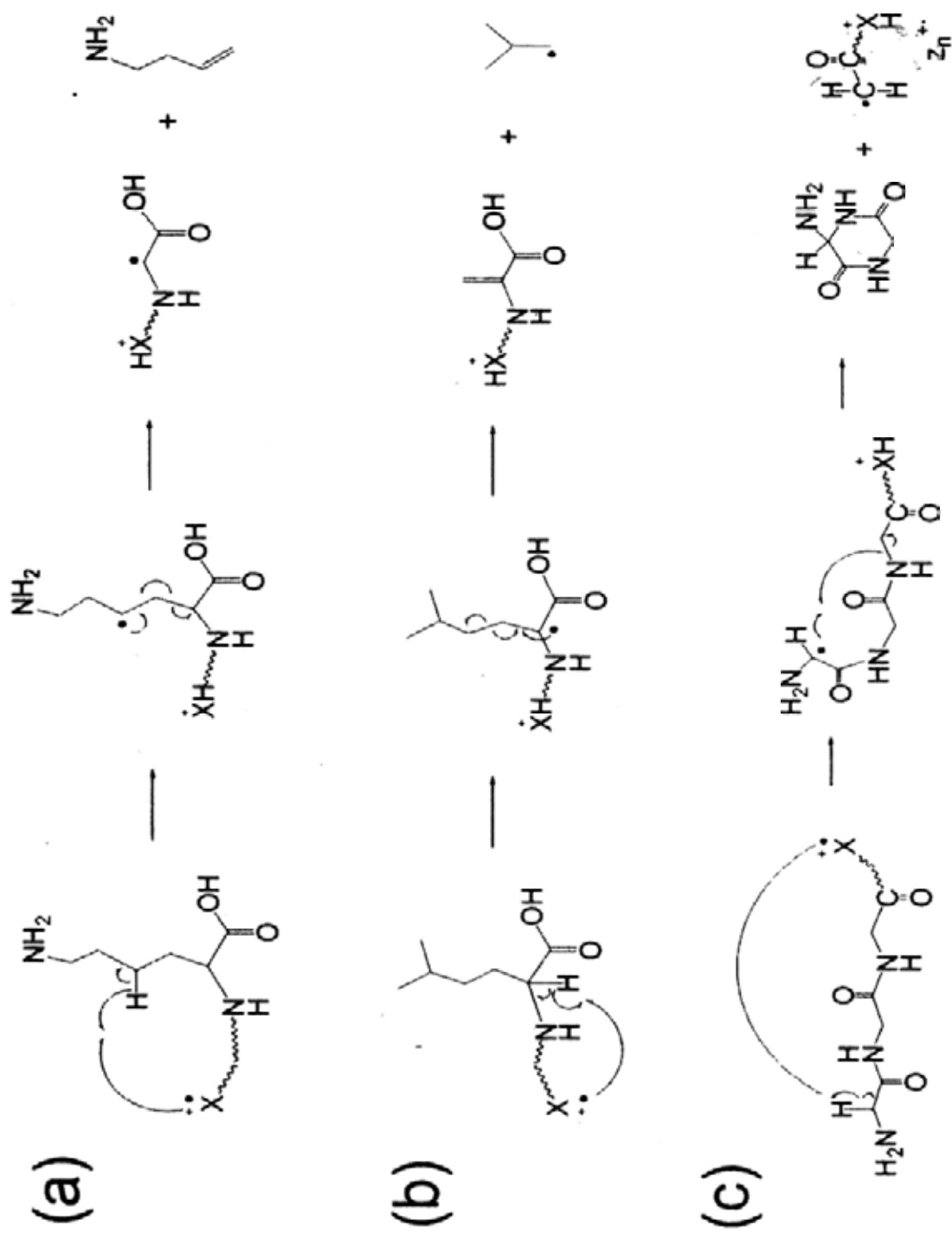


Figure 3. 2 Typical SORI-CID spectra of $G_4XG_4K^{+\bullet}$, where X is (a) I, (b) E and (c) W (— indicates CO_2 loss from corresponding backbone fragments)



Scheme 3.1 The proposed dissociation pathways of (a) K even-electron side chain loss from $M^{\bullet\bullet}$, (b) L odd-electron side chain loss from $M^{\bullet\bullet}$, (c) z^{\bullet} ion

$M^{+\bullet}$ was believed to be initiated by radical, γ and z' ions might also have been formed when the heteroatom radical abstracted a hydrogen atom at α -carbon from glycine. A proposed formation of γ ion was put forth by O'Hair and co-workers [77], whilst a possible formation of z' ion is proposed via Scheme 3.1 (c). The observed more abundance of side chain loss from $M^{+\bullet}$ than backbone cleavages suggests that the abstraction of hydrogen atom from α - or γ -carbon of X was easier than that from α -carbon of glycine.

A summary of the fragment ions generated from SORI-CID of $M^{+\bullet}$ is given in Table 3.2. In all the cases involved, γ ions were observed. Yet in some cases, side chain loss from z' ions (w ions) was observed but z' ions were not found. It is suspected that this might be due to the relatively low stability of odd-electron z' ions (compared to even-electron γ ions) which had caused them to undergo secondary dissociation easily to form the w ions. However, there were research groups [113, 115] who observed that more backbone fragments such as b , γ and z' ions were generated in their experiments. This difference in findings is believed to be attributable to the use of different types of instruments. In literature, ion trap MS was used to perform CID of $[Cu(L)M]^{2+}$. But in this study, a first attempt was made to use FTICR-MS for such purpose. In the 'literature' case, the cooling gas used caused the pressure in the ion trap MS to be higher than that of the ICR cell. It followed that the ions in the trapping region (of the ion trap MS) had a higher internal energy and hence a higher probability of backbone cleavages.

As illustrated via Table 3.2, $[M-CO_2]^{+\bullet}$ was only obtained in G_4EG_4K and G_4WG_4K during the dissociation of $M^{+\bullet}$. However, in the dissociation of $[Cu(Tpy)M]^{2+}$, $[M-CO_2]^{+\bullet}$ was observed in all G_4XG_4K cases and its relative intensity in most cases was found to be higher than that in the dissociation of $M^{+\bullet}$.

Table 3.2 Relative abundance of SORI-CID fragments of G₄XG₄K^{•+} (M^{•+}). (%)

| X | [M-CO ₂] ^{•+} | [M-H ₂ O] ^{•+} | [M ^{•+} -K _{sc}] | [M ^{•+} -X _{sc}] | y ₉ ⁺ | y ₈ ⁺ | $\sum_{i=1}^9 [b_i \cdot K_{sc}]^{\bullet+}$ | $\sum_{i=1}^9 [z_i \cdot K_{sc}]^{\bullet+}$ | $\sum_{i=1}^9 [z_i \cdot X_{sc}]^{\bullet+}$ | Other products |
|---|------------------------------------|------------------------------------|-------------------------------------|-------------------------------------|-----------------------------|-----------------------------|----------------------------------------------|----------------------------------------------|----------------------------------------------|------------------------------------------------------------|
| I | -- | -- | 100.0 ^a | 45.6 | -- | 28.0 | -- | -- | -- | [M-I _{sc} -H ₂ O] ^{•+} (8.4) |
| | -- | -- | (19.4) ^b | (51.2) | -- | -- | -- | -- | -- | [b ₉ -H ₂ O] ^{•+} (14.4) |
| L | -- | -- | 96.0 | 100.0 | -- | 23.5 | -- | -- | -- | [M-L _{sc} -K _{sc}] ^{•+} (19.7) |
| | -- | -- | (14.3) | (91.2) | -- | -- | -- | -- | -- | [M-L _{sc} -K _{sc}] ^{•+} (19.3) |
| | | | | | | | | | | [y ₈ -H ₂ O] ^{•+} (8.8) |
| S | -- | 8.0 | 100.0 | -- | -- | 14.1 | -- | -- | -- | [b ₉ -H ₂ O] ^{•+} (5.9) |
| | -- | -- | (17.8) | -- | -- | -- | -- | -- | -- | [y ₈ -H ₂ O] ^{•+} (9.8) |
| E | 2.5 | -- | 59.6 | 100.0 | 14.6 | 14.5 | -- | 11.2 | 5.7 | [M-K _{sc} -H ₂ O] ^{•+} (2.0) |
| | -- | -- | (12.0) | (47.4) | -- | -- | (8.5) | (5.0) | -- | [M-E _{sc} -H ₂ O] ^{•+} (6.0) |
| | | | | | | | | | | [M ^{•+} -E _{sc} -CO ₂] (4.6) |
| | | | | | | | | | | [b ₉ -H ₂ O] ^{•+} (9.1) |
| W | 56.8 | -- | 89.7 | 22.5 | 24.7 | 22.2 | -- | 18.5 | 6.6 | [M-W _{sc} -CO ₂] ^{•+} (44.7) |
| | -- | -- | -- | (100.0) | -- | -- | -- | (16.2) | -- | b ₅ ⁺ (5.4) |
| | | | | | | | | | | $\sum_{i=1}^9 [b_i \cdot H_2O]^{\bullet+}$ (39.9) |

^aThe value indicates loss of odd-electron side chain from the corresponding species.^bThe value in () indicates loss of even-electron side chain from the corresponding species

These observations presumably imply that the loss of CO₂ was not induced by the excessive internal energy in M⁺ but might be related to the binding mode of copper-terpyridine complex.

To illustrate the postulation as mentioned above, deprotonated N-acetyl-glycine in model 1 was used to study whether the binding mode of copper-terpyridine complex would lead to the loss of CO₂ in MS². Since the coordination number of copper in the complex was unknown, optimizations of several geometries were performed. Figure 3.3 shows three binding modes pursued. Among them, the square planar structure (bm1) was found to be the most stable one.

The [Cu^{II}(Tpy)(M-H)]⁺ complex (**1a**) shown in Scheme 3.2 was roughly a planar around the copper center and nitrogen atoms of terpyridine – the preferred geometry for Cu^{II} in gas phase [115, 116]. Upon SORI-CID, the distance between carboxyl oxygen of C-terminus and the copper center was increased from 1.867 Å to 2.062 Å while the C-C_α backbone bond was lengthened from 1.549 Å to 2.375 Å, as shown in TS1ab. As a result, **1a** dissociated to give **1b** and [Cu(Tpy)]⁺ with CO₂ simultaneously lost from **1b**. The reaction was found to be endothermic ($\Delta H_{rxn} = 12$ kJ mol⁻¹), with an activation barrier of 110 kJ mol⁻¹. This calculation suggests that the cleavage of C-C_α backbone bond in the activated copper ternary complex would lead to the loss of CO₂. Alternatively, when the dissociation of copper ternary complex existed as bm2 or bm3, [M-H]⁺ and [Cu(Tpy)]⁺ would be generated as major fragment ions. Scheme 3.3 shows the dissociation pathways of bm2 and bm3. Based on these findings, it is suspected that the loss of CO₂ from peptide in SORI-CID of [Cu(Tpy)M]²⁺ might probably be a copper mediated-reaction for certain binding modes.

The fragmentation patterns between SORI-CID of G₄XG₄K⁺ in this study

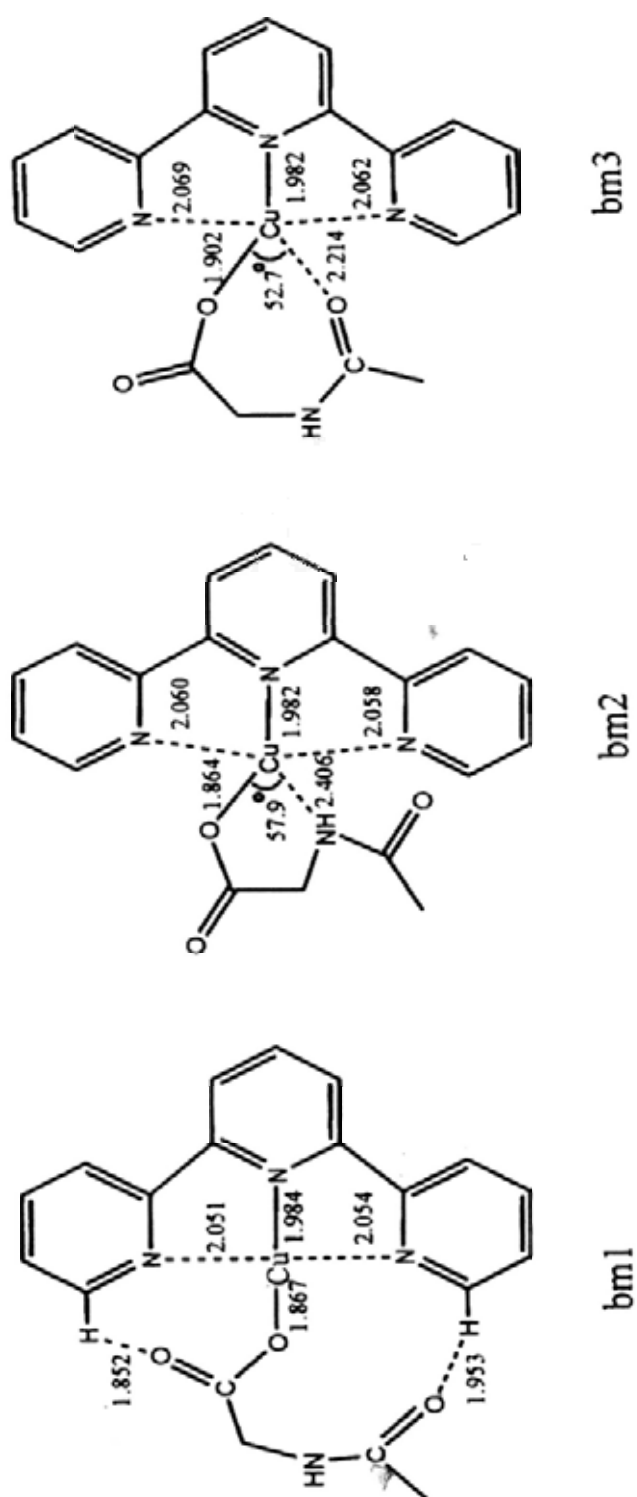
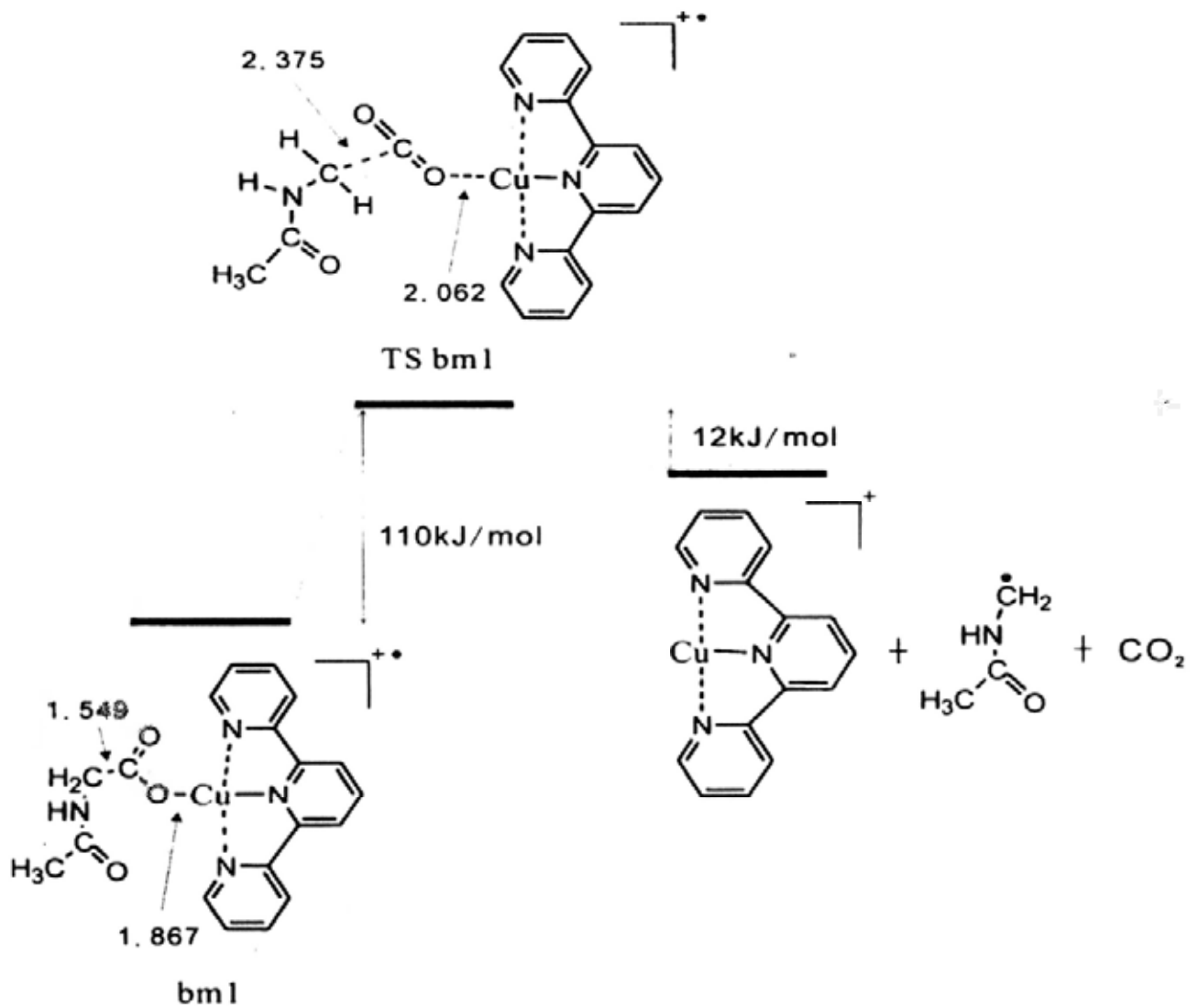
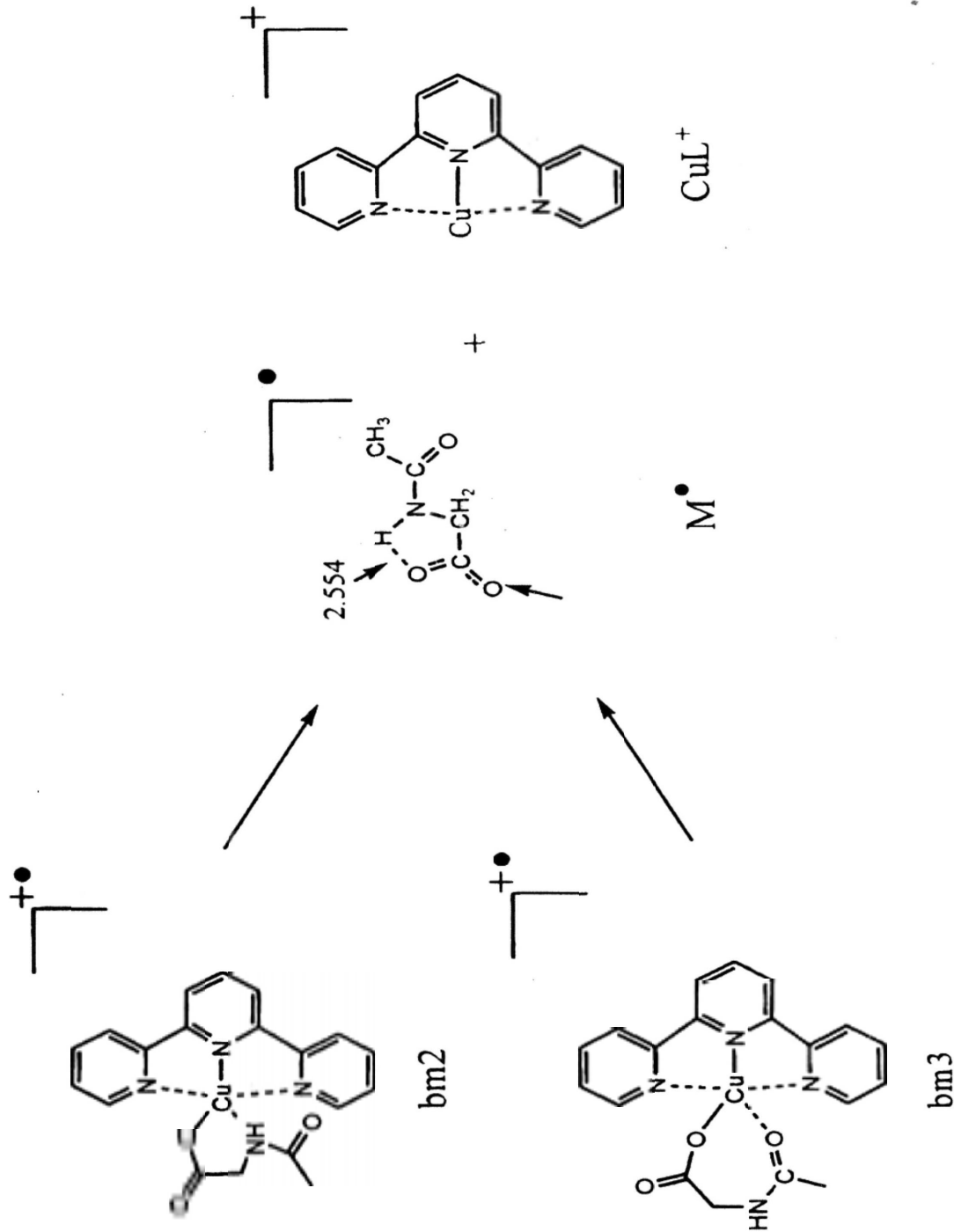


Figure 3.3 Three binding modes of truncated peptide binding to the copper-terpyridine complex



Scheme 3.2 Dissociation pathway of $[\text{Cu}^{\text{II}}(\text{Tpy})\text{M}]^+$, where M is truncated peptide, using B3LYP/6-31+G(d,p)[C,H,N,O]/ECP/LANL2DZ[Cu]//B3LYP/3-21G(d)[C,H,N,O]/ECP/LANL2DZ[Cu].



Scheme 3.3 Dissociation pathway of $[\text{Cu}^{\text{II}}(\text{Tpy})\text{M}]^+$ for bm2 and bm3, where M is truncated peptide, using B3LYP/6-31+G(d,p)[C,H,N,O]/ECP/LANL2DZ[Cu]//B3LYP/3-21G(d)[C,H,N,O]/ECP/LANL2DZ[Cu].

and SORI-CID of GXR^{++} by O'Hair and co-workers [77] were compared. In the small system of GXR^{++} , X side chain loss from M^{++} and y_1 ions were the major fragments. But in the system adopted in this study, X and K side chain loss from $G_4XG_4K^{++}$ were the most abundant fragment ions while y_8 and y_9 ions were the minor fragments yielded. Although the speciation of fragments in the two systems was the same, the preferential dissociation channels were not identical. Furthermore, while side chain loss from M^{++} were the most intense fragments in both cases, the intensities of y ions produced from GXR^{++} were much higher than those from $G_4XG_4K^{++}$ (due presumably to the steric effect of X or R side chain(s) in the small system which had resulted in structures favouring the formation of y ions). These comparative results suggested that the chain length of peptide ions would determine the flexibility of the backbone which in turn altered the dissociation channels.

3.3.1.3 Comparison between SORI-CID of $[M+H]^+$, M^{++} and ECD of $[M+2H]^{2+}$

Figure 3.4 sets out the typical mass spectra of G_4LG_4K (M) in (a) SORI-CID of $[M+H]^+$, (b) SORI-CID of M^{++} and (c) ECD of $[M+2H]^{2+}$. It shows that SORI-CID of $[M+H]^+$ produced a myriad of backbone fragments, mainly b/y ions, which had a high sequence coverage. In SORI-CID of M^{++} , side chain loss from M^{++} was the most dominant fragment species and only a few backbone fragments were obtained. As to ECD of $[M+2H]^{2+}$, it generated primarily c/z^+ ions while a , b , x , y and w ions (i.e., side chain loss from z^+ ions) were observed as minor fragments.

As the speciation of precursor ions differed, naturally the species of fragment ions produced from the dissociation of $[M+H]^+$ and M^{++} under SORI-CID were different. Obviously, SORI-CID of even-electron $[M+H]^+$ was driven by 'mobile proton' while the SORI-CID of odd-electron M^{++} by radical. During the SORI-CID

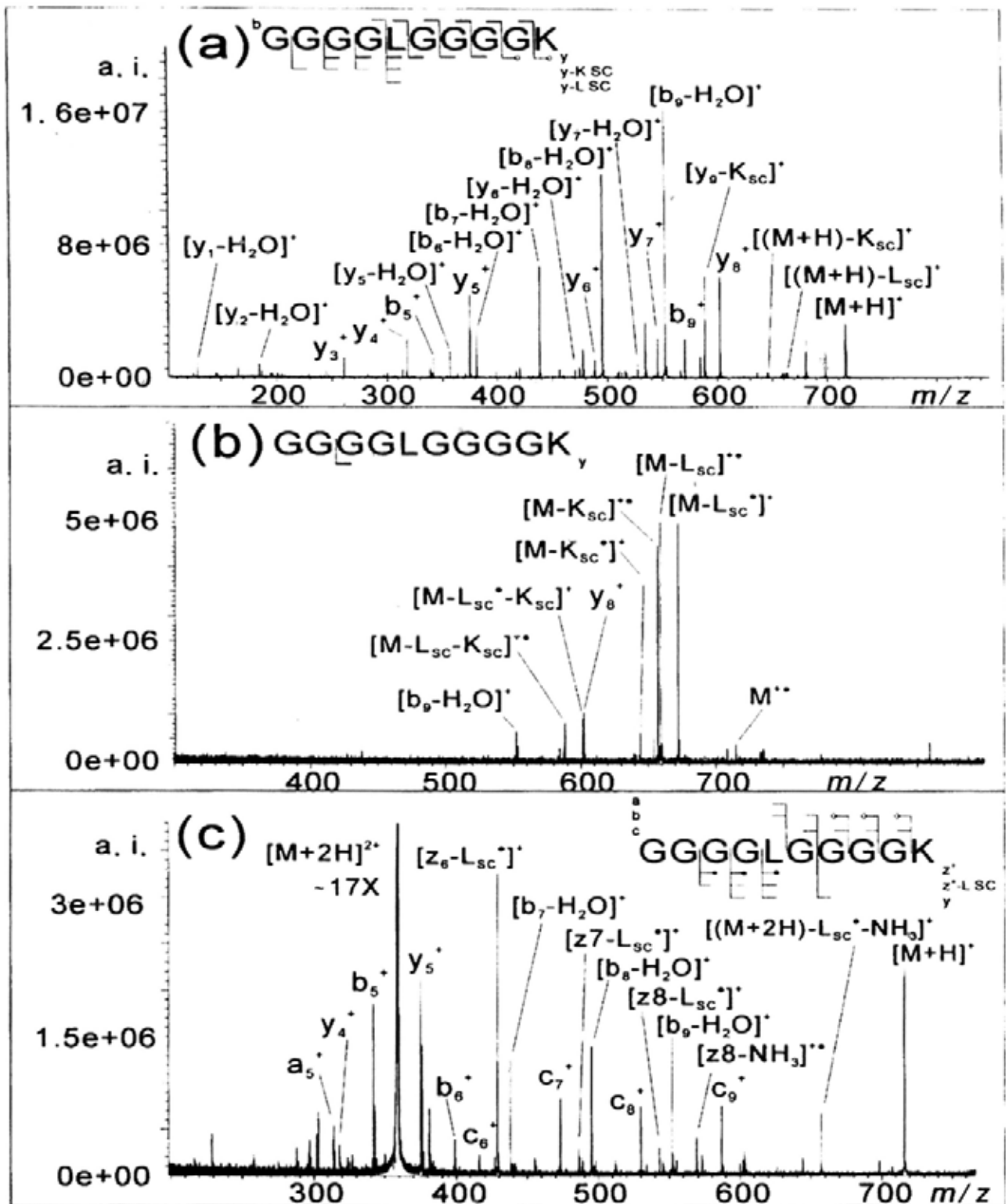


Figure 3. 4 Typical mass spectra of G₄LG₄K (M) in (a) SORI-CID of [M+H]⁺, (b) SORI-CID of M^{••} and (c) ECD of [M+2H]²⁺ (— indicates CO₂ loss, — indicates H₂O loss and — indicates NH₃ loss from the corresponding backbone fragments)

process, stepwise increments of internal energy in the precursor ions led to preferential cleavage of the weakest bond in molecular ions. Since the yield of side chain loss from $[M+H]^+$ was lower than that of backbone fragments, this implies that cleavage of covalent amide linkage in $[M+H]^+$ required less energy when compared to side chain loss. As regards the dissociation of M^{++} , since odd- and even-electron side chain loss from M^{++} were the major fragment ions, presumably the abstraction of hydrogen at side chain had a lower activation barrier when compared to that of α -carbon of glycine residues.

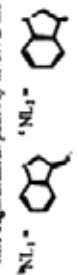
The dissociation of different radical species (M^{++} and $[M+2H]^{++}$) was examined by two techniques – SORI-CID and ECD. In SORI-CID of M^{++} , the most abundant fragments were odd- or even-electron side chain loss from M^{++} ; whilst in ECD of $[M+2H]^{2+}$, backbone fragments (c/z' ions) were the major fragments. A comparison of the side chain cleavages of peptides was made between SORI-CID of M^{++} and ECD of $[M+2H]^{2+}$. Table 3.3 summarizes the small fragments lost from the precursor ions and z_n^{++} in both CID and ECD with peptides G_4XG_4K . From the table, it can be seen that the speciation of side chain loss from M^{++} was different from that of $[M+2H]^{++}$ but more or less identical to those from z' ion in ECD.

In SORI-CID of M^{++} , the heteroatom radical abstracted a hydrogen at α - or γ -carbon of X or K (Scheme 3.1) resulting in side chain loss. This dissociation pathway was similar to that of the secondary dissociation of z' ion in ECD [117-120] since the radical in z' ion is located at α -carbon which is a carbon based radical [121]. Table 3.3 indicates that both odd- or even-electron X side chain(s) was lost from $[(M+2H)-NH_3]^{++}$ in ECD. The loss of NH_3 presumably implies that the protonated amine group had captured an electron, forming hypervalent nitrogen which induced the formation of carbon radical by losing 17.02Da (NH_3). This carbon radical in turn

Table 3.3 Small fragments loss from the precursor ion and z_n^{••} in CID and ECD with peptides GGGXGGGGK, where X is I, L, S, E and W.

| Cleavage type | Peptide | CID of M ^{••} | | | ECD of [M+2H] ^{••} | | | | |
|---------------------------------------------|-------------------------|------------------------|-------------------------------------------------|---------------------------------------------------------------------------------------------------------------------------------|-----------------------------|-----------|----------------------------------------------------------------------------------|----------------------------------------------------------------------------------|-----------|
| | | Mass loss | Molecular formula | Assignment | Exception | Mass loss | Molecular formula | Assignment | Exception |
| <i>From Precursor ions</i> | | | | | | | | | |
| <i>General</i> | | | | | | | | | |
| | Lysine (K) | 71.0735 | C ₆ H ₈ N | H ₂ C-CH ₂ CH ₂ CH ₂ NH ₂ | W | 46.0662 | *C ₂ H ₄ N | *CH ₂ CH ₂ [I] & NH ₂ | |
| | | 58.0657 | *C ₂ H ₄ N | *CH ₂ CH ₂ CH ₂ NH ₂ | | | | | |
| | | 89.0841 | C ₆ H ₁₀ NO | H ₂ C-CH ₂ CH ₂ CH ₂ NH ₂ [K] & H ₂ O | L,L,W | 73.0891 | C ₄ H ₆ N | CH ₂ CH=CHCH ₂ [L] & NH ₂ | |
| | | 76.0763 | *C ₂ H ₄ NO | *CH ₂ CH ₂ CH ₂ NH ₂ [K] & H ₂ O | L,L,E,W | 60.0813 | *C ₂ H ₄ N | *CH(CH ₂) ₂ [L] & NH ₂ | |
| | | 75.0922 | *C ₂ H ₄ N ₂ | *CH ₂ CH ₂ CH ₂ NH ₂ [K] & NH ₂ | L,L,S,W | | | | |
| <i>Sequence specific</i> | | | | | | | | | |
| | Isoleucine (I) | 56.0626 | C ₆ H ₈ | CH ₂ CH-CHCH ₂ | | | | | |
| | | 29.0397 | *C ₂ H ₄ | *CH ₂ CH ₂ | | | | | |
| | | 47.0603 | *C ₂ H ₄ O | *CH ₂ CH ₂ [I] & H ₂ O | | | | | |
| | Leucine (L) | 56.0626 | C ₆ H ₈ | CH ₂ CH-CHCH ₂ | | | | | |
| | | 43.0548 | *C ₂ H ₄ | *CH(CH ₂) ₂ | | | | | |
| | | 127.1361 | C ₆ H ₈ N | H ₂ C-CH ₂ CH ₂ CH ₂ NH ₂ [K] & CH ₂ CH-CHCH ₂ [L] | | | | | |
| | | 114.1283 | *C ₂ H ₄ N | H ₂ C-CH ₂ CH ₂ CH ₂ NH ₂ [K] & *CH(CH ₂) ₂ [L] | | | | | |
| | Serine (S) | 219.1093 | . | unidentified | | 221.1250 | . | unidentified | |
| | Glutamic Acid (E) | 72.0211 | C ₃ H ₄ O ₂ | CH ₂ -CHCOOH | | 89.0476 | C ₃ H ₄ ON | CH ₂ -CHCOOH [E] & NH ₂ | |
| | | 59.0133 | *C ₂ H ₄ O | *CH ₂ COOH | | 76.0398 | *C ₂ H ₄ O,N | *CH ₂ COOH [E] & NH ₂ | |
| | | 116.0109 | C ₃ H ₄ O ₂ | CH ₂ -CHCOOH [E] & CO ₂ | | | | | |
| | | 103.0031 | *C ₂ H ₄ O | *CH ₂ COOH [E] & CO ₂ | | | | | |
| | | 77.02386 | *C ₂ H ₄ O | *CH ₂ COOH [E] & H ₂ O | | | | | |
| | | 143.0946 | C ₃ H ₃ NO ₂ | CH ₂ -CHCOOH [E] & H ₂ C-CH ₂ CH ₂ NH ₂ [K] | | | | | |
| | | 130.0868 | *C ₄ H ₅ NO ₂ | CH ₂ -CHCOOH [E] & *CH ₂ CH ₂ CH ₂ NH ₂ [K] | | | | | |
| <i>Tryptophan (W)</i> | | | | | | | | | |
| | | 129.0579 | C ₆ H ₆ N | NL ₁ ^a | | 146.0844 | C ₆ H ₆ N | NL ₂ [W] & NH ₂ | |
| | | 116.0505 | *C ₆ H ₆ N | NL ₁ ^a | | | | | |
| | | 173.0477 | C ₆ H ₅ NO ₂ | NL ₂ [W] & CO ₂ | | | | | |
| | | 160.0403 | *C ₆ H ₅ NO ₂ | NL ₂ [W] & CO ₂ | | | | | |
| | | 200.1314 | C ₁₃ H ₁₆ N ₂ | NL ₁ [W] & H ₂ C-CH ₂ CH ₂ CH ₂ NH ₂ [K] | | | | | |
| | | 187.1236 | *C ₁₀ H ₁₀ N | NL ₁ [W] & *CH ₂ CH ₂ CH ₂ NH ₂ [K] | | | | | |
| <i>From z_n^{••} ions</i> | | | | | | | | | |
| <i>General</i> | | | | | | | | | |
| | Lysine (K) | 71.0735 | C ₆ H ₈ N | H ₂ C-CH ₂ CH ₂ CH ₂ NH ₂ | L | 17.0265 | NH ₂ | H ₂ C-CH ₂ CH ₂ CH ₂ NH ₂ | L |
| | | | | | | | | | L,L,E,W |
| <i>Sequence specific</i> | | | | | | | | | |
| | Isoleucine (I) | 29.0397 | *C ₂ H ₄ | *CH ₂ CH ₂ | | | | *CH ₂ CH ₂ | |
| | Leucine (L) | 43.0548 | *C ₂ H ₄ | *CH(CH ₂) ₂ | | | | *CH(CH ₂) ₂ | |
| | Serine (S) ^a | 58.0298- | *C ₃ H ₄ NO | CH ₂ CO(O)(H)NCH ₂ CO(O) _n NH | | 57.0215m | *C ₃ H ₄ NO(C ₂ H ₅ NO) _n | CH ₂ CO(O)(H)NCH ₂ CO(O) _n NH | |
| | | 57.0215m | (C ₂ H ₅ NO) _n | | | | | | |
| | Glutamic Acid (E) | 116.0505 | *C ₆ H ₆ N | NL ₁ | | 59.0133 | *C ₃ H ₄ O ₂ | *CH ₂ COOH | |
| | Tryptophan (W) | | | | | 129.0579 | C ₆ H ₆ N | NL ₁ | |
| | | | | | | 116.0505 | *C ₆ H ₆ N | NL ₂ | |

^a This fragmentation pathway involves the cleavage of N-C_α linkage at the N-terminal side of serine residues and will generate the same secondary fragment ion, from their z_n^{••} species, where n equal or larger than 7.



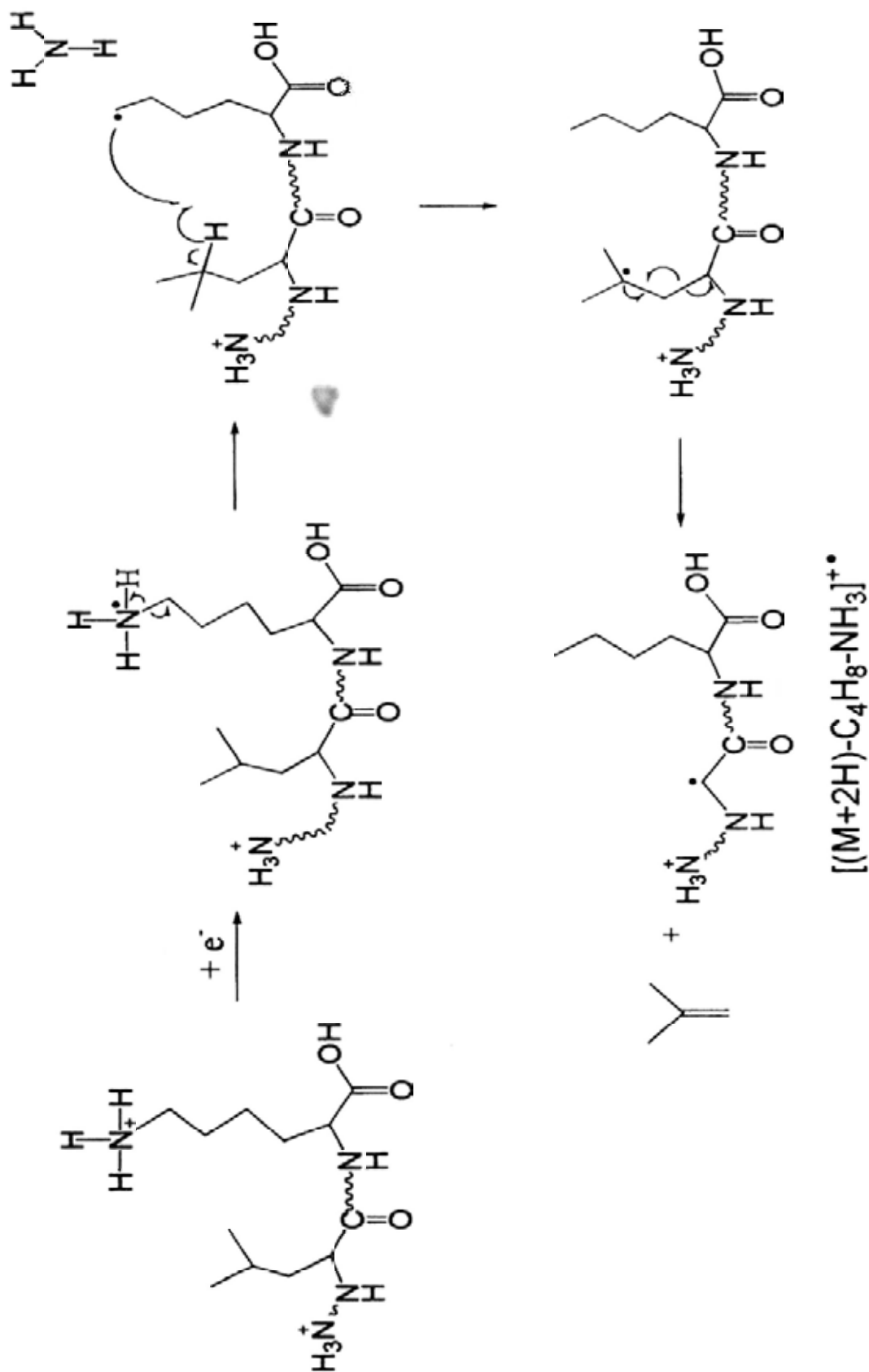
abstracted a hydrogen atom at X side chain and resulted in side chain loss. Consecutive losses of NH_3 and X side chain loss generated $[(\text{M}+2\text{H})-\text{X}_{\text{SC}}-\text{NH}_3]^{2+}$, which is more stable than $[(\text{M}+2\text{H})-\text{NH}_3]^{2+}$ as it is a captodative stabilized radical [115]. The possible dissociation pathways of the consecutive losses of NH_3 and X side chain are proposed via Scheme 3.4.

3.3.2 The $\text{ZG}_5\text{WG}_5\text{Z}'$ series

3.3.2.1 SORI-CID of $[\text{Cu}(\text{Tpy})(\text{M}+\text{H})]^{3+}$

In order to investigate the role of proton in the dissociation of M^{2+} and $[\text{M}+2\text{H}]^{2+}$, the dissociation patterns of $[\text{M}+\text{H}]^{2+}$ and $[\text{M}+2\text{H}]^{3+}$ were compared. Figure 3.5 sets out the typical SORI-CID mass spectra of $[\text{Cu}(\text{Tpy})(\text{M}+\text{H})]^{3+}$, where M is (a) $\text{RG}_5\text{WG}_5\text{R}$, (b) $\text{RG}_5\text{WG}_5\text{K}$, (c) $\text{KG}_5\text{WG}_5\text{R}$ and (d) $\text{KG}_5\text{WG}_5\text{K}$. It shows that the dissociation of $[\text{Cu}(\text{Tpy})(\text{M}+\text{H})]^{3+}$ generated mainly one-electron oxidized peptide radical cations ($[\text{M}+\text{H}]^{2+}$); copper-related species such as $[\text{Cu}(\text{Tpy})]^+$ and $[\text{Cu}(\text{Tpy})(\text{y}_n-\text{H})]^+$; and protonated ligand $[\text{Tpy}+\text{H}]^+$. In the SORI-CID of $[\text{Cu}(\text{Tpy})(\text{M}+\text{H})]^{3+}$ of $\text{RG}_5\text{WG}_5\text{R}$ and $\text{RG}_5\text{WG}_5\text{K}$, $[\text{M}+\text{H}]^{2+}$ and side chain loss from $[\text{M}+\text{H}]^{2+}$ were the most abundant fragment ions when N-terminus was arginine. However, when the N-terminus switched from arginine to lysine (i.e. SORI-CID of $[\text{Cu}(\text{Tpy})(\text{M}+\text{H})]^{3+}$ where M is $\text{KG}_5\text{WG}_5\text{R}$ or $\text{KG}_5\text{WG}_5\text{K}$), fragment peaks related to backbone cleavages (e.g. $[\text{Cu}(\text{Tpy})\text{y}_{12}]^{2+}$, $[\text{Cu}(\text{y}_{12}-\text{H})]^+$ and y_{12}^+) significantly increased.

Besides lysine, the scenario of using histidine as the charge carrier was also studied. Figure 3.6 shows the typical SORI-CID mass spectra of $[\text{Cu}(\text{Tpy})(\text{M}+\text{H})]^{3+}$, where M is (a) $\text{RG}_5\text{WG}_5\text{H}$, (b) $\text{HG}_5\text{WG}_5\text{R}$ and (c) $\text{HG}_5\text{WG}_5\text{H}$. Major fragments ($[\text{Cu}(\text{Tpy})\text{y}_{12}]^{2+}$, b^+ and y^+) generated through proton transfer, $[\text{M}+\text{H}]^{2+}$ and its



Scheme 3.4 A proposed dissociation pathway of the consecutive loss of NH_3 and L side chain

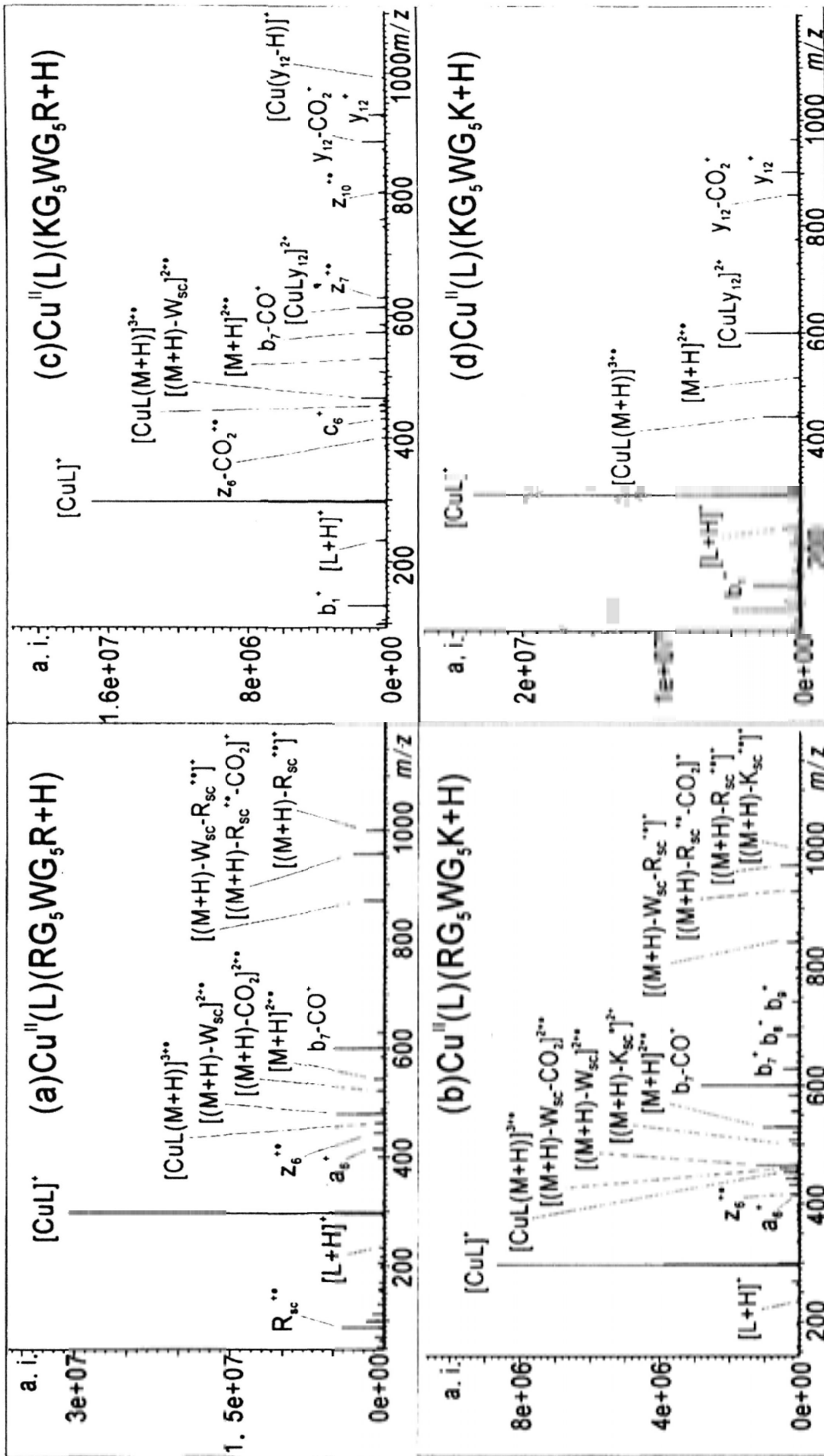


Figure 3.5 SORI-CID spectra of $[\text{Cu}(\text{L})(\text{M}+\text{H})]^{3+}$, where L is Tpy and M is (a) $\text{RG}_5\text{WG}_5\text{R}$, (b) $\text{RG}_5\text{WG}_5\text{K}$, (c) $\text{KG}_5\text{WG}_5\text{R}$ and (d) $\text{KG}_5\text{WG}_5\text{K}$.

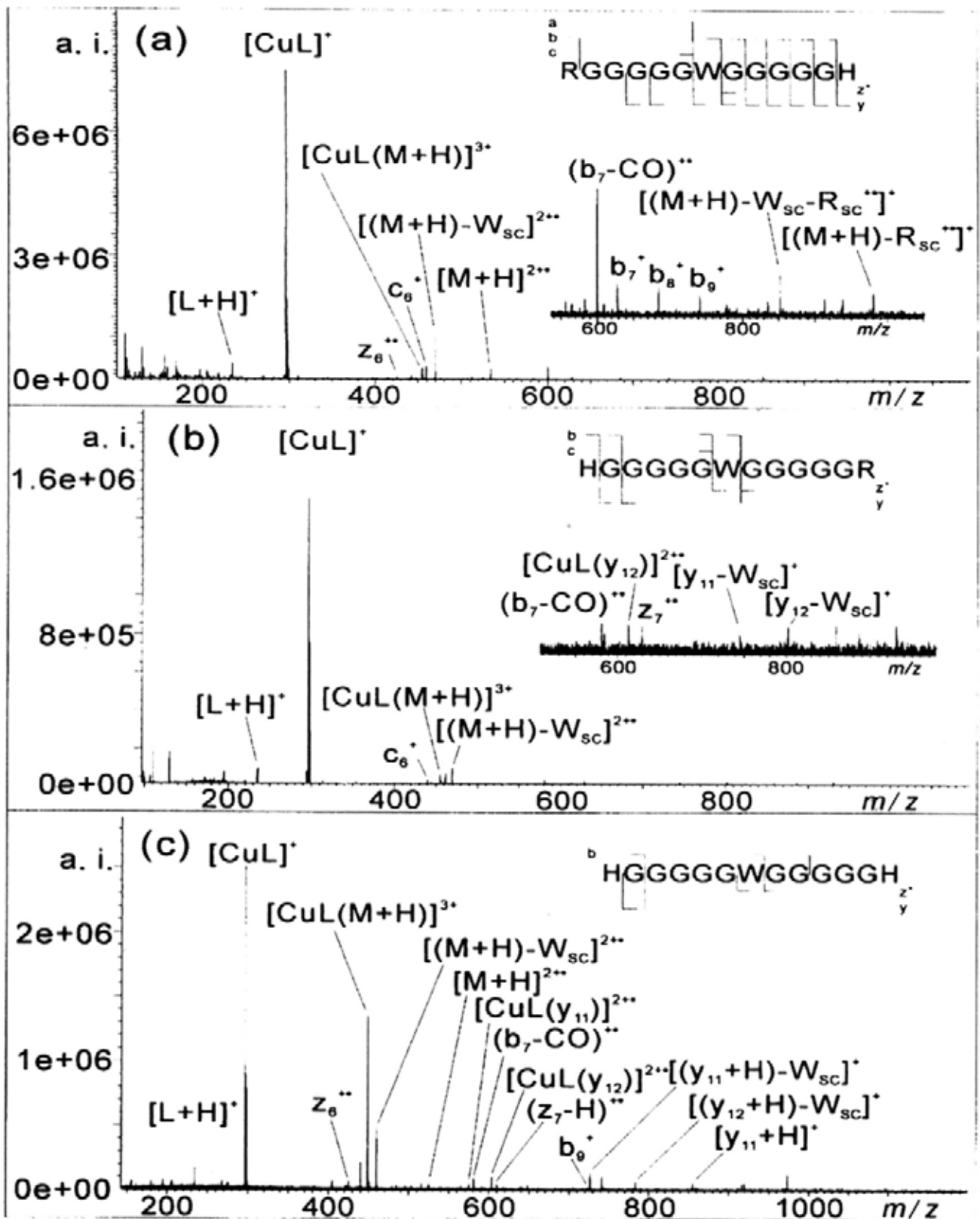


Figure 3. 6 SORI-CID mass spectra of $[\text{Cu}(\text{Tpy})(\text{M}+\text{H})]^{3+}$, where M is (a) $\text{RG}_5\text{WG}_5\text{H}$, (b) $\text{HG}_5\text{WG}_5\text{R}$ and (c) $\text{HG}_5\text{WG}_5\text{H}$.

related species could be seen. Further to this, as in the case with lysine-containing peptides, the dissociation of copper complexes with histidine-containing peptides was found to favour proton transfer reactions as the proton affinity of histidine is lower than that of arginine.

In all the cases mentioned in the above paragraphs, backbone cleavages were particularly abundant at both sides of tryptophan (W) (e.g. a_6^+ , b_7^+ , c_6^+ , z_6^{++} , etc), suggesting that the heteroatom radical (generated during the transfer of electron in SORI-CID of $[\text{Cu}(\text{Tpy})(\text{M}+\text{H})]^{3+}$) was probably located at tryptophan or hydrogen bond was formed between the heteroatom radical and tryptophan residue, which easily induced backbone cleavages at both N- and C-terminus to tryptophan.

Table 3.4 shows the dissociation patterns of SORI-CID of $[\text{Cu}(\text{Tpy})(\text{M}+\text{H})]^{3+}$. For all the peptides concerned, subsequent loss of tryptophan side chain from $[\text{M}+\text{H}]^{2++}$ (generated from the dissociation of the complex) was relatively abundant in all $[\text{M}+\text{H}]^{2++}$ related fragments. Besides side chain losses, fragment ions generated through proton transfer reactions were also observed. But in the case of $\text{RG}_5\text{WG}_5\text{R}$, dissociation channels through proton transfer were prohibited as the proton was sequestered tightly by arginine and thus no $[\text{Cu}(\text{Tpy})\text{y}_{12}]^{2+}$ and $[\text{L}+\text{H}]^+$ were seen. However, for lysine-containing peptides, high intensities of backbone fragments such as $[\text{Cu}(\text{Tpy})\text{y}_n]^{2+}$ and γ ions were observed in addition to side chain loss from $[\text{Cu}(\text{Tpy})(\text{M}+\text{H})]^{3+}$ and $[\text{M}+\text{H}]^{2++}$. Such change of dissociation channels is attributable to the lower proton affinity of lysine which favoured mobile proton initiated reactions.

The protonated arginine side chain ($\text{C}_3\text{H}_9\text{N}_3^{++}$) and $[(\text{M}+\text{H})-\text{R}_{\text{SC}}]^{++}$ seen in Figure 3.5 (a) implies that the protonation site was located on the arginine side chain. Similarly in Figure 3.5 (b), both protonated arginine ($\text{C}_3\text{H}_9\text{N}_3^{++}$) and

Table 3.4 Relative abundance of SORI-CID fragments of $[\text{Cu}(\text{Tpy})(\text{ZG}_5\text{WG}_5\text{Z}^+\text{H})]^{3+}$ (%)

| Z | Z' | M ³⁺ related species | | | | | | | | | | | | |
|---|----|-----------------------------------------------------------------------------------|----------------------------------------------------------------------------------------------------------|--------------------------------------------------------------------------------|-----------|-----------------------------|-----------|-----------|-----------|-----------|-----------|-----|------|-----|
| | | $\frac{[\text{M}+\text{H}]^{2+}}{[(\text{M}+\text{H})-\text{K}_{\text{SC}}]^{+}}$ | $\frac{[(\text{M}+\text{H})-\text{R}_{\text{SC}}]^{+}}{[(\text{M}+\text{H})-\text{W}_{\text{SC}}]^{2+}}$ | $\frac{[\text{Cu}(\text{Tpy})]^{+}}{[\text{Cu}(\text{Tpy})(\text{Y}_a)]^{2+}}$ | b_n^{-} | $[\text{Tpy}+\text{H}]^{+}$ | a_n^{+} | x_n^{+} | y_n^{+} | c_n^{+} | z_n^{+} | | | |
| R | R | 3.4 (-) ^a | N/A | 16.6 | 23.1 | 100.0 | - | 2.0 | - | 6.3 | 1.3 | - | - | 3.6 |
| R | K | 10.6 (3.3) | 1.1 | 7.3 | 15.7 | 100.0 | 2.2 | 15.9 | 1.6 | 10.5 | - | 6.1 | 6.1 | 3.9 |
| R | H | 6.0 (2.7) | N/A | 4.1 | 44.2 | 100.0 | 4.7 | 17.1 | 3.3 | 5.9 | 1.1 | 4.8 | 13.3 | 4.8 |
| K | R | 5.7 (2.7) | 0.3 | 1.8 | 9.1 | 100.0 | 9.6 | 17.8 | 4.1 | 2.4 | 1.9 | 6.3 | 2.1 | 6.6 |
| H | R | 0.6 (-) | N/A | 0.9 | 5.9 | 100.0 | 4.4 | 2.7 | 4.6 | - | 1.0 | 2.0 | 2.7 | 0.9 |
| K | K | 2.3 (0.8) | - | N/A | 1.2 | 100.0 | 17.1 | - | 6.0 | - | - | - | 5.7 | 0.7 |
| H | H | 2.1 (-) | N/A | N/A | 19.7 | 100.0 | 6.5 | 6.9 | 7.0 | - | - | - | 8.8 | 2.9 |

^aThe value in () indicates loss of CO₂ from the corresponding species.

lysine ($C_3H_9N^{++}$) side chain loss from $[M+H]^{2++}$ were found. Since the gas-phase basicity of arginine is much higher than that of lysine [122, 123], the probability for arginine to become protonated was higher than that of lysine. As a result, the intensity of $[(M+H)-R_{SC}^{++}]^+$ was higher than that of $[(M+H)-K_{SC}^{++}]^+$. Regarding the dissociation patterns of histidine-containing peptides, they were similar to those of lysine-containing peptides as proton transfer reactions were observed to be the dominant dissociation pathways.

3.3.2.2 Comparison between SORI-CID of $[M+H]^{2++}$ and ECD of $[M+3H]^{3+}$

Figure 3.7 shows the dissociation patterns of (a) SORI-CID of $[RG_5WG_5K+H]^{2++}$, (b) SORI-CID of $[KG_5WG_5R+H]^{2++}$, (c) ECD of $[RG_5WG_5K+3H]^{3+}$ and (d) ECD of $[KG_5WG_5R+3H]^{3+}$. In the SORI-CID of $[M+H]^{2++}$ as illustrated in Figure 3.7 (a) and (b), only a few fragment ions (arginine or tryptophan side chain loss from $[M+H]^{2++}$, y_{11}^+ and y_{12}^+) were yielded and the structural information provided was thus limited. At the same time, side chain loss reactions were observed to be dominant in the dissociation of $[RG_5WG_5K+H]^{2++}$ while y ions were the major fragments in the dissociation of $[KG_5WG_5R+H]^{2++}$. In the former case, it was highly probable that the proton was sequestered at the arginine side chain. Presumably, the heteroatom radical cation formed at the lysine side chain abstracted a hydrogen atom from α -carbon of tryptophan or arginine, thus causing the elimination of protonated arginine or tryptophan side chain. This observation is similar to the finding of Chu and co-workers [124] in which side chain loss from $[M+H]^{2++}$ was much more abundant than backbone fragments. Whilst in the latter case, the structure of the heteroatom radical cation formed at the lysine side chain (N-terminus) is believed to have favoured the abstraction of hydrogen atom at the glycine side chain (as a six-member ring was formed) and led

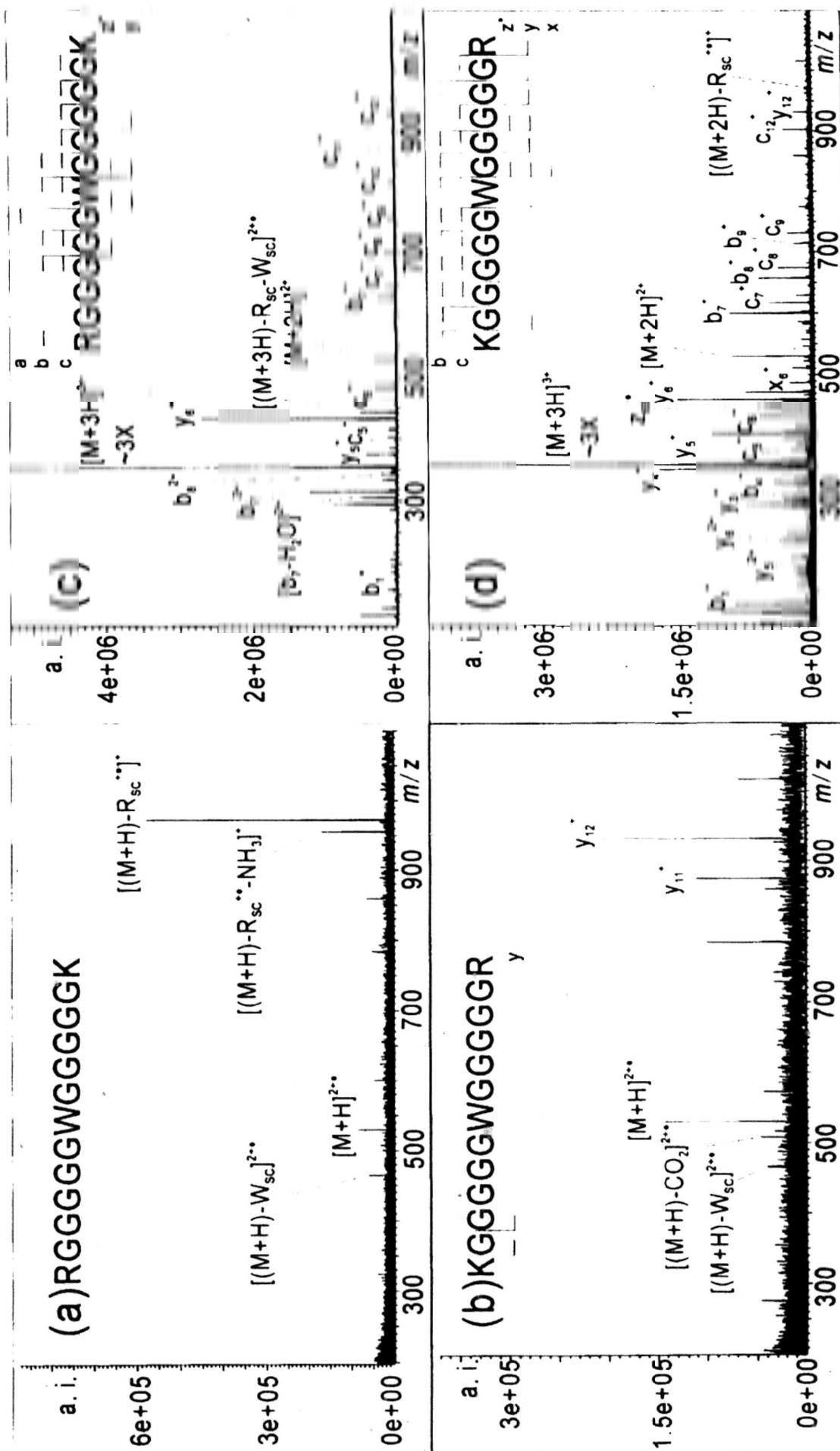


Figure 3.7 Dissociation patterns of (a) SORI-CID of $[RG_5WG_5K+H]^{2+\bullet}$, (b) SORI-CID of $[KG_5WG_5R+H]^{2+\bullet}$, (c) ECD of $[RG_5WG_5K+3H]^{3+\bullet}$ and (d) ECD of $[KG_5WG_5R+3H]^{3+\bullet}$.

to the generation of abundant y_{12} ions. Since side chain loss reactions were the major dissociation pathways in SORI-CID of $[M+H]^{2+}$ as previously discussed, the fragmentation pattern of $[M+H]^{2+}$ is similar to that of M^{+} . In a nutshell, it is speculated that the dissociation in these two cases was initiated by the heteroatom radical.

In contrast to the observations contained in Figure 3.7 (a) and (b), abundant backbone cleavages were seen in the ECD spectra in Figure 3.7 (c) and (d). The dissociation of $[M+3H]^{2+}$ is believed to be initiated by the migration of H^{\cdot} to backbone carbonyl, which typically resulted in the generation of c/z^{\cdot} ions as the major fragments and sometimes b/y ions as the minor fragment ions. Generation of b/y ions was as expected since three protons had been added to the peptide chain but only two of them were sequestered by the basic amino acids. The proton which was not held by basic amino acid could mobilize easily and led to the formation of b/y ions.

The above experiments indicate clearly that the distinctive difference in the fragmentation patterns of the two radical precursors was due to the different properties of the radicals involved. SORI-CID of the hydrogen-deficient radical cation, $[M+H]^{2+}$, was driven by the heteroatom radical through abstraction of a hydrogen atom, which eventually led to predominantly side chain loss from the precursor ion. The dissociation of the hydrogen-surplus radical cation (i.e. $[M+3H]^{2+}$) via ECD, on the other hand, generated mainly backbone cleavages. As proposed in the Cornell mechanism, the dissociation was initiated by the migration of H^{\cdot} to the backbone carbonyl, leading to $N-C_{\alpha}$ cleavages. Whilst in the Utah-Washington mechanism [72], the charge-reduced precursor ion, $[M+3H]^{2+}$, could be a heteroatom radical anion (because the amide π^* orbital would capture an electron,

leading to the formation of amide carbonyl oxygen radical anion). This heteroatom radical anion abstracted a proton from an amino acid residue and generated a labile aminoketyl radical which was dissociated readily by N-C_α bond cleavage.

3.3.2.3 Comparison of [Cu(Tpy)(M+H)]³⁺ between MS² and MS³

A comparison of [Cu(Tpy)(M+H)]³⁺ (where M is RG₅WG₅K) between MS² and MS³ (Figure 3.5 (b) and Figure 3.7 (a)) revealed that while MS² yielded more backbone fragments than MS³, the speciation of side chain loss from the precursor ions concerned was similar. For other peptides, there was the same observation that more backbone cleavages were found in MS² than in MS³.

3.4 Conclusion

Three series of model peptides were used to generate hydrogen-deficient peptide radical cations (M^{•+} or [M+H]^{2•+}) from their respective copper ternary complexes. SORI-CID of M^{•+} and [M+H]^{2•+} was performed and it is found that upon dissociation, the hetero-atom radical cation would abstract α- or γ-hydrogen at amino acid residue of interest, leading to abundant side chain loss. It is also noted that in SORI-CID of M^{•+}, [M-CO₂]^{•+} with different intensities would be obtained from MS² and MS³, presumably due to the binding mode of the copper ternary complex. The loss of CO₂ from SORI-CID of [Cu(Tpy)M]^{2•+} is therefore believed to be a copper-mediated reaction.

The comparative study related to the dissociation patterns of M^{•+}/[M+H]^{2•+} in SORI-CID and [M+2H]^{•+}/[M+3H]^{2•+} in ECD reveals that the respective dissociation pathways differ substantially. The dissociation of hydrogen-deficient radical cations in SORI-CID is believed to be driven by the abstraction of α- or

γ -hydrogen of amino acid of interest. On the other hand, the dissociation of hydrogen-surplus radical cations in ECD is initiated by the migration of H^\bullet to the backbone carbonyl, invoking N-C $_{\alpha}$ cleavages in the end. On this basis, it is envisaged that SORI-CID of peptide radical cation does not provide as much sequence information as ECD of protonated peptide.

Chapter 4

Probing Structural Effect of Radical Cations on their Generation and Fragmentation

4.1 Introduction

When using conventional dissociation techniques such as CID, the labile PTM groups in proteins are found to cleave preferentially as compared to backbone cleavages, yielding fragment ions that are only useful in characterizing the type of PTM(s) but not the site(s) of modifications. Alternatively, ECD is found to be able to preserve the labile side chain modified groups while inducing extensive backbone cleavages. A combination of ECD and CID has demonstrated to be an extremely powerful MS methodology for characterization and localization of PTM(s) in proteins. However, current information on the factors affecting the dissociation preference, in particular backbone cleavages versus loss of labile PTM functional groups, is rather limited. In order to gather more information about the preservation of labile PTM groups in radical cations ($[M+2H]^{+\bullet}$) in ECD, the dissociation of PTM(s) containing peptide radical cations ($M^{+\bullet}$) was studied. A direct comparison between the dissociation pathways of $[M+H]^+$, $M^{+\bullet}$ and $[M+2H]^{+\bullet}$ was then conducted using PTM(s) containing peptides i.e. methionine oxidation (M(O)) or serine phosphorylation (pS).

O'Hair and co-workers have shown that besides peptide radical cations, radical cations of constituents of nucleic acid (including nucleobases, nucleosides and nucleotides) could be formed in CID of ternary metal complexes [125]. Aiming to explore the possibility of forming biomolecule radical cations through the dissociation of metal ternary complexes, this systematic study on CID of

$[\text{Cu}(\text{Tpy})\text{M}]^{2+}$ was further expanded to include oligosaccharides.

Regarding structural analyses for oligosaccharides, several research groups have investigated the dissociation patterns of metalated oligosaccharides under IRMPD, CID or/and ECD conditions [126, 127]. Their results have indicated that ECD of metalated oligosaccharides would provide structural information complementary to that obtained from CID and IRMPD. An attempt was therefore made in this study to generate oligosaccharide radical cations ($\text{M}^{+\bullet}$) in SORI-CID of copper-terpyridine-oligosaccharide ($[\text{Cu}(\text{Tpy})\text{M}]^{2+}$). Both SORI-CID and ECD were performed on copper-adducted oligosaccharides ($[\text{Cu}+\text{M}]^{2+}$) to study their fragmentation patterns. In addition, linear and branched oligosaccharides were also examined to ascertain the branching effect of $[\text{Cu}(\text{Tpy})\text{M}]^{2+}$ on CID.

Since the dissociation patterns of copper ternary complexes are different from those of the corresponding copper-adducted species, it is believed that the presence of ligand moiety in the complex would alter its dissociation preference and pattern. Conformational change induced by the non-covalent interaction between protein/peptide and ligand would cause abnormalities which may result in diseases [128]. The fragmentation patterns of ligand-peptide complexes have been examined by numerous researchers. Their ECD experimental results revealed that ligand (e.g. spermine) retention was found in the fragment ions (i.e. α -synuclein, Parkinson's disease related protein) after the dissociation process and thus the binding site of ligand could be located [129]. As for the case of CID, ligand was found to be eliminated and no direct cleavage of peptide was observed [130]. This implies that the interaction between ligand and protein was weaker than amide bonds in protein backbone, thus generating less structural information. A systematic study on ECD of crown ether-peptide complexes $[\text{L}+(\text{M}+2\text{H})]^{2+}$ (where L and M are 12-crown-4 and

peptide respectively) was therefore carried out in this study to evaluate the retention of weak non-covalent interaction between 12-crown-4 and peptide after ECD. Apart from this, an investigation was conducted to examine how the addition of 12-crown-4 to peptides would affect the latter's dissociation patterns and fragmentation efficiencies under typical ECD conditions.

4.2 Experimental section

Custom-synthesized model peptides GGGGXGGGGR (where X= M, M(O), S and pS), truncated peptide from Histone H3 fragment 217-223 (INSMLPR) with its PTM analogue, in both oxidized methionine form (INSM(O)LPR) and phosphorylated serine form (INpSMLPR), were purchased from Pepton Inc., (Daejeon, South Korea) and used without further purification. Copper ternary complexes were prepared *in situ* by first mixing 49 μL of 1.6 mM $\text{CuSO}_4 \cdot 5\text{H}_2\text{O}$ (Riedel-de Haen, Seelze, Germany) with 49 μL of 0.3 mM peptide in 50/50 water/methanol solution. The sample was vortexed for one minute and 2 μL of saturated 2,2':6',2''-terpyridine (Tpy) (Sigma, St Louis MO, USA) was added to the 98 μL sample. For SORI-CID and ECD experiments related to protonated peptides, analyte solutions were prepared at peptide concentrations of 250 μM in 50/50 water/methanol solution with 3% acetic acid (Riedel-de Haen, Seelze, Germany).

Maltoheptaose and 3 α ,6 α -Mannopentaose were purchased from Sigma (St Louis MO, USA). Copper ternary complexes were then prepared *in situ* in the same way as described above. For SORI-CID and ECD experiments concerning metal-adducted oligosaccharides, analyte solutions were prepared at oligosaccharide concentrations of 250 μM in 50/50 water/methanol solution with 3 mM of $\text{CuSO}_4 \cdot 5\text{H}_2\text{O}$ (Riedel-de Haen, Seelze, Germany).

Several truncated peptides of INSMLPR were examined and their analogues were NSMLPR, SMLPR, NLPR, LPR and PR. All peptides were synthesized in-house using a HiPep Laboratories (Kyoto, Japan) Peti-Syzer[®] Model PSS-510 Personal Synthesizer and used without further purification. Standard Fmoc synthesis procedures were employed [131, 132]. All reagents used for peptide synthesis were obtained from Sigma and Aldrich (St Louis MO, USA), LC Science (Houston, TX, USA) and Advanced ChemTech (CreoSalus Inc., Louisville, KY, USA). HPLC grade methanol was purchased from LabScan, Ireland; while acetic acid (98.7%) and 12-crown-4 (98%) from Riedel-de Haen (Seezle, Germany) and Sigma and Aldrich (St Louis MO, USA) respectively. Ligand-peptide complexes $[L+(M+2H)]^{2+}$ (where L = 12-crown-4 and M = peptide) were prepared *in situ* by mixing the 12-crown-4 (3mM) with peptide solution (3mM) in 5:1 volume ratio in 1:1 water/methanol solution (v:v). For ECD experiments concerning protonated peptides ($[M+2H]^{2+}$), analyte solutions were prepared at peptide concentrations of 250 μ M in 1:1 water/methanol solution with 3-5% acetic acid.

All experiments were conducted via a 4.7 Tesla FTICR-MS (APEX I, Bruker Instrument Inc., Boston, MA), a computer system and associated electronics upgraded to APEX III. For detailed instrumental arrangements and sample preparation procedures, please refer to Chapter 2. As for SORI-CID and ECD experiment conditions, reference should be made to Chapter 3.

4.3 Results and Discussion

4.3.1 Comparison of fragmentation patterns between peptide radical cations (M^+ and $[M+2H]^+$) and protonated peptides ($[M+H]^+$) with post-translational modification(s) containing peptides

4.3.1.1 SORI-CID of $[Cu(Tpy)M]^{2+}$

The dissociation pattern of $[\text{Cu}(\text{Tpy})\text{M}]^{2+}$ was examined by a series of simplified model peptide GGGGXGGGGR ($\text{G}_4\text{XG}_4\text{R}$), where X denotes M, M(O), S and pS. While the introduction of C-terminal arginine was to resemble the trypsin-digested real peptide fragments consisting of a C-terminal arginine, the glycine residues served to minimize side-chain interactions and confine the globular structure of the peptides.

Figure 4.1 shows the SORI-CID mass spectra of $[\text{Cu}(\text{Tpy})\text{G}_4\text{XG}_4\text{R}]^{2+}$, where X is (a) M, (b) M(O), (c) S and (d) pS. Assignments of all labeled side chain in the spectra are shown in Appendix III. The major product ions shown in Figures 4.1 (a) to (c) were $[\text{Cu}(\text{Tpy})]^+$ and M^{++} related fragments, whereas the major fragments in Figure 4.1 (d) were $[\text{Tpy}+\text{H}]^+$ and $[\text{Cu}^{\text{II}}(\text{M}-\text{H})]^+$ related fragments. For the real peptides, truncated peptide from Histone H3 fragment 217-223 (INSMLPR) was selected randomly in real protein. Its PTM analogue, methionine oxidized form (INSM(O)LPR) and phosphorylated serine form (INpSMLPR), were also examined.

Figure 4.2 shows the SORI-CID mass spectra of $[\text{Cu}(\text{Tpy})\text{M}]^{2+}$, where M is (a) INSMLPR, (b) INSM(O)LPR and (c) INpSMLPR. These spectra revealed that the dissociation patterns of real peptides were quite different from those of model peptides as shown in Figure 4.1. In Figures 4.2 (a) and (b), a high intensity of $[\text{Tpy}+\text{H}]^+$ and $[\text{Cu}^{\text{II}}(\text{M}-\text{H})]^+$ related fragments was observed, indicating that proton transfer reaction (from peptide to ligand) was the major dissociation channel. The base peak, as shown in Figure 4.2 (c), was y_4^+ instead of $[\text{Cu}^{\text{II}}(\text{M}-\text{H})]^+$. This implies that the dissociation of $[\text{Cu}(\text{Tpy})\text{M}]^{2+}$ (M being phosphorylated serine containing peptide) was triggered easily by the presence of mobile protons in the peptides.

Table 4.1 is a summary of the fragment ions obtained from SORI-CID of $[\text{Cu}(\text{Tpy})\text{M}]^{2+}$. It shows the major dissociation channel of model peptides ($\text{G}_4\text{XG}_4\text{R}$)

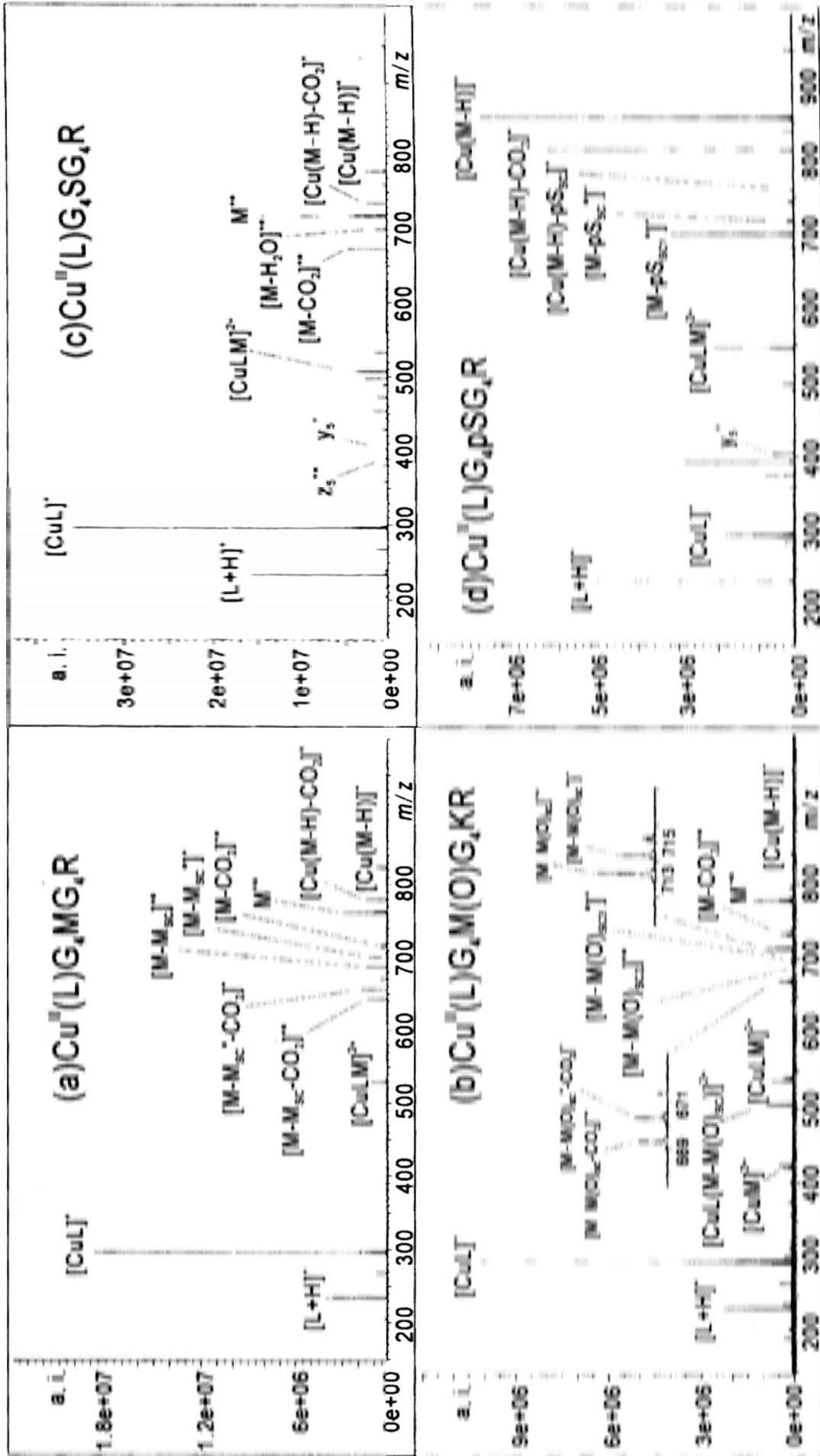


Figure 4. 1 SORI-CID spectra of $[Cu(L)G_xXG_yR]^{2+}$, where L is Tpy and X is (a) M, (b) M(O), (c) S and (d) pS.

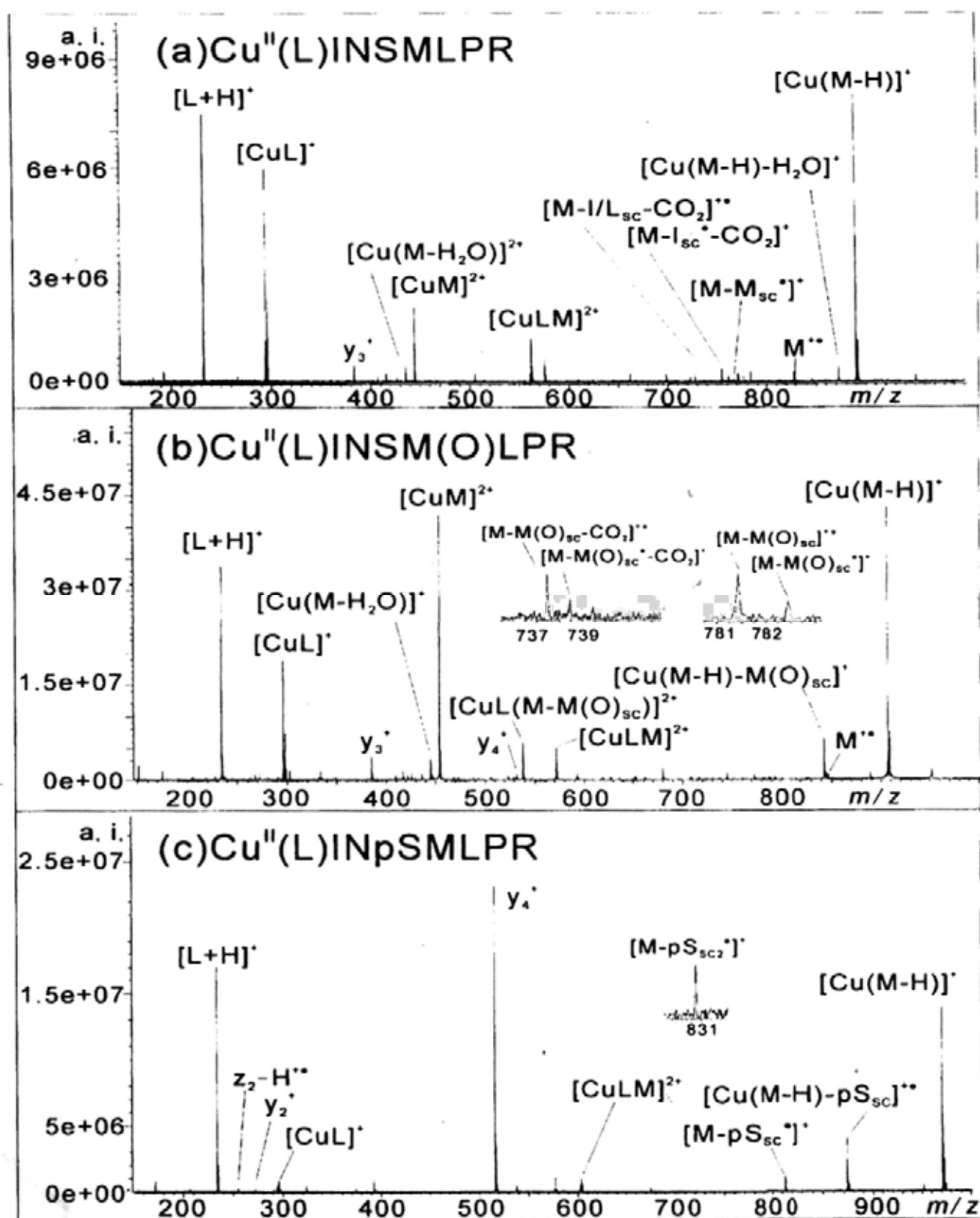


Figure 4. 2 SORI-CID spectra of $[Cu(L)M]^{2+}$, where L is Tpy and M is (a) INSMLPR, (b) INSM(O)LPR and (c) INpSMLPR.

Table 4.1 Relative abundance of SORI-CID fragments of $[\text{Cu}(\text{TPy})\text{G}_n\text{XG}_n\text{R}]^{2+}$ and $[\text{Cu}(\text{TPy})\text{INSMLPR}]^{2+}$ (with PTM(S)). (%)

| Peptide | M ⁺ | M ⁺ -X _{sc} ^b | [Cu(TPy)] ⁺ | [Cu ^{II} (M-H)] ⁺ | [Cu ^{II} (M-H)-X _{sc}] ⁺⁺ | [TPy+H] ⁺ | [Cu ^{II} M] ²⁺⁺ | y _s ⁺ | z _s ⁺⁺ | Other fragments |
|-------------------------------------|----------------|----------------------------------------------|------------------------|---------------------------------------|---------------------------------------------------------|----------------------|-------------------------------------|-----------------------------|------------------------------|---------------------------------------------------------------------------------------------------------------------------|
| G ₄ MG ₄ R | 14.9 (6.0) | 32.8 | 100.0 | 4.6 (9.3) | -- | 18.5 | -- | -- | -- | b _s ⁺ [0.7] ^c |
| G ₄ M(O)G ₄ R | 23.3 (6.0) | 35.1 | 100.0 | 13.8 (4.4) | -- | 22.1 | 8.0 | 1.9 | -- | [Cu ^{II} (TPy)(M-M(O)sc)] ²⁺⁺ [28.3] |
| G ₄ SG ₄ R | 38.4 (18.6) | -- | 100.0 | 7.1 (8.6) | -- | 40.2 | 1.4 | 2.0 | 0.7 | -- |
| G ₄ pSG ₄ R | -- | 49.6 | 23.4 | 100.0 (10.4) | 2.6 | 43.5 | -- | 7.2 | -- | -- |
| INSMLPR | 3.9 (4.0) | 3.9 | 74.8 | 100.0 (8.6) | -- | 93.9 | 27.2 (6.3) | 8.7 | 1.7 | [Cu ^{II} (y _s -H)] ⁺⁺ [3.3] |
| INSM(O)LPR | 1.7 (0.5) | 2.2 | 43.8 | 100.0 (3.5) | 18.1 | 66.5 | 98.5 (19.9) | 11.8 | 1.0 | [Cu ^{II} (TPy)(M-M(O)sc)] ²⁺⁺ [14.8] [Cu ^{II} (y _s -H)] ⁺⁺ [6.4] |
| INpSMLPR | -- | 6.7 | 3.7 | 60.2 | 17.3 | 73.5 | -- | 100.0 | 1.7 | [Cu ^{II} (y _s -H)] ⁺⁺ [1.4] |

^a The value in () included CO₂, H₂O and side chain loss from the corresponding species.

^b X_{sc} included side chain of M, M(O), S or pS if any of them exist in peptide.

^c The value in [] shows the relative percentage of the fragment ions.

was electron transfer from the peptide to the copper center, whereas proton transfer from the peptide to ligand was the major dissociation channel of real peptides. Apart from this, an abundance of $[\text{Cu}^{\text{II}}(\text{M-H})]^+$ and $[\text{Cu}^{\text{II}}(\gamma\text{-H})]^+$ was detected in the real peptides, implying that the protons concerned could easily be mobilized. In some cases of SORI-CID of $[\text{Cu}(\text{Tpy})\text{M}]^{2+}$ involving real peptide and its PTM analogues, ligands were seen detached from the complexes easily during the dissociation process, producing a high intensity of $[\text{CuM}]^{2+}$. This indicates the interaction between copper and ligand was weaker than that of copper and peptide, presumably due to the steric effect of side chains containing different functionalities.

For oxidized methionine containing peptides, loss of even-electron $\text{M}(\text{O})$ side chain (CH_3SOH) from M^{++} , $[\text{Cu}^{\text{II}}(\text{M-H})]^+$ and $[\text{Cu}(\text{Tpy})\text{M}]^{2+}$ was detected (see Figures 4.1 (b) and 4.2 (b)). However, significant amount of oxidized methionine side chain loss from $[\text{Cu}(\text{Tpy})\text{M}]^{2+}$ or/and $[\text{Cu}^{\text{II}}(\text{M-H})]^+$ but no methionine side chain loss from $[\text{Cu}(\text{Tpy})\text{M}]^{2+}$ and $[\text{Cu}^{\text{II}}(\text{M-H})]^+$ were observed in Figure 4.1 (a–b) and Figure 4.2 (a–b), implying that oxidized methionine side chain was more labile than methionine side chain upon SORI-CID.

As regards phosphorylated serine containing peptides, the major dissociation channel of $[\text{Cu}(\text{Tpy})\text{M}]^{2+}$ was observed to be proton-initiated reaction, with $[\text{Cu}^{\text{II}}(\text{M-H})]^+$ or/and γ ion being the major fragment ions. Unlike oxidized methionine containing peptides, there was no phosphorylated serine side chain loss from $[\text{Cu}(\text{Tpy})\text{M}]^{2+}$ and M^{++} . It is suspected that the phosphoric acid might have easily released a mobile proton which either transferred to the ligand or induced backbone cleavages and generated $[\text{Cu}^{\text{II}}(\text{M-H})]^+$ or γ ions respectively. Apart from this, even-electron phosphorylated serine side chain (H_3PO_4) was found to be lost from $[\text{Cu}^{\text{II}}(\text{M-H})]^+$ while only odd-electron phosphorylated serine side chain (H_2PO_4^-)

and PO_3^-) was lost from M^{++} . No loss of H_3PO_4 from M^{++} was observed, which is believed to be related to the absence of mobile proton. As shown in Figures 4.1 (d) and 4.2 (c), although no M^{++} was found in the spectra, there was a significant amount of $(\text{M}-\text{H}_2\text{PO}_4)^+$ and $(\text{M}-\text{HPO}_3)^+$. This implies that the phosphoric acid group was so labile that phosphoric acid side chain was lost preferentially from $[\text{Cu}(\text{Tpy})\text{M}]^{2+}$ or $[\text{Cu}^{\text{II}}(\text{M}-\text{H})]^+$ under SORI-CID conditions.

4.3.1.2 Dissociation patterns of methionine and oxidized methionine containing model peptides

Figure 4.3 shows the mass spectra of $\text{G}_4\text{MG}_4\text{R}$ (M) in (a) SORI-CID of $[\text{M}+\text{H}]^+$, (b) SORI-CID of M^{++} and (c) ECD of $[\text{M}+2\text{H}]^{2+}$. It was found that SORI-CID of $[\text{M}+\text{H}]^+$ produced a myriad of backbone fragments (b_n and y_n ions) that provided profuse sequence information. In SORI-CID of M^{++} , odd- or even-electron methionine side chain loss from M^{++} were the dominant fragment species but no backbone fragments were obtained. But in ECD of $[\text{M}+2\text{H}]^{2+}$, the usual ECD backbone fragments, i.e. c and z' ions, as well as b , y and secondary fragmentation of z' ions (forming w ions) were detected.

Figure 4.4 shows the mass spectra of $\text{G}_4\text{M}(\text{O})\text{G}_4\text{R}$ (M) in (a) SORI-CID of $[\text{M}+\text{H}]^+$, (b) SORI-CID of M^{++} and (c) ECD of $[\text{M}+2\text{H}]^{2+}$. In SORI-CID of $[\text{M}+\text{H}]^+$, typical oxidized methionine side chain (CH_3SOH) was preferentially cleaved from the peptide, giving a very high intensity of $[(\text{M}+\text{H})-\text{CH}_3\text{SOH}]^+$ and a small amount of backbone fragments. In SORI-CID of M^{++} , the major fragment ions observed were odd- or even-electron oxidized methionine side chain (CH_3SO^+ , CH_3SOH , $\text{C}_2\text{H}_5\text{SO}^+$ and $\text{C}_3\text{H}_6\text{SO}$) lost from M^{++} . ECD of $[\text{M}+2\text{H}]^{2+}$, on the other hand, generated mainly y , c and z' ions with oxidized methionine side chain remaining intact in the precursor ions [133, 134]. In addition, loss of odd- or even-electron oxidized

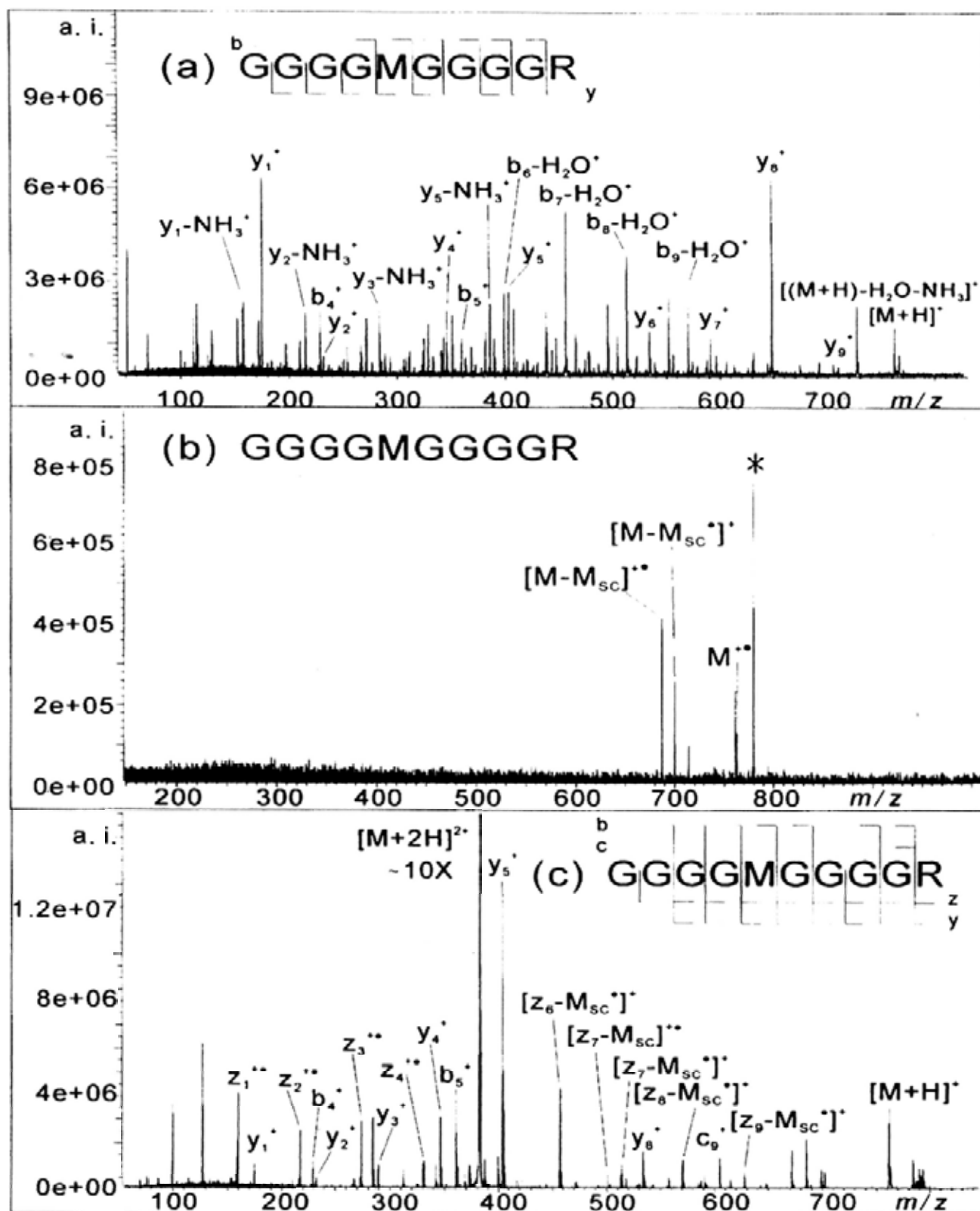


Figure 4.3 Mass spectra of G₄MG₄R (M) in (a) SORI-CID of [M+H]⁺; (b) SORI-CID of M^{••}; and (c) ECD of [M+2H]²⁺.

* indicates peak that could not be clean in isolation.

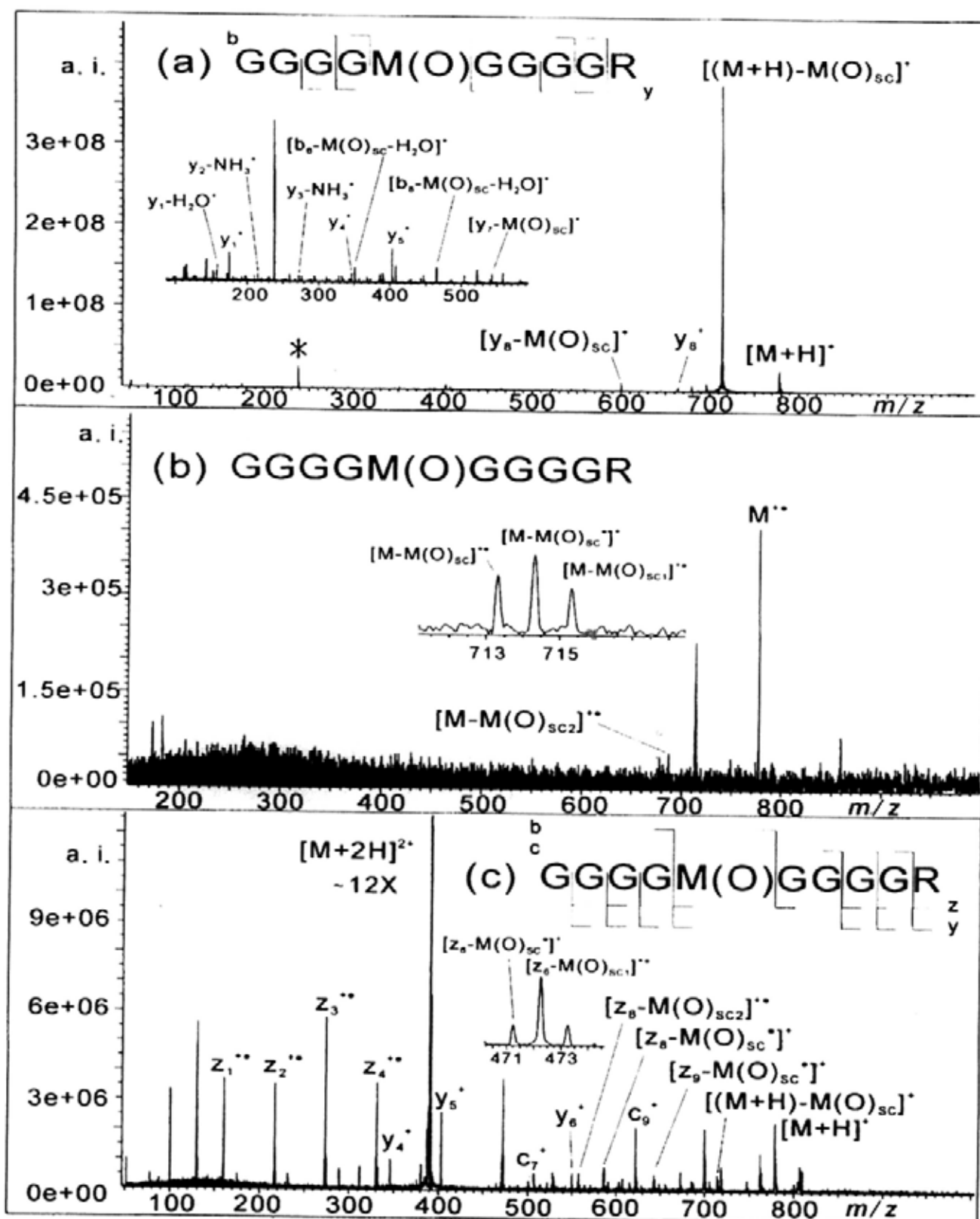


Figure 4.4 Mass spectra of $G_4M(O)G_4R$ (M) in (a) SORI-CID of $[M+H]^+$; (b) SORI-CID of $M^{\bullet\bullet}$; and (c) ECD of $[M+2H]^{2+}$.

methionine side chain from z' ions and $[(M+2H)-NH_3]^{2+}$ was observed. It can be concluded from the findings in Figure 4.4 (a–c) that there was characteristic oxidized methionine side chain (CH_3SOH) elimination from the precursor ions or/and fragment ions.

4.3.1.3 Dissociation patterns of serine and phosphorylated serine containing model peptides

In SORI-CID of $[Cu(Tpy)M]^{2+}$, the intensity of M^{2+} generated from phosphorylated serine containing peptides was relatively low given that proton transfer from peptide to ligand was the preferred dissociation channel. Although SORI-CID of M^{2+} could not be performed using G_4SG_4R and G_4pSG_4R , the fragment ions related to M^{2+} obtained in MS^2 (see Figure 4.1 (c) and (d)) were examined. In the case of G_4SG_4R , there was loss of H_2O and CO_2 loss from M^{2+} but no serine side chain loss. For G_4pSG_4R , loss of odd-electron side chain ($H_2PO_4^{\cdot}$ or HPO_3^{\cdot}) from M^{2+} was detected. This observation differed from that of oxidized methionine containing peptides. In SORI-CID of $[G_4M(O)G_4R]^{2+}$, odd- or even-electron side chain(s) (CH_3SO^{\cdot} , $C_2H_5SO^{\cdot}$, CH_3SOH and C_3H_6SO) were lost from M^{2+} (Figure 4.1 (b)) but there was no characteristic side chain (H_3PO_4) loss in (Figure 4.1 (c)).

Figure 4.5 illustrates the dissociation patterns of (a) SORI-CID of $[G_4SG_4R+H]^+$, (b) ECD of $[G_4SG_4R+2H]^{2+}$, (c) SORI-CID of $[G_4pSG_4R+H]^+$ and (d) ECD of $[G_4pSG_4R+2H]^{2+}$. The high complexity noted in SORI-CID of $[G_4SG_4R+H]^+$ was due to the loss of small molecules (e.g. H_2O and CO_2) from b and y ions during the dissociation process. Such loss was the result of the presence of hydroxyl group in serine side chain which easily led to water loss. In SORI-CID of $[G_4pSG_4R+H]^+$, labile even-electron phosphoric acid (H_3PO_4) was seen to cleave preferentially [135]. As for ECD of $[G_4SG_4R+2H]^{2+}$ and $[G_4pSG_4R+2H]^{2+}$, they yielded the usual

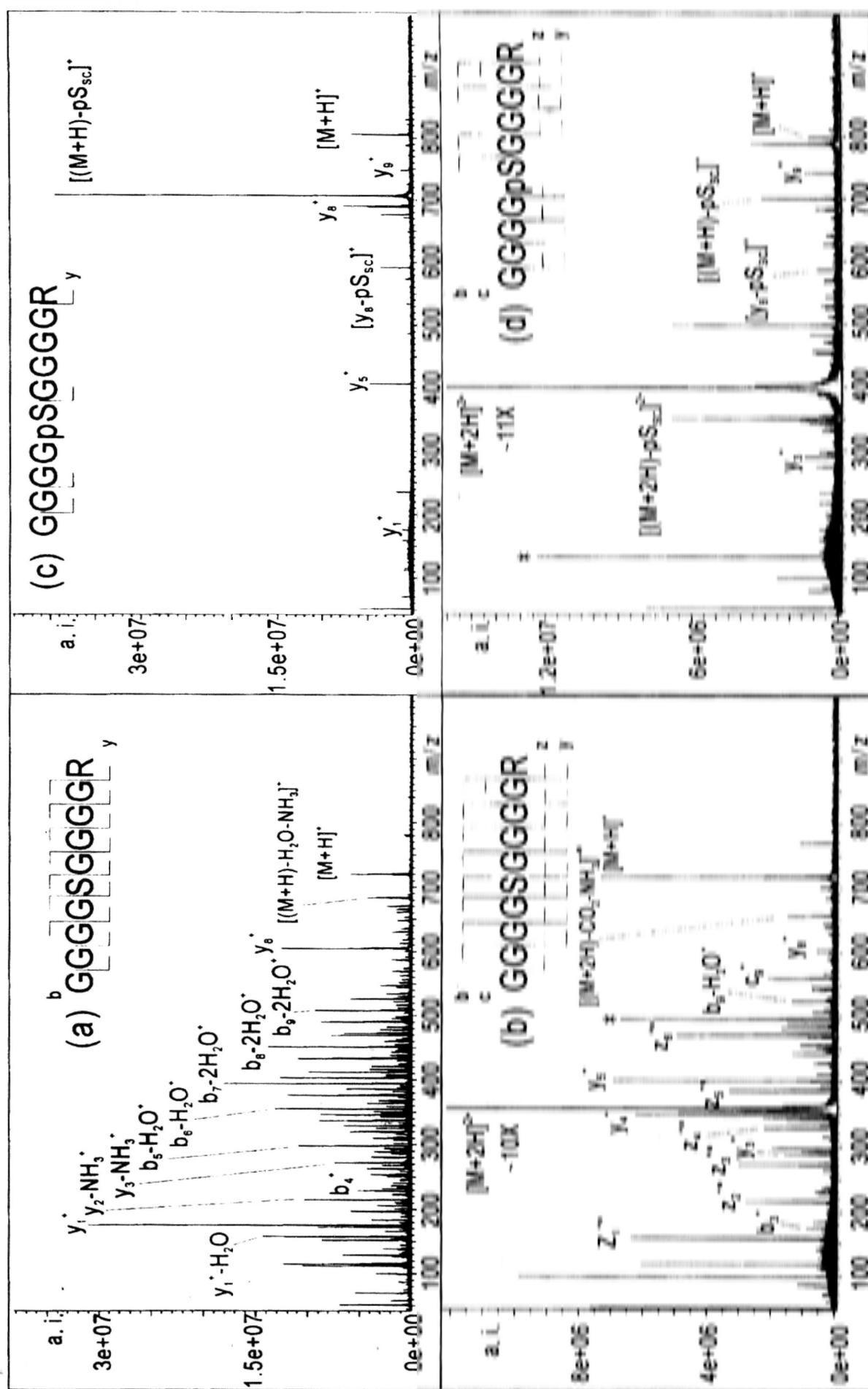


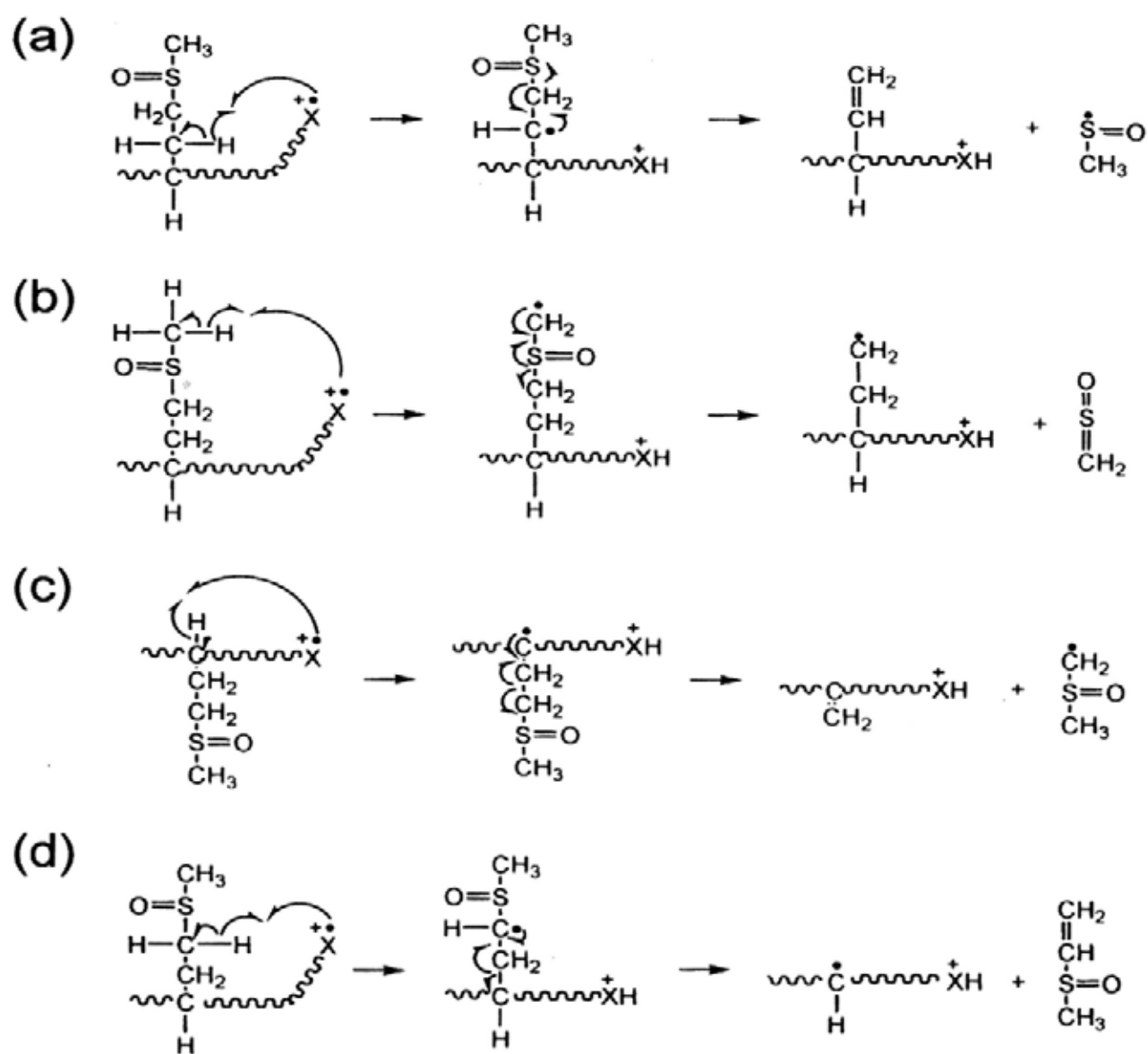
Figure 4.5 Typical mass spectra of (a) SORI-CID of $[G_pSG_pR+H]^+$, (b) ECD of $[G_pSG_pR+2H]^{2+}$, (c) SORI-CID of $[G_pSG_pR+H]^+$ and (d) ECD of $[G_pSG_pR+2H]^{2+}$.

backbone fragments such as *c*, *z'*, *b* and *y*, ions. Subsequent loss of even-electron phosphoric acid from *z'*, *b* and *y* ions respectively was also observed.

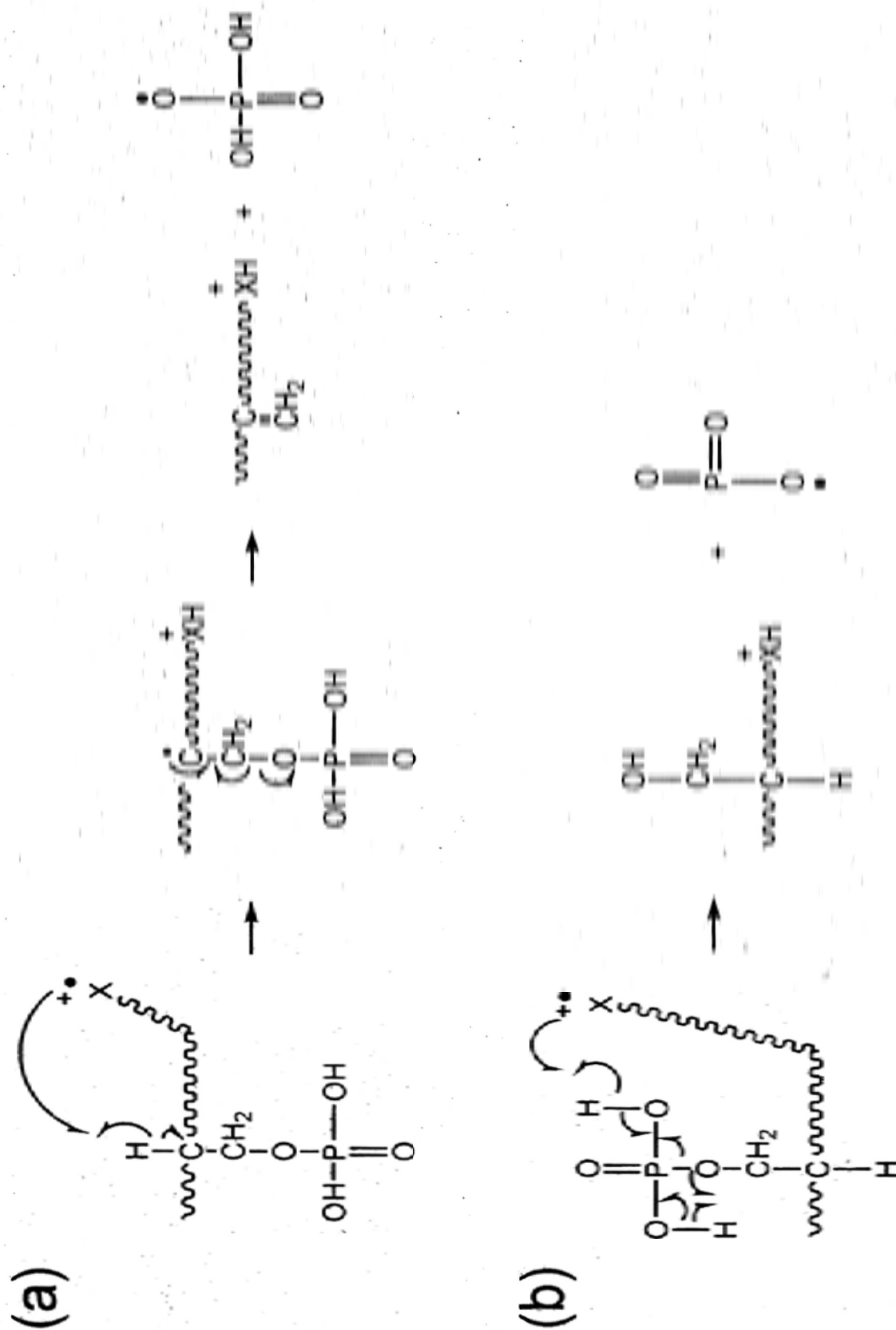
4.3.1.4 Comparison of dissociation patterns between $[M+H]^+$, $M^{+\bullet}$ and $[M+2H]^{2+}$

PTM groups are labile in protonated peptides and were found to cleave preferentially in SORI-CID of $[M+H]^+$ (see Figure 4.4 (a)). However in SORI-CID of $M^{+\bullet}$ (or fragments related to $M^{+\bullet}$ obtained in the dissociation of $[\text{Cu}(\text{Tpy})\text{M}]^{2+}$), side chain loss reactions were the major fragments even though no PTM groups were present in the peptides (see Figure 4.3 (a) and 4.4 (a)). Such difference in the production of fragment ions from SORI-CID of $[M+H]^+$ and $M^{+\bullet}$ (or $[\text{Cu}(\text{Tpy})\text{M}]^{2+}$) despite the use of the same dissociation technique could be attributed to the speciation of the precursor ions. It is surmised that the dissociation of even-electron $[M+H]^+$ under SORI-CID was driven by 'mobile proton' propagated along the peptide backbone, leading to backbone cleavage [37-41]. But for odd-electron $M^{+\bullet}$ under SORI-CID, the dissociation was driven by radical as discussed in Chapter 3 – the heteroatom radical abstracted a hydrogen atom, causing loss of odd- or even-electron side chain. The proposed dissociation pathways of odd- and even-electron oxidized methionine side chain(s) loss from $M^{+\bullet}$ are shown in Scheme 4.1, while the corresponding pathway of odd-electron phosphorylated serine side chain(s) loss from $M^{+\bullet}$ is shown in Scheme 4.2.

In order to obtain additional sequence information [93, 117-121], an analysis on the dissociation patterns of secondary fragmentation of precursor ions was conducted. Table 4.2 summarizes the different types of side chain loss during SORI-CID of $[M+H]^+$, $[\text{Cu}(\text{Tpy})\text{M}]^{2+}$ and $M^{+\bullet}$; and ECD of $[M+2H]^{2+}$. As indicated in the table, for peptides with no PTM groups, there was no side chain loss from



Scheme 4.1 The proposed dissociation pathways of odd- and even-electron M(O) side chain (a) $\text{CH}_3\text{SO}^\bullet$, (b) CH_2SO , (c) $\text{C}_2\text{H}_5\text{SO}^\bullet$ and (d) $\text{C}_3\text{H}_7\text{SO}$ loss from heteratom peptide radical



Scheme 4.2 The proposed dissociation pathways of odd-electron pS side chain
(a) $\text{H}_2\text{PO}_3^\bullet$ and (b) PO_3^\bullet loss from heteroatom peptide radical

Table 4.2 Types of side chain loss during the dissociation of CID of $[M+H]^+$; $Cu(Tpy)M^{2+}$ and M^{2+} ; ECD of $[M+2H]^{2+}$ relative to the most intense peak in the spectrum. (%)

| Cleavage type | G_4, XG_4R | Assignment | Mass loss | SORI-CID | | SORI-CID | | ECD | |
|-------------------|-----------------------|------------------------|-----------|-----------|----------------------|----------|----------|-----------|----------------------|
| | | | | $[M+H]^+$ | $Cu^{II}(Tpy)M^{2+}$ | M^{2+} | z^{**} | $[M+H]^+$ | $[(M+2H)-NH_3]^{2+}$ |
| Sequence specific | M | $CH_2=CHSCH_3$ [M] | 74.0190 | -- | -- | 15.3 | 1.1 | -- | 1.3 |
| | | *CH_2SCH_3 [M] | 61.0117 | -- | -- | 17.5 | 5.4 | -- | 1.5 |
| | M(O) | CH_3SOH [M(O)] | 63.9983 | 65.8 | 28.3 | 15.1 | 0.2 | 0.6 | 0.4 |
| | | *CH_3SO [M(O)] | 62.9905 | -- | -- | 10.6 | 2.3 | -- | 1.6 |
| | | CH_2SO [M(O)] | 61.9826 | -- | -- | -- | 3.1 | -- | 1.0 |
| | | $CH_2=CHSOCH_3$ [M(O)] | 90.0139 | -- | -- | 2.8 | 0.7 | -- | 1.1 |
| | *CH_2SOCH_3 [M(O)] | 77.0061 | -- | -- | 1.9 | 0.5 | -- | 0.3 | |
| S | -- | -- | -- | -- | -- | -- | -- | -- | |
| pS | pS | H_3PO_4 [pS] | 97.9769 | 43.3 | 2.6 ^a | -- | 1.1 | 2.6 | 2.6 |
| | | *H_2PO_4 [pS] | 96.9691 | -- | -- | 44.3 | 1.1 | -- | -- |
| | | *PO_3 [pS] | 78.9585 | -- | -- | 5.3 | -- | -- | -- |
| General | M(O) | $C_4H_9N_3$ [R] | 99.0796 | -- | -- | 1.0 | -- | -- | -- |
| | | S | -- | 0.1 | -- | 1.4 | -- | -- | -- |
| | M(O) | $C_2H_{10}N_5$ [R] | 104.0936 | -- | -- | -- | -- | -- | 0.1 ^b |
| | | S | 60.0561 | -- | -- | -- | -- | -- | 0.5 |

^a Loss from $Cu(M-H)$.^b Loss from $[M+2H]^{2+}$.

protonated peptide in SORI-CID. However, for PTM containing peptides, characteristic oxidized methionine (CH_3SOH) and phosphorylated serine (H_3PO_4) side chains were eliminated from the precursor ions in SORI-CID.

An additional observation was that in SORI-CID of $[\text{Cu}(\text{Tpy})\text{M}]^{2+}$ and ECD of $[\text{M}+2\text{H}]^{2+}$, the same kind of odd- and even-electron PTM side chains were lost from the fragment ions (i.e. M^{+} , z^{+} and $[(\text{M}+2\text{H})-\text{NH}_3]^{+}$) as all of them are heteroatom radicals (radical in z^{+} and $[(\text{M}+2\text{H})-\text{NH}_3]^{+}$ is located at carbon or nitrogen). Presumably, the dissociation of heteroatom radical was initiated by the abstraction of a hydrogen atom at side chain, which eventually invoke odd- or even-electron side chain(s) loss (refer to Schemes 4.1 and 4.2). Similar loss was not observed in the charge-reduced precursor ion ($[\text{M}+2\text{H}]^{+}$) generated in ECD.

4.3.2 Analysis of the Fragmentation Patterns of Copper Ternary Complexes and Metal-adducted Oligosaccharide under SORI-CID and/or ECD conditions

4.3.2.1 General features of spectra

Figure 4.6 shows the dissociation patterns of (a) SORI-CID of $[\text{Cu}(\text{Tpy})\text{M}]^{2+}$, (b) SORI-CID of $[\text{Cu}+\text{M}]^{2+}$ and (c) ECD of $[\text{Cu}+\text{M}]^{2+}$, where M is maltoheptaose. Product ion marked with an asterisk (*) denotes it is a non-metalated species, all other product ions contained $[\text{Cu}(\text{Tpy})]^{2+}$ and $\text{Cu}^{2+/1+}$ which were generated in SORI-CID of $[\text{Cu}(\text{Tpy})\text{M}]^{2+}$, SORI-CID of $[\text{Cu}+\text{M}]^{2+}$ and ECD of $[\text{Cu}+\text{M}]^{2+}$ respectively. B and Z; C and Y; $^{2,4}\text{A}$ and $^{0,2}\text{X}$; and $^{0,2}\text{A}$ and $^{2,4}\text{X}$ were isomeric fragments due to the symmetric property of maltoheptaose [136, 137]. They are labeled as B/Z, C/Y, $^{2,4}\text{A}/^{0,2}\text{X}$; and $^{0,2}\text{A}/^{2,4}\text{X}$ in the spectrum.

In SORI-CID of $[\text{Cu}(\text{Tpy})\text{M}]^{2+}$, the most abundant fragment yielded was

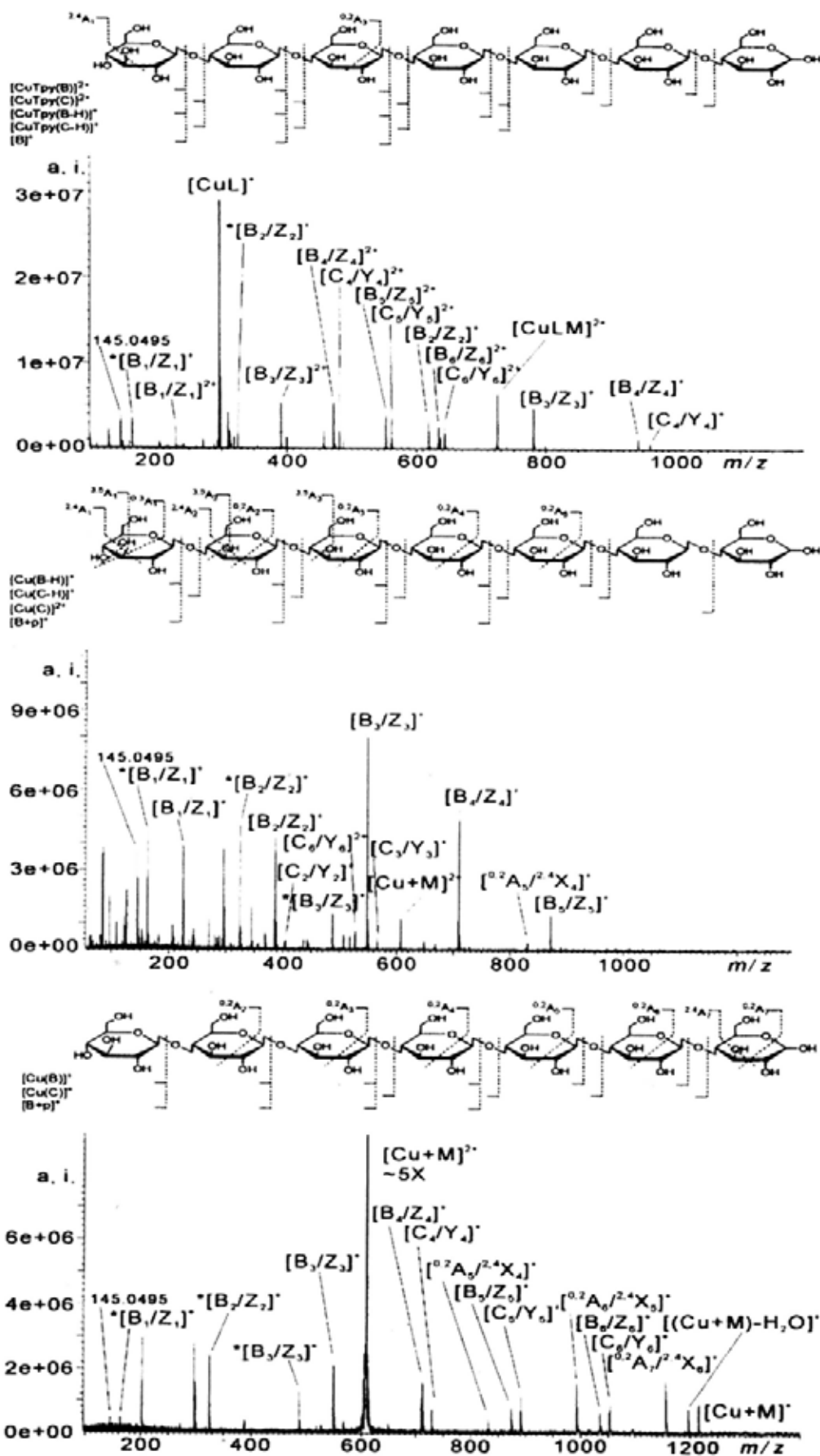


Figure 4. 6 Dissociation patterns of (a) SORI-CID of $[Cu(L)M]^{2+}$, (b) SORI-CID of $[Cu+M]^{2+}$ and (c) ECD of $[Cu+M]^{2+}$, where L is Tpy and M is maltoheptaose. * denotes non-metallated species.

$[\text{Cu}(\text{Tpy})]^+$ but its counter part, M^{2+} , was not observed. The presence of $[\text{Cu}(\text{Tpy})]^+$ implies the electron had transferred from the oligosaccharide to the copper center, leading to the formation of M^{2+} which subsequently dissociated to give B_n^+ fragments due its instability. Fragmentation of $[\text{Cu}(\text{Tpy})\text{M}]^{2+}$ also generated doubly-charged glycosidic bond cleavages (i.e. $[\text{Cu}(\text{Tpy})\text{B}/\text{Z}]^{2+}$ and $[\text{Cu}(\text{Tpy})\text{C}/\text{Y}]^{2+}$) as the major fragments. Besides, several singly-charged glycosidic fragments (i.e. $[\text{Cu}(\text{Tpy})(\text{B}/\text{Z}-\text{H})]^+$ and $[\text{Cu}(\text{Tpy})(\text{C}/\text{Y}-\text{H})]^+$) were also formed due to the transfer of proton to the complementary B/Z ions (labeled as $^*[\text{B}/\text{Z}]^+$). Most of the glycosidic cleavages retained to bind with $[\text{Cu}(\text{Tpy})]^{2+}$, and only a few singly-charged $[\text{B}/\text{Z}]^+$ and a fragment at m/z 145.0495 (could be assigned as $[\text{B}/\text{Z}-\text{H}_2\text{O}]^+$) were generated. These singly-charged non-metalated fragment ions were also seen in the SORI-CID of $[\text{Cu}+\text{M}]^{2+}$ and ECD of $[\text{Cu}+\text{M}]^{2+}$, where most of the fragment ions produced were copper-adducted species (both glycosidic and cross-ring cleavages).

The SORI-CID spectrum of $[\text{Cu}+\text{M}]^{2+}$ was substantially different from that of $[\text{Cu}(\text{Tpy})\text{M}]^{2+}$. Abundant peaks corresponding to singly-charged glycosidic cleavage fragments were noticeable in the spectrum (Figure 4.6 (b)) with relatively low intensity of cross-ring cleavage fragments. Rather similar results were noted in ECD of $[\text{Cu}+\text{M}]^{2+}$ (Figure 4.6 (c)), which generated a mixture of glycosidic and cross-ring cleavages, a charge-reduced precursor ion ($[\text{Cu}+\text{M}]^{+}$) and a fragment ion related to its neutral loss ($[(\text{Cu}+\text{M})-\text{H}_2\text{O}]^{+}$).

Figure 4.7 outlines the dissociation patterns of (a) SORI-CID of $[\text{Cu}(\text{Tpy})\text{M}]^{2+}$, (b) SORI-CID of $[\text{Cu}+\text{M}]^{2+}$ and (c) ECD of $[\text{Cu}+\text{M}]^{2+}$, where M is 3 α ,6 α -mannopentaose. Table 4.3 summarizes all the spectral information concerned. A singly-charged $[\text{B}/\text{Z}]^+$ and a fragment at m/z 145.0495 were seen in each spectrum. The SORI-CID spectrum of $[\text{Cu}(\text{Tpy})\text{M}]^{2+}$ was similar to that of the linear

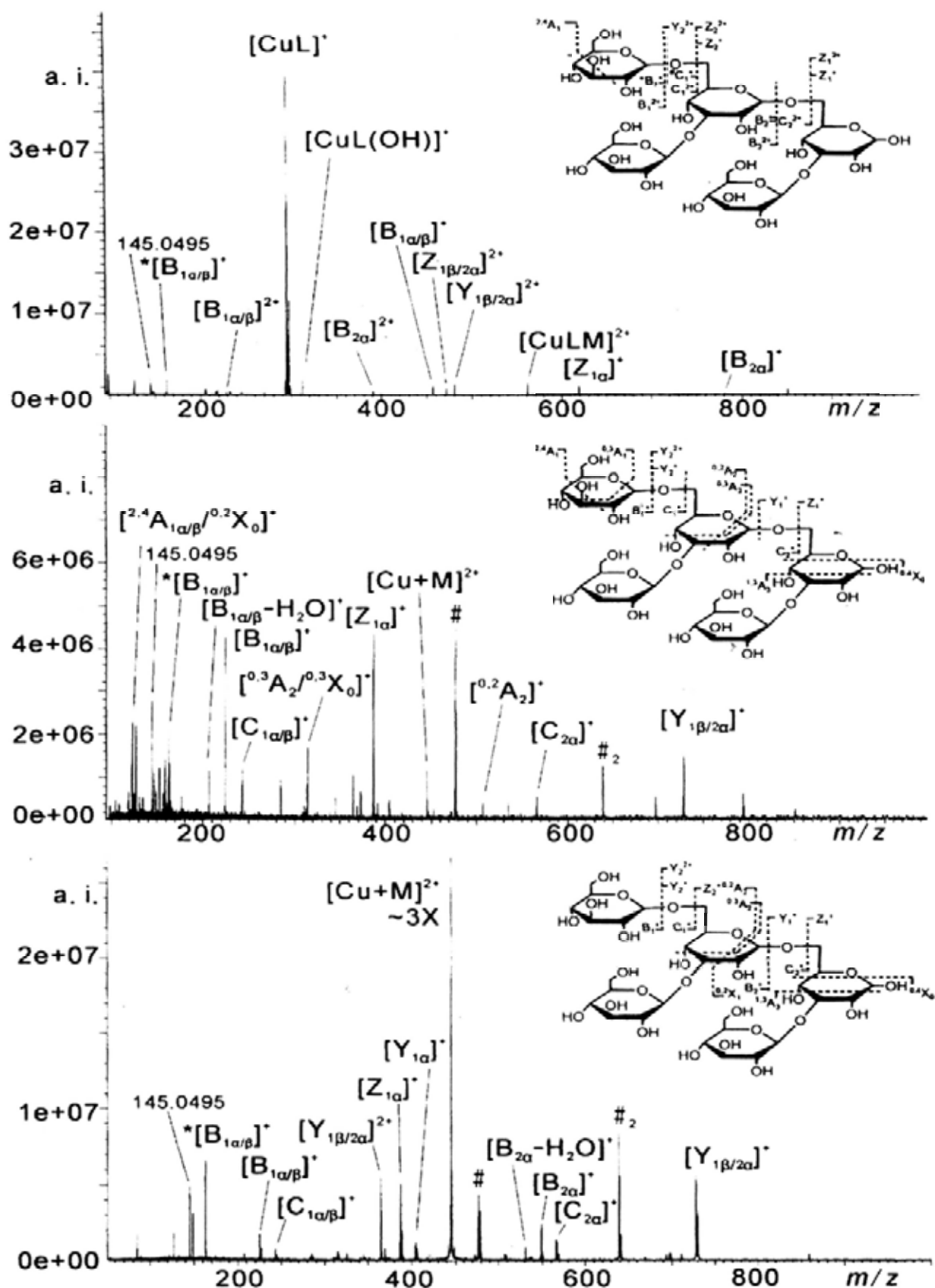


Figure 4.7 Dissociation patterns of (a) SORI-CID of $[Cu(L)M]^{2+}$, (b) SORI-CID of $[Cu+M]^{2+}$ and (c) ECD of $[Cu+M]^{2+}$, where L is Tpy and M is $3\alpha,6\alpha$ -mannopentaose. # indicates $[C_2+14-B_1]^+$, #₂ indicates $[C_2+14]^+$ and * denotes non-metallated species.

Table 4.3 Relative abundance of fragment species of $[\text{Cu}(\text{Tpy})\text{M}]^{2+}$ and $[\text{Cu}+\text{M}]^{2+}$ under SORI-CID and ECD conditions. (%)

| Fragment species | Maltoheptaose | | | $3\alpha,6\alpha$ -Mannopentaose | | |
|-----------------------------------|----------------------------------------------------|-----------------------------------------|------------------------------------|----------------------------------------------------|-----------------------------------------|------------------------------------|
| | SORI-CID $[\text{Cu}(\text{Tpy})\text{M}]^{2+}$ | SORI-CID $[\text{Cu}+\text{M}]^{2+}$ | ECD $[\text{Cu}+\text{M}]^{2+}$ | SORI-CID $[\text{Cu}(\text{Tpy})\text{M}]^{2+}$ | SORI-CID $[\text{Cu}+\text{M}]^{2+}$ | ECD $[\text{Cu}+\text{M}]^{2+}$ |
| Glycosidic Cleavages | | | | | | |
| $*[\text{B}_n/\text{Z}_n]^+$ | 16.3 | 22.7 | 14.2 | 21.1 | 8.4 | 14.8 |
| $[\text{B}_n]^{2+}$ | 39.0 ^a | -- | -- | 9.3 | -- | -- |
| $[\text{B}_n]^+$ | 18.5 ^a | 55.1 ^a | 48.3 ^a | 25.8 | 20.7 | 11.6 |
| $[\text{Y}_n]^{2+}$ | N/A | N/A | N/A | 14.4 | 4.0 | -- |
| $[\text{Y}_n]^+$ | N/A | N/A | N/A | -- | 8.6 | 25.0 |
| $[\text{C}_n]^{2+}$ | 20.0 ^b | 1.5 ^b | -- | 2.5 | -- | -- |
| $[\text{C}_n]^+$ | 5.1 ^b | 5.0 ^b | 16.5 ^b | 1.8 | 11.4 | 24.1 |
| $[\text{Z}_n]^{2+}$ | N/A | N/A | N/A | 11.9 | -- | -- |
| $[\text{Z}_n]^+$ | N/A | N/A | N/A | 11.3 | 20.2 | 16.8 |
| Cross-ring Cleavages | | | | | | |
| $[\text{A}_n/\text{X}_{(n-1)}]^+$ | 1.1 | 15.7 | 21.0 | 1.8 | 26.7 | 7.7 |

*Indicates fragment is protonated species, otherwise, they are copper adducted in dissociation of $[\text{CuM}]^{2+}$ and copper-ligand adducted in dissociation of $[\text{Cu}(\text{Tpy})\text{M}]^{2+}$.

^a m/z of B ion is the same as Z ion.

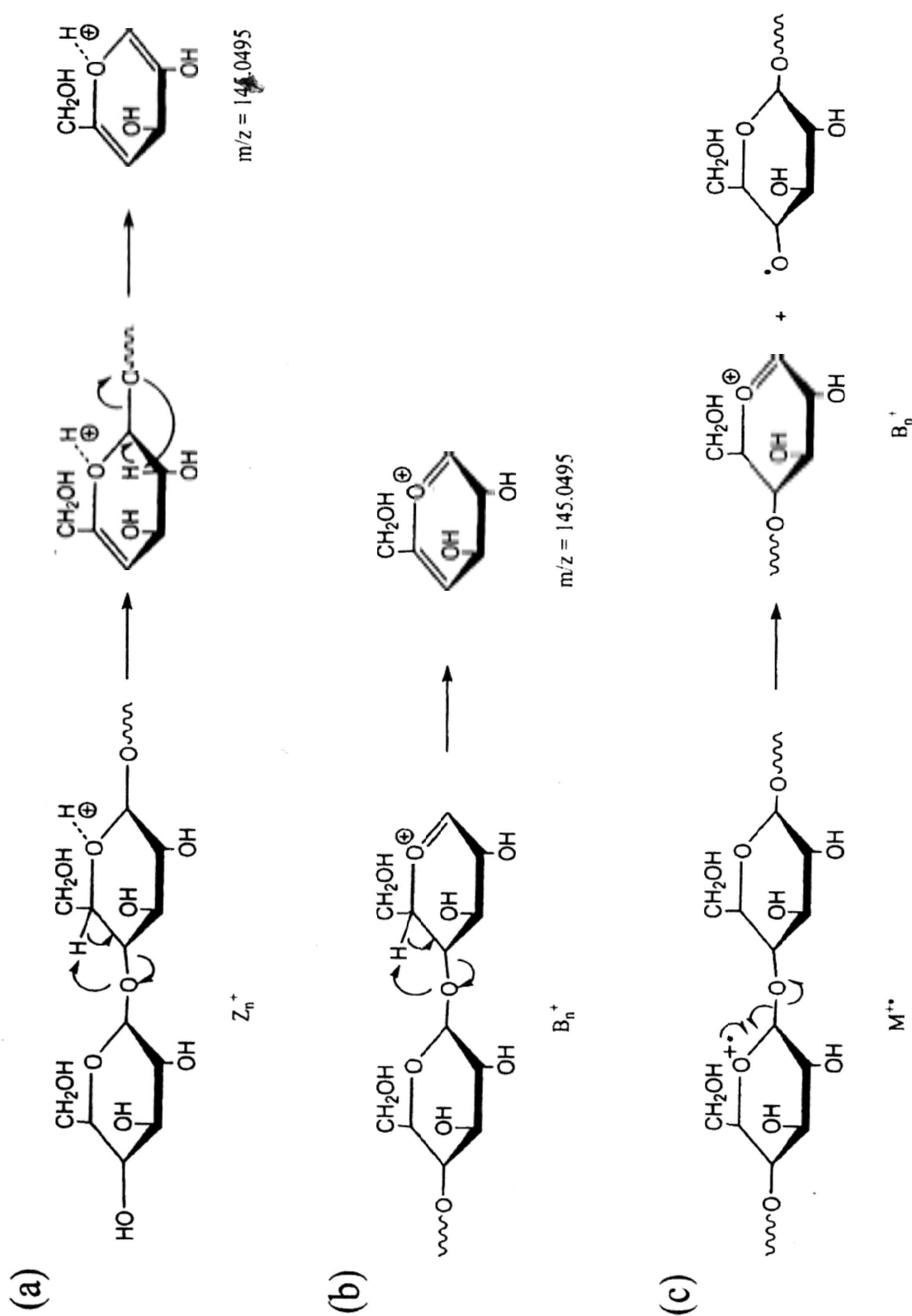
^b m/z of C ion is the same as Y ion.

oligosaccharide in SORI-CID of $[\text{Cu}(\text{Tpy})\text{M}]^{2+}$ as shown in Figure 4.6(a). The most abundant fragment yielded was $[\text{Cu}(\text{Tpy})]^+$ but its counter part, M^+ , was not seen. Further, the intensities of all fragment ions yielded were relatively low except $[\text{Cu}(\text{Tpy})]^+$. The low-intensity fragment ions included one cross-ring fragment ($^{2,4}\text{A}$ ion) and a series of singly- and doubly-charged glycosidic bond cleavages (mainly B/Z ions). In SORI-CID of $[\text{Cu}+\text{M}]^{2+}$, prominent singly-charged ions corresponding to both glycosidic and cross-ring cleavages were produced. As to ECD of $[\text{Cu}+\text{M}]^{2+}$, glycosidic cleavages were the major fragments whereas cross-ring cleavages the minor fragments with relatively low intensity. Unlike the case of linear oligosaccharide, more abundant cross-ring cleavages (including $^{0,3}\text{A}$, $^{0,2}\text{A}$, $^{2,4}\text{A}_{1\alpha\beta}$, $^{0,2}\text{X}$, $^{1,3}\text{A}$ and $^{0,4}\text{X}$) were observed in SORI-CID than in ECD of $[\text{Cu}+\text{M}]^{2+}$.

4.3.2.2 Comparison between SORI-CID and ECD of $[\text{Cu}+\text{M}]^{2+}$

As illustrated via Table 4.3, most of the fragment ions obtained in the SORI-CID of $[\text{Cu}+\text{M}]^{2+}$ and ECD of $[\text{Cu}+\text{M}]^{2+}$ were singly-charged species. In all MS/MS spectra of $[\text{Cu}+\text{M}]^{2+}$, singly-charged $[\text{B}/\text{Z}]^+$ and ions with m/z 145.0495 (upon further dissociation of the singly-charged $[\text{B}/\text{Z}]^+$) were observed. The possible dissociation pathways of m/z 145.0495 are proposed via Scheme 4.3.

For maltoheptaose (linear oligosaccharide), the relative percentages of different kinds of fragment ions (glycosidic and cross-ring cleavages) obtained in SORI-CID of $[\text{Cu}+\text{M}]^{2+}$ and ECD of $[\text{Cu}+\text{M}]^{2+}$ were similar as shown in Table 4.3. These results were congruent with those of CAD and 'hot' ECD of permethylated linear malto-oligosaccharides performed by Zhao and co-workers [138]. Among all the fragment ions obtained in the SORI-CID and ECD experiments concerned, the relative intensities of B/Z ions were much higher than those of C/Y ions while the



Scheme 4.3 Proposed dissociation pathway of (a) Z_n^+ , (b) B_n^+ (further dissociate to generate $m/z = 145.0495$) and (c) M^{2+}

relative intensities of A/X ions were more or less identical. The studies by Harvey [137] and Carr et al. [139] have shown that the product ions formed from cleavage on the non-reducing side of glycosidic oxygen (B and Y ions) are more abundant than those formed from cleavage on the reducing side (C and Z ions). However, given the symmetric nature of maltoheptaose, B and Z ions could not be distinguished on the basis of their m/z and thus the experimental results in this study could not be compared with those obtained in the previous studies as mentioned.

As to 3 α ,6 α -mannopentaose (branch oligosaccharide), B and Z ions were the major fragment ions, whereas C and Y ions the major product ions observed in SORI-CID of $[\text{Cu}+\text{M}]^{2+}$ and ECD of $[\text{Cu}+\text{M}]^{2+}$ respectively. In addition, cross-ring cleavages (A/X ions) were found more abundant in SORI-CID than in ECD. For branch oligosaccharide, its $[\text{Cu}+\text{M}]^{2+}$ exhibited similar fragmentation pattern as that of the linear oligosaccharide under SORI-CID conditions. However, a different ECD dissociation pattern was found for copper-adducted branch oligosaccharide ($[\text{Cu}+\text{M}]^{2+}$), probably due to the specific binding mode between the copper ion and the branch oligosaccharide. This is because during the ECD process, the electron neutralized a charge and induced fragmentation in a relatively short time. The cleavage position is thus speculated to be affected by the structure of precursor ion as well as the position of the neutralization site.

In contrast to ECD, the precursor ion in SORI-CID heated up slowly and the dissociation time should be sufficient for structural relaxation of the copper-adducted branch oligosaccharide. Presumably, the relaxed structure of copper-adducted branch oligosaccharide was similar to that of copper-adducted linear oligosaccharide, thus rendering it possible for the copper ion to transfer to a position more favourable for inducement of glycosidic cleavages (B/Z ion) and cross-ring cleavages (A/X ion). As

a result, the SORI-CID fragmentation pattern of copper-adducted branch oligosaccharide was similar to the SORI-CID and ECD patterns of copper-adducted linear oligosaccharide.

4.3.2.3 Comparison of SORI-CID of $[\text{Cu}(\text{Tpy})\text{M}]^{2+}$ with $[\text{Cu}+\text{M}]^{2+}$

For both linear and branch oligosaccharides, no M^{++} was observed in SORI-CID of $[\text{Cu}(\text{Tpy})\text{M}]^{2+}$ (see Figure 4.6 (a) and 4.7 (a)). The observed abundance $[\text{Cu}(\text{Tpy})]^+$ indicates that the electron had transferred from the oligosaccharide to the copper center. Similar to SORI-CID of $[\text{Cu}(\text{Tpy})\text{M}]^{2+}$ (where M is $\text{G}_4\text{pSG}_4\text{R}$ (peptide)) as illustrated via Figure 4.1 (d), M^{++} is believed to have dissociated readily after its generation and therefore no M^{++} was observed. This implies that the stability of oligosaccharide radical cations was much lower than that of peptide radical cations. It is also believed that the presence of weak bonds in the oligosaccharide promoted fragmentation (as in the case with nucleic acids [125]), and the unstable oligosaccharide radical cation (M^{++}) dissociated to give B ions by cleaving the glycosidic linkages. A possible dissociation pathway of oligosaccharide radical cation is shown in Scheme 4.3.

In SORI-CID of $[\text{Cu}(\text{Tpy})\text{M}]^{2+}$ and $[\text{Cu}+\text{M}]^{2+}$, B and Z ions were the major fragments yielded (Figures 4.6 (a–b) and 4.7 (a–b) are relevant). Table 4.3 shows that the glycosidic cleavages were mainly doubly-charged in SORI-CID of $[\text{Cu}(\text{Tpy})\text{M}]^{2+}$ but singly-charged in SORI-CID of $[\text{Cu}+\text{M}]^{2+}$. It also indicates that the dissociation of $[\text{Cu}(\text{Tpy})\text{M}]^{2+}$ only yielded a few cross-ring cleavages (A/X ions) with very low intensities. Based on empirical correlation, the differences in the dissociation patterns of SORI-CID of $[\text{Cu}(\text{Tpy})\text{M}]^{2+}$ and $[\text{Cu}+\text{M}]^{2+}$ could be related to the presence of terpyridine ligand. These observations suggest that the presence of ligand could alter

the dissociation channel and therefore torque the charge state of glycosidic cleavages between 2+ and 1+.

In order to gain an additional insight of how the presence of ligand would affect the preference of dissociation, conformational searches of $[\text{Cu}(\text{Tpy})\text{M}]^{2+}$ and $[\text{Cu}+\text{M}]^{2+}$ (where M is maltoheptaose) were performed to extract the features of their low-energy structures. From the structures obtained, which are shown in Figure 4.8 (a) and (b) respectively, the copper center was found to be octahedral-coordinated in both complexes. Figure 4.8 (a) shows that three out of the six coordination sites of the copper center were occupied by terpyridine, leaving three coordination sites to interact with the hydroxyl oxygen in the oligosaccharide. Whilst in Figure 4.8 (b), all of six coordination sites of the copper center interacted with the oxygenated groups (including oxygen atom in the ring and hydroxyl oxygen). These are indicative of the ability of the metal center to coordinate oxygen atoms in multiple positions of the oligosaccharide, thereby invoking increased fragmentation. This assumption is in line with the observations of Harvey [140]. A further finding from the low-energy structures procured is that the coordination between copper and oligosaccharide was different in $[\text{Cu}(\text{Tpy})\text{M}]^{2+}$ and $[\text{Cu}+\text{M}]^{2+}$. Since cross-ring cleavages involve multiple bond cleavages [141], the copper ion will not be detached from the oligosaccharide easily after cleavage of the first bond if more interactions exist between the copper center and the oligosaccharide in $[\text{Cu}+\text{M}]^{2+}$. This explains why more cross-ring cleavages were yielded from the SORI-CID of $[\text{Cu}+\text{M}]^{2+}$.

Further to the above, it is found that the charge state of the glycosidic cleavages obtained from $[\text{Cu}(\text{Tpy})\text{M}]^{2+}$ and $[\text{Cu}+\text{M}]^{2+}$ was altered in the presence of ligand. It is believed that ligand lowered the polarizing ability of the copper ion (as dative bonds were formed between nitrogen atoms and copper center) and thus

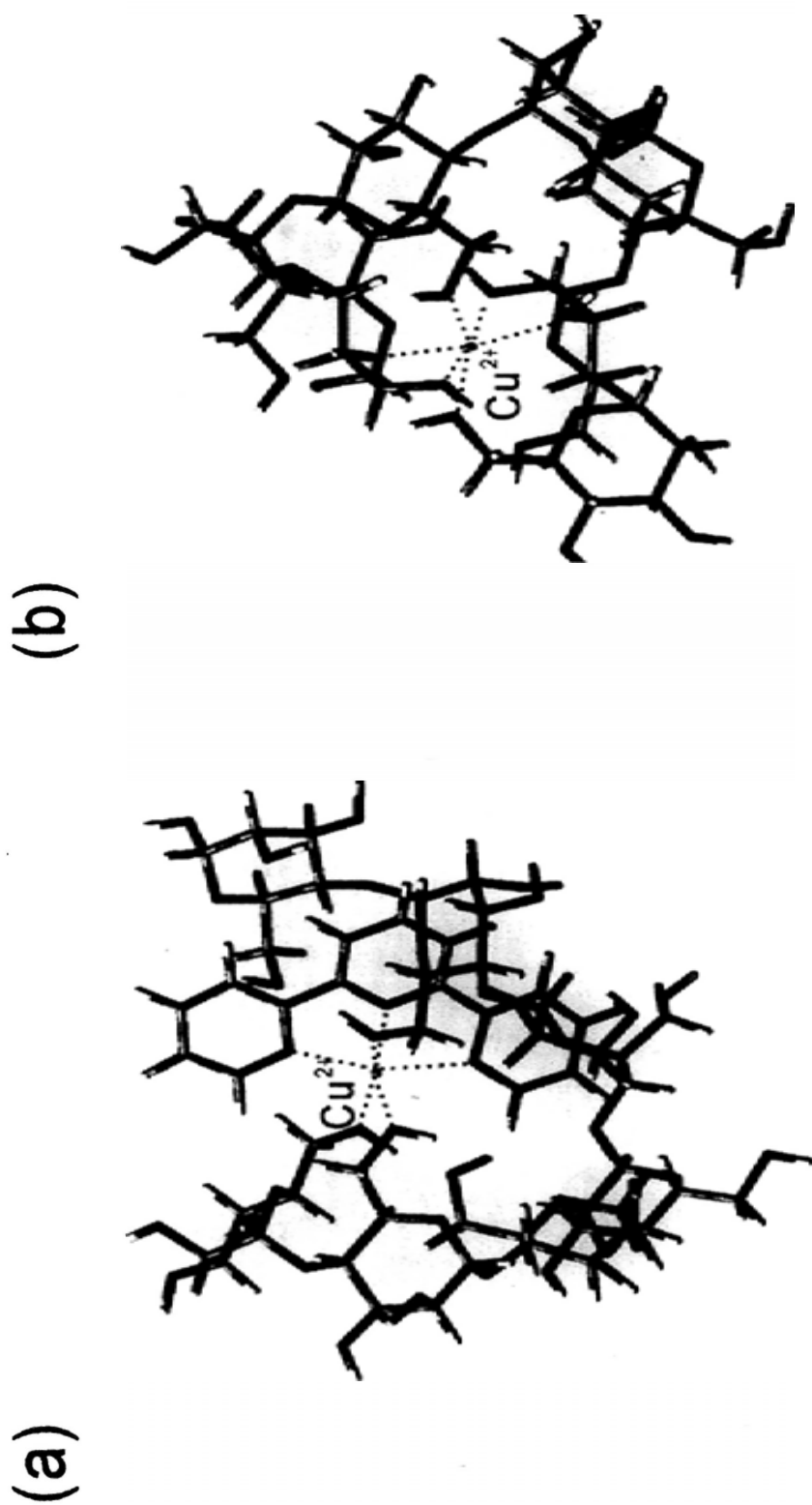


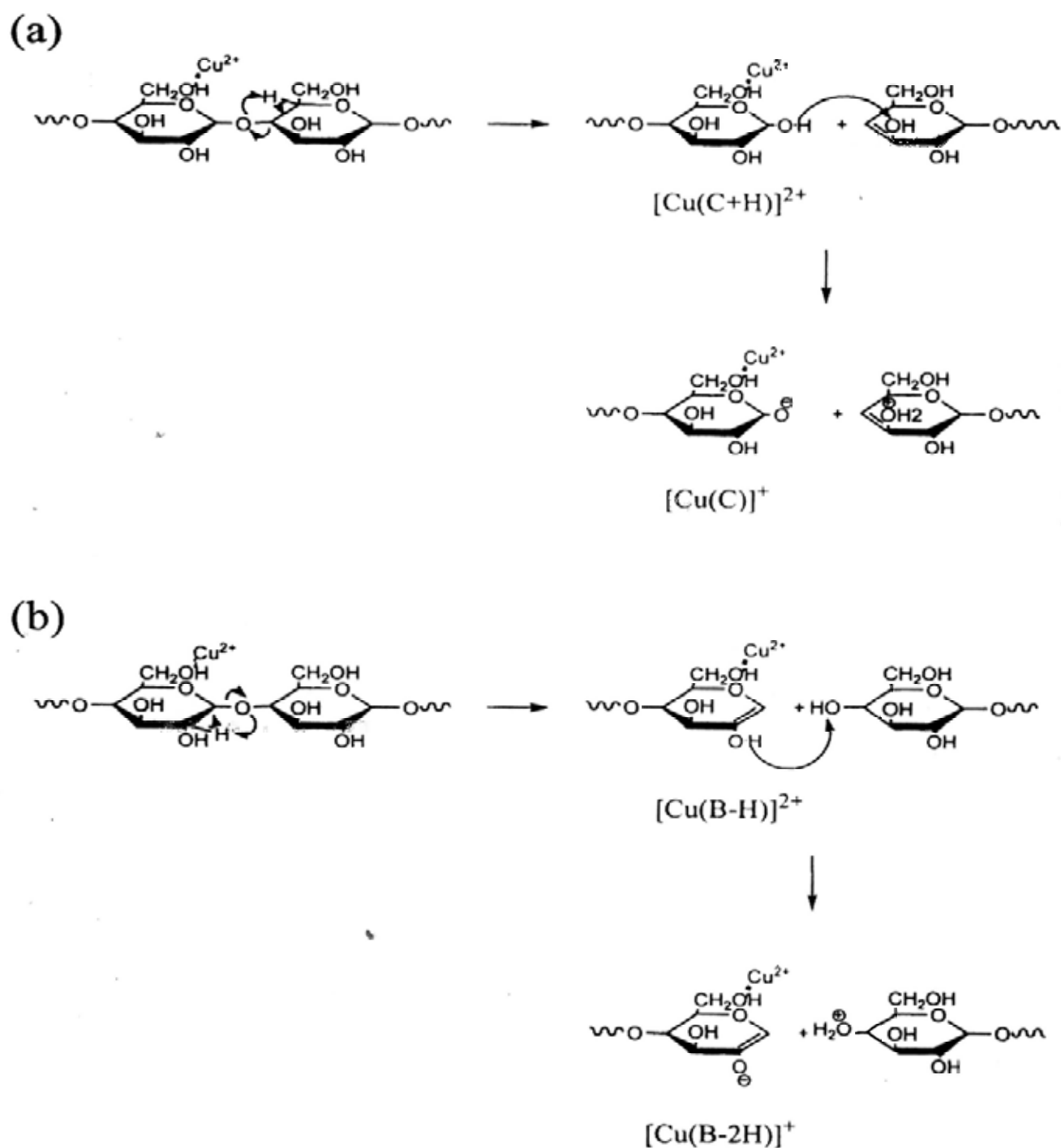
Figure 4. 8 The low-energy structures of (a) $[\text{Cu}(\text{Tpy})\text{M}]^{2+}$ and (b) $[\text{Cu}+\text{M}]^{2+}$ obtained by conformational searches. The dotted lines represent the interactions between the copper center and the oligosaccharide (interactions with ligand were also included).

weakened the interaction(s) between the copper center and the oligosaccharide. Amidst this weak interaction, glycosidic fragments continued to bind with copper-terpyridine after cleavage of the glycosidic linkage, resulting in $[\text{Cu}(\text{Tpy})\text{B}/\text{Z}]^{2+}$ and $[\text{Cu}(\text{Tpy})\text{C}/\text{Y}]^{2+}$ as the major fragments in SORI-CID of $[\text{Cu}(\text{Tpy})\text{M}]^{2+}$. And since the polarity of copper ion is higher in $[\text{Cu}+\text{M}]^{2+}$ than in $[\text{Cu}(\text{Tpy})\text{M}]^{2+}$, the interaction between copper ion and oligosaccharide should be stronger in $[\text{Cu}+\text{M}]^{2+}$. As a result, the two fragments were held by the copper ion in $[\text{Cu}+\text{M}]^{2+}$ for a longer period after cleavage of the glycosidic linkage and this provided enough time for a proton transfer between them. Consequently, instead of doubly-charged glycosidic cleavages, the major fragments generated in SORI-CID of $[\text{Cu}+\text{M}]^{2+}$ were singly-charged $[\text{Cu}(\text{B}/\text{Z}-\text{H})]^+$ and $[\text{Cu}(\text{C}/\text{Y}-\text{H})]^+$ (identical to those reported by Harvery [137]). The proposed dissociation pathways of doubly- and singly-charged glycosidic cleavages ($[\text{CuTpy}]^{2+}$ or Cu^{2+} adducted) are shown in Scheme 4.4.

4.3.3 Investigation of the Effect of Non-Covalent binding of (12-crown-4) on Peptide Dissociation under ECD conditions

4.3.3.1 General features of spectra

Figure 4.9 sets out the ECD mass spectra of $[\text{L}+(\text{M}+2\text{H})]^{2+}$ and $[\text{M}+2\text{H}]^{2+}$, where L is 12-crown-4 and M is ENSMLPR. Dissociation of $[\text{L}+(\text{M}+2\text{H})]^{2+}$ led to the generation of several z' ions; neutral side chain loss from z' ions and $[\text{M}+2\text{H}]^+$; high intensities of $[\text{M}+2\text{H}]^+$ and $[\text{M}+2\text{H}]^{2+}$; and ligand retention in only a few backbone fragment ions. In the dissociation of $[\text{M}+2\text{H}]^{2+}$, major fragments of side chain loss from z' ions and $[\text{M}+2\text{H}]^+$ and minor backbone fragments such as b/y ions were detected. This apart, the intensities of $[\text{M}+2\text{H}]^+$ and $[(\text{M}+2\text{H})-\text{NH}_3]^+$ were



Scheme 4.4 Proposed dissociation pathway of CuTpy and Cu adducted glycosidic fragments (a) C ion and (b) B ion

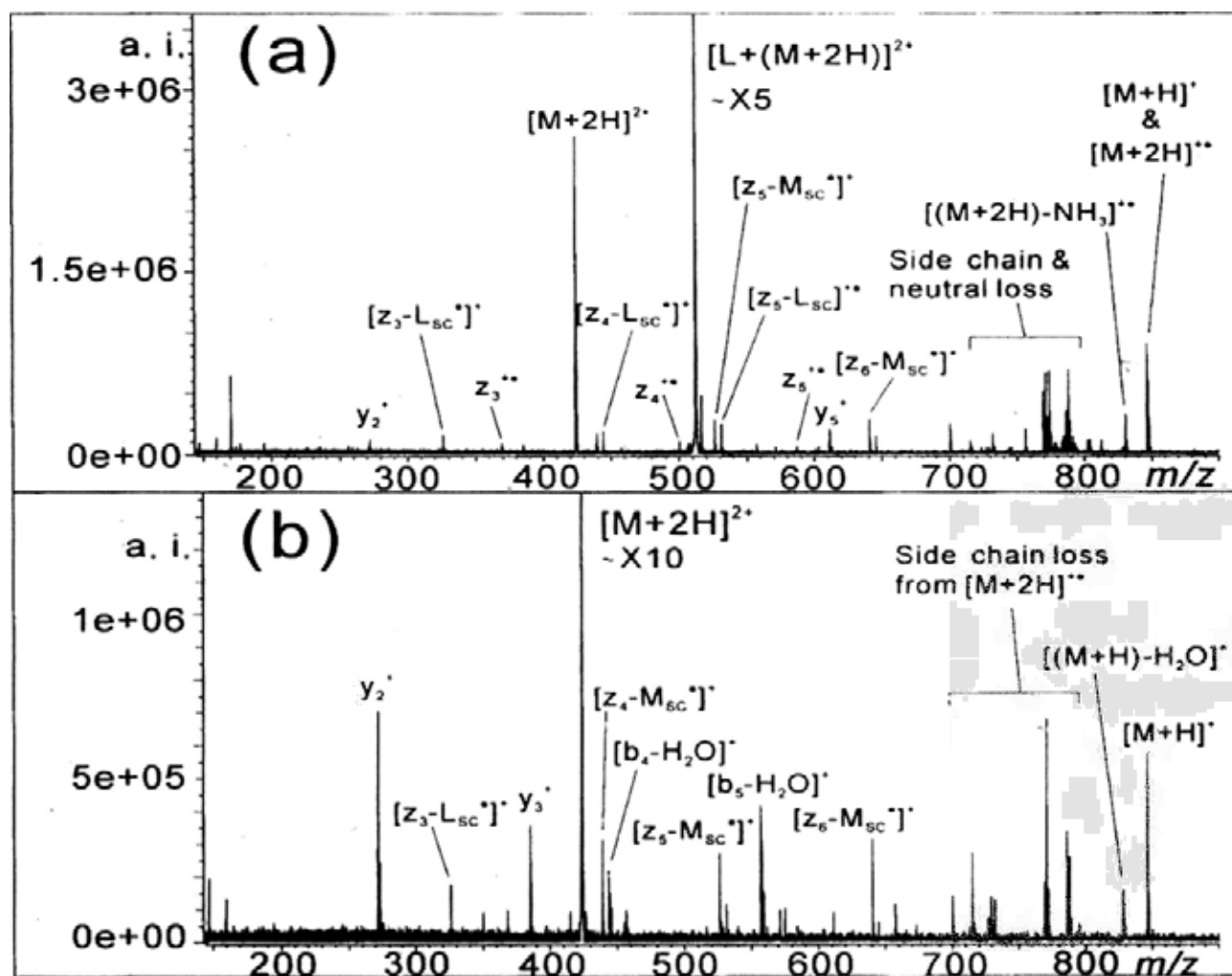


Figure 4. 9 ECD mass spectra of (a) $[L+M+2H]^{2+}$ and (b) $[M+2H]^{2+}$, where L is 12-crown-4 and M is ENSMLPR.

much less abundant. In both spectra concerned, no z_2 ion was found due to the presence of proline (P) which had suppressed backbone cleavages at the N-terminal side of P [65].

The high intensity of $[M+2H]^{2+}$ yielded in ECD of $[L+(M+2H)]^{2+}$ was observed to have been dissociated to give exactly the same kind of fragment ions as its parent ion. To ensure the backbone fragments obtained were generated directly from $[L+(M+2H)]^{2+}$ and not from the derived secondary ion, a double resonance (DR) experiment was carried out [101, 141-145] whereby $[M+2H]^{2+}$ was ejected. For comparison purpose, Figure 4.10 shows the mass spectra of (a) $[L+(M+2H)]^{2+}$ under ECD, (b) DR-ECD of $[M+2H]^{2+}$ and (c) DR-ECD of $[M+2H]^+$, where L is 12-crown-4 and M is INSMLPR. The spectra in Figure 4.10 (a) and (b) show that the ejection of $[M+2H]^{2+}$ did not have a profound effect on both the dissociation pattern and the intensities of the fragment ions. As a few relatively low-intensity *b/y* ions were seen present in the ECD experiment but not the DR-ECD, this indicates that majority of the fragment ions were dissociated directly from $[L+(M+2H)]^{2+}$ and not from $[M+2H]^{2+}$.

Separately, as it might be possible that the *c/z'* ion pair(s) generated from $[M+2H]^+$ was held together by non-covalent hydrogen bond(s) or salt bridge(s) during the ECD process, another DR experiment was performed with the excitation of $[M+2H]^+$ in order to provide a rough measurement of the product ion lifetime for fragments. (However, it must be pointed out that there is a limitation in this experiment as the time scale of DR excitation is in microseconds (μ s) and so, if the dissociation rate was faster than μ s, the target ejected ions could escape from the DR excitation and the fragment ions produced would be observed.) Comparison of Figure 4.10 (a) with Figure 4.10 (c) shows that no product ions disappeared upon

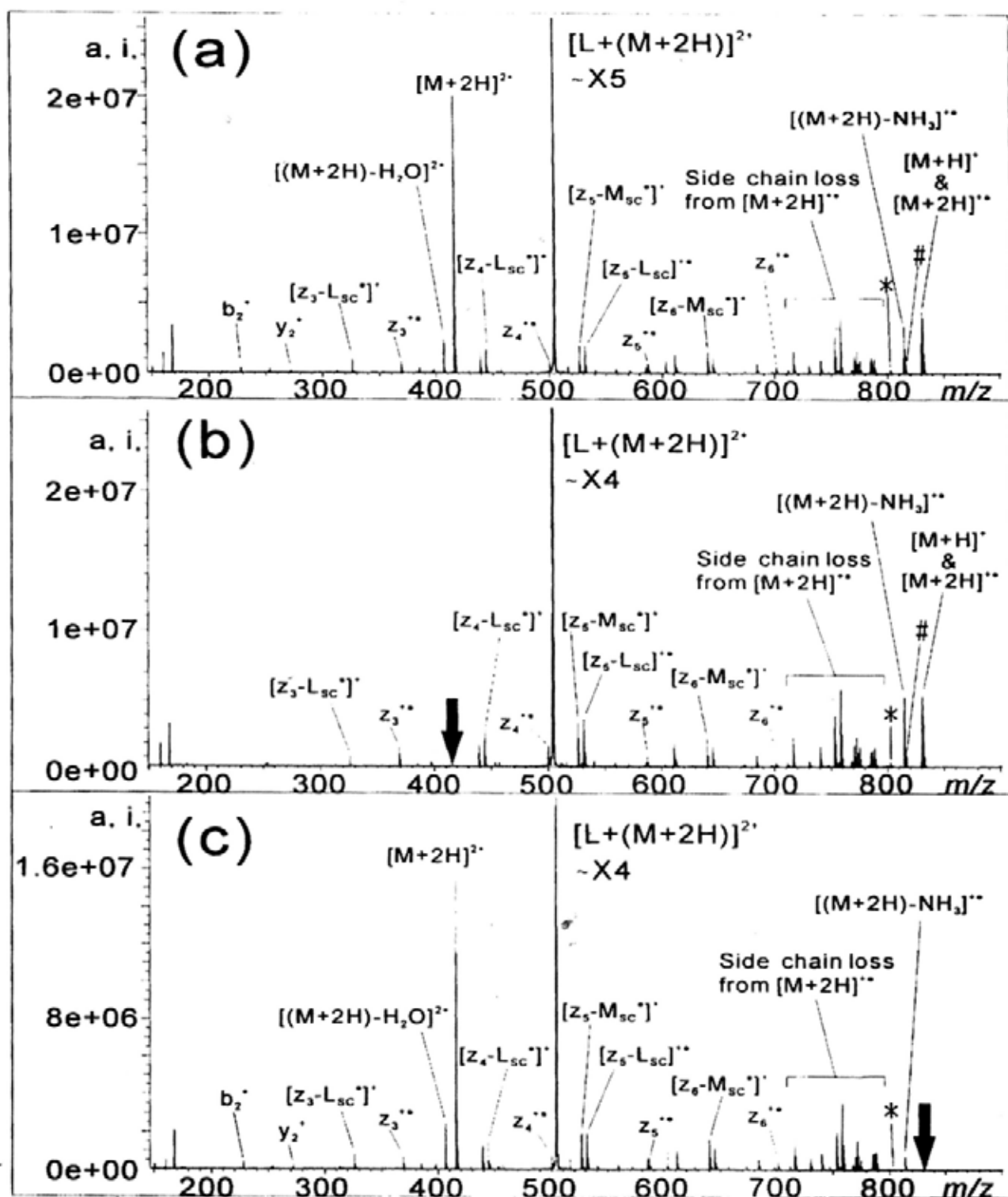


Figure 4. 10 Mass spectra of $[L+M+2H]^{2+}$ (a) ECD, (b) DR-ECD of $[M+2H]^{2+}$ and (c) DR-ECD of $[M+2H]^{\bullet+}$, where L is 12-crown-4 and M is INSMLPR.
* indicates $[L+(z_6-M_{sc})]^{\bullet+}$ and # indicates $[L+(z_6-M_{sc})]^{\bullet+}$

ejection of $[M+2H]^{+}$. This suggests that hydrogen bond(s) which could hold fragment pairs together after their cleavage was absent from the peptide ions.

4.3.3.2 DR-ECD experiments

Table 4.4 summarizes the spectral information yielded from DR-ECD experiments as illustrated via Figure 4.10. It shows that the DR-ECD experiments for both $[M+2H]^{2+}$ and $[M+2H]^{+}$ had posed only a mild effect on the various side chain loss from z' ions, $[M+2H]^{+}$ and their associated fragment ions. It is noteworthy that some abnormal ECD fragments formed in the DR-ECD experiments for ions such as $[b_3-H_2O]^+$ and $[b_5-H_2O]^+$ were not observed in the delay experiment.

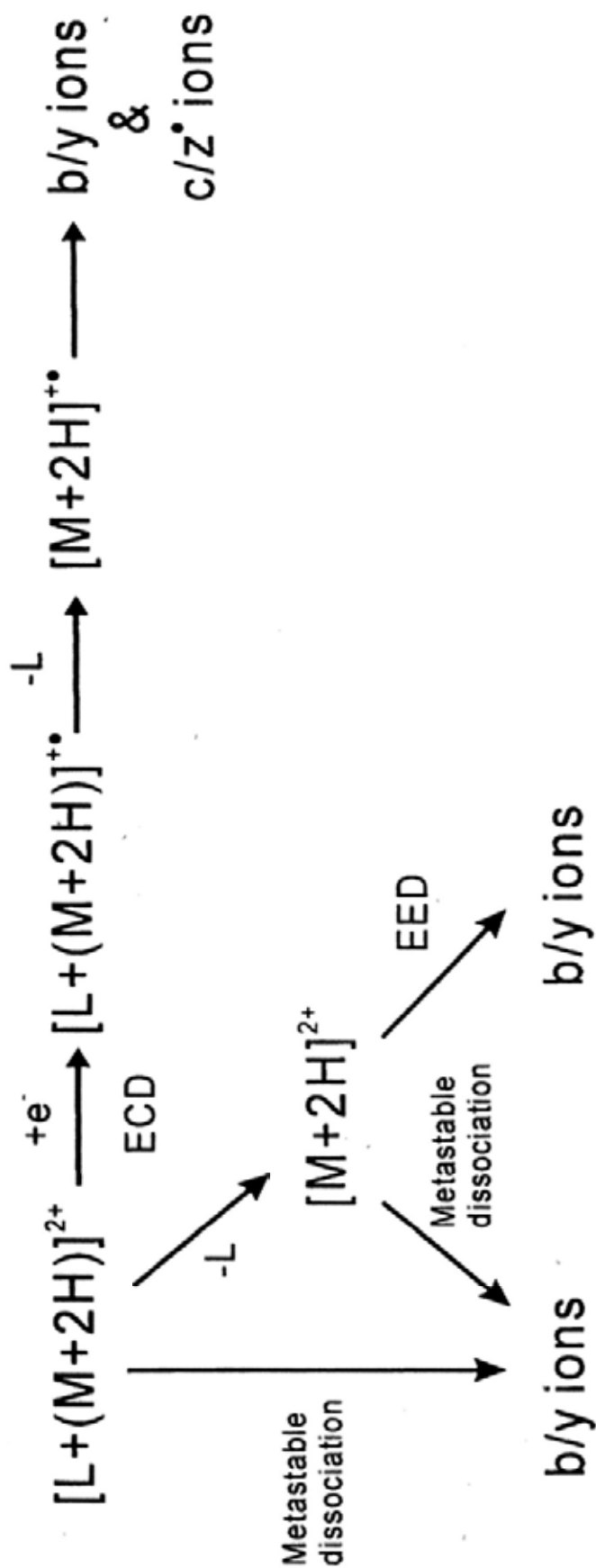
Scheme 4.5 shows the different dissociation channels of $[L+(M+2H)]^{2+}$ under ECD conditions. Besides ECD event, b/y ions could also be generated through metastable dissociation and electron excitation dissociation (EED). Table 4.4 shows that most of the b/y ions observed in the delay experiment were generated through metastable dissociation. It is envisaged that if the ions were observed in DR-ECD for both $[M+2H]^{2+}$ and $[M+2H]^{+}$ but not in the delay experiment, they should have been produced through ECD; however, if they were found in DR-ECD of $[M+2H]^{+}$ and not in DR-ECD of $[M+2H]^{2+}$ or the delay experiment, the ions should have been generated through EED of $[M+2H]^{2+}$ (despite that the major products from EED were proposed to be a and c ions [69, 146, 147] in the literature).

In the literature, there were a few proposed mechanisms for the formation of b ions under ECD conditions. The presence of b ions in ECD was first investigated by Cooper [148] who observed that more b ions were formed in the dissociation of lysine-containing peptides when compared to arginine-containing peptides. By conducting DR-ECD experiments, she also found that b ions were not

Table 4.4 Summary of spectral information in DR-ECD experiments of $[L+(M+2H)]^{2+}$, where L is 12-crown-4 and M is INSMLPR.

| Theoretical mass | Ion type | ECD | | DR $[M+2H]^{2+}$ | | DR $[M+2H]^{2+}$ | | Delay | | Dissociation channel |
|------------------|---------------------------------|--------|--------|------------------|--------|------------------|--------|--------|--------|----------------------|
| | | S/N | r.i. | S/N | r.i. | S/N | r.i. | S/N | r.i. | |
| 177.1121 | $[L+H]^+$ | 14.3 | 0.3% | 11.7 | 0.2% | 12.7 | 0.2% | | | |
| 503.7837 | $[L+(M+2H)]^{2+}$ | 5461.8 | 100.0% | 5957.8 | 100.0% | 5340.0 | 100.0% | 8792.0 | 100.0% | |
| 415.7313 | $[M+2H]^{2+}$ | 1322.9 | 24.2% | | | 1297.4 | 24.3% | 2052.2 | 23.3% | MD |
| 831.4626 | $[M+2H]^{2+}$ | 187.5 | 3.4% | 160.0 | 2.7% | | | | | |
| 830.4553 | $[M+H]^+$ | 203.9 | 3.7% | 220.9 | 3.7% | | | 45.9 | 0.5% | |
| 758.3810 | $(M+2H)^+-C_2H_5[I]-CH_4N_7[R]$ | 200.7 | 3.7% | 254.6 | 4.3% | 190.0 | 3.6% | | | |
| 802.4184 | $(M+2H)^+-C_2H_5[I]$ | 15.3 | 0.3% | 12.8 | 0.2% | 12.5 | 0.2% | | | |
| 785.3918 | $(M+2H)^+-C_2H_5[I]-NH_3$ | 52.5 | 1.0% | 52.7 | 0.9% | 46.1 | 0.9% | | | |
| 716.3517 | $(M+2H)^+-C_2H_5N_3[[L] \& R]$ | 77.1 | 1.4% | 97.0 | 1.6% | 93.8 | 1.8% | | | |
| 770.4224 | $(M+2H)^+-CONH_2[N]-NH_3$ | 60.2 | 1.1% | 70.5 | 1.2% | 39.5 | 0.7% | | | |
| 753.4243 | $(M+2H)^+-C_2H_5S[M]-NH_3$ | 130.7 | 2.4% | 163.0 | 2.7% | 104.6 | 2.0% | | | |
| 711.4025 | $(M+2H)^+-C_2H_5N_3S[M \& R]$ | 15.9 | 0.3% | 15.8 | 0.3% | 15.5 | 0.3% | | | |
| 788.4088 | $(M+2H)^+-C_2H_5[L]$ | 50.0 | 0.9% | 63.1 | 1.1% | 61.4 | 1.2% | | | |
| 730.3673 | $(M+2H)^+-C_4H_{11}N_3[R]$ | 29.0 | 0.5% | 37.9 | 0.6% | 36.9 | 0.7% | | | |
| 772.4143 | $(M+2H)^+-CH_3N_3[R]$ | 78.7 | 1.4% | 100.7 | 1.7% | 89.2 | 1.7% | | | |
| 406.7260 | $[(M+2H)-H_2O]^{2+}$ | 185.9 | 3.4% | 4.7 | 0.1% | 221.1 | 4.1% | | | |
| 814.4360 | $(M+2H)^+-NH_3$ | 164.2 | 3.0% | 224.5 | 3.8% | 218.5 | 4.1% | | | |
| 228.1343 | b_7^+ | 29.7 | 0.5% | | | 39.0 | 0.7% | 42.5 | 0.5% | MD |
| 297.1557 | $b_5^+-H_2O$ | 8.1 | 0.1% | | | 11.3 | 0.2% | | | EED |
| 446.2068 | b_4^+ | 11.0 | 0.2% | 11.8 | 0.2% | 15.0 | 0.3% | | | ECD |
| 559.2908 | b_5^+ | 14.0 | 0.3% | 12.4 | 0.2% | 13.6 | 0.3% | | | ECD |
| 541.2803 | $b_5^+-H_2O$ | 14.5 | 0.3% | | | 15.2 | 0.3% | | | EED |
| 175.1190 | y_1^+ | 7.3 | 0.1% | | | 9.8 | 0.2% | 5.3 | 0.1% | MD |
| 272.1717 | y_2^+ | 17.9 | 0.3% | | | 21.3 | 0.4% | 19.0 | 0.2% | MD |
| 385.2558 | y_3^+ | 22.2 | 0.4% | 6.6 | 0.1% | 27.8 | 0.5% | 25.7 | 0.3% | MD |
| 516.2963 | y_4^+ | 29.7 | 0.5% | 21.6 | 0.4% | 37.1 | 0.7% | 36.7 | 0.4% | MD |
| 603.3283 | y_5^+ | 44.7 | 0.8% | 9.2 | 0.2% | 55.4 | 1.0% | 58.4 | 0.7% | MD |
| 585.3177 | $y_5^+-H_2O$ | 31.6 | 0.6% | 8.3 | 0.1% | 41.1 | 0.8% | 43.3 | 0.5% | MD |
| 717.3712 | y_6^+ | 31.3 | 0.6% | 41.8 | 0.7% | 41.1 | 0.8% | | | ECD |
| 673.3702 | c_6^+ | 13.6 | 0.2% | 18.8 | 0.3% | 13.3 | 0.2% | | | |
| 159.1002 | z_1^{2+} | 11.9 | 0.2% | 5.6 | 0.1% | 12.2 | 0.2% | | | |
| 160.1081 | $z_1^{2+}+H$ | 106.0 | 1.9% | 128.8 | 2.2% | 49.9 | 0.9% | | | |
| 369.2371 | z_5^{2+} | 55.1 | 1.0% | 72.2 | 1.2% | 64.0 | 1.2% | | | |
| 587.3096 | z_5^{2+} | 36.3 | 0.7% | 49.5 | 0.8% | 40.4 | 0.8% | | | |
| 701.3525 | z_6^{2+} | 25.2 | 0.5% | 34.8 | 0.6% | 31.4 | 0.6% | | | |
| 326.1823 | $z_5^{2+}-C_2H_7[L]$ | 56.0 | 1.0% | 46.2 | 0.8% | 59.6 | 1.1% | | | |
| 457.2227 | $z_4^{2+}-C_2H_7[L]$ | 20.1 | 0.4% | 15.4 | 0.3% | 20.1 | 0.4% | | | |
| 313.1745 | $z_5^{2+}-C_4H_8[L]$ | 14.7 | 0.3% | 16.2 | 0.3% | 15.5 | 0.3% | | | |
| 444.2149 | $z_4^{2+}-C_4H_8[L]$ | 99.9 | 1.8% | 118.9 | 2.0% | 111.9 | 2.1% | | | |
| 531.2470 | $z_5^{2+}-C_4H_8[L]$ | 103.0 | 1.9% | 134.1 | 2.3% | 117.1 | 2.2% | | | |
| 645.2899 | $z_6^{2+}-C_4H_8[L]$ | 53.2 | 1.0% | 71.8 | 1.2% | 63.2 | 1.2% | | | |
| 439.2658 | $z_4^{2+}-C_2H_5S[M]$ | 76.2 | 1.4% | 59.3 | 1.0% | 76.9 | 1.4% | | | |
| 526.2979 | $z_5^{2+}-C_2H_5S[M]$ | 103.8 | 1.9% | 117.2 | 2.0% | 114.7 | 2.1% | | | |
| 640.3408 | $z_6^{2+}-C_2H_5S[M]$ | 75.6 | 1.4% | 92.0 | 1.5% | 85.0 | 1.6% | | | |
| 627.3335 | $z_6^{2+}-C_3H_6S[M]$ | 7.7 | 0.1% | 10.6 | 0.2% | 9.4 | 0.2% | | | |
| 657.3389 | $z_6^{2+}-CONH_2[N]$ | 6.5 | 0.1% | | | | | | | |
| 571.2908 | $z_6^{2+}-C_4O_2N_2H_7[N \& S]$ | 15.1 | 0.3% | 17.1 | 0.3% | 14.7 | 0.3% | | | |
| 684.3260 | $z_6^{2+}-NH_3$ | 34.6 | 0.6% | 40.5 | 0.7% | 34.5 | 0.6% | | | |
| 816.4457 | $(z_6^{2+}+L)-C_2H_5S[M]$ | 28.1 | 0.5% | 39.6 | 0.7% | | | | | |
| 803.4384 | $(z_6^{2+}+L)-C_3H_6S[M]$ | 8.6 | 0.2% | 7.3 | 0.1% | 7.1 | 0.1% | | | |
| 832.4485 | b_6^++L | 64.2 | 1.2% | 28.3 | 0.5% | | | | | |
| 611.2970 | $x_5^+-H-H_2O$ | 65.3 | 1.2% | 77.9 | 1.3% | 57.5 | 1.1% | | | |

MD = Metastable Dissociation, ECD = Electron Capture Dissociation and EED = Electron Excitation Dissociation



Scheme 4. 5 Dissociation channels of $[L+(M+2H)]^{2+}$ under ECD conditions

generated from the secondary fragmentation of *c* ions. A possible mechanism for the formation of *b* ions was believed to be the generation of non-radical charge-reduced cation ($[M+nH]^{n+}$), which dissociated subsequently through typical peptide bond cleavage pathway [149, 150]. In the experiments performed by Uggerud and co-workers [151], the formation of *b* ions were speculated to be the result of the existence of nitrogen-protonated peptide conformers.

4.3.3.3 Comparison of ECD dissociation patterns between $[L+(M+2H)]^{2+}$ and $[M+2H]^{2+}$

In order to investigate the effect that ligand and the chain lengths of peptides would have on the ECD dissociation patterns of peptides, several truncated peptides together with their corresponding ligand-bound peptides were used in this study. Table 4.5 summarizes the relative abundance of $[M+H]^+$, $[M+2H]^{2+}$ and $[(M+2H)-NH_3]^+$; the branching ratio of $[M+2H]^{2+}/[M+H]^+$; the sum of *z'* ions; and the various side chain loss from *z'* ions and $[M+2H]^{2+}$. The branching ratios of $[M+2H]^{2+}/[M+H]^+$ in ECD of $[L+(M+2H)]^{2+}$ were seen to be generally much higher than the ratio of $[M+2H]^{2+}$, implying that $[M+2H]^{2+}$ yielded in the dissociation of $[L+(M+2H)]^{2+}$ was more abundant. These observations were in agreement with the experimental results of Chakraborty and co-workers [152], who proposed that unsolvated ions would favour H^+ loss from charge-reduced precursor ions ($[M+2H]^{2+}$) and that ammonia loss from highly solvated ions was a competitive process in ECD [153]. They were also congruent with the findings of Williams and co-workers, who observed a change in peptide conformation that altered the dissociation pattern after using water or methanol molecules to act as a 'cage' to solvate the peptide ions. It is believed that similar phenomena would happen when the water or methanol molecules are changed to 12-crown-4.

Table 4.5 Relative abundance and sum of fragment ions related to $[M+2H]^{2+}$ and z^{**} in ECD of $[L+(M+2H)]^{2+}$ and $[M+2H]^{2+}$, where L is 12-crown-4. (%)

| Peptide | Relative abundance (%) | | Branching ratio | Sum of fragment ions (%) | |
|--------------------------------------------|------------------------|---------------|-----------------|--------------------------|----------------------|
| | $[M+H]^+$ | $[M+2H]^{2+}$ | | $[M+2H]^{2+}/[M+H]^+$ | $[M+2H]^{2+} - SC^a$ |
| <i>ECD of $[L+(M+2H)]^{2+}$</i> | | | | | |
| INSMLPR | 5.0 | 4.5 | 0.9 | 16.6 | 5.0 |
| ENSMLPR | 5.5 | 3.7 | 0.7 | 22.1 | 2.5 |
| NSMLPR | 30.5 | 18.6 | 0.6 | 21.8 | 3.1 |
| SMLPR | 70.9 | 34.9 | 0.5 | 16.3 | 2.6 |
| <i>ECD of $[M+2H]^{2+}$</i> | | | | | |
| INSMLPR | 3.1 | 1.0 | 0.3 | 6.4 | 2.3 |
| ENSMLPR | 5.1 | 2.1 | 0.4 | 16.8 | 1.6 |
| NSMLPR | 3.4 | 1.0 | 0.3 | 8.6 | 0.5 |
| SMLPR | 16.4 | 1.3 | 0.1 | 2.4 | 0.4 |

^a SC indicates odd- or even-electron side chains

Apart from the more abundance of $[M+2H]^+$, the intensities of side chain loss from $[M+2H]^+$ in the dissociation of $[L+(M+2H)]^{2+}$ were also higher than those of $[M+2H]^{2+}$ as shown in Table 4.5. It is thus speculated that the higher intensity of $[M+2H]^+$ in the dissociation of $[L+(M+2H)]^{2+}$ led to more abundant side chain loss from $[M+2H]^+$.

Besides $[M+2H]^+$ related ions, z' ions were the major ECD fragments generated in the experiments under this study. As Table 4.5 shows, both the sum of the relative intensities of z' ions and side chain loss from z' ions generated from ECD of $[L+(M+2H)]^{2+}$ were generally greater than those from $[M+2H]^{2+}$. This higher stability of $[M+2H]^+$ and z' ions is presumably attributable to the elimination of ligand, which took away with it a portion of the ion-electron recombination energy. This led to a reduction of the internal energies of z' ions and $[M+2H]^+$ and hence reduced the subsequent loss of side chain and H' from the z' ions and $[M+2H]^+$ respectively. This assumption is in agreement with literature calculation results which suggested that the ion-electron recombination energies of crown ether-diammonium alkane ions were lower than those of its respective free diaminoalkane cations [154].

The sum of the relative intensities of side chain loss from z' ions, the ratio of odd- and even-electron side chain(s) of methionine (M), and the loss of leucine (L) from $[M+2H]^+$ and z' ions in ECD of $[L+(M+2H)]^{2+}$ and $[M+2H]^{2+}$ were analyzed and the results summarized in Table 4.6. It suggests that the presence of ligand reduced the probability of losing odd-electron M and L side chain(s) from z' ions. However, as the relative intensities of even-electron L side chain loss from both $[M+2H]^+$ and z_n^+ in ECD of $[L+(M+2H)]^{2+}$ were remarkably higher than those in

Table 4.6 Relative abundance of odd- and even-electron M and L side chain (s) loss from $[M+2H]^+$ and z_n^{**} in ECD of $[L+(M+2H)]^{2+}$ and $[M+2H]^{2+}$, where L is 12-crown-4. (%)

| | ECD of $[L+(M+2H)]^{2+}$ | | | | ECD of $[M+2H]^{2+}$ | | | |
|--------------------------------------|--------------------------|---------------|----------------|--------------|----------------------|---------------|----------------|--------------|
| | $C_2H_5S^+$ [M'] | C_3H_6S [M] | $C_3H_7^+$ [L] | C_4H_8 [L] | $C_2H_5S^+$ [M'] | C_3H_6S [M] | $C_3H_7^+$ [L] | C_4H_8 [L] |
| <i>From $[M+2H]^{2+}$</i> | | | | | | | | |
| INSMLPR | 2.7% | 0.0% | 0.9% | 1.4% | 2.5% | 0.0% | 1.4% | 1.3% |
| ENSMMLPR | 3.5% | 2.1% | 0.8% | 3.0% | 2.7% | 0.0% | 3.5% | 0.0% |
| NSMLPR | 6.4% | 0.0% | 0.0% | 7.2% | 7.2% | 3.7% | 0.0% | 2.7% |
| SMLPR | 6.2% | 0.0% | 1.0% | 1.5% | 2.1% | 0.0% | 0.0% | 0.0% |
| <i>From z_n^{**}</i> | | | | | | | | |
| INSMLPR | 4.7% | 0.1% | 1.4% | 5.0% | 9.7% | 0.0% | 4.3% | 2.6% |
| ENSMMLPR | 3.6% | 0.0% | 1.0% | 3.0% | 9.6% | 0.0% | 4.5% | 1.4% |
| NSMLPR | 5.0% | 0.0% | 2.3% | 1.7% | 11.4% | 0.0% | 8.6% | 0.0% |
| SMLPR | 4.1% | 0.0% | 4.8% | 0.6% | 7.8% | 0.0% | 0.6% | 3.4% |

^a The value is equal to the relative abundance of even-electron side chain loss since no odd-electron side chain was lost from the corresponding ions.

$[M+2H]^{2+}$, it implies that the addition of ligand caused a change in the energy of the dissociation pathway and resulted in the enhancement of even-electron L side chain loss reaction. According to literature calculation results [117], the loss of even-electron L side chain from z_n^{+} creates a relatively low activation barrier for certain peptide conformation. It could thus be presumed that the high intensity of even-electron L side chain loss from $[M+2H]^{2+}$ and z_n^{+} observed in this study was due to the conformation of the peptides.

4.3.3.4 ECD fragmentation efficiency of $[L+(M+2H)]^{2+}$ and $[M+2H]^{2+}$

The ECD fragmentation efficiency ($ECD_{frag-eff}$) of doubly-charged precursor ions of standard peptide in FTICR was investigated [71, 155]. The equations derived from these experiments were compared and re-defined via equation 4.1 below:

$$ECD_{frag-eff} = \frac{\sum I_{\{ECD_{fragmentions}\}}}{\left[\left(I_{\{PrecursorIonIsolation\}} / 2\right) + \left(I_{\{PrecursorIonDelay\}} / 2\right)\right] / 2} \times 100\% \quad [4.1]$$

$\sum I_{\{ECD_{fragmentions}\}}$ represents the sum of the intensities of ECD fragments which include typical c/z' ions, side chain loss from z' ions and $[M+2H]^{2+}$. $I_{\{PrecursorIonIsolation\}}$ and $I_{\{PrecursorIonDelay\}}$ are the precursor ion intensities after isolation prior to electron irradiation and after delay (the consequence of long storage time or kinetic excitation (*vide infra*) has been taken into account). The equation assumes that the peak height in mass spectra is proportional to the charge state of the ions and therefore the signal intensities of the precursor ions in isolation and delay should be divided by two. The denominator in the equation takes the average of precursor ion intensities both after isolation and delay, the reason being that underestimation would happen if only the precursor ion after isolation is used, and conversely, overestimation could result if only the precursor ion after delay is used.

Figure 4.11 summarizes the calculated ECD fragmentation efficiency values of $[L+(M+2H)]^{2+}$ and $[M+2H]^{2+}$, where L is 12-crown-4. In order to investigate the reproducibility of the results, the ECD experiments of $[INSMLPR+2H]^{2+}$ were performed thrice. The average value of ECD fragmentation efficiency was calculated to be 20.68% with a standard deviation of 2.02%. Given this relatively small deviation, the trend obtained from the experiments was considered to be valid.

As indicated by the trend of ECD fragmentation efficiency of $[M+2H]^{2+}$ in Figure 4.11, the $ECD_{\text{frag-eff}}$ of $[M+2H]^{2+}$ decreased with a reduction in the peptide chain length while the $ECD_{\text{frag-eff}}$ of INSMLPR was lower than that of ENSMLPR (as a result of the more abundant glutamate (E) side chain loss from $[M+2H]^{2+}$ and z' ions in ENSMLPR when compared to isoleucine (I) side chain loss reactions in INSMLPR). As the charge-charge repulsion existing in peptide ions increased with decreased peptide chain length, the $ECD_{\text{frag-eff}}$ of NSMLPR and SMLPR were lower than that of INSMLPR and ENSMLPR.

Figure 4.11 also shows that the trend of $ECD_{\text{frag-eff}}$ of $[L+(M+2H)]^{2+}$ was slightly different from that of $[M+2H]^{2+}$. In general, the addition of ligand to peptide would lower the $ECD_{\text{frag-eff}}$ of $[L+(M+2H)]^{2+}$ (when compared to their corresponding $[M+2H]^{2+}$). Since the elimination of ligand in the former case (i.e. ECD of $[L+(M+2H)]^{2+}$) removed a portion of the ion-electron recombination energy, fewer fragments were produced and the $ECD_{\text{frag-eff}}$ therefore decreased. However, the $ECD_{\text{frag-eff}}$ of $[(12\text{-crown-4})+INSMLPR+2H]^{2+}$ was found to be unexpectedly high with the presence of ligand. This is tentatively attributable to the change in the hydrogen bonding pattern of the peptide ion.

4.3.3.5 Comparison between ECD and ECID

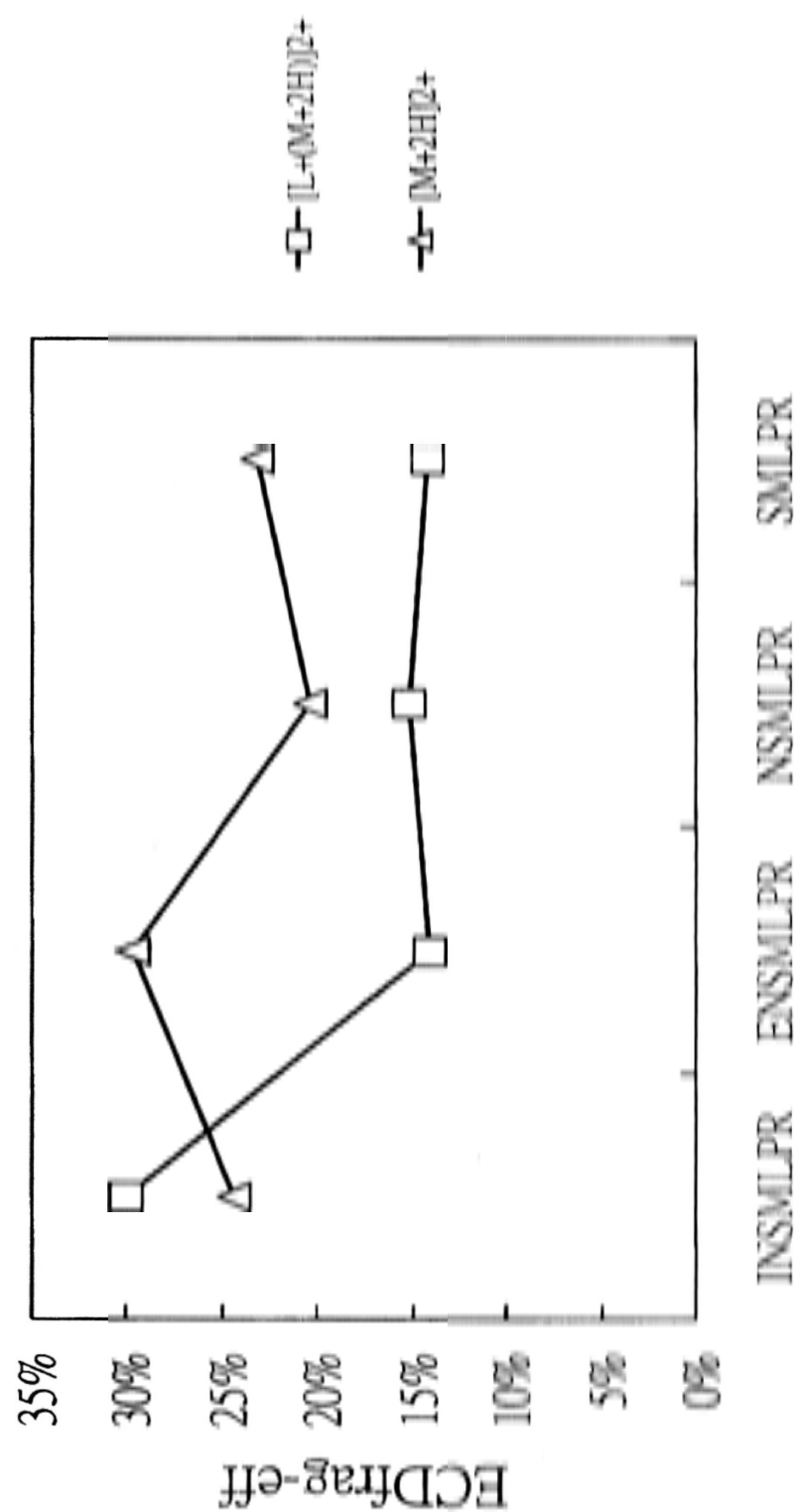


Figure 4. 11 The calculated ECD fragmentation efficiency values of $[L+(M+2H)]^{2+}$ and $[M+2H]^{2+}$, where L is 12-crown-4.

Electron capture induced dissociation (ECID) was developed to mimic ECD in a sector beam mass spectrometer [156, 157]. Holm et al. [154] who conducted a comparative study on ECD and ECID experiments found that crown ether ligand had a substantial effect on the recombination energy of the ammonium cation and contributed to their different ECD and ECID dissociation patterns. In the ECID experiments done by Bernigauda et al. [158], it was found that backbone cleavages happened with equal probabilities in ECD and ECID.

The ECD results of $[L+(M+2H)]^{2+}$ obtained in this study were compared with the ECID of $M^{2+}(CE)$ (M is dipeptide, AK, and CE is crown ether) data obtained by Bernigauda et al. [158]. The dissociation patterns observed in both experiments were rather similar since the major fragments obtained in both studies were $N-C_{\alpha}$ bond cleavages (producing c and z' ions as well as H' and leading to NH_3 loss from $[M+2H]^{+}$). However, there were two notable differences: first, ligand retention was found only in $[M+2H]^{+}$ and z' ions in ECID but not in ECD experiments; second, secondary dissociation of $[M+2H]^{+}$ and z' ions was only observed in ECD experiments. These findings could possibly account for the different electron energies and time scales in the two dissociation processes as discussed by Holm et al. [154].

4.4 Conclusion

The dissociation channels of $[Cu(Tpy)M]^{2+}$ of peptides, both with and without PTM groups (oxidized methionine and phosphorylated serine), have been examined in detail. It is found that the dissociation patterns of the copper ternary complex would change with the presence of modified groups, which may probably affect the binding mode of peptide and copper-ligand. In MS^2 , the PTM group cleave

preferentially in $[\text{Cu}(\text{Tpy})\text{M}]^{2+}$; whereas in MS^3 , odd- or even-electron side chain loss from $\text{M}^{+\bullet}$ is the dominant dissociation pathway for all peptides. Given that structural information provided by MS^3 is also obtainable from MS^2 , the latter excels the former in providing structural information on the binding mode of peptide and copper-ligand.

The comparative study related to SORI-CID of $[\text{M}+\text{H}]^+$, SORI-CID of $\text{M}^{+\bullet}$ and ECD of $[\text{M}+2\text{H}]^{2+}$ indicates that SORI-CID of $[\text{M}+\text{H}]^+$ would preferentially cleave the modified groups when compared to backbone cleavage. It also reveals that SORI-CID of $\text{M}^{+\bullet}$ would lead to abundant side chain loss with the PTM group preserved in peptide backbone under ECD conditions. A further observation is that oxidized methionine and phosphorylated serine side chains (CH_3SOH and H_3PO_4) would be lost from the precursor ions ($[\text{M}+\text{H}]^+$, $[\text{Cu}(\text{Tpy})\text{M}]^{2+}$) in SORI-CID, whereas only specific odd- and even-electron side chains would be lost from the heteroatom radical fragment ions ($\text{M}^{+\bullet}$, $\text{z}^{+\bullet}$ and $[(\text{M}+2\text{H})-\text{NH}_3]^{+\bullet}$) generated during SORI-CID of $[\text{Cu}(\text{Tpy})\text{M}]^{2+}$ and ECD of $[\text{M}+2\text{H}]^{2+}$. It is believed that the preferential cleavage of the PTM groups in SORI-CID of $\text{M}^{+\bullet}$ is related to the property of the hydrogen-deficient heteroatom radical, while the preservation of PTM groups in the dissociation of hydrogen-surplus radical ($[\text{M}+2\text{H}]^{+\bullet}$) under ECD conditions is attributable to the involvement of H^\bullet which induces backbone cleavages.

As revealed by the study on SORI-CID of $[\text{Cu}(\text{Tpy})\text{M}]^{2+}$ (where M is linear or branch oligosaccharides), oligosaccharide would be ionized as high abundance of $[\text{Cu}(\text{Tpy})]^+$ was observed in the experimental results. However, since no $\text{M}^{+\bullet}$ was found, there is an implication that other than the ionization potential (IP) of oligosaccharide, its stability is also an important factor governing the generation of

radical cations in the dissociation of $[\text{Cu}(\text{Tpy})\text{M}]^{2+}$. Had weak bond(s) been present, $\text{M}^{+\bullet}$ would have undergone further dissociation to generate biomolecule fragments (i.e. glycosidic fragments). Although no SORI-CID of $\text{M}^{+\bullet}$ could be performed, sequence information on oligosaccharides could still be obtained from SORI-CID of $[\text{Cu}(\text{Tpy})\text{M}]^{2+}$, in which a series of glycosidic fragments would be observed.

The study related to SORI-CID of $[\text{Cu}+\text{M}]^{2+}$ and ECD of $[\text{Cu}+\text{M}]^{2+}$ shows that the dissociation patterns of these complexes are rather similar in both linear and branch oligosaccharides (except ECD of branch oligosaccharide). This is tentatively attributable to the coordination of the copper center with the branch oligosaccharide. The study also sheds light on the proposition that the dissociation patterns in SORI-CID of $[\text{Cu}(\text{Tpy})\text{M}]^{2+}$ and $[\text{Cu}+\text{M}]^{2+}$ are significantly different due to the effect of ligand. The ligand present in SORI-CID of $[\text{Cu}(\text{Tpy})\text{M}]^{2+}$ would lower the coordination number between the copper center and oligosaccharide as well as the polarizing ability of the copper ion; as a result, cross-ring cleavages would be reduced, thereby favouring the formation of doubly-charged copper-terpyridine adducted glycosidic fragments.

From the investigation concerning the dissociation patterns and fragmentation efficiencies of (12-crown-4)-peptide complexes under typical ECD conditions, it is noted that the non-covalent interaction between 12-crown-4 and peptide is weak (as no retention of ligand was found in most of the fragment ions produced in the experiments).

Following the cross-comparisons made on the dissociation results of $[\text{L}+(\text{M}+2\text{H})]^{2+}$ and $[\text{M}+2\text{H}]^{2+}$, it is proposed that ligand could alter the dissociation patterns in ECD of $[\text{L}+(\text{M}+2\text{H})]^{2+}$. When ligand is present, the intensities of z' ions and the branching ratio of $[\text{M}+2\text{H}]^{+\bullet}/[\text{M}+\text{H}]^+$ would be higher than those of

$[M+2H]^{2+}$. A postulation is that elimination of ligand from $[L+(M+2H)]^{2+}$ would drain off a portion of the ion-electron recombination energy, thereby reducing subsequent loss of side chain and H^+ from z' ions and $[M+2H]^+$ respectively. It is also believed that ligand would affect the conformation of peptide ions and favour certain dissociation channels such as even-electron L side chain loss reactions.

Chapter 5

Natural Structural Motifs that Suppress Peptide Ion Fragmentation after Electron Capture

5.1 Introduction

ECD involves the reaction between multiply-charged ions and low-energy electrons. Besides the formation of charge-reduced precursor ions, $[M+nH]^{(n-1)+}$, the recombination energy released is strong enough to cause backbone N-C $_{\alpha}$ cleavages, producing a series of *c* or *z'* ions and, to a lesser extent, a series of *a'* or *y* ions. Other ECD events include the elimination of an H $^{\bullet}$ to form $[M+(n-1)H]^{(n-1)+}$ and the loss of amino acid side chains from *z'* ions and/or $[M+nH]^{(n-1)+}$. Cleavages in ECD are non-specific [64] and the relative propensities for dissociation of various amino acid residues have been found to fall within a narrow range. Because of the ring-type structure, only the fragment ions resulting from backbone cleavages at the N-terminal side of proline (P) are suppressed [65].

The importance of radical in the charge-reduced precursor ion in ECD was investigated by a number of researchers who incorporated synthetically single and multiple radical trap, spin trap and charge tag moieties in model peptides. In his radical trap experiments, Belyayev et al. [159] attached coumarin labels onto the N-terminal amino group (or/and lysine side chain) and demonstrated that the presence of a radical trap in a peptide ion could inhibit backbone fragmentation under typical ECD conditions. Jones and co-workers had similar observations when using 2-(4'-carboxypyrid-2'-yl)-4-carboxamide group (pepy) [160] as the spin trap label. In fixed charge experiments, Li et al. attached 2,4,6-trimethylpyridinium (TMP)

[161] to the N-terminal amino group (or/and lysine side chain) of some model peptides and found that the usual backbone cleavage fragments were suppressed and some label-related neutral side chains were lost from the reduced precursor ions. Chamot-Rooke and co-workers obtained similar results by using tris-(2,4,6-trimethoxyphenyl)-phosphonium-methylenecarboxamido (TMPP-ac) groups [162] as the fixed charge carriers.

It has also been confirmed that ECD of linear peptide and cyclic peptide at a low temperature (e.g. 86K) would dramatically reduce the number of backbone fragments [163]. Researchers concerned attributed the reduction of backbone fragments to the decrease in number of conformers at a low temperature. Hongo et al. found that backbone cleavages were suppressed in ECD of triantennary complex-type N-glycosylated peptides [164]. This suppression of backbone cleavages was due tentatively to the presence of carbamoylmethylated cysteine, which might serve as a 'radical trap', in the peptide. Glycopeptides with both cysteine residue and NeuNAc were also found to induce very few or no backbone fragments.

More recently, Sohn and co-workers [165] investigated the ECD behaviour of electron affinity tuned peptides and have demonstrated that typical ECD or ETD backbone fragmentations could be completely inhibited in peptides with substituent tags having EA over 1.00 eV.

To ensure proper spectral interpretation and further improve the analytical utilities of ECD methods, it is important to identify factors that influence the dissociation efficiency and pathways of peptide ions, including especially the role of radical in a charge-reduced precursor ion during its dissociation. This study aims to provide evidence to show that certain natural structural motifs in proteins could

inhibit backbone fragmentation of charge-reduced peptide ions under ECD conditions. Coupled with conformational search, a hypothesis based on the interaction between carboxylic oxygen of E side chain (or N) and backbone amide hydrogen was used to account for the extra-stability of charge-reduced precursor ions. Both Glutamic acid (E) and asparagine (N) residues were used because fibrinopeptide-B, a bioactive peptide, has been found to be an analogue system for demonstrating the generalization of the suppression effect. It is believed that similar observations would be obtained by using aspartic acid (D) and glutamine (Q).

5.2 Experimental section

A series of model peptides with sequence of RGE GEGEGEGEGEGEGR, RGE GEGEGGGEGEGEGR, RGGEGGGEGGGEGGGR, RGGGGEGGGEGGGGR, RGE GNGEGEGNGEGR and RGE GNGGGNGGEGEGR were purchased from Pepton Inc., (Daejeon, South Korea) and used without further purification. Fibrinopeptide-B (EGVNDNEEGFFSAR) and its analogue, i.e. REGVNDNEEGFFSA and REGVNDNEEGFFSAR, were synthesized in-house using Personal Synthesizer (Peti-Syzer[®] Model PSS-510, HiPep Laboratories, Kyoto, Japan) and used without further purification. Standard Fmoc synthesis procedures were employed [131, 132]. All reagents used for peptide synthesis were obtained from Sigma and Aldrich (St. Louis, MO, USA), LC Science (Houston, TX, USA) and Advanced ChemTech (CreoSalus Inc., Louisville, KY, USA). All samples were prepared at a concentration of 2.5×10^{-5} M in 1:1 water:methanol (Labscan Ltd., Bangkok, Thailand) with 3-5% acetic acid (Riedel-de Haen, Seelze, Germany).

All experiments were conducted by using a 4.7 Tesla Fourier transform ion cyclotron resonance mass spectrometer (FTICR-MS) (APEX I, Bruker Instrument

Inc., Boston, MA), a computer system and associated electronics which were upgraded to APEX III. Please see Chapter 2 for detailed instrumental arrangements and sample preparation procedures.

In ECD experiments, a standard electrically-heated filament source was used to produce pulses of electron beam. Typical experimental conditions were 3.2 A filament heating current, 4.5 V average filament bias voltage and 300 ms electron irradiation time. 30 scans were summed to improve the signal-to-noise ratio. All ECD mass spectra were acquired in broadband mode using 128k data points and they were zero-filled twice prior to Fourier transformation.

For the low-energy structures of RGEGEGEGEGEGEGR examined, calculations were performed via MacroModel program. For calculations, please refer to Chapter 2.

5.3 Results and Discussion

5.3.1 General features of ECD spectra of doubly protonated peptides

Figure 5.1 shows the typical ECD spectra of doubly-protonated diarginated peptides, $[M+2H]^{2+}$, with sequence of RGGGGEGGGEGGGGR, RGEGGEGGGEGGEGEGR and RGEGEGEGEGEGEGEGR, respectively. Typical ECD induced fragments, i.e. c_4^+ to c_{14}^+ , z_8^{+*} to z_{14}^{+*} , and peaks corresponding to charge-reduced precursor ion ($[M+2H]^+$) were observed. Attributable to the low stability of odd-electron species, the z^* ions were generally weaker in intensities than c_n^+ [70], the even-electron species. Besides the usual c and z^* ions, $[c-H]^+$ and $[z+H]^+$ species and cleavage products related to the loss of NH_3 , CO, side chain of glutamic acid (E) and/or arginine (R) from the reduced precursor ions, $[M+2H]^+$, were also observed in the ECD spectra. Moreover, both the number and the intensities of c and

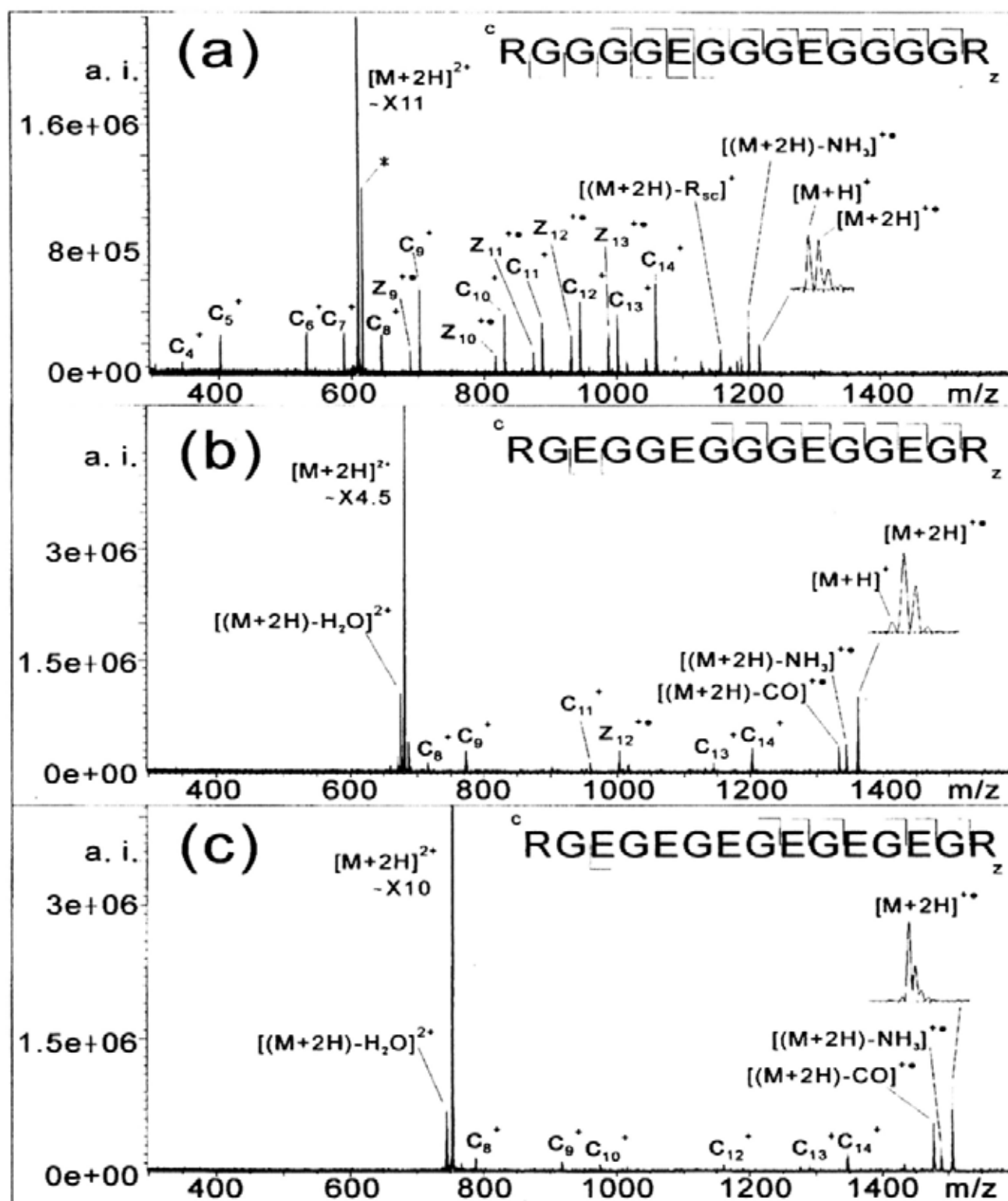


Figure 5.1 Typical ECD spectra of $[M+2H]^{2+}$, where M is (a) RGGGGEGGGEGGGGR, (b) RGEGGGEGGGEGGGR and (c) RGEGEGEGEGER.

z' ions were found to decrease progressively as the number of E residues increased. In addition, hydrogen radical (H^\bullet) loss from $[M+2H]^{2+}$ was found to decrease dramatically with increasing number of E in the diarginated model peptides.

Compared to Figure 5.1 (a) and (b), the high abundance of $[M+2H]^{2+}$ shown in Figure 5.1 (c) was evidence of a successful electron capture event and suppression of backbone cleavages. Figure 5.2 (a) shows the percentages of H^\bullet loss from $[M+2H]^{2+}$ of the diarginated model peptides examined. (Calculation concerned has taken into account the isotopic contribution of the charge-reduced precursor ions. Measurement of error was obtained by three replicate experiments of RGEGNGEGEGNGEGR and the error of percentage of H^\bullet loss from $[M+2H]^{2+}$ was found to be $\pm 0.6\%$. Since the error was significantly smaller than the differences between data points, no further estimations of measurement of error were performed on other samples.) Substantial loss of H^\bullet from $[M+2H]^{2+}$ was observed when the E to R ratio in peptide equaled to 1:1. However, the percentage of H^\bullet loss decreased progressively from 73% to 0% when the E to R ratio increased from 1:1 to 3:1. The fact that no $[M+H]^+$ was observed in ECD of doubly-protonated peptide with 6E implies no H^\bullet was lost from the charge-reduced precursor ions. Since the extent of H^\bullet loss from the reduced precursor ions was lower in the cases of 6E and 4E than the corresponding (4E+2N) and (2E+2N) cases, the impact of E on the suppression of cleavage could be said to be greater than that of N.

Apart from the H^\bullet loss from $[M+2H]^{2+}$, the number and the intensities of backbone fragments were found to decrease as the number of E residues increased. In order to investigate the suppression effect of backbone cleavages on the doubly-charged precursor ions of diarginated model peptides, the probability for dissociation in ECD (ECD_{Pro_Disso}) of these peptides was calculated by equation 5.1

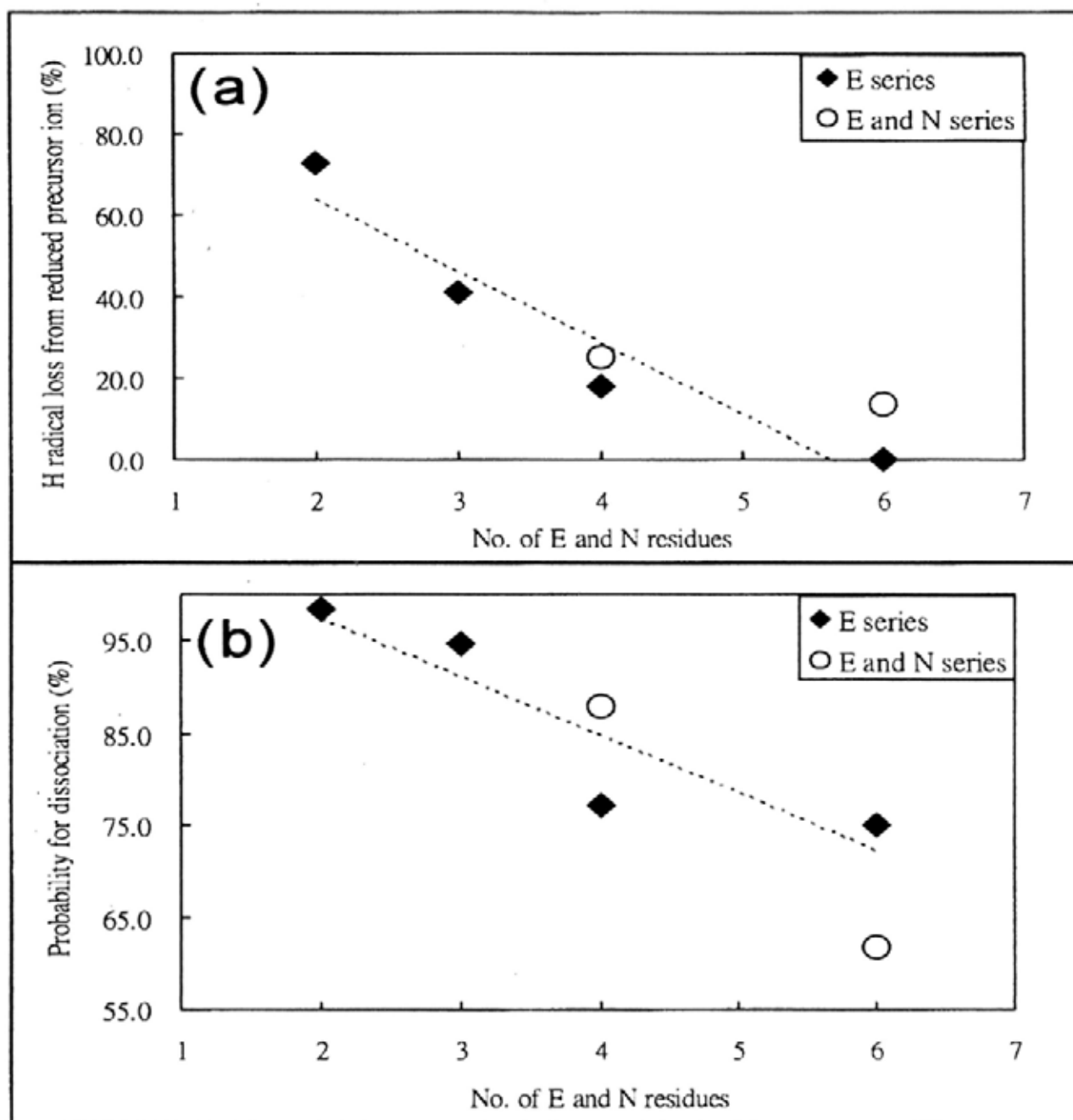


Figure 5.2 (a) Percentage loss of H[•] loss from [M+2H]⁺⁺ of diarginated model peptides and (b) Probability for dissociation in ECD of diarginated model peptides

as follows:

$$ECD_{Pro_Disso} = \frac{\sum I_{[ECD_Fragments]}}{\sum I_{[ECD_Fragments]} + I_{[Reduced_Precursor_Ion]}} \times 100\% \quad [5.1]$$

$\sum I_{[ECD_Fragments]}$ represents the sum of the intensities of ECD induced fragments which includes typical *c* and *z'* ions, [c-H]⁺ and [z+H] ions, side chain loss from z_n^{+} and peaks related to [M+2H]²⁺. $I_{[Reduced_Precursor_Ion]}$ represents the reduced precursor ion intensity.

Figure 5.2 (b) summarizes the calculated ECD_{Pro_Disso} values of [M+2H]²⁺ of the diarginated model peptides. (In the three replicate measurements, the error of ECD_{Pro_Disso} of RGEGNGEGEGNGEGR was found to be $\pm 0.9\%$.) The probability for dissociation in ECD of [M+2H]²⁺ was found to decrease progressively as the number of E and N residues increased. As for the model peptides with 6E (or 4E + 2N) residues, a strong suppression of fragmentation was observed. This phenomenon is rather similar to the result of H⁺ loss from [M+2H]²⁺ as shown in Figure 5.2 (a).

5.3.2 Comparison between ECD of [M+2H]²⁺ and [M+3H]³⁺

Figure 5.3 shows the typical ECD spectra of triply-protonated model peptide ions, [M+3H]³⁺, with sequence of RGGGGEGGGEGGGGR, RGEGGGEGGGEGGEGR and RGEGEGEGEGEGEGR respectively. While typical ECD fragments (i.e. c_3^+ to c_{14}^+ , z_4^{+} to z_{14}^{+}), E side chain loss from *z*-ions and peaks corresponding to the charge-reduced precursor ions ([M+3H]²⁺) were observed in the spectra, there was no [c-H]⁺, [z+H] and double-electron reduced precursor ions ([M+3H]²⁺). In addition, some complementary *c* and *z'* ion pairs were detected, including c_5^+/z_{10}^{+} ; c_6^+/z_9^{+} ; c_7^+/z_8^{+} ; c_8^+/z_7^{+} and c_9^+/z_6^{+} . For peptides with higher

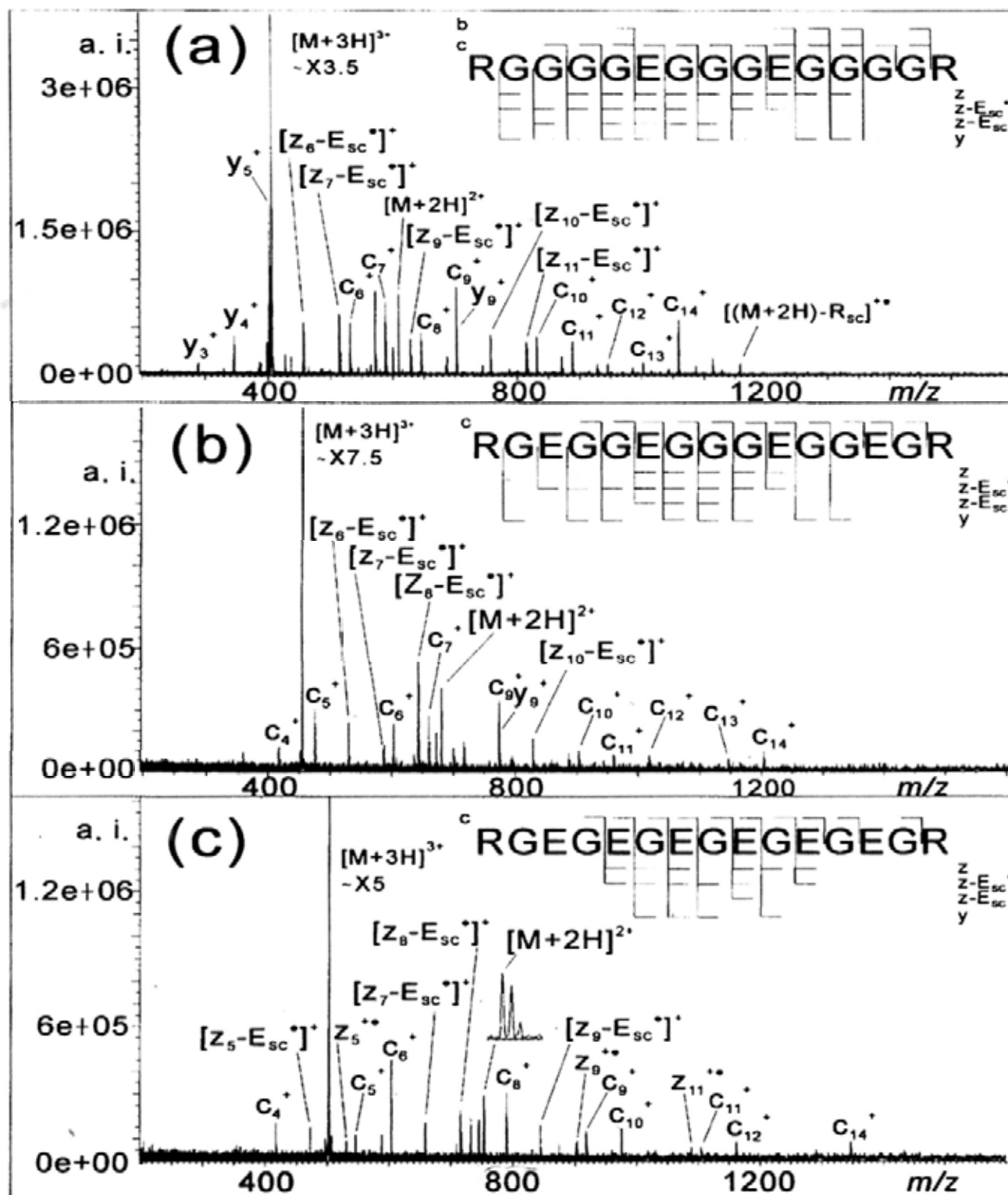


Figure 5.3 Typical ECD spectra of $[M+3H]^{3+}$, where M is (a) RGGGGEGGGEGGGGR, (b) RGEGGGEGGGEGGEGR and (c) RGEGEGEGEGER.

number of E residues, more peaks related to E side chain loss (both odd- or even-electron) from z' ions were observed. And other than typical ECD backbone fragments of c and z' ions, b and y ions produced by non-standard ECD channel(s) were observed. However, the extent of non-standard ECD cleavages was found to reduce as the number of E increased.

Unlike the doubly-protonated peptides (Figure 5.1), the extent of backbone cleavages in the corresponding triply-protonated peptides (Figure 5.3) was less dependent on the number of E residues. A comparison of Figure 5.1 (c) and Figure 5.3 (c) reveals that ECD of $[M+2H]^{2+}$ exhibited suppression of backbone fragments, whereas ECD of $[M+3H]^{3+}$ generated abundant backbone fragments. Besides suppression of backbone cleavages, the percentage of H⁺ loss from the reduced precursor ions of the doubly-protonated peptide ions was much lower than that in the triply-protonated diarginated E-rich peptide ions. Although the relative percentage of the loss of hydrogen atom from ECD of $[M+2H]^{2+}$ and $[M+3H]^{3+}$ was in line with the charge-state effect demonstrated by K. Breuker et al. [166] (who used 7+ to 13+ of ubiquitin ions), the charge-state effect could not be used to explain the concurrent suppression of backbone cleavages in the case of $[M+2H]^{2+}$. More experiments should be carried out to ascertain the origin(s) of these suppression effects.

5.3.3 Fibrinopeptide-B and its analogues

Suppression of backbone cleavages achieved by using the model peptides concerned was re-confirmed by analyzing the N-arginated Fibrinopeptide-B (i.e., REGVNDNEEGFFSAR). This peptide contains four acidic residues (i.e. 3E and 1D) and 2N residues. Figure 5.4 shows the ECD spectra of doubly- and triply-protonated N-arginated Fibrinopeptide-B molecules. ECD of $[M+2H]^{2+}$ species generated

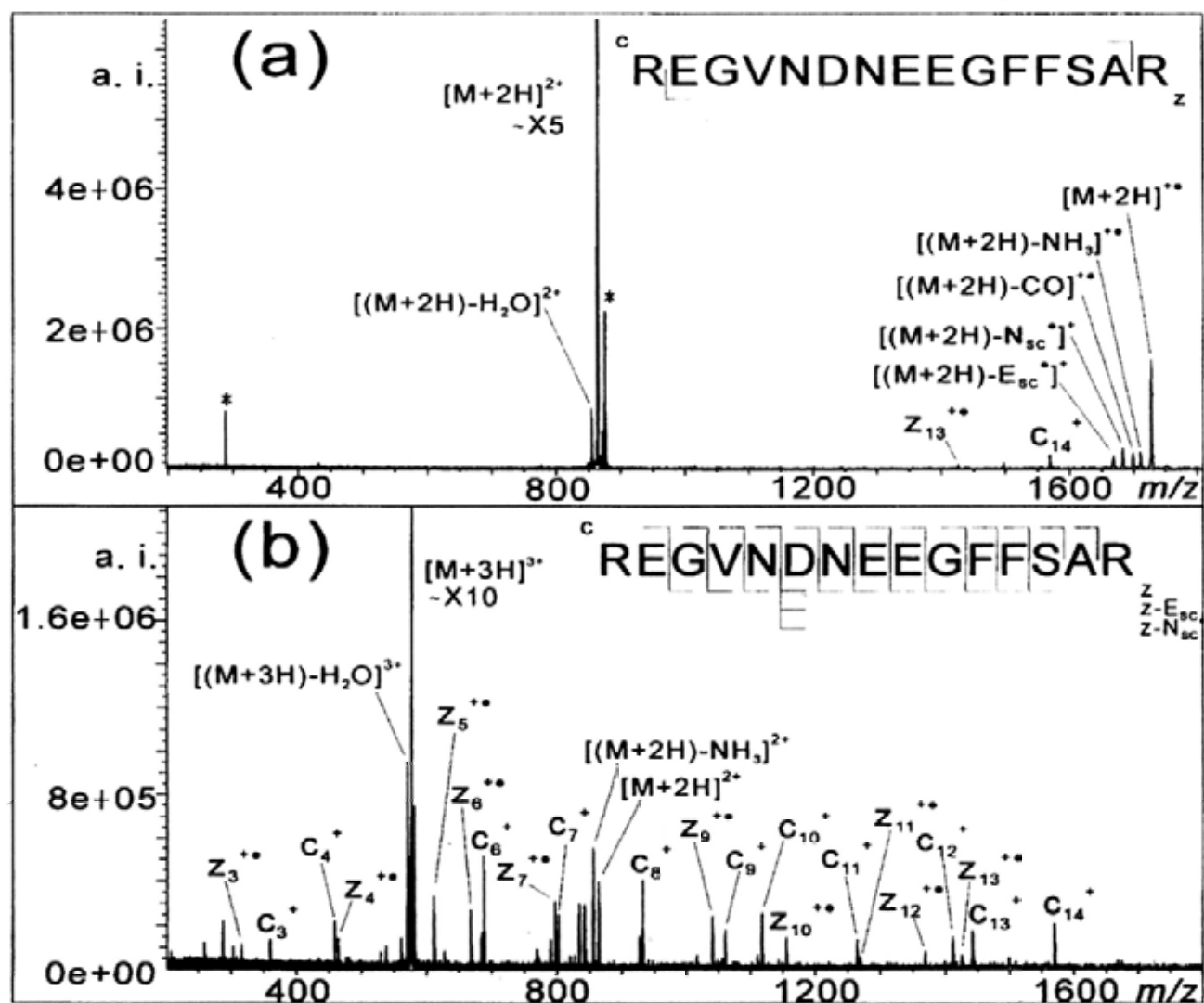


Figure 5.4 ECD spectra of (a) $[M+2H]^{2+}$ and (b) $[M+3H]^{3+}$ where M is N-arginated Fibrinopeptide-B. * denotes ions that could not be cleaned in isolation process.

predominantly $[M+2H]^{2+}$ whereas ECD of $[M+3H]^{3+}$ species induced extensive backbone cleavages. These results resembled those of diarginine model peptide with 6E as shown in Figures 5.1 (c) and 5.3 (c).

The importance of arginine residue (R) as proton carrier was revealed by examining the ECD behaviors of Fibrinopeptide-B (EGVNDNEEGFFSAR) and its analogue (REGVNDNEEGFFSA). The results arising from ECD of doubly-protonated EGVNDNEEGFFSAR and REGVNDNEEGFFSA are shown in Figures 5.5 (a) and (b) respectively. Contrast to ECD of doubly-protonated REGVNDNEEGFFSAR (Figure 5.4 (a)), ECD of doubly-protonated EGVNDNEEGFFSAR and REGVNDNEEGFFSA exhibited extensive backbone cleavages, yielding a series of z^* and c ions, respectively.

The role of arginine residue as charge carrier on cleavage suppression is unknown. However, it has been confirmed that both doubly-protonated monoarginated peptides and triply-protonated diarginated model peptides (see Figure 5.3) have no suppression effect on backbone cleavages. Empirically, clutching of added protons by arginine residues seems to be one of the prerequisites for strong suppression of backbone cleavage and H^+ loss from $[M+2H]^{2+}$.

5.3.4 Structural motif that suppresses backbone cleavages in diarginated E-rich peptides

There are two possible scenarios to account for the suppression of backbone cleavages in the ECD experiments of diarginated E-rich peptides. The charged-reduced precursor ions (i.e. $[M+2H]^{2+}$) formed under typical ECD conditions might have undergone usual cleavages to form c/z^* fragments. However, these c/z^* fragments were held together for an extended period of time (beyond the

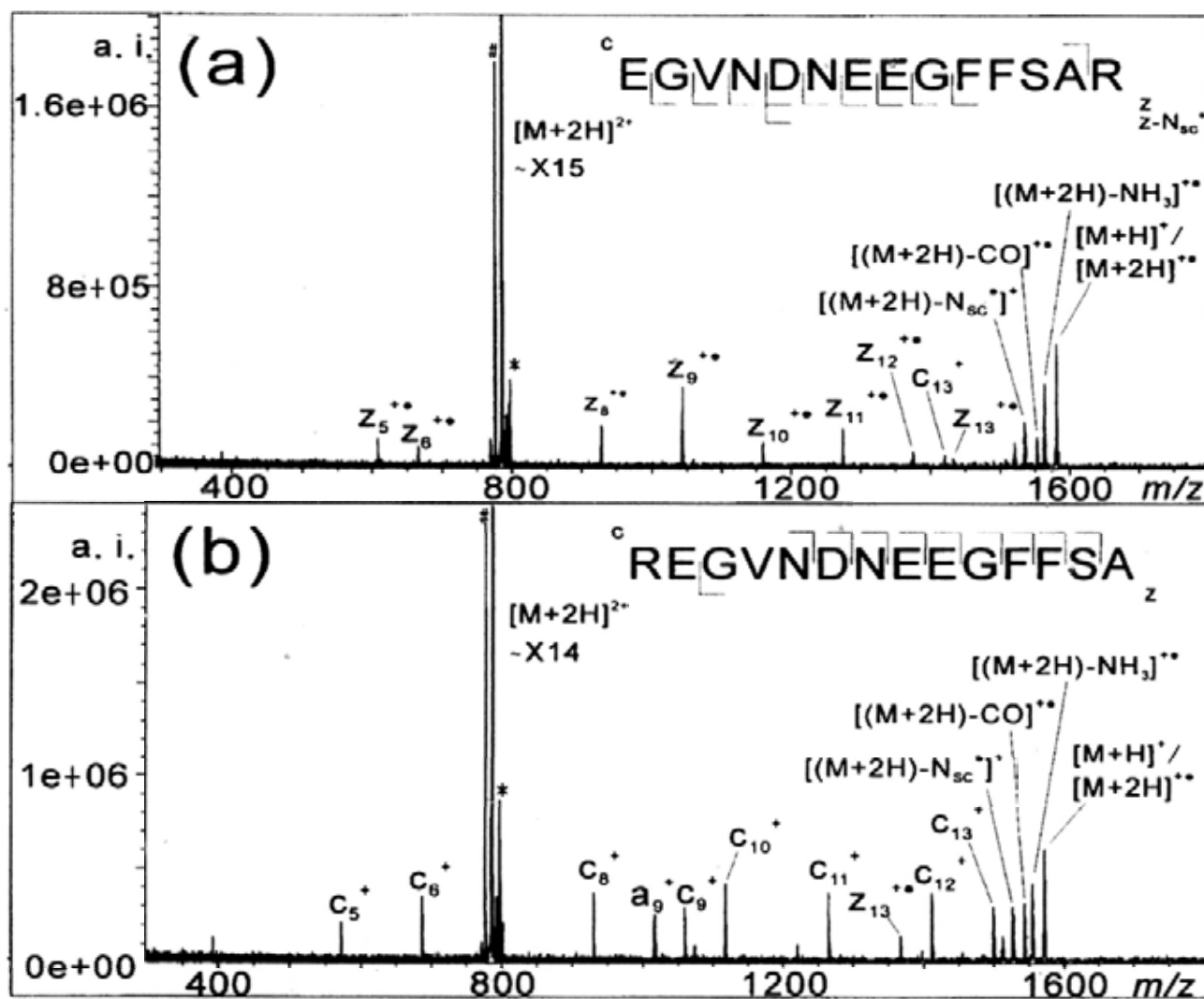


Figure 5.5 Typical ECD spectra of $[M+2H]^{2+}$ where M is (a) EGVNDNEEGFFSA (Fribinopeptide-B) and its analogue (b) REGVNDNEEGFFSA. # indicates $[(M+2H)-H_2O]^{2+}$ and * denotes ions that could not be cleaned in isolation process.

time-scale of typical FTICR excitation and detection events) by strong and/or multiple hydrogen bonds, and as a result, $[M+2H]^{2+}$ instead of backbone fragments was observed. Another possible scenario is that the $[M+2H]^{2+}$ formed might have somehow been stabilized and the usual backbone cleavage channels were therefore inhibited.

To determine the relevance of the above scenarios, the dissociation behaviours of charge-reduced precursor ions upon additional activation were examined. Figure 5.6 shows the ECD spectra of doubly-protonated RGE GEGEGEGEGEGEGR (a) with an extended time delay (3 s) after electron irradiation prior to ion excitation and detection processes, and (b) with subsequent pulsing of inert gas (1.2 ms) after the electron irradiation event and followed by a delay (3 s). Table 5.1 summarizes the fragment ions shown in Figures 5.1 (c), 5.6 (a) and (b). The ECD experiment generated only a few backbone fragments, and loss of H^+ from $[M+2H]^{2+}$ was largely suppressed (see Table 5.1 (i)). As expected, the insertion of a long delay after the electron capture event allowed metastable dissociation of the charge-reduced precursor ions (Table 5.1 (ii)). However, it is important to note that only *b* and *y* ions were observed in this case and typical *c/z*^{*} fragments were largely suppressed (the data of *b* and *y* ions are not shown). As shown in Table 5.1 (iii), temporary elevation of the cell pressure by pulsing argon gas into the trapped ion cell after the electron irradiation event had significant impact on the associated ECD spectrum. Apart from the expected *b* and *y* ions, several *c* and *z*^{*} fragment ions were generated. In addition, a high percentage of charge-reduced precursor ions were found to have lost H^+ to form $[M+H]^+$ ions.

The above experimental findings serve to support the notion that capture of a low-energy electron by doubly-protonated RGE GEGEGEGEGEGEGR ion liberates

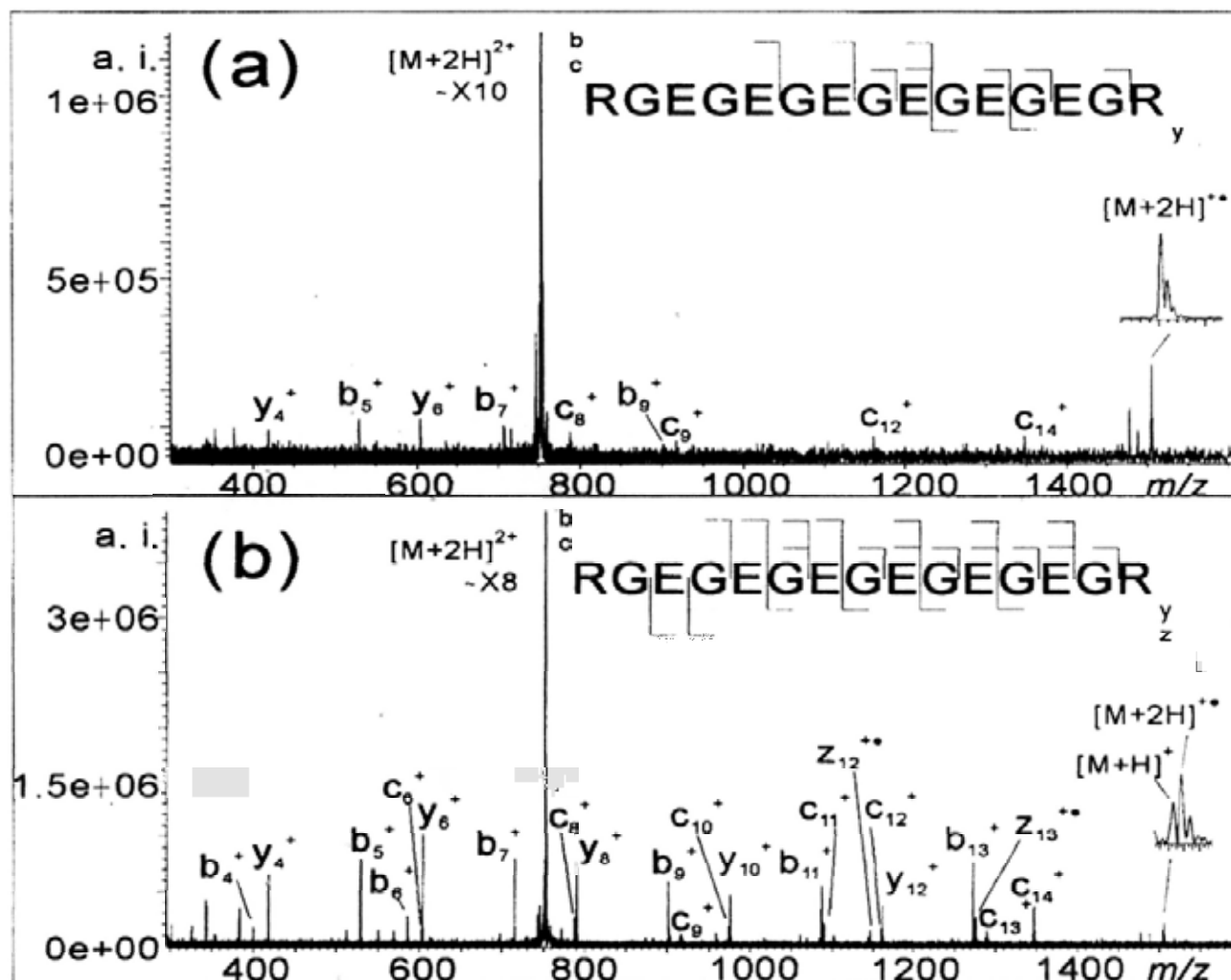


Figure 5. 6 ECD spectra of $[RGEGEGEGEGEGR+2H]^{2+}$ (a) with an extended time delay (3 s) after the electron irradiation prior to the ion excitation and detection; and (b) with subsequent pulsing of inert gas (1.2 ms) after the electron irradiation event and followed with a delay (3 s).
*Ions labeled in blue were formed in metastable dissociation while ions labeled in red were ECD fragments generated after reactivation of $[M+2H]^{2+}$.

Table 5.1 Summary of fragment peaks of [RGEGEGEGEGR+2H]²⁺ (i) under typical ECD conditions; (ii) with an extended time delay (3 s) after the electron irradiation prior to the ion excitation and detection; and (iii) with subsequent pulsing of inert gas after the electron irradiation event and followed with a 3 s delay.

| Assignment | Theoretical mass | Relative intensities (%) ^c | | |
|-------------------------------------------------------------------|-----------------------|---------------------------------------|----------------------------------|-------------------------------------------------|
| | | (i) Normal ECD | (ii) ECD with Delay ^a | (iii) ECD with Pulse gas and Delay ^b |
| [M+2H] ²⁺ | 752.8166 | 100.00 | 100.00 | 100.00 |
| [(M+2H)-H ₂ O] ²⁺ | 743.8113 | 1.07 | -- | 1.07 |
| [M+2H] ⁺⁺ | 1505.6331 | 2.96 | 1.11 | 0.81 |
| [M+H] ⁺ | 1504.6258 | -- | -- | 0.56 |
| [(M+2H)-NH ₃] ⁺⁺ | 1488.6066 | 0.85 | 0.37 | 0.47 |
| [(M+2H)-CO] ⁺⁺ | 1477.6382 | 1.69 | 0.63 | 0.49 |
| [(M+H)-CO] ⁺ | 1460.6360 | 0.11 | -- | -- |
| [(M+2H)-CH ₂ COOH] ⁺ [E] | 1446.6198 | 0.17 | 0.17 | 0.23 |
| [(M+2H)-CH ₂ CHCOOH] ⁺ [E] | 1433.6120 | 0.27 | 0.17 | 0.20 |
| c ₁₄ ⁺ / [c ₁₄ -H] ⁺⁺ | 1347.5407 / 1346.5334 | 0.65 / 0.49 | 0.31 / 0.18 | 1.32 / 0.44 |
| c ₁₃ ⁺ / [c ₁₃ -H] ⁺⁺ | 1290.5192 / 1289.5120 | 0.17 / 0.28 | 0.18 / 0.14 | -- / 0.52 |
| c ₁₂ ⁺ / [c ₁₂ -H] ⁺⁺ | 1161.4766 / 1160.4694 | 0.20 / 0.25 | 0.12 / 0.30 | 0.40 / 0.62 |
| c ₁₁ ⁺ -H ⁺ | 1103.4479 | -- | -- | 0.37 |
| c ₁₀ ⁺ / [c ₁₀ -H] ⁺⁺ | 975.4126 / 974.4053 | 0.16 / 0.26 | 0.18 / -- | 0.49 / 0.67 |
| c ₉ ⁺ / [c ₉ -H] ⁺⁺ | 918.3911 / 917.3839 | 0.28 / 0.35 | 0.15 / 0.25 | 0.33 / 0.42 |
| c ₈ ⁺ / [c ₈ -H] ⁺⁺ | 789.3485 / 788.3413 | 0.44 / 0.48 | 0.17 / 0.35 | 0.41 / 0.95 |
| c ₇ ⁺ -H ⁺ | 731.3198 | -- | -- | 0.33 |
| c ₆ ⁺ -H ⁺ | 602.2772 | -- | -- | 0.51 |
| z ₁₃ ⁺⁺ / [z ₁₃ +H] ⁺ | 1275.4845 / 1276.4918 | -- / 0.20 | -- / 0.23 | 0.44 / 1.01 |
| z ₁₂ ⁺⁺ +H ⁺ | 1147.4492 | -- | -- | 0.53 |
| z ₁₁ ⁺⁺ +H ⁺ | 1090.4278 | -- | -- | 0.77 |
| z ₁₀ ⁺⁺ +H ⁺ | 961.3852 | -- | -- | 0.24 |

^a The extended time delay after the electron irradiation prior to the ion excitation and detection is 3 s.

^b With subsequent pulsing of inert gas (1.2 ms) after the electron irradiation event and followed with a 3 s delay.

^c b/y fragment ions were excluded from this table for clarity purposes.

recombination energy. This energy randomizes along different degrees of freedom and finally invokes the usual C-N cleavages through the mobile proton channels. The radical-initiated cleavage channels are largely inhibited in ECD of diarginated E-rich peptide ions, with the production of charge-reduced precursor ions (i.e. $[M+2H]^{+*}$) remaining largely intact. However, the inhibiting factor would somehow be lifted through collisions with inert gas molecules. As a result, both N- C_α cleavage and H^+ loss channels are activated leading to the generation of additional c^- , z^- and $[M+H]^+$ fragment ions.

To further understand the suppression effect, conformational search for the doubly-protonated RGE GEGEGEGEGEGEGR was performed to extract the conformational features of the low-energy structures. In order to avoid the lengthy process of computing and comparing the exact energies of the various forms of this peptide, the zwitterion form of this peptide was taken as the predominant species subsequent to several literature studies involving systems with similar functions. It was noted, for instance, that Rodriguez et al. performed detailed computational analysis of gaseous bradykinin (BK) at different charge states [167]. Similar to the model peptide used in this study, BK has arginine residues at both termini. For doubly-protonated bradykinin, $[BK+2H]^{2+}$, the zwitterion form of peptide is found to have lower energy than that of the canonical form. As regards peptides containing acidic residues, Li and co-workers [168] preferred deprotonation of the main chain C-terminal carboxylic group instead of the side chain carboxylic group. The hydrogen bonding patterns of the low-energy structures obtained in these conformational searches are set out in Appendix IV. Table 5.2 summarized the details of these calculation results and the overall distribution of hydrogen-bonds formed at backbone amide linkages of the lowest energy structures.

Figure 5.7 shows the lowest energy zwitterion structure of $[\text{RGEGEGEGEGEGR}+2\text{H}]^{2+}$ obtained by conformational search. For clarity purpose, only hydrogen atoms capable of forming classical hydrogen bonds are shown. Hydrogen bonds between carboxylic oxygen of E side chain and backbone amide hydrogen are illustrated by dotted lines. (The distances are in angstroms.) As revealed in the figure, a salt bridge is formed between C-terminal carboxylic anion and N-terminal protonated amine. Such phenomenon concurs with the previous theoretical studies on the lowest energy structures of doubly-protonated Bradykinin species [167]. In these studies, two protonated arginine side chains were mainly solvated by backbone carbonyl groups while four hydrogen bonds were formed between carbonyl oxygen of E side chains and backbone amide hydrogen atoms. The hydrogen bonds are believed to be a significant factor that inhibits the usual N-C_α cleavages.

Scheme 5.1 shows a proposed pathway for suppression of backbone cleavages in diarginated E-rich peptides. Besides inducing N-C_α cleavage, abstraction of H^\bullet from the guanidine group to the backbone carbonyl oxygen may lead to the transfer of hydrogen from backbone amide nitrogen to carboxylic oxygen of E side chains. The hydrogen bonds formed between the carboxylic oxygen of E side chains and the backbone amide hydrogen atoms can inhibit the usual N-C_α cleavages by resonantly stabilizing the radical intermediate. As a result, the charge-reduced precursor ion will remain intact as no backbone linkage will be cleaved. Upon collisional activation, the charge-reduced precursor could be activated and undergo further dissociation through two alternative pathways, including H^\bullet loss from $[\text{M}+2\text{H}]^{+\bullet}$ and N-C_α cleavage. This explains why a few more c and z' ions were produced and $[\text{M}+\text{H}]^+$ was observed when argon gas was pulsed into the cell after

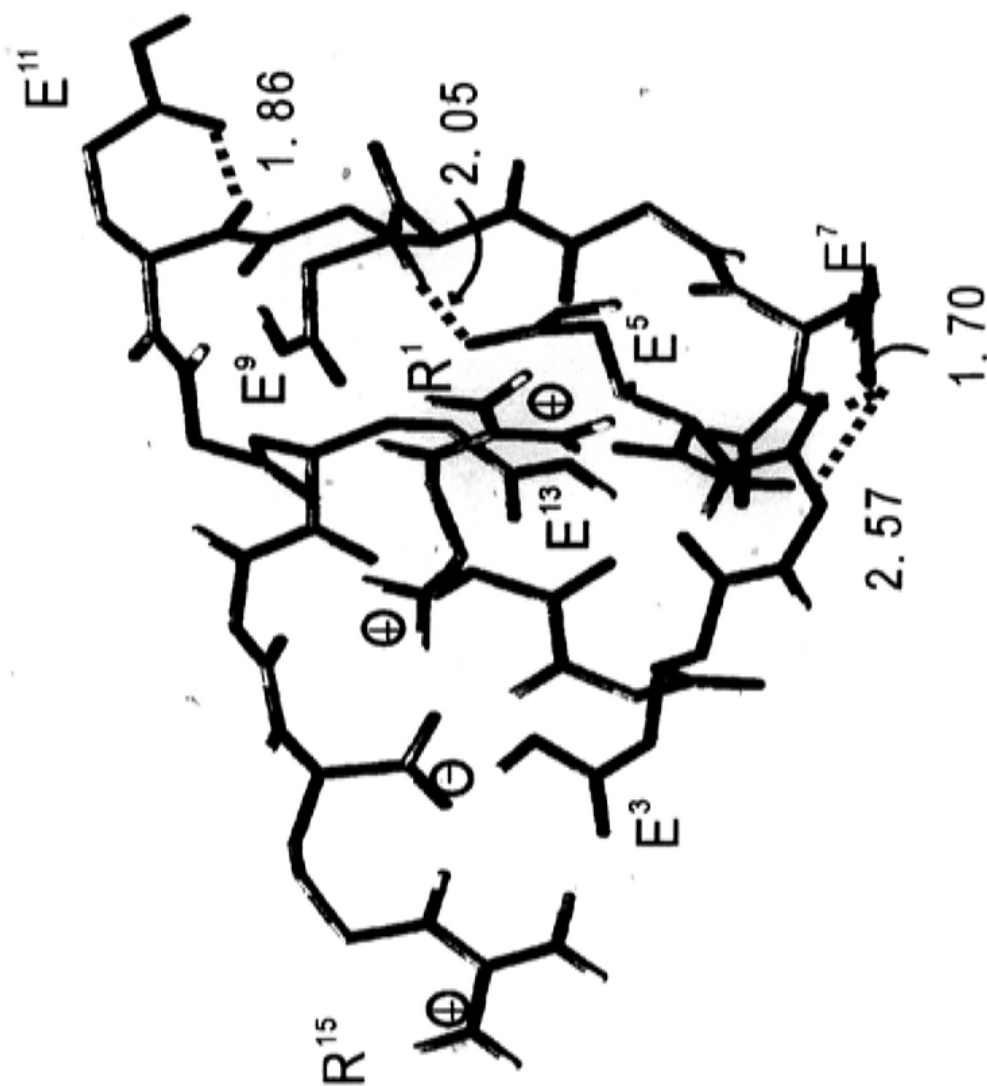
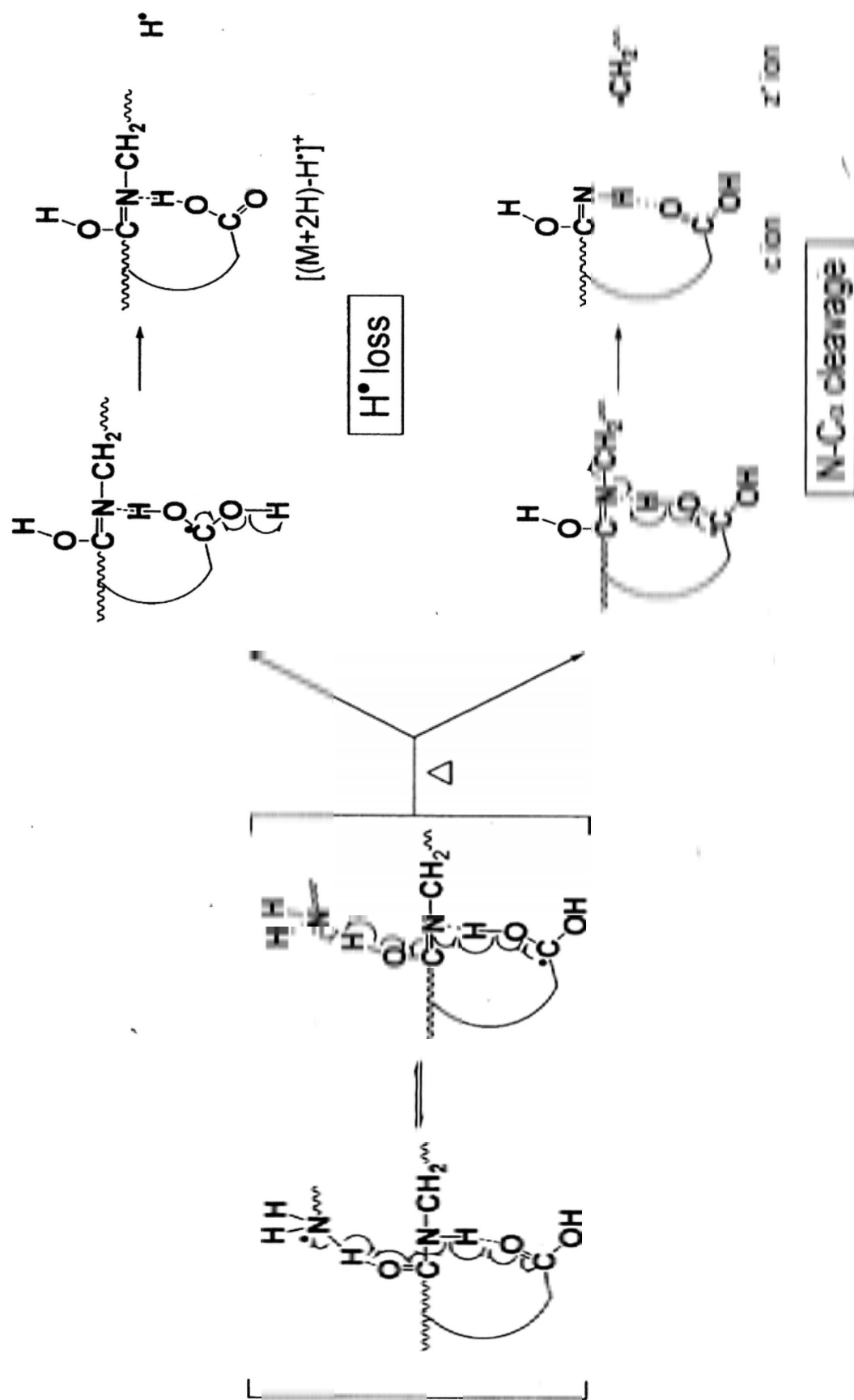


Figure 5.7 The lowest energy zwitterion structure of [RGEGEGEGEGR+2H]²⁺ obtained by conformational search. Hydrogen bonds between carboxylic oxygen of E side chain and backbone amide hydrogen are illustrated by dotted line.



Scheme 5.1 A possible mechanism to account for the stabilization of $[M+2H]^+$ by using interactions between carboxylic oxygen of E side chain and backbone amide hydrogen.

ECD.

5.4 Conclusion

This study on a series of diarginated model peptides with different number of glutamic acid (E) and asparagine (N) residues has revealed that backbone cleavage and loss of hydrogen atom (H^\bullet) from reduced precursor ions ($[M+2H]^{+\bullet}$) would be suppressed under ECD conditions. As the ECD spectra of doubly-protonated peptides show a heavy dependence on the number of E and N residues, it appears that both backbone cleavages and H^\bullet loss from $[M+2H]^{+\bullet}$ would be suppressed as the number of E and N residues increases. Also, strong inhibition of the backbone cleavages and H^\bullet loss are noted for peptides with 6E residues (or 4E + 2N residues). The experimental results obtained by using these model peptides have been re-confirmed by analyzing N-arginated Fibrinopeptide-B (i.e. REGVNDNEEGFFSAR). It is found that ECD of triply-protonated peptides would extensive backbone cleavages, whereas ECD of doubly-protonated species would yield predominantly charge-reduced precursor ions. This suggests that peptide ions with all surplus protons sequestered in arginine-residues would exhibit enhanced stability under ECD conditions as the number of acid-residue increases.

A possible hypothesis for the suppression of backbone cleavages and the H^\bullet loss from $[M+2H]^{+\bullet}$ is related to the presence of alternative dissociation pathways apart from the usual $N-C_\alpha$ cleavages. As observed from the lowest-energy structure of diarginated E-rich peptides, there are interactions between carboxylic oxygen of E side chains and hydrogen of backbone amides. It is tentatively believed that these hydrogen bonds could inhibit the usual $N-C_\alpha$ cleavages and H^\bullet loss by resonantly stabilizing the radical intermediate shown in Scheme 5.1. When charge-reduced

precursor ion is activated, it can further dissociate through two alternative pathways, i.e. either N-C_α cleavages or H⁺ loss from reduced precursor ion.

Chapter 6

Conclusions

In the investigation of the generation and dissociation of polypeptide and oligosaccharide ions, the dissociation pathways of even-electron precursor ions generated by protonation ($[M+H]^+$) or metalation ($[Metal+M]^{n+}$), odd-electron hydrogen-deficient precursor ions ($M^{+\bullet}$) generated by SORI-CID of $[Cu(Tpy)M]^{2+}$ and odd-electron hydrogen-surplus precursor ions ($[M+2H]^{+\bullet}$) generated by ECD of $[M+2H]^{2+}$ were examined and cross-compared with each other. The results have indicated that side chain loss reactions are the dominant pathways for dissociation of $M^{+\bullet}$ while backbone cleavages, leading to the formation of *b/y* and *c/z* ions, are the dominant dissociation pathways of $[M+H]^+$ and $[M+2H]^{+\bullet}$ under SORI-CID and ECD conditions respectively. Backbone cleavages in SORI-CID is believed to be initiated by mobile proton whereas those in ECD by radicals. Similarly, for the peptides-containing PTM(s), the labile PTM groups would cleave preferentially in the dissociation of $M^{+\bullet}$ and $[M+H]^+$ but be preserved in the fragmentation of $[M+2H]^{+\bullet}$. The different preferences in the dissociation of these two radical systems are tentatively attributable to the nature of the radical, with $M^{+\bullet}$ being a heteroatom radical and $[M+2H]^{+\bullet}$ a hydrogen one (refer to Cornell model). And similar to the secondary dissociation of $z^{+\bullet}$ fragments, $M^{+\bullet}$ favours side chain loss reactions through abstraction of the α - or γ -hydrogen of the amino acid residue of interest. These observations seem to suggest that the type of radicals, but not the type of dissociation conditions, is the predominant factor governing the preferred dissociation pathway.

The systematic study using copper II ions as charge carrier and

oligosaccharide as targets has indicated that different systems (i.e. SORI-CID of $[\text{Cu}(\text{Tpy})\text{M}]^{2+}$, SORI-CID and ECD of $[\text{Cu}+\text{M}]^{2+}$) seem to generate rather similar MS/MS spectra and that cleavage of the weak glycosidic linkage plays a dominant role in governing the final appearance of the MS/MS spectra. The study has also revealed a notable effect of terpyridine ligand on substantial reduction of cross-ring cleavages. It is proposed that ligand limits the coordination of copper ion and oligosaccharide, thereby inhibiting cross-ring cleavages.

In the course of evaluating the various structural effects of peptides on their dissociation patterns, it was discovered that the presence of ligand would pose a solvation effect on peptides and therefore reduce their fragmentation efficiencies, especially in the secondary fragmentation of z' ions. A postulation in this regard is that part of the recombination energy is used to remove the ligand and thus reduced energy is left for invoking secondary fragmentation.

A separate but related conclusion is that certain natural structural motifs would inhibit backbone fragmentation and loss of hydrogen atom (H^\bullet) from $[\text{M}+2\text{H}]^{+}$, as a positive correlation is found between the extent of cleavage inhibition and the number of glutamic acid (E) residues. Given the global minimum structure of the doubly-protonated diargininated E-rich peptide ion, it is believed that hydrogen bond interactions between carboxylic oxygens of the E side chains and backbone amide hydrogens may stabilize the radical intermediate and thus inhibit the usual $\text{N}-\text{C}_\alpha$ cleavages and H^\bullet loss from $[\text{M}+2\text{H}]^{+}$. Further investigations into the effect of other structural parameters, such as charge carrier and peptide chain length, on suppression of $\text{N}-\text{C}_\alpha$ cleavages and H^\bullet loss from $[\text{M}+2\text{H}]^{+}$ should be conducted.

References

1. Roher AE, Lowenson JD, Clarke S, Wolkow C, Wang R, Cotter RJ, Reardon IM, Zurcher-Neely HA, Heinrikson RL, Ball MJ. *J. Biol. Chem.* 1993; **268**: 3072.
2. Karlsson KA. *Annu. Rev. Biochem.* 1989; **58**: 3090.
3. Varki A. *Glycobiology* 1993; **3**: 97.
4. Edman P. *Acta. Chem. Scand.* 1950; **4**: 283.
5. Katsuki S, Scott JE, Yamashin I. *Biochem. J.* 1965; **97**: C25.
6. Hunkapiller T, Tempst P, Hood L. *Nature* 1984; **310**: 105.
7. Takasaki S, Mizuochi T, Kobata A. *Methods Enzymol.* 1982; **83**: 263.
8. Tarentino AL, Plummer TH. *Methods Enzymol.* 1994; **230**: 44.
9. Thomson JJ. *Philos. Mag.* 1899; **48**: 547.
10. Bleakney W. *Phys. Rev.* 1929; **34**: 157.
11. Munson SB, Field FH. *J. Am. Chem. Soc.* 1966; **88**: 2621.
12. Beckey HD. *Principles of Field Ionization and Field Desorption Mass Spectrometry*. Pergamon: Oxford, England, 1977.
13. Barber M, Bordoli RS, Sedgwick RD, Tyler AN. *Nature* 1981; **293**: 270.
14. Kofel P, Allemann M, Kellerhals H, Wanczek KP. *Int. J. Mass Spectrom. Ion Processes* 1985; **65**: 97.
15. Macfarlane RD, Torgerson DF. *Science* 1976; **191**: 920.
16. Desiderio DM, Katakuse I. *Anal. Biochem.* 1983; **129**: 425.
17. Karas M, Bachmann D, Bahr U, Hillenkamp F. *Int. J. Mass Spectrom. Ion Processes* 1987; **78**: 53.
18. Yamashita M, Fenn JB. *J. Phys. Chem.* 1984; **88**: 4451.
19. Fenn JB, Mann M, Meng CK, Wong SF, Whitehouse CM. *Science* 1989; **246**: 64.
20. Wilm MS, Mann M. *Int. J. Mass Spectrom. Ion Processes* 1994; **136**: 167.
21. Hunt DF, Henderson RA, Shabanowitz J, Sakaguchi K, Michel H, Sevilir N, Cox AL, Appella E, Engelhard VH. *Science* 1992; **255**: 1261.
22. Mortz E, O'connor PB, Roepstorff P, Kelleher NL, Wood TDm, McLafferty FW, Mann M. *Proc. Natl. Acad. Sci. U. S. A.* 1996; **93**: 8264.
23. Kelleher NL, Lin HY, Valaskovic GA, Aserud DJ, Fridriksson EK, McLafferty FW. *J. Am. Chem. Soc.* 1999; **121**: 806.
24. Sze SK, Ge Y, Oh H, McLafferty FW. *Proc. Natl. Acad. Sci. U. S. A.* 2002; **99**: 1774.
25. Roepstorff P, Fohlman J. *Biomed. Mass Spectrom.* 1984; **11**: 601.
26. Johnson RS, Martin SA, Biemann K, Stults JT, Watson JT. *Anal. Chem.* 1987;

- 59: 2621.
27. Domon B, Costello CE. *Glycoconj. J.* 1988; **5**: 397.
 28. Jennings KR. *Int. J. Mass Spectrom. Ion Phys.* 1968; **1**: 227.
 29. Cody RB, Frelser BS. *Anal. Chem.* 1982; **54**: 96.
 30. Mabud DA, Dekrey MJ, Cooks RG. *Int. J. Mass Spectrom. Ion Processes* 1985; **67**: 285.
 31. Price WD, Schnier PD, Williams ER. *Anal. Chem.* 1996; **68**: 859.
 32. Grant ER, Coggiola MJ, Leem YT, Schulz PA, Sudbo AS, Shen YR. *Chem. Phys. Lett.* 1977; **52**: 595.
 33. Gauthier JW, Trautman TR, Jacobson DB. *Anal. Chim. Acta* 1991; **246**: 211.
 34. Boering KA, Rolfe J, Brauman JI. *Rapid Commun. Mass Spectrom.* 1992; **6**: 303.
 35. Lee SA, Jiao CQ, Huang YQ, Freiser BS. *Rapid Commun. Mass Spectrom.* 1993; **7**: 819.
 36. Somogyi A, Wysocki VH. *J. Am. Soc. Mass Spectrom.* 1994; **5**: 704.
 37. Rodriguez CF, Cunje A, Shoeib T, Chu IK, Hopkinson AC, Siu KWM. *J. Am. Chem. Soc.* 2001; **123**: 3006.
 38. Paizs B, Csonka IP, Lendvay G, Suhai S. *Rapid Commun. Mass Spectrom.* 2001; **15**: 637.
 39. Csonka IP, Paizs B, Lendvay G, Suhai S. *Rapid Commun. Mass Spectrom.* 2000; **14**: 417.
 40. Gu C, Somogyi A, Wysocki VH, Medzihradzky KF. *Anal. Chim. Acta*, 1999; **397**: 247.
 41. Harrison AG, Yalcin T. *Int. J. Mass Spectrom. Ion Proc.* 1997; **165/166**: 339.
 42. Nair H, Wysocki VH. *Int. J. Mass Spectrom. Ion Proc.* 1998; **174**: 95.
 43. Vaisar T, Urban J. *J. Mass Spectrom.* 1998; **33**: 505.
 44. Yalcin T, Csizmadia IG, Peterson MR, Harrison AG. *J. Am. Soc. Mass Spectrom.* 1996; **7**: 233.
 45. Summerfield SG, Bolgar MS, Gaskell SJ. *J. Mass Spectrom.* 1997; **32**: 225.
 46. Cordero MM, Houser JJ, Wesdemiotis C. *Anal. Chem.* 1993; **65**: 1594.
 47. Nold MJ, Wesdemiotis C, Yalcin T, Harrison AG. *Int. J. Mass Spectrom. Ion Proc.* 1997; **164**: 137.
 48. Eckart K, Holthausen MC, Koch W, Spiess J. *J. Am. Soc. Mass Spectrom.* 1998; **9**: 1002.
 49. Harrison AG, Csizmadia IG, Tang T, Tu Y. *J. Mass Spectrom.* 2000; **35**: 683.
 50. Paizs B, Suhai S. *Rapid Commun. Mass Spectrom.* 2001; **15**: 651.
 51. Yalcin T, Khouw C, Csizmadia IG, Peterson MR, Harrison AG. *J. Am. Soc. Mass Spectrom.* 1995; **6**: 1165.

52. Paizs B, Lendvay G, Vekey K, Suhai S. *Rapid Commun. Mass Spectrom.* 1999; **13**: 525.
53. Farrugia JM, O'Hair RAJ, Reid GE. *Int. J. Mass Spectrom.* 2001; **210/211**: 71.
54. Becker CH, Wu KJ. *J. Am. Soc. Mass Spectrom.* 1995; **6**: 883.
55. Turecek F, Carpenter FH, Polce MJ, Wesdemiotis C. *J. Am. Chem. Soc.* 1999; **121**: 7955.
56. Masterson DS, Yin HY, Chacon A, Hachey DL, Norris JL, Porter NA. *J. Am. Chem. Soc.* 2004; **126**: 720.
57. Yin H, Chacon A, Porter NA, Yin HY, Masterson DS. *J. Am. Soc. Mass Spectrom.* 2007; **18**: 807.
58. Hodyss R, Cox HA, Beauchamp JL. *J. Am. Chem. Soc.* 2005; **127**: 12436.
59. Zubarev RA, Kelleher NL, McLafferty FW. *J. Am. Chem. Soc.* 1998; **120**: 3265.
60. Zubarev RA, Haselmann KF, Budnik B, Kjeldsen F, Jensen F. *Eur. J. Mass Spectrom.* 2002; **8**: 337.
61. Fung YME, Adams CM, Zubarev RA. *J. Am. Chem. Soc.* 2009; **131**: 9977.
62. Syka JEP, Coon JJ, Schroeder MJ, Shabanowitz J, Hunt DF. *Proc. Natl. Acad. Sci. U. S. A.* 2004; **101**: 9528.
63. Chu IK, Rodriquez CF, Lau TC, Hopkinson AC, Siu MKW. *J. Phys. Chem. B* 2000; **104**: 3393.
64. Zubarev RA, Kruger NA, Fridriksson EK, Lewis MA, Horn DM, Carpenter BK, McLafferty FW. *J. Am. Chem. Soc.* 1999; **121**: 2857.
65. Leymarie N, Berg EA, McComb ME, O'Connor PB, Grogan J, Oppenheim FG, Costello CE. *Anal. Chem.* 2002; **74**: 4124.
66. Horn DM, Ge Y, McLafferty FW. *Anal. Chem.* 2000; **72**: 4778.
67. Tsybin YO, Hakansson P, Budnik BA, Haselmann KF, Kjeldsen F, Gorshkov M, Zubarev RA. *Rapid Commun. Mass Spectrom.* 2001; **15**: 1849.
68. Haselmann KF, Budnik BA, Olsen JV, Nielsen ML, Reis CA, Clausen H, Johnsen AH, Zubarev RA. *Anal. Chem.* 2001; **73**: 2998.
69. Haselmann KF, Budnik BA, Kjeldsen F, Nielsen ML, Olsen JV, Zubarev RA. *Eur. J. Mass Spectrom.* 2002; **8**: 117.
70. Kjeldsen F, Haselmann KF, Budnik BA, Jensen F, Zubarev RA. *Chem. Phys. Lett.* 2002; **356**: 201.
71. Gorshkov MV, Masselon CD, Nikolaev EN, Udseth HR, Pasa-Tolic L, Smith RD. *Int. J. Mass Spectrom.* 2004; **234**: 131.
72. Syrstad EA, Turecek F. *J. Am. Soc. Mass Spectrom.* 2005; **16**: 208.
73. Chen XH, Turecek F. *J. Am. Chem. Soc.* 2006; **128**: 12520.
74. Chu I K, Rodriquez CF, Lau TC, Hopkinson AC, Siu KWM. *J. Phys. Chem. B* 2000; **104**: 3393.

75. Chu IK, Lau TC, Siu KWM. *J. Mass Spectrom.* 1998; **33**: 811.
76. Barlow CK, Wee S, McFadyen WD, O'Hair RAJ. *Dalton Trans.* 2004; **20**: 3199.
77. Wee S, O'Hair RAJ, McFadyen WD. *Int. J. Mass Spectrom.* 2004; **234**: 101.
78. Chu IK, Sju SO, Lam CNW, Chan JCY, Rodriguez CF. *Rapid Commun. Mass Spectrom.* 2004; **18**: 1798.
79. Barlow CK, Wee S, McFadyen WD, O'Hair RAJ. *J. Am. Chem. Soc.* 2005; **127**: 6109.
80. Pedersen JZ, Finazzi-Agro A. *FEBS Letters* 1993; **325**: 53.
81. Mirgorodskaya E, Roepstorff P, Zubarev RA. *Anal. Chem.* 1999; **71**: 4431.
82. Kelleher RL, Zubarev RA, Bush K, Furie B, Furie BC, McLafferty FW, Walsh CT. *Anal. Chem.* 1999; **71**: 4250.
83. Stensballe A, Jensen ON, Olsen JV, Haselmann KF, Zubarev RA. *Rapid Commun. Mass Spectrom.* 2000; **14**: 1793.
84. Shi SDH, Hemling ME, Carr SA, Horn DM, Lindh I, McLafferty FW. *Anal. Chem.* 2001; **73**: 19.
85. Guan ZQ, Yates NA, Bakhtiar R. *J. Am. Soc. Mass Spectrom.* 2003; **14**: 605.
86. Cournoyer JJ, Pittman JL, Ivlevaver AB, Fallows E, Waskell L, Costello CE, O'Connor PB. *Protein Sci.* 2005; **14**: 452.
87. Cournoyer JJ, Lin C, O'Connor PB. *Anal. Chem.* 2006; **78**: 1264.
88. Cournoyer JJ, Lin C, Bowman MJ, O'Connor PB. *J. Am. Soc. Mass Spectrom.* 2007; **18**: 48.
89. Li XJ, Cournoyer JJ, Lin C, O'Connor PB. *J. Am. Soc. Mass Spectrom.* 2008; **19**: 855.
90. Robinson NE, Robinson AB. *Molecular Clocks: Deamidation of Asparaginyl and Glutaminyl Residues in Peptides and Proteins.* Althouse Press: Cave Junction, OR, 2004.
91. Schindler P, Muller D, Marki W, Grossenbacher H, Richter WJ. *J. Mass Spectrom.* 1996; **31**: 967.
92. Johnson RS, Martin SA, Biemann K, Stults JT, Watson JT. *Anal. Chem.* 1987; **59**: 2621.
93. Kjeldsen F, Haselmann KF, Sorensen ES, Zubarev RA. *Anal. Chem.* 2003; **75**: 1267.
94. Comisarow MB, Marshall AG. *Chem. Phys. Lett.* 1974; **25**: 282.
95. Grosshans PB, Shields PJ, Marshall AG. *J. Chem. Phys.* 1991; **94**: 5341.
96. Marshall AG, Grosshans PB. *Anal. Chem.* 1991; **63**: A215.
97. Dunbar RC. *Int. J. Mass Spectrom. Ion Processes* 1984; **56**: 1.
98. Dunbar RC, Chen JH, Hays JD. *Int. J. Mass Spectrom. Ion Processes* 1984; **57**:

- 39.
99. Mitchell DW. *Int. J. Mass Spectrom. Ion Processes* 1991; **107**: 417.
100. Schweikhard L, Ziegler J, Bopp H, Lutzenkirchen K. *Int. J. Mass Spectrom. Ion Processes* 1995; **141**: 77.
101. Marshall AG, Hendrickson CL, Jackson GS. *Mass Spectrom. Rev.* 1998; **17**: 1.
102. Fong WYK, Chan TWD. *J. Am. Soc. Mass Spectrom.* 1999; **10**: 72.
103. Caravatti P, Allemann M. *Org. Mass Spectrom.* 1991; **26**: 514.
104. Frisch MJ, Trucks GW, Schlegel HB, Scuseria GE, Robb MA, Cheeseman JR, Montgomery JA, Jr Vreven T, Kudin KN, Burant JC, Millam JM, Iyengar SS, Tomasi J, Barone V, Mennucci B, Cossi M, Scalmani G, Rega N, Petersson GA, Nakatsuji H, Hada M, Ehara M, Toyota K, Fukuda R, Hasegawa J, Ishida M, Nakajima T, Honda Y, Kitao O, Nakai H, Klene M, Li X, Knox JE, Hratchian HP, Cross JB, Adamo C, Jaramillo J, Gomperts R, Stratmann RE, Yazyev O, Austin AJ, Cammi R, Pomelli C, Ochterski JW, Ayala PY, Morokuma K, Voth GA, Salvador P, Dannenberg JJ, Zakrzewski VG, Dapprich S, Daniels AD, Strain MC, Farkas O, Malick DK, Rabuck AD, Raghavachari K, Foresman JB, Ortiz JV, Cui Q, Baboul AG, Clifford S, Cioslowski J, Stefanov BB, Liu G, Liashenko A, Piskorz P, Komaromi I, Martin RL, Fox DJ, Keith T, Al-Laham MA, Peng CY, Nanayakkara A, Challacombe M, Gill PMW, Johnson B, Chen W, Wong MW, Gonzalez C, Pople JA. *Gaussian 03, Revision B.04, Gaussian, Inc., Pittsburgh PA*, 2003.
105. Becke AD. *J. Chem. Phys.* 1993; **98**: 5648.
106. Becke AD. *J. Chem. Phys.* 1993; **98**: 1372.
107. Stephens PJ, Delvin FJ, Cabalowski CF, Fisch MJ. *J. Phys. Chem.* 1994; **98**: 11623.
108. Hay PJ, Wadt WR. *J. Chem. Phys.* 1985; **82**: 299.
109. Hay PJ, Wadt WR. *J. Chem. Phys.* 1985; **82**: 270.
110. Scott AP, Radom L. *J. Phys. Chem.* 1996; **100**: 16502.
111. Saunders M, Houk KN, Wu YD, Still WC, Lipton M, Chang G, Guida WC. *J. Am. Chem. Soc.* 1990; **112**: 1419.
112. Kolossvary I, Guida WC. *J. Comp. Chem.* 1999; **20**: 1671.
113. Chu IK, Rodriguez CF, Hopkinson AC, Lau TC, Siu MKW. *J. Am. Soc. Mass Spectrom.* 2001; **12**: 1114.
114. Wee S, O'Hair RAJ, McFadyen WD. *Rapid Commun. Mass Spectrom.* 2002; **16**: 884.
115. Bagheri-Majdi E, Ke YY, Orlova G, Chu IK, Hopkinson AC, Siu KWM. *J. Phys. Chem. B* 2004; **108**: 11170.
116. Seymour JL, Turecek F. *J. Mass Spectrom.* 2005; **37**: 533.

117. Fung YME, Chan TWD. *J. Am. Soc. Mass Spectrom.* 2005; **16**: 1523.
118. Cooper HJ, Hudgins RR, Håkansson K, Marshall AG. *J. Am. Soc. Mass Spectrom.* 2002; **13**: 241.
119. Haselmann KF, Budnik BA, Kjeldsen F, Polfer NC, Zubarev RA. *Eur. J. Mass Spectrom.* 2002; **8**: 461.
120. Cooper HJ, Håkansson K, Marshall AG, Hudgins RR, Haselmann KF, Kjeldsen F, Budnik BA, Polfer NC, Zubarev RA. *Eur. J. Mass Spectrom.* 2003; **9**: 221.
121. Kjeldsen F, Zubarev RA. *J. Am. Chem. Soc.* 2003; **125**: 6628.
122. Wu Z, Fenselau CJ. *Rapid Commun. Mass Spectrom.* 1992; **6**: 403. and Wu Z, Fenselau CJ. *Rapid Commun. Mass Spectrom.* 1994; **8**: 777.
123. Harrison AG. *Mass Spectrom. Rev.* 1997; **16**: 210.
124. Chu IK, Lam CNW. *J. Am. Soc. Mass Spectrom.* 2005; **16**: 1795.
125. Wee S, O'Hair RAJ, McFadyen WD. *Rapid Commun. Mass Spectrom.* 2005; **19**: 1797.
126. Zhao C, Xie B, Chan SY, Costello CE, O'Connor PB. *J. Am. Soc. Mass Spectrom.* 2008; **19**: 138.
127. Adamson JT, Hakansson K. *J. Am. Soc. Mass Spectrom.* 2007; **18**: 2162.
128. Pramanik BN, Ganguly AK, Gross ML Eds., *Detection of Noncovalent Complexes by Electrospray Ionization Mass Spectrometry. In Applied Electrospray Mass Spectrometry*, Marcel Dekker: New York, 2002; p. 361.
129. Xie YM, Zhang J, Yin S, Loo JA. *J. Am. Chem. Soc.* 2006; **128**: 14432.
130. Lee SW, Lee HN, Kim HS, Beauchamp JL. *J. Am. Chem. Soc.* 1998; **120**: 5800.
131. Chan WC, White PD. Oxford University Press; New York, 2000
132. Bacsá B, Desai B, Dibo G, Kappe CO. *J. Pept. Sci.* 2006; **12**: 633.
133. Guan ZQ, Yates NA, Bakhtiar R. *J. Am. Soc. Mass Spectrom.* 2003; **14**: 605.
134. Chowdhury SM, Munske GR, Ronald RC, Bruce JE. *J. Am. Soc. Mass Spectrom.* 2007; **18**: 493.
135. Stensballe A, Jensen ON, Olsen JV, Haselmann KF, Zubarev RA. *Rapid Commun. Mass Spectrom.* 2000; **14**: 1793.
136. Adamson JT, Hakansson K. *Anal. Chem.* 2007; **79**: 2901.
137. Harvey DJ. *J. Am. Soc. Mass Spectrom.* 2001; **12**: 926.
138. Zhao C, Xie B, Chan SY, Costello CE, O'Connor PB. *J. Am. Soc. Mass Spectrom.* 2008; **19**: 138.
139. Carr SA, Reinhold VN, Green BN, Haas JR. *Biomed. Mass Spectrom.* 1985; **12**: 288.
140. Harvey DJ. *J. Mass Spectrom.* 2000; **35**: 1178.
141. Carroll JA, Willard D, Lebrilla CB. *Analytica Chimica Acta.* 1995; **307**: 431.
142. Asam MR, Glish GL. *J. Am. Soc. Mass Spectrom.* 1999; **10**: 119.

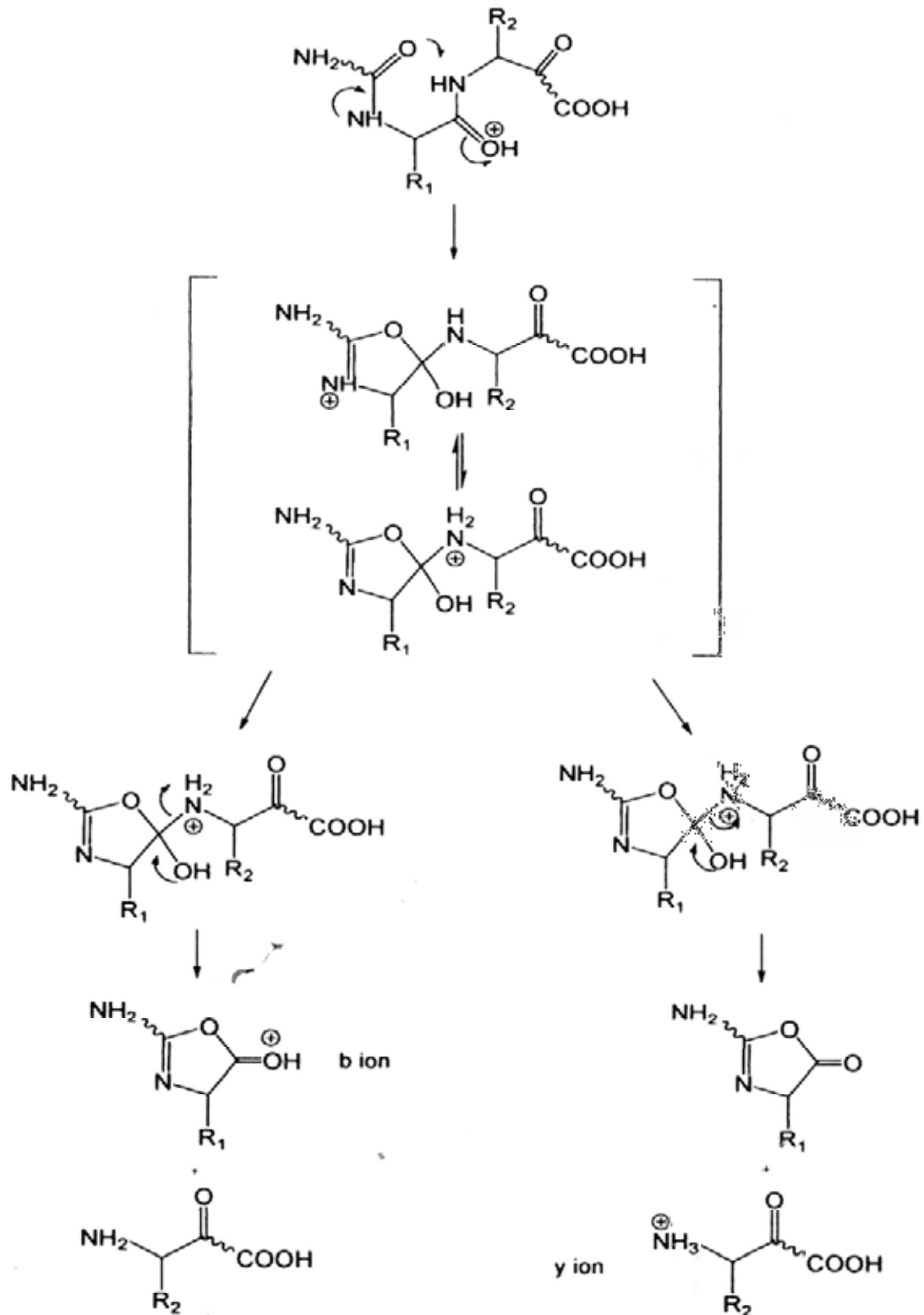
143. Anders LR, Beauchamp JL, Dunbar RC, Baldeschwieler JD. *J. Chem. Phys.* 1966; **45**: 1062.
144. Comisarow MB, Marshall AG. *Chem. Phys. Lett.* 1974; **25**: 282.
145. Cheng L, Cournoyer JJ, O'Connor PB. *J. Am. Soc. Mass Spectrom.* 2006; **17**: 1605.
146. Nielsen ML, Budnik BA, Haselmann KF, Olsen JV, Zubarev RA. *Chem. Phys. Letters* 2000; **330**: 558.
147. Cooper HJ, Håkansson K, Marshall AG. *Mass Spectrom. Rev.* 2005; **24**: 201.
148. Cooper HJ. *J. Am. Soc. Mass Spectrom.* 2005; **16**: 1932.
149. Haselmann KF, Schmidt M. *Rapid Commun. Mass Spectrom.* 2007; **21**: 1003.
150. Lee S, Chung G, Kim J, Oh HB. *Rapid Commun. Mass Spectrom.* 2006; **20**: 3167.
151. Bakken V, Helgaker T, Uggerud E. *Eur. J. Mass Spectrom.* 2004; **10**: 625.
152. Chakraborty T, Holm AIS, Hvelplund P, Nielsen SB, Pouilly J, Worm ES, Williams ER. *J. Am. Soc. Mass Spectrom.* 2006; **17**: 1675.
153. Prell JS, O'Brien JT, Holm AIS, Leib RD, Donald WA, Williams ER. *J. Am. Chem. Soc.* 2008; **130**: 12680.
154. Holm AIS, Larsen MK, Panja S, Hvelplund P, Nielsen SB, Leib RD, Donald WA, Williams ER, Hao C, Turecek F. *Int. J. Mass Spectrom.* 2008; **276**: 116.
155. McFarland MA, Chalmers MJ, Quinn JP, Hendrickson CL, Marshall AG. *J. Am. Soc. Mass Spectrom.* 2005; **16**: 1060.
156. Hvelplund P, Liu B, Nielsen SB, Tomita S. *Int. J. Mass Spectrom.* 2003; **225**: 83.
157. Hvelplund P, Liu B, Nielsen SB, Panja S, Pouilly J, Stochkel K. *Int. J. Mass Spectrom.* 2007; **263**: 66.
158. Bernigauda V, Cederquist H, Haag N, Holm AIS, Huber BA, Hvelplund P, Kadhane U, Larsen MK, Manil B, Nielsen SB, Panja S, Ptasinska S, Rangama J, Reinhed P, Schmidt HT, Streletskii AV, Stochkel K, Worm ES, Zettergren H. *Int. J. Mass Spectrom.* 2008; **276**: 77.
159. Belyayev MA, Cournoyer JJ, Lin C, O'Connor PB. *J. Am. Soc. Mass Spectrom.* 2006; **17**: 1428.
160. Jones JW, Sasaki T, Goodlett DR, Turecek F. *J. Am. Soc. Mass Spectrom.* 2007; **18**: 423.
161. Li XJ, Cournoyer JJ, Lin C, O'Connor PB. *J. Am. Soc. Mass Spectrom.* 2008; **19**: 1514.
162. Chamot-Rooke J, Malosse C, Frison G, Turecek F. *J. Am. Soc. Mass Spectrom.* 2007; **18**: 2146.
163. Mihalca R, Kleinnijenhuis AJ, McDonnell LA, Heck AJR, Heeren RMA. *J. Am.*

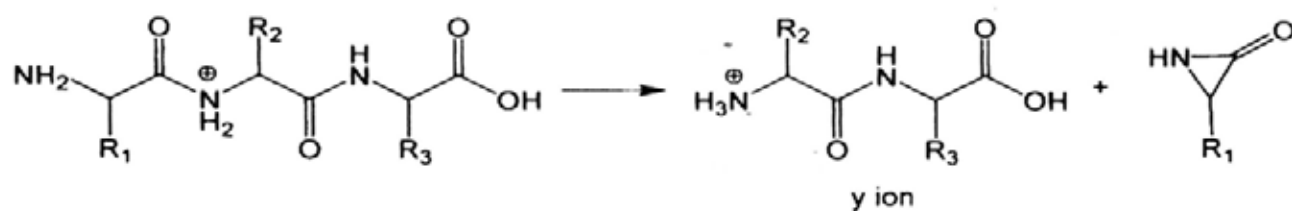
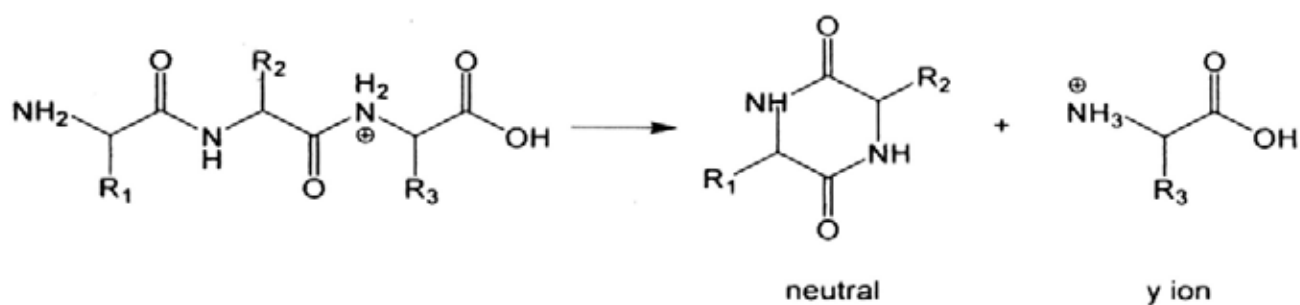
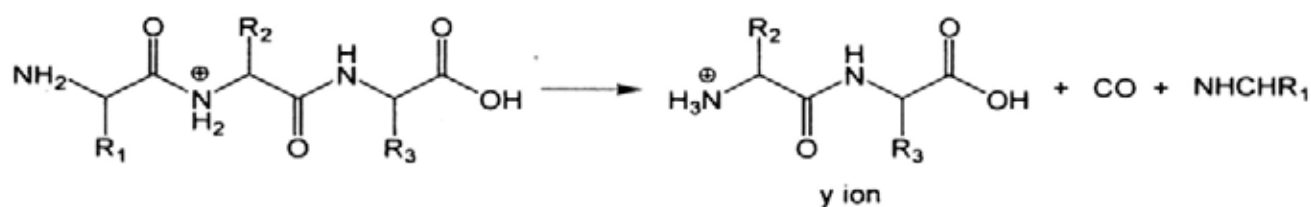
- Soc. Mass. Spectrom.* 2004; **15**: 1869.
164. Hongo Y, Nakamura T, Sato A. *J. Mass Spectrom. Soc. Jpn.* 2007; **55**: 77.
165. Sohn CH, Chung CK, Yin S, Ramachandran P, Loo JA, Beauchamp JL. *J. Am. Chem. Soc.* 2009; **131**: 5444.
166. Breuker K, Oh HB, Cerda BA, Horn DM, McLafferty FW. *Eur. J. Mass Spectrom.* 2002; **8**: 177.
167. Rodriguez CF, Orlova G, Guo YZ, Li XM, Siu CK, Hopkinson AC, Siu KWM. *J. Phys. Chem. B* 2006; **110**: 7528.
168. Li Z, Matus MH, Velazquez HA, Dixon DA, Cassady CJ. *Int. J. Mass Spectrom.* 2007; **265**: 213.

Appendix I

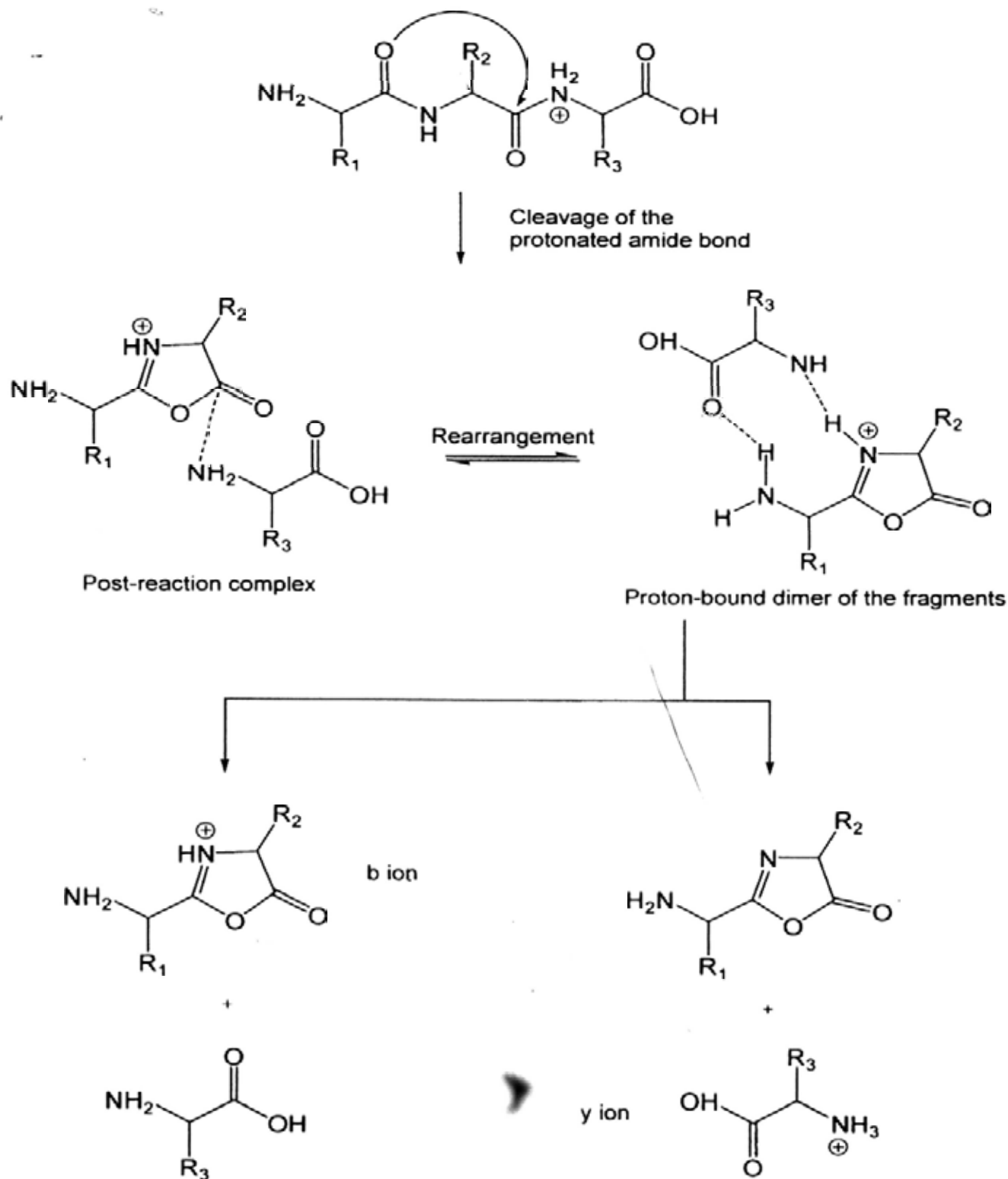
Proposed dissociation mechanisms of protonated peptide under low-energy CID conditions

'Amino-O' Pathway



'Aziridinone' Pathway**'Diketopiperazine' Pathway****'a₁-y_x' pathway**

'Oxazolone' Pathway



Appendix II

Pulse programs for MS and MSⁿ experiments

| Block | MS | | MS ² | | | MS ³ | |
|------------------------------------|-----|-----|-----------------|-----|--------|--------------------|---------|
| | ESI | MIF | CID | ECD | DR-ECD | (CID) ² | ECD-CID |
| Initialization | * | * | * | * | * | * | * |
| Start scan accumulation | * | * | * | * | * | * | * |
| Source quench | * | * | * | * | * | * | * |
| Cell quench | * | * | * | * | * | * | * |
| Hexapole accumulation | * | | * | * | * | * | * |
| Ionization | * | | * | * | * | * | * |
| Ionization (multiple ions) | | * | | | | | |
| Cooling gas | | * | | | | | |
| Pumping delay | | * | | | | | |
| Isolation | | | * | * | * | * | * |
| Cleanup shots | | | * | * | * | * | * |
| ECD | | | | * | | | * |
| DR-ECD | | | | | * | | |
| Delay | | | | * | * | | * |
| Pulsed valve | | | * | | | * | * |
| Parent ion activation | | | * | | | * | * |
| Reaction delay | | | * | | | * | * |
| | | | | | | # | |
| Excitation | * | * | * | * | * | * | * |
| Detection | * | * | * | * | * | * | * |
| Stop | * | * | * | * | * | * | * |
| Phase program definitions for FCUs | * | * | * | * | * | * | * |

Repeat once from 'Isolation' to 'Reaction delay'.

* Indicates blocks should be present in sequential order in the pulse programs and

the source codes of each of these blocks are as follows:

Initialization

```

;Initialization Block
;#ES_block "Initialization"
;#ES_bitmap "init3.bmp"
;#ES_conditional_pp DM bb          1u setnmr3|30          ; bit 30 hi = unmixed signal to
ADC
;#ES_conditional_pp DM hires      1u setnmr3^30          ; bit 30 low = mixed signal to ADC
;#ES_conditional_pp RGAIN high    1u setnmr3^28          ; bit 28 low = Receiver gain high
;#ES_conditional_pp RGAIN low     1u setnmr3|28          ; bit 28 hi = Receiver gain low

```

Start scan accumulation

```

;Start Scan Accum Block (NS loop)
;#ES_block "Start Experiment"
;#ES_bitmap "start2.bmp"
;#ES_eventtype user_delay
;#ES_parameter d0
1 ze          ; clear memory buffers in RCU
10 d0 setnmr4|7 ; turn on Ultra RF amp (AGPP_OUT[0])
                ; NOTE: d0 must be 100ms or greater!
10u reset:f1  ; reset phase of DDS in FCU 1

```

Source quench

```

;Source Quench Block
;#ES_block "ESI Source Quench" optional
;#ES_bitmap "ESIquench1.bmp"
;#ES_eventtype quench
;#ES_parameter d3
d3 setnmr3|24 ; quench the ion guide (DEFLECTION)
1u setnmr3^24

```

Cell quench

```

;Cell Quench Block
;#ES_block "Cell Quench" optional
;#ES_bitmap "quench.bmp"
;#ES_eventtype quench
;#ES_parameter d4
d4 setnmr3|27 ; cell quench (QUENCH)
1u setnmr3^27

```

Hexapole accumulation

```

;Hexapole Accumulation Block
;#ES_block "Hexapole Accumulation"
;#ES_bitmap "hex_fill.bmp"
;#ES_eventtype user_delay
;#ES_parameter d1
    d1                ; post quench delay

```

Ionization

```

;Ionization Block
;#ES_block "Ion Generation"
;#ES_bitmap "ion_gen2.bmp"
;#ES_eventtype user_pulse
;#ES_parameter d2 d5
    d2 setnmr3|24      ; external ionization pulse (DEFLECTION)
    lu setnmr3^24
    d5                 ; post ionization delay

```

Ionization (multiple ions)

```

;Ionization Block
;#ES_block "Multiple-Ion Generation" optional
;#ES_bitmap "ion_gen2.bmp"
;#ES_eventtype user_pulse
;#ES_parameter d2 d7
30 d7                ; delay
    d2 setnmr3|24      ; external ionization pulse (DEFLECTION)
    lu setnmr3^24

```

Cooling gas

```

;Pulsed Valve Block
;#ES_block "Cooling gas" optional
;#ES_bitmap "p_valve.bmp"
;#ES_eventtype user_pulse
;#ES_parameter d13
    d13 setnmr3|22     ; Pulsed Valve 1 (VALVE1)
    lu setnmr3^22
    lo to 30 times l30 ; loop back to the ion generation pulse (line number30)

```

Pumping delay

```

;Reaction Delay Block
;#ES_block "Pumping Delay" optional
;#ES_bitmap "react_del4.bmp"

```

```

;#ES_eventtype user_delay
;#ES_parameter d8
    d8          ; reaction delay

```

Isolation

```

;MS/MS Selection Block
;#ES_block "Isolation (MS-2)" optional
;#ES_bitmap "msms_sel_a.bmp"
;#ES_eventtype corr_sweep
;#ES_parameter p4 p14
    10u p14:f1      ; set attenuation for correlated sweep (FCU-1)
20 (p4 ph2 fq1):f1 ; correlated sweep
    lo to 20 times l0 ; L[0] steps in sweep
;#ES_flag_comment ;#FC_ fq1:f1 corr_sweep 0

```

Cleanup shots

```

;Cleanup Shots Block
;#ES_block "Isolation Shots (MS-2)" optional
;#ES_bitmap "cl_shots.bmp"
;#ES_eventtype corr_shot
;#ES_parameter p7 p17
    10u p17:f1      ; set attenuation for shots (FCU-1)
30 (p7 ph2 fq1):f1 ; high resolution clean-up shots
    lo to 30 times l3 ; L[3] total shots
;#ES_flag_comment ;#FC_ fq1:f1 corr_shot 0

```

ECD

```

;ECD Block
;#ES_block "ECD" optional
;#ES_bitmap "ECD.bmp"
;#ES_eventtype user_pulse
;#ES_parameter d7
    d7 setnmr3|26 ; ECD pulse (INT_GATE)
    10u setnmr3^26

```

DR-ECD

```

;DRECD Block
;#ES_block "ECD" optional
;#ES_bitmap "ECD.bmp"
;#ES_eventtype corr_shot
;#ES_parameter d7 p9 p19
    d7 setnmr3|26 ; ECD pulse (INT_GATE)
    10u p19:f1      ; set attenuation for shots (FCU-1)

```

```

70 (p9 ph2 fq1):f1      ; high resolution clean-up shots
  lo to 70 times l4    ; L[4] total shots
  10u setnmr3^26
;#ES_flag_comment      ;#FC_fq1:f1 corr_shot 0

```

Delay

```

;Delay Block
;#ES_block "Delay" optional
;#ES_bitmap "ECD.bmp"
;#ES_eventtype user_pulse
;#ES_parameter d12
  d12

```

Pulse valve

```

;Pulsed Valve Block
;#ES_block "Pulsed Valve (MS-2)" optional
;#ES_bitmap "p_valve.bmp"
;#ES_eventtype user_pulse
;#ES_parameter d26
  d26 setnmr3|22      ; Pulsed Valve 1 (VALVE1)
  lu setnmr3^22

```

Parent ion activation

```

;Parent Ion Activation Block
;#ES_block "Ion Activation (MS-2)" optional
;#ES_bitmap "activate.bmp"
;#ES_eventtype ion_activation
;#ES_parameter p8 pl8
  10u pl8:f1          ; set attenuation for activation (FCU-1)
  (p8 ph2 fq1):f1    ; activation shot on the parent ion
;#ES_flag_comment    ;#FC_fq1:f1 parent_ion_activation 0

```

Reaction delay

```

;Reaction Delay Block
;#ES_block "Pumping Delay (MS-2)" optional
;#ES_bitmap "react_del4.bmp"
;#ES_eventtype user_delay
;#ES_parameter d6
  d6                  ; reaction delay

```


Excitation

```

;Excitation Block
;#ES_block "Excitation"
;#ES_bitmap "excite.bmp"
;#ES_eventtype excitation_sweep
;#ES_parameter p3 pl3
    10u pl3:f1          ; set attenuation for excitation (FCU-1)

;#ES_conditional_pp EM shot
    (p3 ph1 fq1):f1          ; detection excitation shot
;#ES_conditional_pp EM shot    ;#FC_fq1:f1 excitation_shot
;#ES_conditional_pp EM sweep
40 (p3 ph1 fq1):f1          ; detection excitation sweep
;#ES_conditional_pp EM sweep
    lo to 40 times l31          ; L[31] steps in sweep
;#ES_conditional_pp EM sweep    ;#FC_fq1:f1 excitation_sweep

```

Detection

```

;Detection Block
;#ES_block "Detection"
;#ES_bitmap "detect.bmp"
;#ES_eventtype detection
;#ES_parameter d30
    1u setnmr4^7          ; turn off Ultra RF amp before detect (AGPP_OUT[0])
    d30                    ; receiver dead time
    go = 10 ph1            ; scan accumulation (loop to 10 times NS)

```

Stop

```

;Stop Block
;#ES_block "Exit"
;#ES_bitmap "exit.bmp"
    wr #0                  ; write data to disk
    exit                    ; end acquisition/experiment

```

Phase program definitions for FCUs

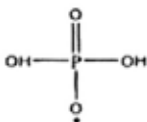
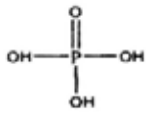
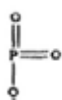
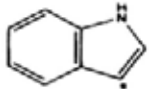
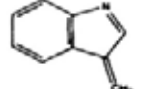
```

; Phase program definitions for FCUs
    ph1=0 0 2 2          ; phase program: 0 0 180 180 (exc/det RF)
    ph2=0 0 0 0          ; phase program: 0 0 0 0 (all other RF)

```

Appendix III

Assignments of labeled side chain in mass spectra

| Amino acid | Odd-electron species | | Even-electron species | |
|----------------------------|----------------------------------|-------------------------------------------------------------------------------------------|-----------------------|---------------------------------------------------------------------------------------|
| | Label | Assignment | Label | Assignment |
| Glycine [G] | -- | -- | -- | -- |
| Alanine [A] | -- | -- | -- | -- |
| Valine [V] | V _{SC} [•] | [•] CH ₃ | -- | -- |
| Leucine [L] | L _{SC} [•] | [•] CH(CH ₃) ₂ | L _{SC} | CH ₃ CH=CHCH ₃ |
| Isoleucine [I] | I _{SC} [•] | [•] CH ₂ CH ₃ | I _{SC} | CH ₃ CH=CHCH ₃ |
| Proline [P] | -- | -- | -- | -- |
| Lysine [K] | K _{SC} [•] | [•] CH ₂ CH ₂ CH ₂ NH ₂ | K _{SC} | H ₂ C=CHCH ₂ CH ₂ NH ₂ |
| Arginine [R] | K _{SC} ^{••} | [•] CH ₂ CH ₂ CH ₂ NH ₃ ⁺ | | |
| | R _{SC} [•] | [•] NH ₂ C(NH)NH ₂ | R _{SC} | H ₂ C=CHCH ₂ -NHC(NH)NH ₂ |
| | R _{SC} ^{••} | [•] CHCH ₂ -NHC(NH ₂ ⁺)NH ₂ | | |
| Serine [S] | -- | -- | -- | -- |
| Phosphorylated Serine [pS] | pS _{SC} [•] |  | pS _{SC} |  |
| | pS _{SC1} [•] |  | -- | -- |
| Threonine [T] | -- | -- | -- | -- |
| Aspartic Acid [D] | -- | -- | D _{SC} | O=C=O |
| Glutamic Acid [E] | E _{SC} [•] | [•] CH ₂ COOH | E _{SC} | CH ₂ =CHCOOH |
| Asparagine [N] | N _{SC} [•] | [•] C(O)NH ₂ | -- | -- |
| Glutamine [Q] | Q _{SC} [•] | [•] CH ₂ C(O)NH ₂ | Q _{SC} | CH ₂ =CHC(O)NH ₂ |
| Cysteine [C] | C _{SC} [•] | [•] SH | C _{SC} | S=CH ₃ |
| Methionine [M] | M _{SC} [•] | [•] CH ₂ SCH ₃ | M _{SC} | CH ₂ =CHSCH ₃ |
| Oxidized Methionine [M(O)] | M(O) _{SC} [•] | [•] CH ₃ SO | M(O) _{SC} | CH ₃ SOH |
| | M(O) _{SC1} [•] | [•] CH ₂ SOCH ₃ | M(O) _{SC1} | CH ₂ SO |
| | -- | -- | M(O) _{SC2} | CH ₂ =CHSOCH ₃ |
| Phenylalanine [F] | -- | -- | -- | -- |
| Histine [H] | -- | -- | -- | -- |
| Tryptophan [W] | W _{SC} [•] |  | W _{SC} |  |
| Tyrosine [Y] | -- | -- | Y _{SC} | CH ₂ (C ₆ H ₄ O) |

The hydrogen bonding patterns of the low-energy structures obtained in conformational searches

Sample: RGEGEGEGEGR

Form: Zwitterionic form

R G E G E G E G E G E G E G R
1 2 3 4 5 6 7 8 9 10 11 12 13 14

Conformer 1 (Relative energy = -2737.52kJ/mol)

| | | | | | | | | | | | | | | | |
|---------------|--------------------|-------------------|-------------------|-------------------|----------------|----------------|-------------------|----------------|-------------------|----------------------|----|--------------------|--------------------|--------------------|--------------------|
| C=O | 4 | 3 | E ₆ OH | E ₃ OH | R _N | R _N | E ₂ OH | R _N | E ₅ OH | 11,E ₄ OH | 12 | N _{ter} 3 | N _{ter} 2 | N _{ter} 3 | C _{ter} 1 |
| Inter-residue | 1 | 2 | 3 | 4 | 5 | 6 | 7 | 8 | 9 | 10 | 11 | 12 | 13 | 14 | N _{ter} 1 |
| N-H | C _{ter} 1 | E ₁ OH | 2 | 1 | E ₃ | E ₃ | - | - | E ₂ | E ₅ | 10 | 11 | - | - | |

Conformer 2 (Relative energy = -2732.66kJ/mol)

| | | | | | | | | | | | | | | | |
|---------------|--------------------|-------------------|-------------------|-------------------|----------------|----------------|---|----------------|-------------------|-------------------|----|--------------------|----|--------------------|--------------------|
| C=O | 4 | 3 | E ₆ OH | E ₃ OH | R _N | R _N | - | R _N | E ₅ OH | 11 | 13 | N _{ter} 2 | 14 | N _{ter} 3 | C _{ter} 1 |
| Inter-residue | 1 | 2 | 3 | 4 | 5 | 6 | 7 | 8 | 9 | 10 | 11 | 12 | 13 | 14 | N _{ter} 1 |
| N-H | C _{ter} 1 | E ₁ OH | 2 | 1 | E ₃ | E ₃ | - | - | - | E ₅ OH | 10 | - | 11 | 13 | |

Conformer 3 (Relative energy = -2731.12kJ/mol)

| | | | | | | | | | | | | | | | |
|---------------|--------------------|-------------------|-------------------|-------------------|----------------|----------------|---|----------------|-------------------|----|----------------|--------------------|----|--------------------|--------------------|
| C=O | - | 3,4 | E ₂ OH | E ₃ OH | R _N | R _N | - | R _N | E ₅ OH | - | 13 | N _{ter} 2 | 14 | N _{ter} 3 | C _{ter} 1 |
| Inter-residue | 1 | 2 | 3 | 4 | 5 | 6 | 7 | 8 | 9 | 10 | 11 | 12 | 13 | 14 | N _{ter} 1 |
| N-H | C _{ter} 1 | E ₁ OH | 2 | 2 | - | E ₃ | - | - | - | - | E ₂ | - | 11 | 13 | |

Conformer 4 (Relative energy = -2729.26kJ/mol)

| | | | | | | | | | | | | | | | |
|---------------|--------------------|----------------|-------------------|-------------------|----------------|----------------|---|----------------|-------------------|----|----------------|--------------------|----|--------------------|--------------------|
| C=O | 4 | 3 | E ₆ OH | E ₃ OH | R _N | R _N | - | R _N | E ₅ OH | - | 13 | N _{ter} 2 | 14 | N _{ter} 3 | C _{ter} 1 |
| Inter-residue | 1 | 2 | 3 | 4 | 5 | 6 | 7 | 8 | 9 | 10 | 11 | 12 | 13 | 14 | N _{ter} 1 |
| N-H | C _{ter} 1 | E ₆ | 2 | 1 | E ₃ | E ₃ | - | - | - | - | E ₂ | - | 11 | 13 | |

Sample: RGEGEGEGEGEGR

Form: Zwitterionic form

R G E G E G E G E G E G E G R
 1 2 3 4 5 6 7 8 9 10 11 12 13 14

Conformer 5 (Relative energy = -2729.24kJ/mol)

| | | | | | | | | | | | | | | | |
|---------------|--------------------|-------------------|---|---|--------------------|--------------------------------|----------------|--------------------|---|-------------------|-------|-------------------|-------------------|-------------------|--------------------|
| C=O | - | 3 | 4 | 5 | N _{ter} 2 | R _N | R _N | N _{ter} 3 | - | E ₂ OH | 10,13 | E ₁ OH | E ₆ OH | E ₅ OH | C _{ter} 1 |
| Inter-residue | 1 | 2 | 3 | 4 | 5 | 6 | 7 | 8 | 9 | 10 | 11 | 12 | 13 | 14 | N _{ter} 1 |
| N-H | C _{ter} 1 | E ₅ OH | 2 | 3 | 4 | E ₂ ,E ₃ | E ₂ | - | - | 11 | - | - | 11 | - | |

Conformer 6 (Relative energy = -2729.05kJ/mol)

| | | | | | | | | | | | | | | | |
|---------------|--------------------|-------------------|-------------------|-------------------|----------------|----------------|---|----------------|-------------------|----|----------------|--------------------|----|--------------------|--------------------|
| C=O | 4 | 3 | E ₆ OH | E ₃ OH | R _N | R _N | - | R _N | E ₅ OH | - | 13 | N _{ter} 2 | 14 | N _{ter} 3 | C _{ter} 1 |
| Inter-residue | 1 | 2 | 3 | 4 | 5 | 6 | 7 | 8 | 9 | 10 | 11 | 12 | 13 | 14 | N _{ter} 1 |
| N-H | C _{ter} 1 | E ₁ OH | 2 | 1 | E ₃ | E ₃ | - | - | - | - | E ₂ | - | 11 | 13 | |

Conformer 7 (Relative energy = -2728.14kJ/mol)

| | | | | | | | | | | | | | | | |
|---------------|--------------------|-------------------|-------------------|-------------------|----------------|----------------|---|----------------|-------------------|----|----------------|--------------------|----|--------------------|--------------------|
| C=O | 4 | 3 | E ₂ OH | E ₃ OH | R _N | R _N | - | R _N | E ₅ OH | - | 13 | N _{ter} 2 | 14 | N _{ter} 3 | C _{ter} 1 |
| Inter-residue | 1 | 2 | 3 | 4 | 5 | 6 | 7 | 8 | 9 | 10 | 11 | 12 | 13 | 14 | N _{ter} 1 |
| N-H | C _{ter} 1 | E ₁ OH | 2 | 1 | E ₃ | E ₃ | - | - | - | - | E ₂ | E ₆ | 11 | 13 | |

Conformer 8 (Relative energy = -2728.03kJ/mol)

| | | | | | | | | | | | | | | | |
|---------------|--------------------|----------------------------------|---|------------------|--------------------|--------------------------------|----------------|--------------------|---|-------------------|-------|-------------------|-------------------|-------------------|--------------------|
| C=O | - | - | 4 | 5 | N _{ter} 2 | R _N | R _N | N _{ter} 3 | - | E ₂ OH | 10,13 | E ₁ OH | E ₆ OH | E ₅ OH | C _{ter} 1 |
| Inter-residue | 1 | 2 | 3 | 4 | 5 | 6 | 7 | 8 | 9 | 10 | 11 | 12 | 13 | 14 | N _{ter} 1 |
| N-H | C _{ter} 1 | E ₅ OH,E ₅ | - | 3,E ₅ | 4 | E ₂ ,E ₃ | E ₂ | - | - | 11 | - | - | 11 | - | |